Optical Properties of TMDC Monolayers and Their Heterostructures

Dissertation

zur

Erlangung des Doktorgrades

der Naturwissenschaften

(Dr. rer. Nat.)

dem

Fachbereich Physik

der Philipps-Universität Marburg

vorgelegt von

M.Sc. Lorenz Maximilian Schneider

aus

Lohra, geboren in Marburg

Marburg (Lahn), 2020

Vom Fachbereich Physik der Phillips-Universität als Dissertation angenommen am: 09.09.2020

Betreuer: Prof. Dr. rer. Nat. Martin Koch / Dr. rer. Nat. Arash Rahimi-Iman

Erstgutachter: Prof. Dr. rer. Nat. Martin Koch

Zweitgutachter: Dr. rer. Nat. Alexey Chernikov

Tag der mündlichen Prüfung: 23.09.2020

Hochschulkennziffer: 1180

Table of Contents

List of Abbreviations:

AFM	Atomic force microscope
APD	Avalanche photo diode
CB	Conduction band
CCD	Charge coupled device
CIDBROM	Circular in-plane distributed Bragg reflector optical microcavity
CMOS	Complementary metal-oxide-semiconductor
CVD	Chemical vapour deposition
h-BN	Hexagonal boron nitride
ICCD	Intensified charge coupled device
MOVPE	Metal organic vapour phase epitaxy
MQW	Multi quantum well
LA/LO	Longitudinal acoustic/optical (phonon branch)
Laser	Light amplification by stimulated emission of radiation
LED	Light emitting device
LPB	Lower polariton branch
PL	Photoluminescence
PSB	Phonon side band
RC	Reflection contrast
SLE	Semiconductor luminescence equation
s-SNOM	Scattering type scanning near field optical microscope
SQW	Single quantum well
TA/TO	Transversal acoustic/optical (phonon branch)
TMDC	Transition metal dichalcogenide
TRPL	Time-resolved photoluminescence
UPB	Upper polariton branch
VB	Valence band
X	Exciton (neutral)
XX	Biexciton
ZA	z-mode (phonon branch)

1. Introduction

Starting with the first systematic exfoliation and analysis of graphene by Novoselov and Geim fifteen years ago (Novoselov 2004), the promising field of 2D-materials emerged. At the example of graphene, it directly became obvious, that this class of materials hosts amazingly rich physics such as Dirac fermions (Novoselov et al. 2005), spin valley locking (Gmitra and Fabian 2017), extremely high conductivity (Novoselov 2004) and mechanical stability (Frank et al. 2007). Some years later in 2010 the group of Tony Heinz thinned molybdenum disulfide as the first transition metal dichalcogenide (TMDC) down to the monolayer limit (Mak et al. 2010), revisiting the exploration of layered van-der-Waals materials which were previously addressed in the few-layer regime back in the 1970s.

Accordingly, the class of van-der-Waals materials was not unknown (Beal and Liang 1976; Bordas and Davis 1973; Frindt 1963; Liang, Beal, and Knights 1971; Meinhold and Weiser 1976; Weiser 1973), as well as the idea of exfoliation (Frindt and Yoffe 1962) to a single layer (Murray and Yoffe 1972) was not new. Nonetheless it took about 40 years to improve the crystal quality to reach the monolayer limit. In the time after the first exfoliation of graphene, many representatives of other subclasses of 2D-materials have been found. Among the identified 2D insulators hexagonal boron nitride (h-BN) (Watanabe, Taniguchi, and Kanda 2004) has become the most prominent and important one, as it has been shown to be a brilliant substrate for other 2D-materials, improving their optical quality tremendously (Ajayi et al. 2017; Cadiz et al. 2017; Lorenz Maximilian Schneider et al. 2017; Wierzbowski et al. 2017). In addition, more exotic classes have been synthesized and exfoliated (cf. **Table 1**).

***Table 1*| Overview of the 2D materials library with their classification.** The table has been adapted with permission from (Duong, Yun, and Lee 2017) displaying materials with different number of components (1 to 3) in the 2D lattice, different electronic properties, as well as different peculiarities of the structure. The library is not complete but gives an overview over of the possibilities. Copyright 2017 American Chemical Society.

COMP.	NAME		EXAMPLES	INS.	SC.	METAL	MAGNETIC	SUPERC.	NOTES
1	Graphene					X		X	Dirac cones
	Pure SC		Si, Ge, Sn		X				
			P		X				
2	Boron		MgB2			X		X	
	Nitrides		h-BN	X					
			Ca_2N			X			Electride
	Oxides	MO_3	MoO_3,WO_3		X				Strong correlations
	Chalcogenides	MCh	GaSe, InSe		X				
			FeSe			X	X		
		MCh_2	2H-MoS_2, 2H-NbS_2		X	X		X	
			1T-NbS_2, 1T-PtS_2		X	X		X	
			1T-WTe_2			X			Weyl-semimetal
		MCh_3	$NbSe_3$, $ZrTe_3$			X		X	Quasi-1D-Charge density wave
		M_2Ch_3	Bi_2Te_3		X				Topological Insulator
	Halides	MH	ZrBr		X				Quantum spin Hall insulator
		MH_2	CdI_2, $CoCl_2$		X				
		MH_3	$CrCl_3$, $RuCl_3$		X		X		Spin chain
3	Oxyhalides	MOH	FeOCl		X		X		
	Nitrohalides	MNH	TiNCl, ZrNCl					X	Quantum spin Hall insulator
	Posphorous trichalcogenides	$MPCh_3$	$FePS_3$, $SnPS_3$		X		X		
	Sili-tritelerides	M(Si,Ge)Te_3	$CrSiTe_3$		X		X		

These include topological insulators such as Bi_2Se_3 (Qi and Zhang 2010; Y. Zhang et al. 2010) as well as superconductors. See for example (Yokota et al. 2000) for a first encounter of quasi-2D superconductor

when studying the van-der-walls material 2H-$TaSe_2$. Here $NbSe_2$ is an example for a 2D superconductor that has been exfoliated by different groups (Xi et al. 2016; Yokoya 2001). Only recently, also ferromagnetic materials (B. Huang et al. 2017), Mott-insulators (Yijun Yu et al. 2015), topological semimetals (Zaiyao Fei et al. 2017) and many other kinds of 2D-material classes have been shown experimentally as well.

At present, a major goal of the 2D-materials community is to combine different materials in order to engineer new material properties by van-der-Waals stacking or even epitaxy (Geim and Grigorieva 2013; Novoselov et al. 2016a), while taking advantage of the exotic properties of many of the 2D-materials available. Here, the resulting heterostructures not only reveal the properties of the individual layered constituents but they exhibit tailored properties caused by the strong influence of the environment and hybridization of atomic orbitals, from which a mixture of unique and novel properties can arise (Y. K. Luo et al. 2017). Therefore, the picture of a LEGO type building (Geim and Grigorieva 2013) is used often to show the vast options with regard to the combination of 2D crystals in a heterostructure stack. In addition, in contrast to conventional semiconductors, there is no need for lattice matching or a fixed orientation during assembly, although the relative orientation between different or similar 2D lattices may be important for the composed stack's features. One recent prominent example of the inspiring physics related to stacks at a nontrivial twist angle is that of a bilayer graphene stacked at the "magic" angle of 1.1 degrees. (Y. Cao, Fatemi, Fang, et al. 2018). While both constituents are semi-metallic, the overall stack shows to be a superconductor, a metal, a Mott-insulator or even having ferromagnetic order (Sharpe et al. 2019) depending on gating and temperature, whereas at the natural stacking angle only small changes in the band structure occur.

In this context of the very wide 2D materials research, the work presented here focuses on the combination of the semiconducting TMDCs with one another and h-BN. TMDCs have several interesting features like a high oscillator strength (Yilei Li, Chernikov, et al. 2014a), huge exciton binding energies (Chernikov et al. 2014) and spin-valley locking (T. Cao et al. 2012) that make these materials promising for a vast number of technological fields (Jariwala et al. 2014). Here, spin-valley locking is a term describing the fact that at ***K*** and ***K'*** valleys of the Brillouin zone a different spin orientation is observed for the relevant bands and a selective excitation of a valley is possible with circularly polarized light.

In the following, some of the promising application fields and the advantage of 2D materials in these fields will be introduced shortly. As TMDCs are direct semiconductors in the monolayer limit, the most obvious field of interest is very likely that of conventional optoelectronics (Mak and Shan 2016; M. Ye, Zhang, and Yap 2017). Here, the aims are the realization of light emitting devices (LEDs) (Withers et al. 2015), lasers (S. Wu et al. 2015), solar cells (Peng, Ang, and Loh 2015), detectors (Mu, Xiang, and Liu 2017), saturable absorbers (Z. Luo et al. 2016) and other optical elements. Generally, all of these are realized by employing monolayers as single- (SQW) or multi-quantum-well (MQW) systems or "simple" p-n junctions (Novoselov et al. 2016b). While in this area almost no fundamentally new technologies are arising, the absence of need to lattice-match the layer, as well as to match the crystal orientation offers a tremendous amount of new possibilities compared to conventional semiconductors. Furthermore, the material can be easily integrated into flexible electronics. In addition, the van-der-Waals forces allow hybrid approaches (Jariwala, Marks, and Hersam 2017) where TMDC's and other van-der-Waals materials are combined with conventional semiconductors (Sarkar et al. 2015), organic (Jariwala et al. 2016) or molecular materials (C. H. Lee et al. 2014). The citations are just illustrative and are not meant to be complete as there are numerous reports on different approaches.

On the other hand, there are research fields harvesting the more exotic properties of TMDCs. The high oscillator strength together with the high binding energies opens the possibility of polariton formation

(C. Schneider, Glazov, et al. 2018), or in principle even the observation of polariton Bose-Einstein condensates at room temperature (N. Lundt, Maryński, et al. 2017). Even though polaritonic devices (Fraser 2017) and condensate-based technology at room temperature have been reported before for ZnO (L. Sun et al. 2010) or other wide bandgap materials (Guillet and Brimont 2016), TMDCs provide this option even in the range of visible and near infrared energies. Thus, they could provide a huge step forward for bringing polaritonic circuits and devices into real devices. Due to their light mass and therefore drastically higher mobility, they could potentially increase the speed of electronics by orders of magnitude compared to common silicon-based computation and simultaneously allow for relatively facile-integration into existing silicon technology as van-der-Waals materials.

The already mentioned observation of spin-valley locking (Mak, Xiao, and Shan 2018) indeed opened a complete field namely valleytronics, see (Schaibley et al. 2016a; Vitale et al. 2018; Xu et al. 2014) and refs within. In contrast to electronics, where information is encoded in charge, here the valley index or valley pseudospin is used. In contrast to previous approaches in III/V semiconductors (Shkolnikov et al. 2002) and silicon (Ohkawa and Uemura 1976, 1977; Sham et al. 1978), the spin-valley locking of TMDCs enables direct external manipulation (X. Chen et al. 2017; Smolenski et al. 2016; Z. Ye, Sun, and Heinz 2017), potentially even sub-cycle coherent control (Langer et al. 2018) on ps and fs timescales. This opens the path to the employment in quantum computing (Kormányos et al. 2014; Lucatto et al. 2019; Pawłowski, Zebrowski, and Bednarek 2018) or computation at optical clock rates. At the same time, if used in classical computation, the usage of the valley pseudospin can substantially reduce the heat generation due to resistive heating similar to spintronic approaches, and thus reduce the power consumption. Furthermore, valley polaritons have been observed (Y. J. Chen et al. 2017; Dufferwiel et al. 2017; Z. Sun et al. 2017), which combine the world of valleytronics with polariton technology.

It is immediately clear that the vast number of possible combinations of 2D-materials with each other as well as with substrates and with conventional semiconductors or molecular materials offers huge opportunities for engineering and tailoring the material stack properties to meet the demand of an individual application. To do that efficiently and systematically, several questions need to be addressed:

Firstly, the properties of the individual layers have to be understood well. While there has been tremendous progress during the research time devoted to this doctoral dissertation, still the actual influence of dark states (Brem et al. 2018) and higher quasiparticle properties (S.-Y. Chen et al. 2018) as well as basic properties of the exciton dispersion (Deilmann and Thygesen 2019; Qiu, Cao, and Louie 2015; H. Yu et al. 2014) are not yet fully understood. Especially, the last discussion still remains controversial since qualitative and quantitative theoretical predictions of contradicting nature exist. Here, **Chapter 4** shows the contributions of this work to the understanding of the influence of the surrounding on the fundamental properties of 2D-materials, the exciton-phonon coupling and the exciton diffusion. In addition, **Chapter 6** gives a valuable contribution for the discussion of the dispersion as it shows up to my knowledge the first experimental evidence to these theories. Furthermore, it presents the radiative pattern of bright and partially dark states and provides evidence for the phonon-sidebands in agreement with the prediction of Brem et al.

Secondly, the influence of the substrate and the (dielectric) environment should not be underestimated for this kind of materials. While during the time of this work the influence of static contributions by screening (Cudazzo, Tokatly, and Rubio 2011; Katsch et al. 2018; A. Steinhoff et al. 2014; Stroucken and Koch 2016) became well understood, the influence of the microscopic alignment within stacks is only partially known and many open questions remain unanswered. A better understanding of high symmetry alignments (Puretzky et al. 2016; Lorenz Maximilian Schneider, Kuhnert, et al. 2019) has been achieved recently. While formerly only the symmetry of the stack itself

was considered, the study presented in **Chapter 5** shows that also the symmetry of the surrounding has to be considered as it can lift the degeneracy between the layer. Thus, if the surrounding is asymmetric it renders the homobilayers in fact heterojunction. In contrast to high-symmetry stacks the investigations are at the starting point for less symmetric stacks, where moiré pattern (Naik and Jain 2018; Shah, Schneider, and Rahimi-Iman 2019; C. Zhang et al. 2017) and hybridization (Kunstmann et al. 2018) occur. Here a preliminary study showing this effect is shown in the second part of **Chapter 5.** In addition, one has to note that while the understanding in combining the same class of material has already made some progress, the path to understand proximity effects and to tailor properties by combining different material classes has just emerged, e.g. by exploring magnetic and semiconducting 2D-materials (Gmitra and Fabian 2017; Y. K. Luo et al. 2017; Seyler et al. 2018; Zhong et al. 2017).

Thirdly, for the way towards the application it is crucial to understand the challenges in the integration of van-der-Waals materials in established silicon-, III/V semiconductors- or fiber-based technology. Therefore, prototyping of devices integrating van-der-Walls materials in common structures in the field of silicon nitrides waveguides, telecommunication fibers, nanophotonics and nanoresonators is necessary. Here, the effects are studied in **Chapter 7** for one exemplary photonic structure.

The investigations presented in this thesis have been intended as a timely and valuable contribution to these three question blocks. Beginning with a brief theoretical overview on the physics most relevant to this study in **Chapter 2**, the thesis will introduce the experimental setup and methods in **Chapter 3**. Afterwards, four research directions will be summarized in the following **Chapters 4** to **7**, in providing individual summaries on the respective work and findings. The first block of results deals with the influence of the substrate, the production process as well as dielectric environment on the properties of excitonic and many-body complexes in TMDC monolayers. In the second block, the phenomena arising from the microscopic alignment in homojunctions at high symmetry are analyzed for selectively grown CVD samples. Here, especially the consequences for applications in valley- and layertronics are discussed. In addition, a preliminary study on a twisted heterojunction showing signs of moiré features is presented. The third block deals with angle resolved measurements, revealing dispersion most likely due to excitonic and polaritonic effects that can take place in monolayer samples of high quality and gives access to the measurement of valley dephasing mechanism due to exchange interaction. The last result chapter deals with a prototype device which integrates monolayers into sub-micron photonic structures employing circular Bragg gratings for efficient light in- and outcoupling from the 2D material. Not only the effects of this structure, but also generalized concepts (e.g. in the domain of light-matter interactions) have to be kept in mind when integrating van-der-Waals materials to such structures are discussed. The overall results are summarized in the closing chapter.

2. Theoretical Background

In the following a theoretical background of semiconductors optics will be provided. Hereby, the focus will be on introducing the theoretical models that are commonly used to describe the physics in two-dimensional materials. Besides this, the fundamental model differences that arise from their exceptional small thickness compared to 2D-quantum wells shall be mentioned and described as well.

At first, the theory regarding photoluminescence including many body physics will be introduced. As the physics of TMDC's is strongly governed by the presence of quasiparticles, not solely but especially by the presence of excitons, the concept of quasiparticles will be discussed in depth.

Following an overview of the family of van-der-Waals materials with a focus on TMDCs is given. For the group IV-TMDCs, a detailed explanation of the chemical bonding and orbital nature will be given as they are the basis for the peculiar band structure including spin-valley selective selection rules in these chemical compounds.

Many new phenomena discovered in van-der-Waals materials are related to the honeycomb lattice often found in this material class. Therefore, a subchapter will be dedicated to the intrinsic symmetries and their consequences. These consequences are linked to the concept of Berry curvature, valley and layer pseudo spin that are also introduced in detail.

2.1. Semiconductors and Quasiparticles

The source of photoluminescence from semiconductors is not only given by the coherent polarization induced by the pump pulse, but on most timescales dominantly by the incoherent microscopic polarization. While the coherent part can be still be modelled in a classical picture, this is not possible for the incoherent part, which is necessarily described by a quantum mechanical approach (Haug and Koch 2009; Kira and Koch 2006a; Schäfer and Wegener 2002; Stahl 1984). Furthermore, many phenomena occurring already at small carrier densities can only be explained through few or many body physics (Koch et al. 2006). Generally, this means a precise modelling of photoluminescence is a complex task even for an ideal semiconductor at low densities.

The physics of condensed matter is commonly discussed in the picture of quasi-particles. They are not only simplifying the calculations – in the sense of a more appropriate basis set – but also make it possible to comprehend the underlying physics. They actually represent the eigenvectors (or the approximated eigenvectors) of the system's Hamiltonian (Klingshirn 2012). In that sense they represent fundamental excitations of the system. It is essential for the understanding of the whole system to have knowledge of their properties, especially their dispersion as well as the interaction between different types of quasi-particles, e. g. between excitons and phonons.

While the general treatment of semiconductors can be found in standard text books such as (Haug and Koch 2009; Klingshirn 2012) and many more, the approaches used for modelling monolayers require new concepts. In contrast to semiconductor quantum wells, which deliver artificially formed 2D electronic systems with considerable nm-scale expansion in the confinement direction, monolayers are truly 2D crystalline structures with electrons and holes confined to a single unit cell in height or even atom layer(e.g. the crystal's transition-metal plane through the dominant d-orbital covalent component in TMDCs). As a consequence a proper handling of the carrier screening as well excitonic effects is crucial, i.e. the optical properties cannot be modelled by a simple 3D- or 2D-Rydberg series including a static screening (Chernikov et al. 2014). In more recent years, many theoretical groups have developed different approaches to deal with these new challenges (Brem et al. 2020; Cudazzo, Tokatly, and Rubio 2011; Katsch et al. 2018; Alexander Steinhoff et al. 2018; Stroucken and Koch 2017). The list of the groups may not be complete but shall illustrate different approaches to model 2D-materials. In the following, an introduction to the most important quasi particles is given followed by a short

introduction to the many-body modelling of 2D-materials. Here, the focus is laid on the challenges arising in their description.

2.1.1 Excitons – Fundamental Matter Excitations

Generally, if an excitation occurs in a semiconductor, it always creates an electron in the conduction band as well as a hole in valence band. Between such an electron-hole pair, Coulomb interaction is takes place similar to the hydrogen atom (Frenkel 1931; Wannier 1937), however the screening of the solid has to be considered. This is done by integrating the permittivity of the solid ϵ_r into the Wannier equation (Klingshirn 2012; Wannier 1937), with distance r between the electron and hole. Furthermore, the reduced mass of the excitons $\mu_{ex} = \frac{m_e m_h}{m_e + m_h}$, comprised of the effective masses of electron and hole, respectively, must be considered. This includes the interaction with other electrons in the valence band as well as with atomic cores. Note, the similarity with the hydrogen atom is strictly speaking only correct for vanishing carrier densities. If carriers are present, the Wannier equation becomes non-Hermitean and deviations are found (Kira and Koch 2006b).

Equation 2-1 **| Wannier equation**

$$-\left[\frac{\hbar^2\nabla^2}{2\mu} + \frac{e^2}{4\pi\epsilon_r\epsilon_0|r|}\right]\phi_\lambda(r) = E_\lambda\phi_\lambda(r)$$

Such system therefore has qualitatively similar solutions as the hydrogen atom: namely a plane wave with parabolic dispersion for the movement of the center of mass, as well as the usual bound (1s, 2s, 2p and so on) and unbound states (main quantum number $n = \infty$) from the hydrogen atom classified by main quantum number, angular momentum and magnetic quantum number. Experimentally, the exciton has been first observed in cuprous oxide (Hayashi and Katsuki 1952), where now similarly to atoms highly excited Rydberg excitons with several angular momentum can been observed (Mund et al. 2018; Rommel et al. 2020). A typical picture showing the dispersion of excitons in the excitonic picture is presented in **Figure 1a**. **Figure 1b** shows schematically which part of the single particle states are being involved in forming the exciton wavefunction at **K,K'** points of the Brillouin zone of TMDCs. This expansion into single particle wavefunctions shows that indeed more than just a single electron and hole state is needed to describe the exciton wavefunction (Gang Wang et al. 2018a).

Caused by the often high permittivity ϵ_r and small reduced mass μ compared to the electron mass, the binding energies as well as the difference between different excited states is often smaller (some meV to hundreds of meV, for TMDCs about 300 to 500 meV, (Chernikov et al. 2014)) and the corresponding Bohr radius of the wavefunction ϕ_λ is bigger than in a hydrogen atom (about 1.3 nm for TMDCs (Stier, Wilson, et al. 2016)). TMDCs have some modification concerning an unusual quasi-wavevector(q)-dependent screening and predicted linear dispersion, that are discussed in Sections 2.7.2, 2.7.4.1 and 2.8.1.

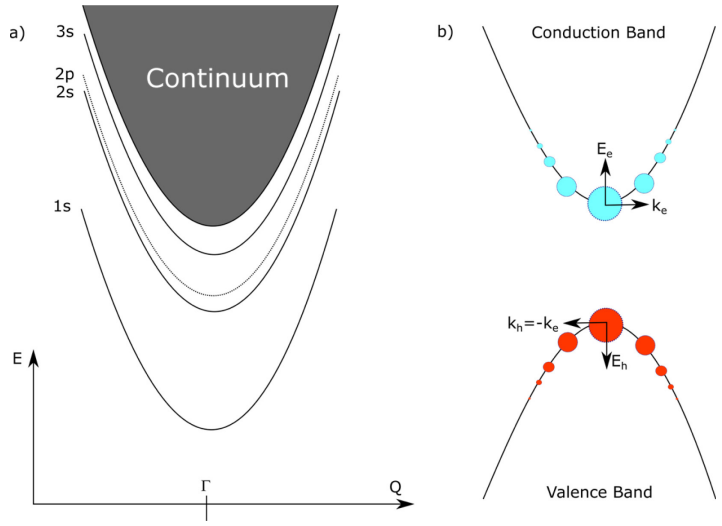

Figure 1 **| Exciton in Reciprocal Space.** (a) schematic drawing of the dispersion of bound and unbound exciton states as function of the center of mass momentum. Generally, all excitonic functions can also be expressed as linear combination of single particle states. (b) shows a schematic representation of the states involved in the 1s-wavefunction. The circles and their magnitude show the contribution of the electron and hole quasiparticle states. (b) has been drawn after (Gang Wang et al. 2018b).

2.1.2 Phonon – Lattice Vibrations

In a semiconductor, not only excitations of the electronic system are present, but also the lattice can be excited. These excitations are referred to as phonons, es explained below. To calculate their band structure and dispersion relation the Hamiltonian is split into two parts (P. Yu and Cardona 2005), one containing the ions and all inner electron $\hat{H}_{ion}$ and one containing the valence band electrons $\hat{H}_e$. Normally these two parts are coupled as they interact with each other. However, if one uses Born Oppenheimer approximation (Born and Oppenheimer 1927), i.e. assuming that the valence electrons follow the core in an adiabatic fashion, and the heavy cores just follow the mean position of the electrons, coupling can be lifted. This is physically motivated by their very different mass and, consequently, inertia.

This possible decoupling enables a simpler phenomenological approach. The Hamiltonian for the ions is written as the sum of two parts, where the first part describes the ions are resting in their equilibrium position $\hat{H}_0(\boldsymbol{r_j})$ and the second operator models the change for small movement of the core $\hat{H}_\delta(\delta\boldsymbol{r_j})$. As the movement of the ions is small compared to the distance between the atoms, the second part can be gained by using a Taylor series of $\hat{H}_{ion}$ for small changes in the atomic positions $\delta(\boldsymbol{r_j} - \boldsymbol{r_k})$. For most applications it is enough to stop the series after the first term, here the quadratic one. This is called the harmonic approximation.

Equation 2-2 **| Lattice Hamiltonian in harmonic approximation**

$$\hat{H}_\delta(\boldsymbol{u}_{kl}) = \frac{1}{2} M_k \left(\frac{d\boldsymbol{u}_{kl}}{dt}\right)^2 + \frac{1}{2}\sum_{k',l'} \boldsymbol{u}_{kl} \cdot \psi(kl, k', l') \cdot \boldsymbol{u}_{k'l'}$$

In this equation $\boldsymbol{u}_{kl}$ denotes the deviation of ion *k* in the unit cell *l* from its equilibrium position. M_k denotes its mass and $\psi(kl, k'l')$ denotes the force constant between two ion cores. To calculate the normal modes, one starts from a Bloch wave ansatz, since the matrix of force constants necessarily has the same translational symmetry as the crystal.

Equation 2-3 **| Blochwave ansatz**

$$\boldsymbol{u}_{kl}(\boldsymbol{q}, \omega) = \boldsymbol{u}_{k0} \exp(i(\boldsymbol{q} \cdot \boldsymbol{r}_l) - \omega t)$$

This approach now allows to analyze the normal modes by using a classical equation of motion and its Fourier transform.

***Equation set 2-4* | Phonon modes and dynamical matrix**

$$M_k\omega^2\boldsymbol{u}_{k0} = \sum_{k',l} \psi(kl, l'0) exp(-i\boldsymbol{q}\cdot\boldsymbol{r_l})\boldsymbol{u}_{k'0}$$

$$\sum_{k'} [D_{kk'}(q) - \omega^2\delta_{kk'}]u_{k'0} = 0$$

Here, $D_{kk'}$ is called the dynamic matrix. The general solution for the dispersion can be found if the term in brackets gets zero. While this calculation has been done using a classical equation of motion, it is clear that we actually deal with quantum mechanical harmonic oscillators for all of the given normal modes. This means that the energy stored in one mode is not continuous anymore but is discrete. The quantum of energy and momentum, that is related with this discretization is modelled using a quasiparticle, the so-called phonon, the quantum of vibration.

2.1.3 Photon – Light, Excitations of the Vacuum Field

Also, the electromagnetic vacuum field can be quantized, and its excitation treated as a particle. Here, we start from the classical Hamilton function, which is the total energy calculated from the vector and scalar potential. By introducing the canonical equation of motion with the canonical variables $p_{k,s}$ and $q_{k,s}$.(Klingshirn 2012)

***Equation 2-5* | Canonical variables**

$$\frac{\partial H}{\partial q_{k,s}} = -\dot{p}_{k,s} \qquad \frac{\partial H}{\partial p_{k,s}} = -\dot{q}_{k,s}$$

Here, k is the wavevector, and *s* are the possible transversal polarizations. In these canonical variables the Hamiltonian reads the following:

***Equation 2-6* |Photon Hamiltonian in free space**

$$H = \frac{1}{2}\sum_{k,s}\left(p_{k,s}^2\right) + \omega_k^2 q_{k,s}^2$$

Thus, it is a usual harmonic oscillator for each possible mode, which is in quantum mechanics appropriately modelled, owing to the correspondence principle, as a quantum mechanical harmonic oscillator. The quantization of the energy stored in a mode is described by its corresponding quantum-mechanical particle, the so-called photon. Its dispersion in vacuum is given by a linear relation $\omega = ck$ as angular frequency and wavenumber for a plane wave in vacuum are inherently linked ($k = 2\pi/\lambda$). Here, ω is the angular frequency of the mode and *c* the speed of light.

2.1.4 Polariton – Polarization Waves in Matter

If one deals with the evolution of electromagnetic waves in a solid, this simple linear dispersion relation is not applicable anymore as the electric field necessarily induced a polarization in the material. If one looks at the Hamiltonian that considers the electrons in the material, the photons and the interaction between both system, the eigenvectors of the system are not excitons or photons anymore, but a new hybrid quasi-particle, the polariton (operator p_k), composed of photons (operator a_k) and other excitations (e.g. excitons, phonons etc. with operator B_k) with different fraction, the Hopfield constants u_k/v_k (Hopfield and Thomas 1963; HUANG 1951; Klingshirn 2012; Pekar 1958; Tolpygo 1950). The polaritons represent the quantum of polarization. The transformation from the normal

many-body picture to the polariton picture (the Bogoliubov-transformation) is shortly outlined below (Haug and Koch 2009; Klingshirn 2012).

Equation 2-7 **| Matter Hamiltonian in the polariton picture**

$$H = \sum_k \hbar\omega_k a_k^\dagger a_k + \sum_{k\prime} E(k')B_{k'}^\dagger B_{k'} + i\hbar \sum_k g_k\left(B_k^\dagger a_k + h.c.\right) = \sum_k {E'}_k p_k^\dagger p_k$$

$$p_k = u_k B_k + v_k a_k$$

While it is generally true for all scenarios that polaritons are the eigenvector of the Hamiltonian, in the case of strong light–matter interaction, the emitted photon from a recombining carrier or exciton can be reabsorbed quickly and recombine again. In such a scenario, the mixing gets strong and the resulting effects of hybridization cannot be neglected, in contrast to energetic regions with flat permittivity, where the dispersion of photons still is (almost) linear.

Mathematically, strong enough coupling means that the real part of permittivity becomes negative in the vicinity of the relevant resonance. This has huge implications. Normally, the polarization relating to coherent excitons is a transversal wave similar to any common electromagnetic wave. This is originates to the Maxwell equation $\nabla \cdot \boldsymbol{D} = \epsilon_0 \nabla \cdot \epsilon_\mathrm{r} \cdot \boldsymbol{E} = 0$, which for finite relative permittivity only allows transversal modes, i.e. transversal excitons ($\omega_0 = \omega_T$) (cf. **Figure 2**). However, if the permittivity crosses zero, another solution is possible (Klingshirn 2012), namely a longitudinal mode or longitudinal exciton branch (ω_L). The splitting of these two modes is strongly dependent on the material and can amount to 0.08 meV for GaAs (Rappel, Feiner, and Schuurmans 1988), 1.3 meV for CdSe (Itoh et al. 1981) or 2 meV in CdS (Weber et al. 1997). However, it can also reach 5 meV in CuCl (Y. et al. 1979) as an example of an ionic crystal or even 60 meV (Hesse et al. 1976) for the mixed mode in molecular crystals of Pentamethinium Cyanine dye. In contrast to most inorganic compounds, such molecular crystals can even exhibit a splitting of up to 1 eV (Hesse et al. 1976). For thin TMDCs, caused by their strong oscillator strength rather large splitting are expected (Mrejen et al. 2019). While there have been theoretical predictions for polaritons in the monolayer as well as experimental measurements for few layer samples (Z. Fei et al. 2016; Karanikolas et al. 2016; Mrejen et al. 2019), no measurements of the monolayer are available.

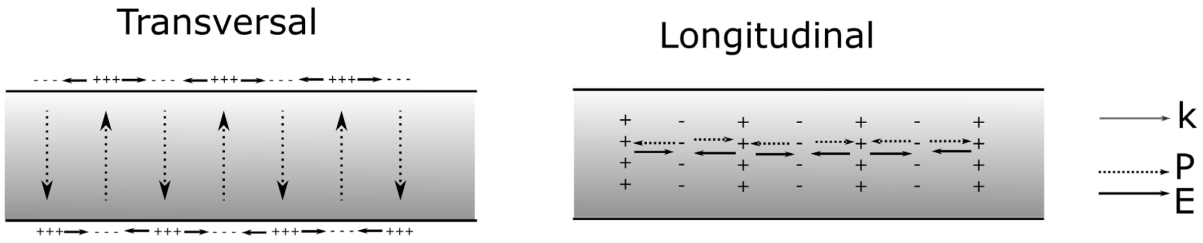

Figure 2 **|Schematic Depiction of the Polarization in a Slab related to Transversal and Longitudinal Coherent Excitons.** (left) transversal and (right) longitudinal modes. Redrawn after (Klingshirn 2012).

At sufficient interaction strength and low dephasing, the states of the individual particles (photons and excitons) mix and form the lower- (LPB) and upper polariton branch (UPB). Here, the lower polariton branch approaches the transversal exciton branch and the upper polariton branch starts from the longitudinal mode (cf. **Figure *3***). The resulting dispersion is often used to discuss the process of recombination and excitation in the solid. For example, an exciton or exciton-polariton cannot recombine radiatively outside the lightcone due to momentum conservation, it first has to scatter to the light like state in the lower part of the polariton branch.

In the following picture (cf. **Figure *3***), the dispersion of a typical polariton is shown together with the lightcone. The picture shows the case of neglected damping in (a) and for small damping in (b). For neglected damping, a clear splitting with a gap in the lightcone is seen while in the case of small damping, states are still available within this gap. (c) shows a schematic example how the polariton picture helps to discuss exciton dynamics.

After excitation in the upper polariton branch, the excitation relaxes to the excitonic part of the lower polariton band. The recombination takes place either by relaxing under the emission of acoustic phonons to the point of splitting resulting in luminescence at the zero-phonon band or radiating at phonon sidebands by emitting optical phonons. For a detailed description, how the dispersion is obtained, see 2.7.3 Exciton-Polaritons. Here, also the possibility of mixed modes, that are expected for a uniaxial crystal like TMDC will be explained.

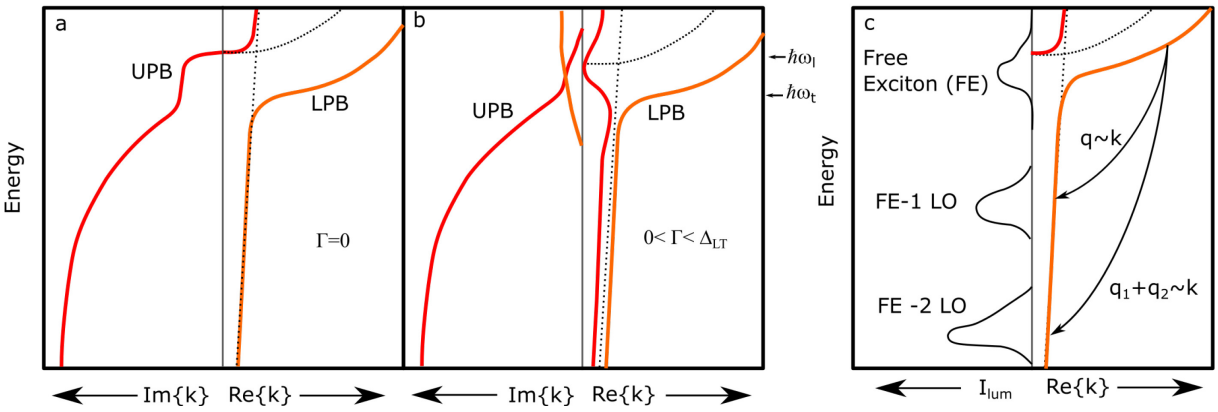

Figure 3 | Idealized Polariton Dispersion and Phonon Sidebands: schematic dispersion (energy over photon wavevektor k) for neglible damping (a) and weak damping (b). The left part shows the imaginary part of the wavevector, that is proportional to the absorbance, while the right part shows the real part that is related to the dispersion. The dashed lines represent the uncoupled disperison of photons (nearly vertical) and excitons (parabolic at low center-of-mass wavevectors q). The transversal and logitudinal branches are marked by two arrows at the side of (b) with corrsponding zero-k energies $\hbar\omega$. The dynamics involved in phonon–assisted emission of exciton-polaritons is depicted in (c). While for weak exciton-phonon coupling, only the zero-phonon line is observed, in the case of strong coupling additional bands can occur under momentum and energy conservation. One can clearly see that this process activates excitons outside the light cone. The schematic has been redrawn after (Klingshirn 2012; Matsushita, Wicksted, and Cummins 1984).

2.1.5 Polarons – Phonon Bound States

The polariton is not the only hybrid quasi-particle. For second-order or even higher phonon-sidebands, a higher order of cluster expansion (see below) would be needed. However, the computational cost is enormous. That's why another approximation can be done, the so called *polaron*-picture or *exciton-polaron* picture. It is a charge carrier respectively an exciton surrounded by a cloud of phonons or polarization. In order to change to the polaron picture, a unitary transform of the Hamiltonian can be performed $H = THT^{\dagger}, T \equiv exp\sum_{k,p} D_p a^{\dagger}_{k-p} a_k (b^{\dagger}_p - b_{-p})$. The details concerning the transformation and a explicit formula for their dispersion can be found in (Feldtmann, Kira, and Koch 2009).

The concept is not only necessary for understanding phonon-assisted emission but is also important at higher carrier densities. While at small densities the assumption of a formation of neutral excitons and trions is valid for TMDCs, for higher doping or medium-to-high carrier densities, the formulation with a repulsive and attractive exciton-polaron branch is the appropriate one (Efimkin and MacDonald 2017). Here, the states have to be considered as excitons dressed by a Fermi sea of free carriers. Also

strongly coupled polaritons for these kind of exciton-polarons could be found experimentally for TMDCs in a cavity if the doping is sufficient (Sidler et al. 2017) .

2.2 Many-Body Theory of Semiconductor Luminescence

To model the photoluminescence of semiconductors, commonly the so called semiconductor luminescence equation (SLE) are used (Chernikov 2011; Haug and Koch 2009; Kira et al. 2001; Kira, Jahnke, and Koch 1998; Kira and Koch 2005; Schmitt-Rink, Chemla, and Miller 1989). For a conventional semiconductor, they are formulated in the picture of quasi-free particles. While this is still possible for 2D-materials, this is not the ideal basis set as at most densities and relevant temperatures, as the physics of TMDCs is governed by excitons. While (Brem et al. 2020) did reformulate them in the picture of bosonic exciton operators, (Katsch et al. 2018) extended the cobosonic description (Ivanov and Haug 1993) – the internal structure of fermionic electron and holes forming the bosonic exciton is explicitly integrated – to include the intra- and intervalley interaction occurring in TMDCs. While the purely bosonic description is only valid in the linear regime, where most of the carrier excitation are excitonic and only negligible exciton-exciton scattering takes place, the cobosonic description is valid until the third order of the electric field. It therefore also includes the Pauli-blocking as well as Dexter- and Förster type interaction between the excitons. Furthermore, a proper treatment of higher excitonic particles is possible. While some of these medium-density effects are present in the later described measurements, the cobosonic treatment is beyond the scope of this introduction. Instead the theory based on bosonic excitons (Brem et al. 2020) will be described, as it shows the most important features. Whenever necessary, higher order effects will be discussed on a phenomenological level rather than within a fully microscopical theory.

In the regime of excitons, the Hamiltonian for an undoped monolayer consists of several parts.

Equation 2-8 **| Many-body Hamiltonian**

$$H = \sum\left(H_{exc} + H_{lattice} + H_{light} + H_{photon-exciton} + H_{exciton-phonon}\right)$$

The first three terms describe the energy of excitons H_{exc}, phonons $H_{lattice}$ and photons H_{light} , while the other parts ($H_{photon-exciton}$ and $H_{exciton-phonon}$) describe the interaction between the individual constituents. Following this description direct photon-phonon interactions are neglected. In the rotating frame they read:

Equation 2-9 **| Hamiltonian for lattice, light and electron system as well as coupling**

$$H_{exc} = E^{\mu}_{\boldsymbol{Q}_{||}} a^{\dagger}_{\mu \boldsymbol{Q}_{||}} a_{\mu \boldsymbol{Q}_{||}} \,,\; H_{lattice} = \Omega^{\alpha}_{\boldsymbol{q}_{||}} b^{\dagger}_{\alpha \boldsymbol{q}_{||}} b_{\alpha \boldsymbol{q}_{||}} \,,\; H_{light} = \omega^{\sigma}_{\boldsymbol{k}} c^{\dagger}_{\sigma \boldsymbol{k}} c_{\sigma \boldsymbol{k}}$$

$$H_{photon-exciton} = M^{\mu}_{\sigma \boldsymbol{k}} c^{\dagger}_{\sigma \boldsymbol{k}} a_{\mu \boldsymbol{k}_{||}} + M^{\mu *}_{\sigma \boldsymbol{k}} a^{\dagger}_{\mu \boldsymbol{k}_{||}} c_{\sigma \boldsymbol{k}}$$

$$H_{exciton-phonon} = D^{\nu \mu}_{\alpha \boldsymbol{q}_{||}} a^{\dagger}_{\nu \boldsymbol{Q}_{||} + \boldsymbol{q}_{||}} a_{\mu Q_{||}} \; (b_{\alpha q_{||}} + b^{\dagger}_{\alpha, -\boldsymbol{q}_{||}})$$

Here, $\boldsymbol{k}, \boldsymbol{q}$ and $\boldsymbol{Q}$ are the momentum of photon, phonon and exciton (here the center of mass momentum). $\boldsymbol{k}_{||}$ denotes the in-plane momentum. For denoting the quasiparticles, the common annihilation (and creation) operators $a^{(\dagger)}_{\mu \boldsymbol{Q}_{||}}$, $b^{(\dagger)}_{\alpha \boldsymbol{q}_{||}}$, $c^{(\dagger)}_{\sigma \boldsymbol{k}}$ are used for excitons in the state μ, phonons in the mode α and photons with polarization σ. μ is a compound index that accounts for the main quantum number as wells as spin, angular and valley quantum number. The dispersion of the individual quasiparticles is considered by the energies $E^{\mu}_{\mathbf{Q}_{||}}, \Omega^{\alpha}_{\boldsymbol{q}_{||}}, \omega^{\sigma}_{\boldsymbol{k}}$.

The photon-exciton part of the Hamiltonian describes the absorption of a photon with the excitation of an exciton and the direct radiative recombination. Both processes are happening with the probability $M^{\mu}_{\sigma \boldsymbol{k}}$. Absorption or emission of phonons by excitons is denoted with the last part of the Hamiltonian. Its strength is given by the exciton phonon matrix element $D^{\nu\mu}_{\alpha \boldsymbol{q}_{||}}$.

In the framework of these kind of theories, the PL can be seen as the temporal change of the expectation value of the photon number $n_{\boldsymbol{k}} = \langle c^{\dagger}_{\boldsymbol{k}} c_{\boldsymbol{k}} \rangle$ (Brem et al. 2020; Haug and Koch 2009; Kira, Jahnke, and Koch 1998). The above Hamiltonian contains several N-particle operators. The equations of motion for such an *N*-particle operator O_N and its expectation value $\langle O_N \rangle$ are generally given in the Heisenberg picture (Kira and Koch 2006b):

Equation 2-10 **| Equation of motion in the Heisenberg picture**

$$i\hbar \frac{\partial}{\partial t} O_N = [O_N, H]$$

$$i \frac{\partial}{\partial t} \langle O_N \rangle = T[\langle N \rangle] + V[\langle N+1 \rangle].$$

The second equation arises as the Hamiltonian is not only composed of single particle operators, but instead also has two particle operators. The functionals *T* and *V* in the above equation are dominated by the non-interacting and interacting parts of the Hamiltonian. This coupling to an *N+1* particle operator leads to an infinite number of equations with all possible combinations and permutations. Therefore, there is a need for a systematic approximation that can be stopped at certain orders without losing the many body physics. This is commonly done in the so-called cluster expansion approach (Brem et al. 2020; Chernikov 2011; Fricke 1996; H.W. Wyld 1963; Kira and Koch 2006a). Below, a short excurse on this is presented before coming back to the description of the application on 2D-materials.

2.2.1 Excurse: Cluster Expansion

In the following, a short introduction of the cluster expansion will be given. A detailed description can be found in the work of (Kira and Koch 2006a). Generally, every *N*-particle operator can be written as a product of single particle operators:

$$O_N = c^{\dagger}_1 \dots c^{\dagger}_{N_1} b^{\dagger}_1 \dots b^{\dagger}_{N_2} a^{\dagger}_1 \dots a^{\dagger}_{N_3} a_{N_4} \dots a_1 b_{N_5} \dots b_1 c_{N_6} \dots c_1 \quad with \ \sum_i N_i = N.$$

The cluster expansion now uses a factorization into operators of different order, that means single-particle operators $\langle 1 \rangle$ (singlet), correlated pairs $\langle 2 \rangle$ (doublets), triplets and so on.

$$\langle N \rangle = \langle N \rangle_S + \langle N-2 \rangle_S \Delta\langle 2 \rangle + \langle N-3 \rangle_S \langle 1 \rangle \Delta\langle 2 \rangle + \dots + \Delta\langle N \rangle$$

Here, the subscript *S* denotes the singlet contribution while the $\Delta\langle J \rangle$ is the purely correlated part of the *J*-particle cluster. Each term includes a sum over all unique possible combinations. The physics of the described system now gives the lower bound, where the model can be truncated to get a closed system of equations. To describe a system where an electron-hole plasma and excitons coexist, one at least has to go to the doublet order, while for trions, biexcitons and phonon sidebands higher orders are needed (Kira and Koch 2006a).

To make it clear, the equation for truncation of the general dynamics to the triplet order will be given:

$$i\hbar \frac{\partial}{\partial t} \langle 1 \rangle = T_1[\langle 1 \rangle] + V_{1a}[\langle 2 \rangle_S] + V_{1b}[\Delta\langle 2 \rangle]$$

$$i\hbar \frac{\partial}{\partial t} \Delta\langle 2 \rangle = T_2[\Delta\langle 2 \rangle] + V_{2a}[\langle 3 \rangle_{SD}] + V_{2b}[\Delta\langle 3 \rangle]$$

$$i\hbar\frac{\partial}{\partial t}\Delta\langle 3\rangle = T_3[\Delta\langle 3\rangle] + V_3[\langle 4\rangle_{SDT}]$$

Here the functionals are known by the definition of the Heisenberg equations of motion. At this order of approximation, the dynamics are obtained by solving the dynamics of all singlets and the correlation of doublets and triplets. Often, the correlation of the triplets is neglected and replaced by a scattering term. In the example of a phonon assisted recombination, the approximation reads: $\langle c_{\boldsymbol{k}}^{\dagger} b_{\boldsymbol{q}}^{\dagger} b_{\boldsymbol{q}'} a_{\boldsymbol{q}-\boldsymbol{q}'}\rangle \approx \langle c_{\boldsymbol{k}}^{\dagger} a_{\boldsymbol{q}-\boldsymbol{q}'}\rangle\langle b_{\boldsymbol{q}}^{\dagger} b_{\boldsymbol{q}'}\rangle + \Delta\langle c_{\boldsymbol{k}}^{\dagger} b_{\boldsymbol{q}}^{\dagger} b_{\boldsymbol{q}'} a_{\boldsymbol{q}-\boldsymbol{q}'}\rangle$ (Brem et al. 2020). If the higher order correlation is neglected, this means the expectation value for the phonon-assisted recombination is given by the product of the matrix element for radiative recombination times the matrix element for creation/annihilation of the corresponding phonon.

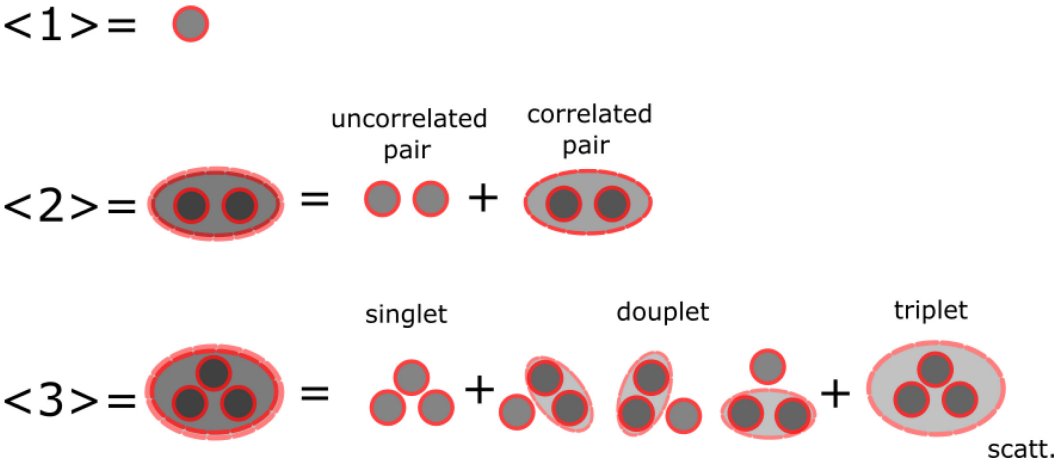

***Figure 4* | Schematic Representation of the Cluster Expansion up to 3rd order:** The schematic shows the expansion of the operators until third order. 2-particle operators can be split into one operator for uncorrelated pairs and their correlated part. 3-particle cluster can be factorized using the lower line. For most applications, where pure triplets (e.g. trions) are not dominant, the last part can be replaced by the scattering approximation. The picture is adapted with permission from (Kira and Koch 2006a) published under Creative Commons License (CC BY NC ND).

2.2.2 Semiconductor Luminescence Equation

If the above truncation is stopped at the triplets, a set of coupled differential equations can be derived. Often these are referred to semiconductor luminescence equation (SLE) (Haug and Koch 2009). The number of photons $n_{\boldsymbol{k}} = \langle c_{\boldsymbol{k}}^{\dagger} c_{\boldsymbol{k}}\rangle$ and their dynamics, i.e. the PL, are coupled with the polarization $S_{\boldsymbol{k}}^{\mu} = \langle c_{\boldsymbol{k}}^{\dagger} a_{\mu\boldsymbol{k}_{||}}\rangle$, the phonon-assisted polarization $U_{\boldsymbol{kq}}^{\mu,\pm} = \langle c_{\boldsymbol{k}}^{\dagger} b_{\pm\boldsymbol{q}}^{(\dagger)} a_{\mu\boldsymbol{k}_{||}-\boldsymbol{q}}\rangle$ and the exciton-phonon correlation $C_{\boldsymbol{kq}}^{\nu\mu,\pm} = \langle a_{\nu\boldsymbol{k}_{||}}^{\dagger} a_{\mu\boldsymbol{k}_{||}-\boldsymbol{q}} b_{\pm\boldsymbol{q}}^{(\dagger)}\rangle$.

***Equation 2-11* | Semiconductor luminesence equation**

$$\frac{d}{dt}n_{\boldsymbol{k}} = \frac{2}{\hbar}\sum_{\mu}\Im\left(M_{\boldsymbol{k}}^{\mu} S_{\boldsymbol{k}}^{\mu}\right)$$

$$i\hbar\frac{d}{dt}S_{\boldsymbol{k}}^{\mu} = \left(E_{\boldsymbol{k}_{||}}^{\mu} - \omega_{\boldsymbol{k}}\right) S_{\boldsymbol{k}}^{\mu} - M_{\boldsymbol{k}}^{\mu *} N_{\boldsymbol{k}_{||}}^{\mu} + \sum_{\nu\boldsymbol{q}\pm} D_{\boldsymbol{q}}^{\mu\nu} U_{\boldsymbol{kq}}^{\mu\pm} + \dot{S}|_{deph.}^{rad}$$

$$i\hbar\frac{d}{dt}U_{\boldsymbol{kq}}^{\nu,\pm} = \left(E_{\boldsymbol{k}_{||}-\boldsymbol{q}}^{\nu} \mp \Omega_{\boldsymbol{q}} - \omega_{\boldsymbol{k}}\right) U_{\boldsymbol{kq}}^{\nu,\pm} - \sum_{\mu} M_{\boldsymbol{k}}^{\mu *} C_{\boldsymbol{kq}}^{\mu\nu,\pm} + \sum_{\mu} D_{\boldsymbol{q}}^{\mu\nu *} \eta_{\boldsymbol{q}}^{\pm} S_{\boldsymbol{k}}^{\mu} + \dot{U}|_{deph.}^{phon}$$

$$i\hbar\frac{d}{dt}C_{\boldsymbol{kq}}^{\nu\mu,\pm} = \left(E_{\boldsymbol{k}_{||}-\boldsymbol{q}}^{\mu} - E_{\boldsymbol{k}_{||}}^{\nu} \mp \Omega_{\boldsymbol{q}}\right) C_{\boldsymbol{kq}}^{\nu\mu,\pm} - D_{\boldsymbol{q}}^{\nu\mu *} Q_{\boldsymbol{kq}}^{\nu\mu,\pm} + \dot{C}|_{deph.}^{rad+phon}$$

Here, $\eta_{\boldsymbol{q}}^{\pm} = \frac{1}{2} \mp \frac{1}{2} + \langle b_{\boldsymbol{q}}^{\dagger} b_{\boldsymbol{q}} \rangle$ denotes the relevant phonon occupation factor for absorption/emission, $N_{\boldsymbol{Q}}^{\mu} = \langle a_{\mu \boldsymbol{Q}}^{\dagger} a_{\mu \boldsymbol{Q}} \rangle$ the exciton occupation and $Q_{\boldsymbol{kq}}^{\nu\mu,\pm} = \eta_{\boldsymbol{q}}^{\mp} N_{\boldsymbol{k}_{||}-\boldsymbol{q}}^{\mu} - \eta_{\boldsymbol{q}}^{\pm} N_{\boldsymbol{k}_{||}}^{\nu}$ the source of the exciton-phonon correlation. It is quantifying the number of occupied and available states and phonons needed for this scattering event. For the rest of the description, (Brem et al. 2020) have truncated after the triplets, however important higher correlation are noted with $(\cdot)|_{deph.}^{phonon}$. They give rise to a center of mass dependent dephasing rate $\Gamma_{\boldsymbol{Q}}^{\mu}$ as well as a radiative dephasing of excitons within the light cone $\gamma_{\boldsymbol{k}_{||}}^{\mu}$. Their explicit form for TMDCs can be found in reference (Brem et al. 2020).

The system of coupled equations shows that the source of luminescence is the coherent and incoherent polarization. These are decaying by radiative recombination or non-radiative recombination. Within the lightcone, it is additionally refilled by exciton-phonon scattering processes. As this can happen in emission and absorption, a correlation between the filled excitonic states and the phonon bath is building up as well.

As the phonon and photon occupation numbers are slowly changing after the initial thermalization of hot excitons, a steady state solution can be found in the adiabatic limit, which is often enough to understand time integrated PL-spectra. For an emission with polarization σ under normal incidence the following analytic expression can be derived (Brem et al. 2020):

Equation 2-12 **| Elliot formula in the excitonic picture** (Brem et al. 2020)**.**

$$I_{\sigma}(\omega) = \frac{2}{\hbar} \sum_{\mu} \frac{\left|M_{\sigma}^{\mu}\right|^2}{\left(E_0^{\mu} - \omega\right)^2 + \left(\gamma_{\sigma 0}^{\mu} + \Gamma_0^{\mu}\right)^2} \left(\gamma_{\sigma 0}^{\mu} N_0^{\mu} + \sum_{\nu,q,\alpha\pm} \left|D_{\alpha \boldsymbol{q}}^{\mu\nu}\right|^2 \frac{N_{\boldsymbol{q}}^{\nu} \eta_{\alpha \boldsymbol{q}}^{\pm} \Gamma_{\boldsymbol{q}}^{\nu}}{\left(E_{\boldsymbol{q}}^{\nu} \pm \Omega_{\boldsymbol{q}}^{\alpha} - \omega\right)^2 + \left(\Omega_{\boldsymbol{q}}^{\nu}\right)^2} \right)$$

The first term resembles the direct recombination within the light cone. As can be seen, the source is the exciton occupation N_0^{μ}. The strength is given by the exciton-photon matrix element times the dephasing rate. The shape and its spectral position are given by the denominator (cf. Lorentz model). Generally, a Lorentzian peak that is broadened by dephasing (here $\gamma_{\sigma 0}^{\mu}$ and Γ_0^{μ}) is expected. Caused by the interaction with phonons, an asymmetric lineshape can occur. However, if the description is done in the electron picture or in the cobosonic one, it can be shown that also free carriers can emit at the exciton resonance, which seems contradictory in a simple picture (Chatterjee et al. 2004; Chernikov 2011; Haug and Koch 2009; Koch et al. 2006). Phenomenologically, the exceeding energy is given to remaining plasma or in theory one can see it as the transition of the plasma from the N-particle state to an N-1-particle state (Koch et al. 2006).

The second part contains phonon-guided scattering to the light cone. New peaks arise from this that are usually called phonon side band (PSB). The sources of this type of recombination is the exciton recombination times the occupation of the relevant phonon states. Its strength is given by the exciton-phonon matrix element *D*.

2.2.3 Symmetries

Symmetries are an important property in solid states physics, as many physical phenomena can be traced back to certain symmetries. Commonly, the crystal structure and the electronic orbitals are classified by their mirror-, rotation- (time reversal and parity) symmetry according to group theory (Klingshirn 2012; Voiry, Mohite, and Chhowalla 2015). This strongly affects the selection rules for linear and non-linear spectroscopy (Qiu, Cao, and Louie 2015; D. Xiao et al. 2012a; J. Xiao et al. 2015). Furthermore, the exact number of possible phonon modes can be given in advance due to given symmetries (Terrones et al. 2014).

Generally, the symmetries of the crystal lattice already restrict the possible Bloch functions, as they inherit the same symmetries. The knowledge of the symmetries therefore gives already some qualitative knowledge about the band structure. Within the scope of this thesis, the following spatial symmetries are of major interest.

A TMD monolayer (cf. **Figure 5**) in its trigonal prismatic form (1H) has a 3-fold rotational symmetry and a mirror symmetry perpendicular to it (D_{3h}-group) (Voiry, Mohite, and Chhowalla 2015). There are two highly symmetric stacking configuration that are stable and can be grown. Naturally for the TMDCs relevant for this thesis, mostly the 2H-phase exists. It has a six-fold rotational symmetry and mirror plane perpendicular to the axis of rotation (D_{6h}^{4}-group). In addition, the 3R-phase exists but can be rarely found. Even more phases like the octahedral phase (1T) or its disorder from (1T') are observed (cf. chapter 2.6) for different TMDCs. The 3R phase has a three-fold rotational symmetry and a mirror plane parallel to the axis (C_{3v}^{5}-group).

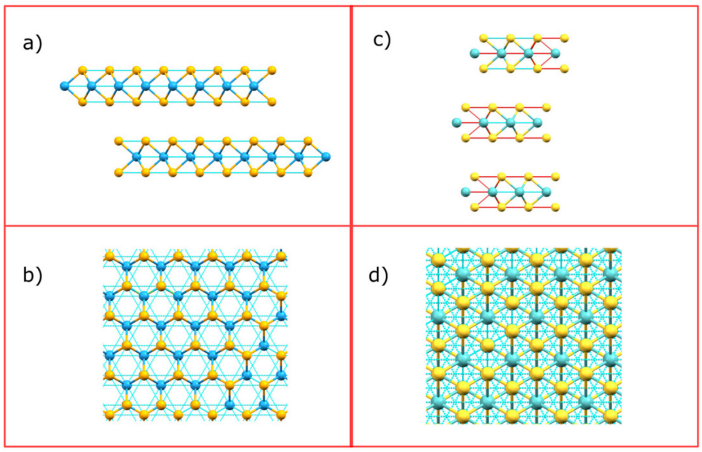

***Figure 5* | Crystal Phases and Moiré Pattern.** 2H-crystal structure shown from the side (a) and the top (b) at the example of WSe_2 (Kalikhman, Gladchenko, and Pravoverova 1972). In contrast the 3R-structure is shown for the example of MoS_2 (structural data from (Semiletov 1961), (Persson 2017), plotted using *Mercury* (Macrea et al. 2008)) in (c -d).

In the case of artificially stacked hetero- or homojunctions any stacking angle and interlayer shifts are generally possible (Geim and Grigorieva 2013). Furthermore, the unit cell size of the individual layers can be different, making the formation of a moiré pattern possible (Kuwabara, Clarke, and Smith 1990; C. Zhang et al. 2017; N. Zhang et al. 2018). Similarly, if a non-trivial rotation is applied between the layers a moiré pattern is formed. In these circumstances a much bigger supercell is needed to describe the heterobilayer, where the global symmetries of the supercell is still given by the one of the constituents (Zeller, Ma, and Günther 2017). However, very different local symmetries can arise (see below). In general, it is very hard to calculate the band structure for these bilayers as the computation time scales cubic with the number of atoms in DFT, thus increasing the necessary number from 6 in the aligned case to hundreds in a supercell is a serious computational problem.

In addition to the symmetry of the lattice, the symmetry of the Hamiltonian and the orbitals can be classified, too. Here, parity, time-reversal and inversion symmetry are of importance within the scope of this work. Parity symmetry classifies the wavefunctions into either symmetric or antisymmetric functions. From the knowledge of these symmetry the cancelling or non-cancelling of integrals over the whole space occurring e. g. in transition matrix elements can be predicted. Time-reversal symmetry is present if the solution of the time-dependent Schrödinger equation for the wavefunction is similar for back and forward propagation of time. For TMDCs, the orbitals in both valleys are time-reversal partners. Both symmetries are essential to predict the selection rules.

2.2.4 Moiré Pattern

Generally, if periodic patterns of different size or the same size but with rotation are put on top of each other, a new larger periodicity is found that is modelled by introducing the concept of a so-called supercell (cf. **Figure 12**). Thus, when transferring a monolayer on a crystalline substrate (Decker et al. 2011; Dendzik et al. 2015) or stacking several van-der-Waals materials (Kuwabara, Clarke, and Smith 1990; Tiefenbacher, Pettenkofer, and Jaegermann 2000; C. Zhang et al. 2017), necessarily a supercell with larger periodicity is formed. Concerning the symmetry when stacking different hexagonal TMDCs, the supercell has the same rotational symmetry as the monolayers comprising it (Zeller, Ma, and Günther 2017). This means that for two stacked TMDC monolayers still a 3-fold rotational symmetry can be found. The size of the moiré period is influenced by the twist angle as well as the lattice mismatch. Therefore, for the same material combination still various moiré periodicity can be achieved and is then given by the chosen twist angle. Especially for small twist angles and small lattice constant mismatch, a moiré periodicity can be achieved that is much larger than the exciton Bohr radius in the order of nanometers (Naik and Jain 2018; Yankowitz et al. 2012) thus spanning over several until cells of the individual monolayers.

In such a scenario the moiré pattern also leads to corrugation of the layers with a periodically changing van-der-Waals gap between the monolayers. Thus, also the coupling between the layers and therefore the amount of hybridization is altered spatially (H. Yu et al. 2017). Furthermore, the exciton selections rules are now influenced by the local (cf. **Figure 12b**) not the global symmetry, resulting in spatially modified selection rules and the formation of moiré exciton subbands for inter- and intralayer excitons (cf. chapter 2.7.2). However, the height of the potential is crucial and not in each case it is high enough that moiré excitons are forming.

2.3 Theory of Second Harmonic Generation

Second harmonic generation can be used as a tool to investigate the sample's symmetry, namely, wether inversion symmetry is broken or present, as well as to confirm the in-plane symmetry. The phenomenon of second harmonic generation can be easily understood in a classical description. The polarization in a material as a function of the electric field is given by multiplication with the susceptibility χ : $P_i(\omega,k) = \chi_{ij}(\omega,k)E_j(\omega,k)$ (Band 2006). For a generalized material, the susceptibility is a tensor and its power dependence on the electric field can be expanded in a Taylor series. If one considers two external fields at (ω_1,k_1) and (ω_2,k_2), the resulting equation up to second order looks the following:

Equation 2-13 **| Polarisation expansion**

$$
\begin{aligned}
P_i(\omega,k) = {} & \chi^1_{ij}(-\omega,-k;\omega_1,k_1)E_j(\omega_1,k_1) + \chi^1_{ij}(-\omega,-k;\omega_2,k_2)E_j(\omega_2,k_2) \\
& + \chi^2_{ijk}(-\omega,-k;\omega_1,k_1,\omega_1,k_1)E_j(\omega_1,k_1)E_j(\omega_1,k_1) + \chi^2_{ijk}(-\omega,-k;\omega_2,k_2,\omega_2,k_2)E_j(\omega_2,k_2)E_j(\omega_2,k_2) \\
& + \chi^2_{ijk}(-\omega,-k;\omega_1,k_1,\omega_2,k_2)E_j(\omega_1,k_1)E_j(\omega_2,k_2) + \chi^2_{ijk}(-\omega,-k;\omega_2,k_2,\omega_1,k_1)E_j(\omega_2,k_2)E_j(\omega_1,k_1) \\
& + \chi^2_{ijk}(-\omega,-k;\omega_1,k_1,-\omega_2,-k_2)E_j(\omega_1,k_1)E_j(\omega_2,k_2)^* \\
& + \chi^2_{ijk}(-\omega,-k;-\omega_1,-k_1,\omega_2,k_2)E_j(\omega_1,k_1)^*E_j(\omega_2,k_2) + \chi^3_{ijkl}\dots
\end{aligned}
$$

The first two terms are the common linear term. The next two terms correspond to second harmonic generation of both incoming waves and the follwing four are all possible sum and difference frequency generation mechanisms. It can be shown in the concept of group-theory that SHG can be only present if inversion symmetry is broken(Band 2006; Franken et al. 1961; Franken and Ward 1963; Shen 1984; Zimmermann, Mette, and Höfer 2016). This can be easily understood in a simple model. For a ML only one dipole exists that can radiate. If now the BL is completed with inversion symmetry, also the dipole is out of phase, thus deconstructive interference is found (Hsu et al. 2014). In contrast if they are

stacked without restoring the inversion symmetry, they can be in phase. If they are perfectly aligned one expects up to four times more SHG radiation. Furthermore, it can be shown that almost all components of the dielectric tensor vanish for the symmetry present in the given TMDCs(Heinz, Loy, and Thompson 1985; Shen 1984; Zimmermann, Mette, and Höfer 2016). Only four independent parameters of the tensor remain (Band 2006). Thus, SHG imaging can be used to identify sample areas with even or add layer numbers, as well as bilayers of different stacking configuration, as used in experiments described later in this work.

2.4 Theory of Raman Spectroscopy

Inelastic scattering of photons allows one to measure the Raman active modes of the material. For 2D materials, this is often used to prove that indeed a monolayer is present (C. Lee et al. 2010; Molina-Sánchez and Wirtz 2011; Terrones et al. 2014) and whether the layer is strained (Ferrari and Basko 2013; Sahin et al. 2013). Also signs of a moiré pattern with a twist angle dependence can be found by newly arising modes (M. L. Lin et al. 2018). If an electromagnetic wave ***E*** is incident on a solid, it induces a polarization ***P*** in the material, in relation to the susceptibility χ.

Equation 2-14 **| Link between polarization and suceptibilty**

$$P(r,t) = \chi(k_i,\omega_i)\cdot E_i(k_i,\omega_i)\cdot\cos(k_i\cdot r-\omega_i t)$$

As shown previously (ch. 2.1.2), also the phonon resembles a wave with wavevector **Q**.

Equation 2-15 **| Phonons as a Bloch wave**

$$Q(r,t) = Q(q,\omega_0)\cdot\cos(q\cdot r-\omega_0 t)$$

Due to this oscillatory motion the susceptibility is changing periodically and can be expanded in a Taylor series around the resting position of the atoms. This then can be inserted to **Equation 2-14**.

Equation 2-16 **| Taylor series for susceptibility for phonons in harmonic approximation.**

$$\chi(k_i,\omega_i Q) \approx \chi_0(k_i,\omega_i) + \left(\frac{\partial\chi}{\partial Q}\right)_{|Q=0}\cdot Q$$

$$P(r,Q,t) = \chi_0\cdot E_i(k_i,\omega_i)\cdot cos(k_i\cdot r-\omega t)$$

$$+\frac{1}{2}\left(\frac{\partial\chi}{\partial Q}\right)_{|Q=0}\cdot Q(q,\omega_0)\cdot E_i(k_i,\omega_i)\cos[(k_i+q)\cdot r-(\omega_i+\omega_0)t]$$

$$+\frac{1}{2}\left(\frac{\partial\chi}{\partial Q}\right)_{|Q=0}\cdot Q(q,\omega_0)\cdot E_i(k_i,\omega_i)\cos[(k_i-q)\cdot r-(\omega_i-\omega_0)t]$$

The results show that sum- and difference-frequency generation between the incident light and the phonons takes place. By analyzing the frequency shift of the scattered light with respect to the laser the phonon energy can be retrieved. If scattered to higher energy and momentum, this is referred to as anti-Stokes process, while if it is scattered to lower frequency, this is referred to as Stokes scattering. In the later discussed experiment, only the Stokes part was measured as the intensity is stronger due to the fact that a phonon has to be emitted and not absorbed, which renders the process more likely. It is important to note that not all phonon lead to a change in susceptibility. Only those which do are Raman active.

2.5 Van-der-Waals Materials

Van-der-Waals materials (vdW-materials) are a class of layered materials, which have strong covalent bonds in the plane but due to missing dangling bonds only weak van-der-Waals forces between the

layers (Y. Liu et al. 2016). While this class is generally not new (Frindt 1963; Frindt and Yoffe 1962; Liang, Beal, and Knights 1971; Meinhold and Weiser 1976; Wilson and Yoffe 1969) in terms of thick layers of this class, they have drawn tremendous interest since the first systematic exfoliation of monolayered graphene (Novoselov 2004). While graphene is a semimetal (Novoselov et al. 2016a), shortly afterwards other vdW-materials of different types have been exfoliated as well.

In the following, a list of examples will be given to illustrate the variety of possibilities. TMDC's have shown to be a direct semiconductor with extraordinary properties in the monolayer case. Their investigation started with the first systematic exfoliation of a monolayer (ML) molybdenum disulfide (Mak et al. 2010). While several 2D-insulators have been found, hexagonal boron nitride (h-BN) (Watanabe, Taniguchi, and Kanda 2004) is the most important one, as it has been shown to be a brilliant substrate for other 2D-materials, improving their optical quality tremendously. In addition, more exotic classes like topological insulators (e.g. Bi2Se3 (Qi and Zhang 2010; Y. Zhang et al. 2010)) as well as superconductors exist. Here, $NbSe_2$ is an example that has been exfoliated by (Xi et al. 2016) and coworkers. Only recently, also ferromagnetic materials (B. Huang et al. 2017), Mott-insulators (Yijun Yu et al. 2015) and topological semimetals (Zaiyao Fei et al. 2017) have been reported as well.

While most of them still belong to the family of transition metal dichalcogenides, the field has started to extent to other compositions such as group III monochalcogenides (Bhimanapati et al. 2015), transition-metal oxides (Ding et al. 2015b; R. Ma and Sasaki 2010; Osada and Sasaki 2009), metal phosphates (Rui et al. 2013; D. Yang et al. 2014), Jarosites (Ding et al. 2015a) and MXenes (Anasori, Lukatskaya, and Gogotsi 2017) (transition metal carbides and nitrides).

Van-der-Waals materials have very interesting properties seen from both the experimental and the theoretical point of view. From the experimental side, it is convenient that the fabrication (Duong, Yun, and Lee 2017) and stacking of different monolayers on top of each other can be achieved rather easy (Castellanos-Gomez et al. 2014) at low cost in almost any lab. Furthermore, as no lattice matching is required (X. Wang and Xia 2015) many different combinations are possible. For many of them, new functionalities can be expected that are beyond the sum of the constituents (Geim and Grigorieva 2013). From the theory side, however, this class gives the opportunity to study strong correlations (Y. Cao, Fatemi, Demir, et al. 2018), strongly bound excitons (S.-Y. Chen et al. 2018), truly 2D- (Stroucken and Koch 2017), relativistic (Z. Q. Li et al. 2008) physics and many more aspects in a system that is comparably easy to study in experiment and resembles a perfect in-plane crystalline entity. While most of these phenomena are not new, often they can only be studied in less easily accessible materials systems such as ultra-cold-gases, conventional low temperature superconductors and so one. Thus, van-der-Waals materials make this exotic and rather complex physics accessible to a broad range of researchers and possible applications.

In this work, the combination of different TMDCs with one another or with h-BN is studied in detail. Primarily, their mutual influence on each other, the role of the substrate or environment as well as intrinsic properties such as exciton diffusion and dispersion are in the focus of the study.

2.5.1 Transition Metal Dichalcogenides

Transition metal dichalcogenides (TMDCs) are after graphene the most studied layered Van-der-Waals material. As the group of the transition metal used for the individual representative of the class strongly effects their properties and their most stable crystal structure (Voiry, Mohite, and Chhowalla 2015), they are often classified by the employed group of the transition metal in the 2D crystal. Generally, monolayers of TMDC's can occur in different crystal structures such as the trigonal prismatic phase (1H, symmetry D_{3h}), the trigonal octahedral phase (1T, symmetry D_{3d}) as well as a distorted version of the octahedral phase (1T') (Voiry, Mohite, and Chhowalla 2015) (cf. **Figure 6**). Here, in all cases the transition metal is sandwiched between layers of chalcogen atoms. Furthermore, the

monolayers of the trigonal prismatic phase can be stacked in two ways, imparting a hexagonal structure (2H phase, symmetry D^4_{6h}) or rhombohedral symmetry (3R, symmetry C^5_{3v}) (cf. **Figure 5**). The group of the transition metal changes the number of electrons, that can be found in the d-orbital. A fully filled orbital favors semiconducting behavior, whereas a partially filled orbital favors metallic behavior. Furthermore, they normally favor either 2H or 1T /1T' structure.

The present work except the studies about the alignment of WS_2 bilayers, only deals with the semiconducting 1H- or the 2H-phase of these materials. In this phase, the d-orbital is filled which results in a semiconducting behavior (Voiry, Mohite, and Chhowalla 2015). In contrast, for the 1T phase of the TMDC of these groups, a metallic behavior is found (Voiry, Mohite, and Chhowalla 2015).

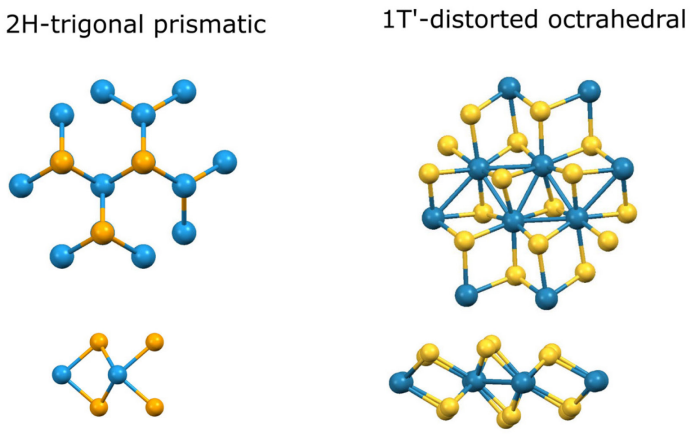

Figure 6 **|Trigonal Prismatic (2H /1H) and Distorted Octahedral (1T') Chrystal Phase.** Top and sideview for the 2H-phase at the example of WSe_2 from the group VI TMDCs (left) and the 1T'-phase of ReS_2 belonging to group VII TMDCs (right). The crystallographic data has been taken from the materials database (Persson 2014, 2017) and plotted with the Mercury software (Macrea et al. 2008).

2.5.2 Group VI – Transition Metal Dichalcogenides

During the time this thesis project was carried out, the field of 2D-materials, especially the field of TMDCs, has advanced vastly. As group VI TMDCs provide a direct semiconductor in the monolayer limit, they have drawn much attention is the semiconductor community. Particularly caused by their symmetry that gives optical access to the investigation of valleytronics. While some phenomena that occurred in our measurements have not been understood in the community at the beginning, some are already common knowledge of the community by now. As the theory and the experiments have advanced in major aspects, the following presentation of models and state-of-the art experiments will also include recent insights, which were not available at the beginning of this work.

The monolayers used in this thesis belong to the group VI of TMDCs. A more detailed explanation of their electric structure and optical properties will be given in the following. The members of this group consist of Molybdenum or Tungsten as the transition metal, and sulfur, selenium or tellurium as chalcogen atom. For the 2H-phase, the Brillouin zone is a hexagon with the maxima of the valence band (VB) and the minima of the conduction band (CB) occurring at the corners, the **K**-points (Gang Wang et al. 2018 and ref within), for the monolayer (cf. **Figure 7**). However, if a consecutive layer is added, a transition from a direct to an indirect bandgap semiconductor (Mak et al. 2010) occurs. While the maxima of the valence band remain at the **K/K'** point, the minima of the conduction band can now be found at the so called $\boldsymbol{\Sigma}$-point, sometimes also called **Q**-pockets. Caused by the time inversion symmetry, opposite **K**-points are not equivalent and are labelled **K** and **K'**.

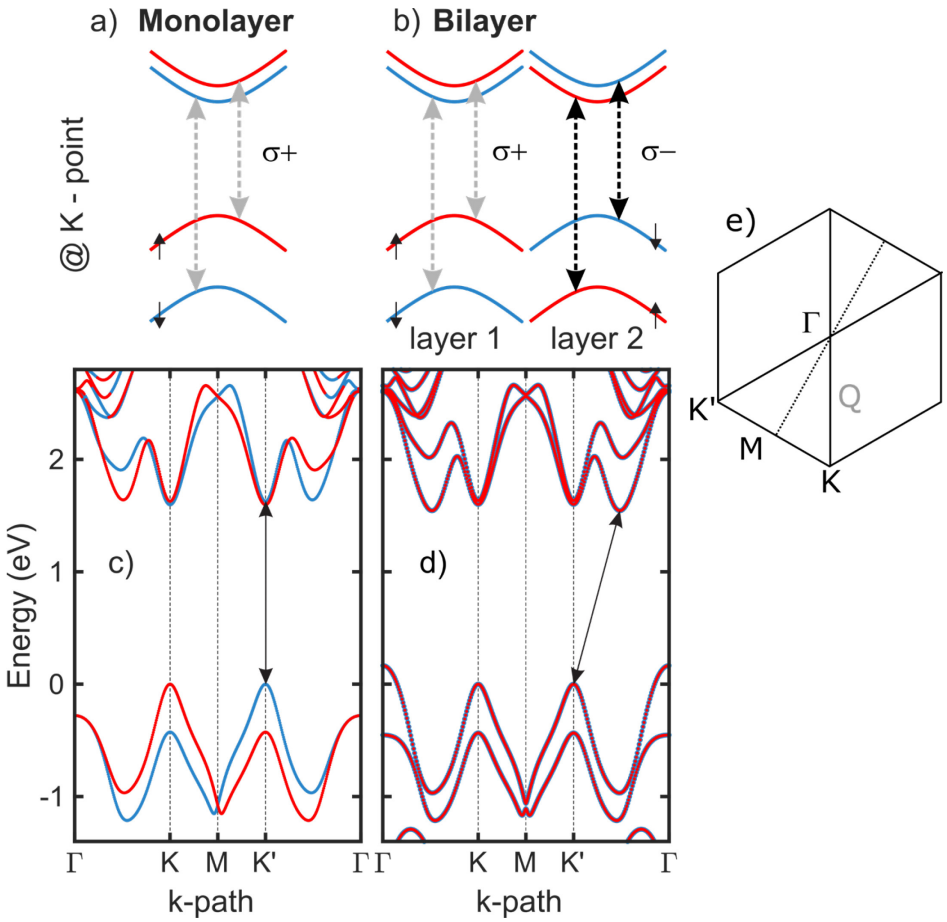

***Figure 7* | Band Structure for ML and BL of Tungsten Disulfide and Optical Selection Rules.** (a, b) show the selection rules for ML and BL (in the most common AA' stacking) at the example of WS_2. Blue lines denote spin-down and red one's spin-up bands. Possible transitions for A and B excitons are shown with grey and black arrows. (c,d) show the electronic bandstructure from DFT calculation. No excitonic effects are included at this stage. (e) shows the Brillouin-zone with the high symmetry points. The point of the indirect bandgap is as usual denoted with Q. The DFT has been performed by Lars Meckbach from the semiconductor quantum theory group of S. W. Koch. Details regarding the calculation can be found in chapter 5. Adapted with permission from (Lorenz Maximilian Schneider, Kuhnert, et al. 2019). Copyright 2019 American Chemical Society.

Caused by the heavy transition metal, a strong spin-orbit interaction can be typically found in TMDCs. While in the conduction band the splitting amounts only a few meV, in the valence band it is on the scale of 200 meV as can be seen from the DFT calculation. Due to the time inversion symmetry, the order of the bands is reversed in the **K** and **K'** valley.

2.5.3 Orbitals and Selection Rules.

Some of the interesting phenomena such as optical helicity or the valley Hall effect are based on the orbital symmetry and their selection rules for excitation and emission. In the following, the orbital nature of the conduction and valence band will be discussed briefly with the focus on their symmetry and implications. This will be done for the case of molybdenum disulfide monolayer (T. Cao et al. 2012). In a simple picture the initial configuration looks the following. The partially filled d-orbitals of the transition metal are in between the bonding and antibonding Mo-S bands. The states of the valence band involve the $d_{x^2-y^2}$ and the d_{xy} of molybdenum as well as the p_x and p_y orbitals of sulfur. The remaining d-orbitals (d_{xz} and d_{yz}) do not fulfill the mirror symmetry of the monolayer and do not take part in the hybridization (D. Xiao et al. 2012a). According to the three fold rotational symmetry of the 1H-phase at the **K** point, as well as translational symmetry of the crystal, the d-states hybridize to $1/\sqrt{2}\left(d_{x^2-y^2}+id_{xy}\right)$ $(l=2)$ interacting with $1/\sqrt{2}\left(p_x+ip_y\right)(l=1)$. In contrast, at **K'** the signs are reversed resulting in $1/\sqrt{2}\left(d_{x^2-y^2}-id_{xy}\right)$ $(l=-2)$ and $1/\sqrt{2}\left(p_x-ip_y\right)(l=-1)$. The conduction

band is mainly given by the $d_{z^2}(l=0)$-orbitals of molybdenum, with almost no contributions of p-orbitals. (T. Cao et al. 2012).

If one now calculates the dipole matrix elements for circular polarized light, one can see that the valley can be addressed individually. The dipole matrix operator for left (right) circular polarized light can be written as $\hat{P}_{\sigma^+} = \hat{P}_x \pm i\,\hat{P}_y$, with $P_\alpha(k) = m_o \left\langle u_c(k) \middle| \frac{1}{\hbar}\frac{\partial \hat{H}}{\partial k_\alpha} \middle| u_v(k) \right\rangle$ (D. Xiao et al. 2012b). The relevant two band Hamiltonian (heavy Dirac fermion Hamiltonian) at **K** or **K'** points looks the following:

Equation 2-17 **| Two band $k \cdot p$ Hamiltonian (Heavy Dirac Fermions)**

$$\hat{H}_0 = at\left(\tau k_x \hat{\sigma}_x + k_y \hat{\sigma}_y\right) + \frac{\Delta}{2}\hat{\sigma}_z - \frac{\lambda\tau(\widehat{\sigma_z}-1)}{2}\,\widehat{s_z},$$

with a the lattice constant, t the effective hopping integral, Δ the energy gap between the two bands, τ the valley index and $\hat{\sigma}$ the Pauli matrices. The last term describes the spin-orbit coupling with 2λ being the spin splitting and $\widehat{s_z}$ the spin operator. It follows for the interband matrix element:

Equation 2-18: **| Interband matrix element**

$$\left|P_\pm(k)\right|^2 = \frac{m_0^2 a^2 t^2}{\hbar^2}\left(1 \pm \frac{\tau\Delta}{\sqrt{\Delta^2 + 4a^2t^2k^2}}\right)^2$$

As $\Delta \gg atk$ is valid, one get almost perfect selectivity for the valleys (D. Xiao et al. 2012a). Left-circular polarization only excites carriers in the **K**-valley and vice-versa for the opposite helicity (cf. **Figure 7**). The fundamental reason is the time reversal symmetry between **K** and **K'** as well as the broken inversion symmetry**.** When the inversion symmetry is restored (e.g. in 2H-bilayer) hybridization with the opposite spin but same energy become possible and spin-valley coupling is gone.

While the main concept is also applicable for all other TMDCs, the order of the hybridization in the conduction band is reversed for tungsten-based materials (cf. **Figure 9**), leading to the fact that a dark exciton is in fact the lowest excited state for tungsten-based materials. This has large consequences for the spin and valley dynamics of the corresponding TMDC.

2.5.4 Excitonic Properties

2.5.4.1 Intralayer Excitons

One important feature of TMDCs is that the electronic correlation in these materials are generally huge. For instance the exciton binding for suspended monolayers can reach up to 0.6 eV (Gerber and Marie 2018b), making it possible to study exciton dominated physics even at room temperature. However, as will be explained and demonstrated in this thesis and has been addressed by other recent prominent work on this subject in the literature (Ajayi et al. 2017; Cadiz et al. 2017; Jakubczyk et al. 2017; Stier, Wilson, et al. 2016), including model work (Horng et al. 2018; Stroucken, Grönqvist, and Koch 2013), among others the binding energy is strongly affected by the electronic screening induced by the environment. For a monolayer supported by an insulating substrate, the binding energies is roughly two thirds of the suspending case (Gerber and Marie 2018a), shrinking even further for encapsulated monolayers (Gerber and Marie 2018b) or on metallic substrates like gold (S. Park et al. 2018). At the same time, a band structure renormalization takes place due to density-dependent effects (Chernikov, Ruppert, et al. 2015) as well as screening through the dielectric environment (Kleinman and Miller 1985; Lars Meckbach, Stroucken, and Koch 2018b) resulting only in a small shift of the main excitonic lines due to an adjustment of the binding energies that nearly cancels out the effect of renormalization on the neutral-exciton's energy position. As the binding energy of higher-order correlation or excitations, which can be all well described in the quasiparticle picture, such as three-particle states (trion (Arora et al. 2019; Plechinger et al. 2016; L.M. Schneider et al. 2017) or

charged exciton) and four-particle Coulomb states (referred to as biexciton (Lorenz Maximilian Schneider et al. 2017; You et al. 2015) or excitonic molecule) in semiconductors are generally around 10 – 20% of the neutral exitonic binding energy (Klingshirn 2012), they can also be easily observed at helium temperatures for TMDCs. Some can even be observed at higher temperatures. Nonetheless, at elevated carrier densities or doping levels exciton-polarons are observed instead of trions and excitons (Efimkin and MacDonald 2017).

Caused by the spin-orbit splitting of the valence and conduction band, as well as the valley degree of freedom, several different configurations of excitons and higher-order quasiparticles exist. On the course scale, excitons composed from the lowest conduction band and highest valence band are called A-exciton, the next possible combination B and so on. **Figure 8** displays a schematic of the possible transitions and their common labeling. Please note that, while the electronic states forming the A and B exciton are located next to the K-point, this is not true anymore for the C and D resonances. Here, states near the Γ and near the K-point contribute to those states without involving these two symmetry points (Ridolfi, Lewenkopf, and Pereira 2018).

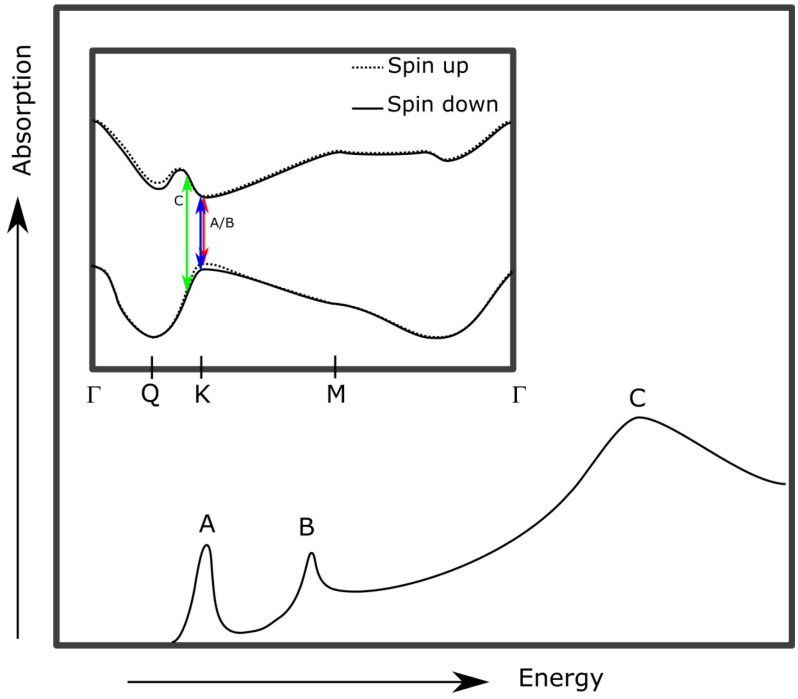

***Figure 8* | Schematic of the Optical Resonances:** The graph shows a schematic absorption spectrum at the example of molybdenum disulfide after (Yilei Li, Chernikov, et al. 2014a) and their common labeling. The inset shows a simplified electronic band structure after (Ridolfi, Lewenkopf, and Pereira 2018). While the A and B excitonic resonances mainly arise due to electronic populations at the **K/K'** point, theoretical solutions of Bethe-Salpeter-equation show, that the C and D resonances of monolayer TMDCs normally originate from states near Γ and **K** (Qiu, Da Jornada, and Louie 2013; Ridolfi, Lewenkopf, and Pereira 2018; A. Steinhoff et al. 2014).

Each member of these excitonic series can be further classified as inter- or intravalley, as well as bright or dark excitons. Generally, only those excitons can recombine radiatively from the lightcone ($Q \approx 0$), where the transition is dipole- and spin allowed. Therefore, they are referred to as bright excitons. All other combinations, including triplet states within the light cone, are considered and labelled dark excitons (cf. **Figure 9**). Even though dark excitons cannot be accessed optically, they have a huge impact on the observation of their bright counterparts, especially on the dynamics and charge-carrier distribution in such systems. Only intravalley excitons can have zero center of mass momentum (Qiu, Cao, and Louie 2015; Selig et al. 2017; F. Wu, Qu, and MacDonald 2015) whereas the momentum of intervalley excitons corresponds to the difference of the momentum of the electron and hole i.e. $Q \approx K \; or \; \Lambda$.

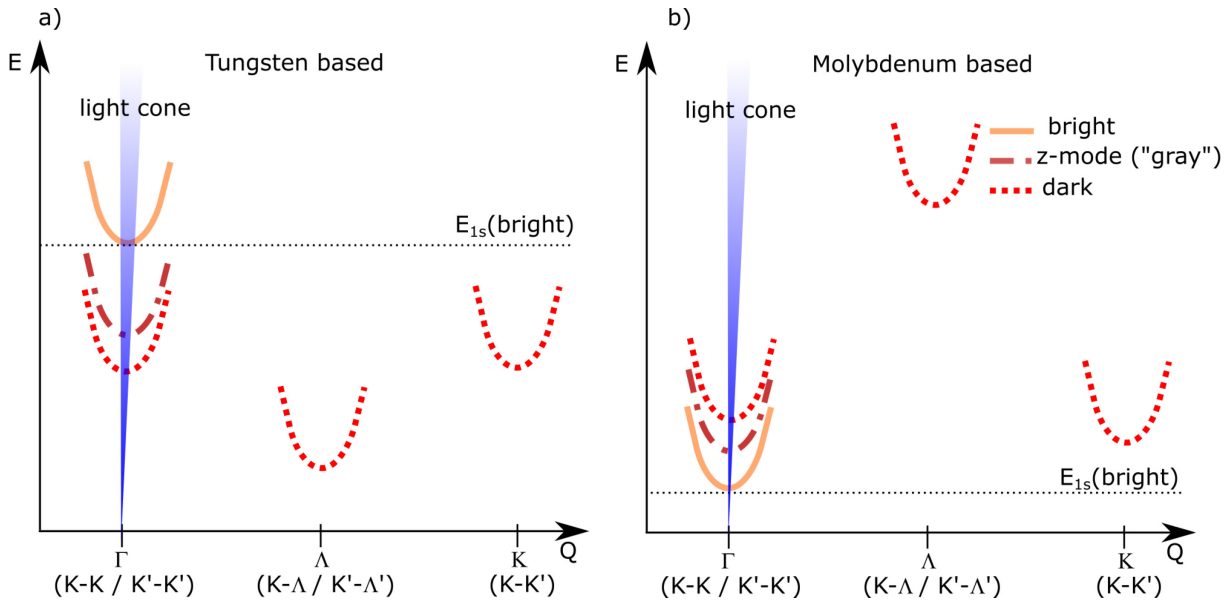

***Figure 9* | Sketch of the Exciton Landscape for Tungsten and Molybdenum based TMDCs :** Schematic drawing of the possible exciton states in tungsten-based (a) and molybdenum-based (b) group-IV TMDC monolayers. This figure was established using model descriptions and diagrams in (Berghäuser et al. 2018; Robert et al. 2017; Selig et al. 2017; G. Wang et al. 2017b). Optical accessible states are depicted by straight lines while inaccessible states are shown dotted. Partial optical accessibility, i.e. only excitable for light with z-polarization, is therefore shown by dash-dotted lines.

The monolayer has been shown to have an extraordinary strong light-matter interaction at the excitonic resonance. Even though just a monolayer of material is present, about 10% (Gerber and Marie 2018b; Yilei Li, Chernikov, et al. 2014b) of the incoming light is absorbed at resonance and about 5% in the range of continuum states.

Coming back to above discussed bright and dark exciton states, higher-order excitonic correlations and quasiparticles are formed and are easily observed in monolayer TMDCs. Normally, trions (Arora et al. 2019; Plechinger et al. 2016), biexciton (Barbone et al. 2018; Alexander Steinhoff et al. 2018; You et al. 2015) and charged biexcitons can be observed (S.-Y. Chen et al. 2018). Many of them can be formed in different configurations having different bands involved. The different possibilities are briefly discussed in the subsection about valleytronics (cf. chapter 2.6.2).

Owing to the large exciton binding energy the different excited states of the excitons (A, B, C and so on) are easily resolvable at low temperatures. Caused by different size of the exciton orbital functions, the amount of screening in the single layer 2D-crystal is different for higher excitations than for the exciton's 1s-state, as a considerably part of the Coulomb interaction involves the surrounding, (Berkelbach, Hybertsen, and Reichman 2013; Chernikov et al. 2014; Cudazzo, Tokatly, and Rubio 2011). Therefore, a non-hydrogenic Rydberg series can be observed, that is also different from a 2D-Hydrogenic series. This non-hydrogenic series can be explained if the screening is treated correctly.

2.5.4.2 Carrier Screening in a 2D-Material

This fundamental difference of electronic screening between a 2D-material in a 3D volume and three dimensional system can be understood in a simple classical approach (Cudazzo, Tokatly, and Rubio 2011; Keldysh 1979; Rytova 1967). If one assumes an infinitely thin sheet at z=0 subject to an external field ϕ_{ext} generated by a point charge at the origin, the potential $\phi(r)$ can then by calculated using the Poisson's equation.

***Equation 2-19* |Poisson's equation**

$$\nabla^2\phi(r) = -4\pi n(r)$$

Here, *n* denotes the charge density that is the sum of the external charge and the induced one. By expressing the induced charge by the polarizability α_{2D}, one arrives at the following formula and its Fourier transform in cylinder coordinates:

***Equation 2-20* |Poisson's equation in real space and momentum space for a 2D-material**

$$\nabla^2\phi(r) = -4\pi e\delta(r) - 4\pi\alpha_{2D}\nabla_\rho^2\phi(\rho, z=0)\delta(z)$$

$$(|q|^2 + k_z^2)\phi(q,k_z) = 4\pi e - 4\pi\alpha_{2D}|q|^2\int\frac{dk_z}{2\pi}\phi(q,k_z)$$

In this equation *q* denotes the in-plane momentum whereas k_z denotes the out-of-plane momentum. The last part can be identified as the Fourier component of the 2D macroscopic potential. By solving this equation, one can obtain the potential as well as the form of the permittivity.

***Equation 2-21* | Scalar potential for a single charge in a 2D-material and resulting permittivity**

$$\phi_{2D}(q) = \frac{2\pi e}{|q|(1+2\pi\alpha_{2D}|q|)}$$

$$\epsilon(q) = 1 + 2\pi\alpha_{2D}|q|$$

The result is striking; the permittivity is not anymore given by a scale invariant multiplication with a simple dielectric constant like in a 3D semiconductor, which renormalizes the electric charge, but is intrinsically *q* dependent. If one takes the inverse Fourier transform of $e\phi_{2D}(q)$ one can retrieve the potential field by an electron residing in the sheet in the presence of another charge.

***Equation 2-22* | Rytova-Keldysh Potential between two charges in a (suspended) 2D material**

$$V_{eff}(\rho) = \frac{e^2}{4\alpha_{2D}}\left[H_0\left(\frac{\rho}{r_0}\right) - Y_0\left(\frac{\rho}{r_0}\right)\right]$$

Here, H_0 and Y_0 are the Struve and second-kind Bessel function and $r_0 = 2\pi\alpha_{2D}$. It is instructive to look at the limiting cases of this function. For large separation, the usual 1/r dependence of the unscreened Coulomb potential is retrieved, for small distances however it scales logarithmically. This means that for higher states, where the mean charge-carrier separation is big, nearly a Rydberg series can be observed (Chernikov et al. 2014), while at low main quantum numbers deviation are found in the energy spacing. When writing the scalar potential as an integral over a charge distribution, another interesting fact can be found. Indeed, such a potential (cf. **Figure 10**) is given by an out-of-plane 1D-string of charge of height $2r_0$, although the actual polarization is, of course, an in-plane circle.

***Equation 2-23* | Charge Distribution induced by a point charge in a 2D-material.**

$$Q(r) = \frac{e\delta(\rho)\exp\left(\frac{|z|}{r_0}\right)}{2r_0}$$

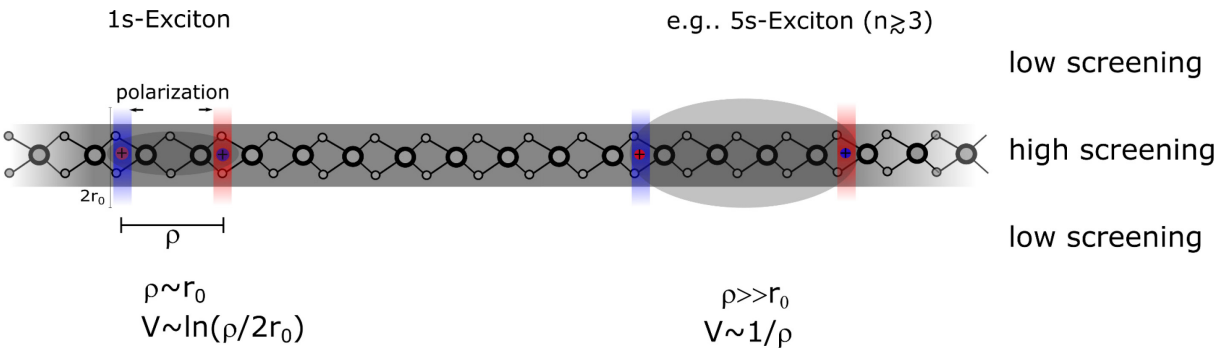

***Figure 10* |Screening in a Suspended, Infinitesimally Thin Material as a Function of the Distance.** For small distances (e.g. 1s-exciton) the potential is similar to the attraction of two 1D-strings and drops logarithmically (Cudazzo, Tokatly, and Rubio 2011). In contrast, for bigger distance, it behaves like the attraction between two point-particles. Thus, the normal 1/r behavior of the Coulomb potential is restored. For example, for 3s and higher excitonic states (Chernikov et al. 2014) the energetic differences are again well described by a hydrogenic Rydberg series.

Actually, this result strictly only is a good approximation for a suspended layer. For a substrate supported layer also the screening by mirror charges in the dielectric surrounding has to be considered (Cho and Berkelbach 2018; Lars Meckbach, Stroucken, and Koch 2018b; Scharf et al. 2019; Trolle, Pedersen, and Véniard 2017), leading to a more complex function. Nevertheless, the qualitative change of a momentum dependent dielectric constant compared to the usual constant is also found in this case. Recently, measurements on exciton in encapsulated monolayers have shown a Rydberg series resembling the physics in a fractal dimension between 2D and 3D (M. R. Molas et al. 2019).

The reduced screening in the surrounding in summary enhances the Coulomb interaction including its exchange interaction. This is especially true for the long-range interactions. Thus there are of bigger importance then in conventional semiconductors such as GaAs.

2.5.4.3 Interlayer and Moiré Excitons

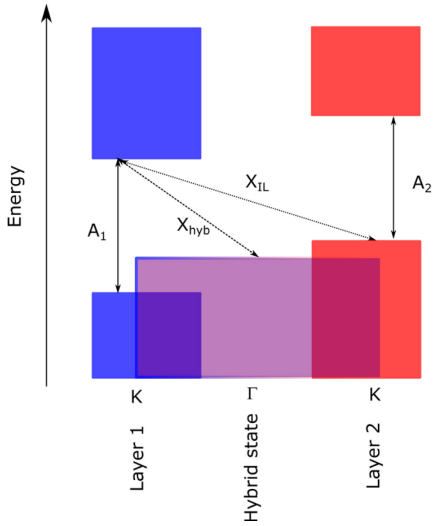

***Figure 11* | Schematic Illustration of Intralayer, Interlayer as well as Hybrid States.** In heterostructures, generally, transition within the material can occur (i.e. intralayer excitons), as well as between both material (i.e. interlayer, charge-transfer or type-II excitons) as well as between a single state, which is localized within one layer (for TMDCs often at the K-point) with another hybridized state (for TMDCs the Γ-point as well as the minimum at Q are important). While such a transition comes from an interlayer exciton it is strictly speaking not a true charge-transfer exciton, since the one type of charge (here hole) is only partially transferred and via hybridization present in both layers. The depiction has been drawn freely after (Kunstmann et al. 2018).

In the above discussion, it was always assumed that excitons are formed from an electron and a hole resting in one layer. But, of course, in stacks of different van-der-Waals materials also space-indirect type-II excitons can form similar to conventional semiconductors (Nagler et al. 2017; J. Zhang et al.

2016), where the hole remains in the first layer and the electron transfers to the second layer. Furthermore, excitons formed from a hole or electron delocalized over both layers in a hybridized state and an electron or hole localized in a specific layer have also been reported (Kunstmann et al. 2018). Both scenarios as well as the intralayer recombination are depicted in **Figure 11**.

Additionally, the twist angle provides an additional degree of freedom to tune the coupling strength between both layers. As such, different oscillator strength (H. Zhu et al. 2017) and a small tuning of the interlayer exciton's energy are possible (Kunstmann et al. 2018), giving strong coupling in the case of almost perfect alignment. However, such a change in the twist angle will also introduce a moiré pattern (cf. **Figure 12a**). The schematic figure shows an exemplary moiré supercell that stretches over several primitive unit cells of the individual crystal (the here given example is for an unrealistic large lattice constant mismatch of 10%; for realistic values the supercell will become even larger). If the moiré periodicity is large, the periodical change in layer coupling, dielectric screening and local symmetry leads to a periodical change in the band minima as well as the binding energies (cf. **Figure 12c**) of both the intra- and the interlayer excitons (H. Yu et al. 2017). At the same time, the local symmetry found at the high symmetry point(s) in real space **Figure 12b**) are considerably different. Thus, the selection rules for inter- and intralayer excitons are altered periodically (cf. **Figure 12c**). The resulting potential landscape in large moiré patterns lead to the formation of moiré subbands between the minima that can be seen as a grid of quantum dots or quantum sheets respectively. The resulting moiré bands are now resolvable in optical experiments due to the increased quality of heterostructure fabrication (Alexeev et al. 2019; Seyler et al. 2019; Tran et al. 2019). In typical PL-experiments, one generally measures an average over the whole supercell, as the moiré periodicity is below the diffraction limit. For small twist angles periodicities of about 10 nm are found (Jin et al. 2019). Nonetheless, the energetic modulation leads to an accumulation of excitons in the minima and spatial modification of transition dipole moment leads to a modified oscillator strength. Thus, the measured results have to be carefully analyzed as a weighted average. The results are often discussed using the paradigm of a mini-Brillouin zone (cf. **Figure 12** d). It is used to describe the hybridized states at the high symmetry points for low twist angles.

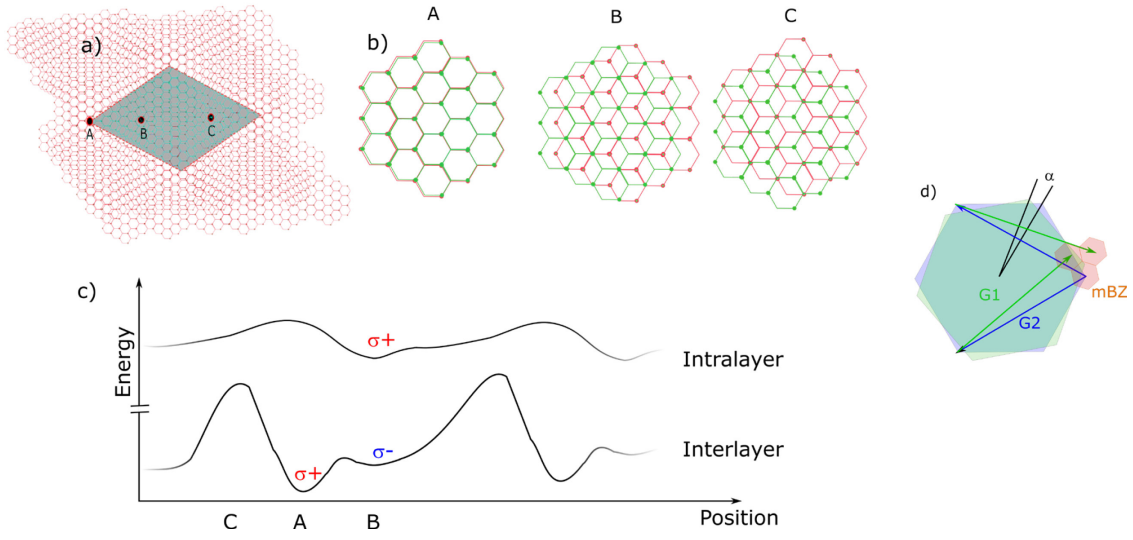

***Figure 12* | Schematic Drawing of Local Symmetry and Energy Shifts in a Moiré Pattern of Two TMDC.** (a) Exemplary moiré pattern together with the moiré supercell. The high-symmetry points of the real-space are labelled A, B, and C. (b) Close-up view of to the high-symmetry points in real-space revealing different local symmetry. (c) Schematic drawing of the effect of the moiré potential to the energetics of inter- and intralayer excitons. The modulations are usually on the 10 meV scale for intra- and 100 meV for interlayer excitons. Diagrams have been drawn freely after (H. Yu et al. 2017). (d) Sketch of the construction of the mini-Brillouin zone from the twisted Brillouin zones of the individual layers.

2.5.5 Properties of the Lattice System

The phonon system of such layered systems also shows rich physics such as circular selection rules (Z. Li et al. 2019; E. Liu et al. 2019), strong exciton-phonon coupling (Shree et al. 2018) and phonon sidebands (Christiansen et al. 2017). In the following section, the main phonon resonances will be presented systematically.

A layer of a TMDC consists generally of three atomic layers, with three atoms in a unit cell. For a monolayer, there are nine possible vibrational modes, where three are acoustic and six are optical. One acoustic branch for longitudinal (LA) and for transversal (TA) in-plane modes as well one out-of-plane mode (ZA) (Terrones et al. 2014). In contrast, for the optical ones there are always two branches. One type, where only the chalcogens are moving relative to the central transition metal, and another one where both atom types are moving. When bilayers or few layers system are considered, the optical phonons of the individual layers couple to each other, leading to the emergance of new coupled modes (Terrones et al. 2014). Together with the different dielectric screening, this leads to small shifts in the phonon energies. This fact is often used to identify the number of layers (C. Lee et al. 2010; Hong Li et al. 2012; W. Zhao et al. 2013), as it is less affected by doping/strain than the PL position. At the same time, the acoustic phonon branches couple to new modes, including the shear and breathing modes (S. Huang et al. 2016; Puretzky et al. 2016; Zeng et al. 2012; Y. Zhao et al. 2013). **Figure 13** shows a schematic representation of the most important optical (Raman) modes. The phonon band structure for ML and bulk can be found for example in (Sahin et al. 2013).

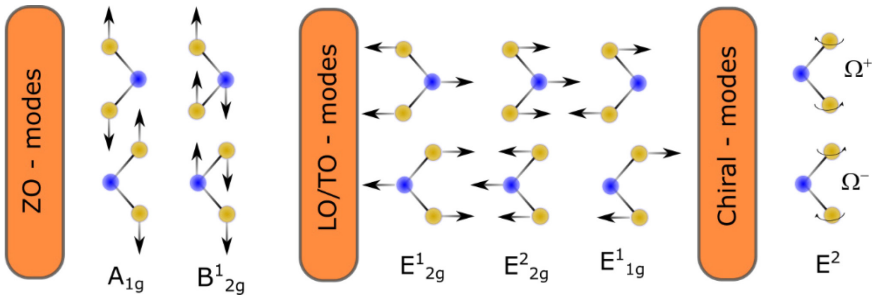

***Figure 13* | Optical Phonon Modes.** The sketch shows the fundamental vibrational optical modes. Besides B^1_{2g} they are Raman active. If a coherent superposition of LO and ZO modes is excited, also chiral modes become possible. The picture has been redrawn from (E. Liu et al. 2019; X. Luo et al. 2013).

While chiral modes are not important in a usual Raman experiment, they are a valuable tool to study the impact of dark excitons, which not or only couple to the z-mode of incoming light. However, it has been shown that, if phonon assisted emission from dark excitons takes place a chiral phonon and a counter-polarized photon is emitted (M. He et al. 2020; E. Liu et al. 2019, 2020). By this relaxation pathway, the valleytronic properties of the dark exciton can be studied that are not accessible directly.

When a common Raman measurement is performed using the 514.8 nm laser line of an Argon laser for WS_2, a clear resonance of the LA phonon at the M-point can be found (Berkdemir et al. 2013) due to a resonance Raman effect, while usually states at the Γ-point are observed in Raman spectrsocopy. Furthermore, higher-order modes start to appear which involve the modes discussed above as well as the LA(M) mode (Berkdemir et al. 2013; Chow et al. 2017).

The longitudinal acoustic mode is also important in valleytronics. In valleytronics, there are two main processes of decoherence (Yilei Li, Ludwig, et al. 2014; Tornatzky, Kaulitz, and Maultzsch 2018). A scattering with

two LA(K) phonons (Tornatzky, Kaulitz, and Maultzsch 2018) as well as interaction due to exchange interaction (Kim, Shin, and Lim 2015) (the process is described later on). The process of the two-phonon scattering process has a major consequence for PL investigations, as well as valleytronic

applications. If the excitation is detuned by more than the energy of these phonons (Tornatzky, Kaulitz, and Maultzsch 2018), the degree of valley polarization is drastically reduced due to the generation of these particular phonons, as could be revealed in photoluminescence excitation spectroscopy (PLE) experiments.

2.6 Valley- and Layertronics

2.6.1 Concept for Excitons

Mono- and few-layer TMDCs are often treated in the framework of the heavy fermion Dirac Hamiltonian (see section 2.5.3 about orbitals and selection rules). From this notation it is clear, that the valley index can be treated as a good quantum number (Xu et al. 2014) (if long-range exchange interaction is neglected (Glazov et al. 2014; Qiu, Cao, and Louie 2015; H. Yu et al. 2014)). Similarly, in some configurations, the interaction in bilayers is weak enough that the individual bands can be attributed to a certain layer. If this is true, the layer index can be seen as a good quantum number (Xu et al. 2014). As in both scenarios (Xu et al. 2014) coherent superposition of excitation in both valleys/layers are possible, the population is normally described by using a valley- or layer pseudospin. They can be depicted in a Bloch sphere, where the poles describe the situation, in which the hole population/state consists of states in one valley or layer. The states at the equator correspondingly represent a state, where a coherent superposition with equal proportion of valleys/layers and a certain phase is present. The valley pseudo spin together with the intrinsic spin of the states are important for the magnetic moment and the valley hall effect. In addition, this is important for the optical selection rules. The layer pseudo spin, however, has to be considered when the electric polarization and the dipole-moments are considered. It can also become important in the selection rules in certain heterostructures.

The states at the equator when depicting the valley pseudo spin are especially important in spectroscopy as they are directly addressed by linear polarized light, while the states at the poles are addressed by circular polarized light. Measuring the degree of linear or circular polarized light of a ML-system therefore can be used the judge on the valley coherence or valley polarization present in the system, respectively.

In the presence of external fields, i.e. electric or magnetic fields (including the optical light field for excitation), the TMDC has to be treated using extended equations of motions (Xu et al. 2014) including the Berry curvature $\boldsymbol{\Omega}$ and the orbital magnetic moment $\boldsymbol{m}$. These pseudovectors allow the spin Hall, valley hall, Zeeman effects as well as the optical excitation to be treated via a semi-classical effective mass model. The Berry curvature here can be seen as a pseudomagnetic field, and the orbital magnetic moment is used to model the renormalization of the given energies. $P_{n,i}$ denotes the interband matrix element of the momentum operator and *m* the electron mass. The general equations as well as the specific one for the example of MoS_2 (D. Xiao et al. 2012b) is given below. For the example, the two band Hamiltonian (cf. chapter2.5.3) is used as a basis. Caused by an inversion symmetry breaking, both valleys have an orbital angular momentum of different sign. Similarly the curvature is opposite for valence and conduction band.

Both, valley and layer pseudo-spin have been proposed for the next generation logic implementation and then are referred to as valleytronics (Schaibley et al. 2016b) or layertronics (Crasto de Lima, Ferreira, and Miwa 2018). Often a coherent control on a sub cycle (Langer et al. 2018) scale of the exciting pulse is the aim, possibly speeding up computation by orders of magnitude compared to current electronics.

***Equation 2-24* | Berry Curvature and Orbital Magnetic Moment**

$$\dot{\boldsymbol{r}} = \frac{1}{\hbar}\frac{\partial E_n(\boldsymbol{k})}{\partial \boldsymbol{k}} - \dot{\boldsymbol{k}} \times \boldsymbol{\Omega_n}(k) \qquad ,\hbar\dot{\boldsymbol{k}} = -e\boldsymbol{E} - e\,\dot{\boldsymbol{r}} \times \boldsymbol{B}$$

$$\boldsymbol{\Omega}_n(k) = \frac{i\,\hbar^2}{m^2}\sum_{i\neq n} P_{n,i}(\boldsymbol{k}) \times \frac{P_{i,n}(\boldsymbol{k})}{\left[E_n^0(\boldsymbol{k}) - E_i^0(\boldsymbol{k})\right]^2}$$

$$\mathbf{m}_{\boldsymbol{n}}(k) = \frac{ie\,\hbar^2}{2m^2}\sum_{i\neq n} P_{n,i}(\boldsymbol{k}) \times \frac{P_{i,n}(\boldsymbol{k})}{E_n^0(\boldsymbol{k}) - E_i^0(\boldsymbol{k})}$$

$$E_n(k) = E_n^0 - \boldsymbol{m}_n(\boldsymbol{k}) \cdot \boldsymbol{B}$$

***Equation 2-25* | Berry curvature for MoS_2 from the two band Hamiltonian (ch. 2.5.3) (D. Xiao et al. 2012b)**

$$\Omega_C(k) = -\Omega_v(k) = -\tau\frac{2a^2t^2\Delta'}{(\Delta'^2 + 4a^2t^2k^2)^{\frac{3}{2}}}$$

$$\Delta' = \Delta - \tau s_z\lambda$$

2.6.2 Extension of the Concept for Higher-Order Excitons

While the concept of valleys and selection rules is relatively clear for the bright excitons, it becomes increasingly more complex when higher-order excitonic complexes comprising three, four or even five particles are involved. In this case, the origin of every hole and electron has to be considered. Obviously, the possible configurations are growing fast (8 for two particle excitons, 12 for negative trions and 4 for positive trions; see SI of (S.-Y. Chen et al. 2018) or (Barbone et al. 2018; Plechinger et al. 2016; Alexander Steinhoff et al. 2018)). For some exemplary configurations see **Figure 14**.

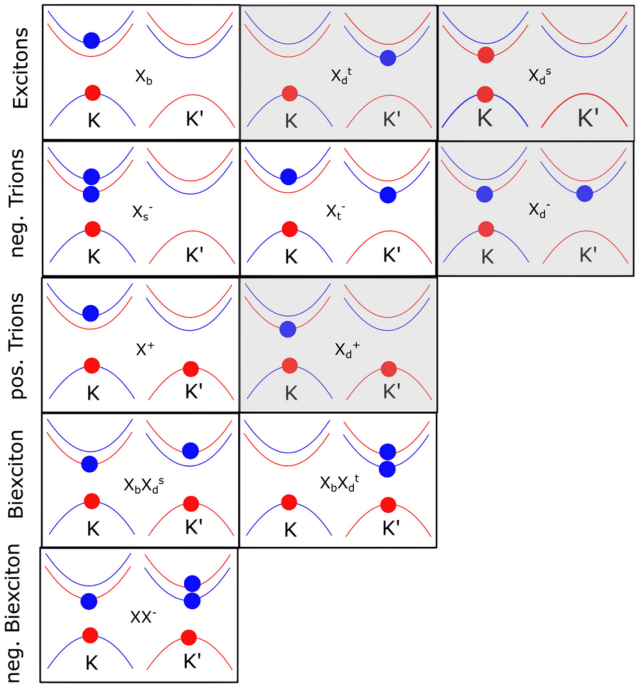

***Figure 14* | Possible Exciton-Complexes:** Sketch of the possible excitonic complexes formed from electrons (blue) and holes (red) at the example of WSe_2 after (Barbone et al. 2018; S.-Y. Chen et al. 2018; Fu, Cruz, and Qu 2019). For the sake of clarity, in this modified version of the chart, electrons of a valley that correspond to dark states are drawn in dark color. *s* and *t* denote singlet and triplet states. While often several possibilities are given, for the biexcitons only the experimentally observed ones by (Barbone et al. 2018; S.-Y. Chen et al. 2018) are shown. Nonetheless, other hybridized biexciton states exist (Alexander Steinhoff et al. 2018). The chart shows only have those possibilities where a hole is in K. If mirrored with a hole in K' the remaining options can be retrieved.

For each of them, fundamental considerations like selection rules, energies and g-factors have to be considered again. For example, the valley polarization of a biexciton, or more precisely a biexciton formed from a dark and a bright exciton, exhibits a negative valley polarization instead of positive one expected for the bright exciton (Nagler et al. 2018). These kinds of considerations make it possible to identify the species that are actually present in the system. Thus, the interpretation of helicity or linear polarization anisotropy of emission has to be handled carefully if dealing with higher order excitonic complexes or phonon sidebands.

2.7 Dispersion of Quasi-Particles

2.7.1 Excitons

As excitonic quasi-particles represent the fundamental excitation of the semiconductor, it is essential to also understand their intrinsic properties in that material system for example their dispersion and dynamics. Generally, the energy-momentum dispersion is the result of the complex interplay of the contributing electrons and wavefunctions involved. However, around their dispersion minima the behaviour of the exciton can well be approximated by a Taylor series up to second order. For a conventional semiconductor, this leads to the following formula (Klingshirn 2012):

***Equation 2-26* | Exciton dispersion in effective mass approximation**

$$E_x(Q) = E(Q=0) + \frac{\hbar^2 Q^2}{2m^*} = E_0 + \frac{\hbar^2 Q^2}{2m^*}$$

with m^* being the excitonic effective mass. In most cases when exotic physics are absent this will simplify to the normal kinetic energy of the center-of-mass with the exciton mass m.

However, recent theoretical predictions (Glazov et al. 2014; Qiu, Cao, and Louie 2015; F. Wu, Qu, and MacDonald 2015; H. Yu et al. 2014) pointed out that for TMDCs, where a non-negligible long-range exchange interaction within and across the layers is present, the dispersion is modified. The short-range interaction, in contrast, is responsible for the splitting of bright and dark states. For small centre-of-mass momentum, this additional term is linear in *Q* and becomes the leading term in the Taylor expansion. Similar to the Coulomb interaction the effect of its long-range exchange interaction becomes much stronger than in III/V quantum wells, where the effect had also been found but is negligible (Andreani and Bassani 1990). Furthermore, for monolayer TMDCs, only the in-plane momentum is defined and has to be considered. The actual Hamiltonian describes a lower parabolic branch as well as an upper one with non-analytic solution. For small momenta, however, an effective Hamiltonian can be found by a Taylor expansion (Qiu, Cao, and Louie 2015):

***Equation 2-27* | Effective Hamiltonian for the fine structure of the neutral exciton due to long range exchange interaction.**

$$H^{BSE} = \mathrm{E}_0 \cdot \mathbf{1} + A\big[\mathbf{1} + \cos(2\theta)\,\boldsymbol{\sigma_x} + \sin(2\theta)\,\boldsymbol{\sigma_y}\big]|\boldsymbol{Q}| + \{\left(\frac{\hbar^2}{2M} + \alpha + \beta\right)\cdot \mathbf{1} + |\beta'|\big[\cos(2\theta)\,\boldsymbol{\sigma_x} + \sin(2\theta)\,\boldsymbol{\sigma_y}\big]\}\ \ \boldsymbol{Q}^2$$

$$E^{+}_{TMDC}(q_{||}) = E_0 + 2A|q_{||}| + \left(\tfrac{\hbar^2}{2M} + \alpha + \beta + |\beta'|\right) q_{||}^2 = E_0 + 2A|q_{||}| + \frac{\hbar^2 \boldsymbol{q}_{||}^2}{2m_2^*}$$

$$E^{-}_{TMDC}(q_{||}) = E_0 + \left(\frac{\hbar^2}{2M} + \alpha + \beta - |\beta'|\right) q_{||}^2 = E_0 + \frac{\hbar^2 \boldsymbol{q}_{||}^2}{2m^*}$$

, where E_0 represent the ground-state energy, θ denotes the in-plane angle of the projected incoming light wave and σ the Pauli matrices. As can be seen from this set of equations, the (long-range) coupled

excitons form two new hybridized states which is one source of valley depolarization. The upper branch has an additional linear term. Here, *A* is a constant describing the linear part of the long-range exchange interaction. In addition, several quadratic terms also arise which effectively change the particle's effective mass on each of the possible branches, E^+ and E^-, from the complete effective exciton mass ($M = m_e + m_h$) to a new effective mass m_2^* and m^*. α describes the contribution from spin-unlike states, and β and β' the contribution from inter- and intravalley exchange interactions, respectively. The associated wavefunction of the upper branch couples to the longitudinal projection of the incoming light, while the lower one couples to the transversal one (Andreani and Bassani 1990; Glazov et al. 2014; Qiu, Cao, and Louie 2015; H. Yu et al. 2014). Nonetheless, the functional form is still under debate as other groups just predict an enhance parabolic dispersion, especially if encapsulated samples are considered (Deilmann and Thygesen 2019).

2.7.2 Higher-Order Excitonic Features

There are not many predictions for the dispersion of higher order excitonic features. For the trion or polaron, for example, a dispersion model has been recently reported by (Efimkin and MacDonald 2017) and can be presented in the following form:

Equation 2-28 **| Dispersion of trions**

$$\omega_{X^*}(q) = E_x - \frac{\left(E_T - \frac{\hbar^2 q^2}{2M_T}\right)\left(E_T - \frac{\hbar^2 p_F^2}{4m} + \frac{\hbar^2 q^2}{4M_T}\right)}{E_T + \frac{\hbar^2 q^2}{4M_T}} \approx_{E_F \ll E_T} E_X - E_T + \frac{\hbar^2 q^2}{2M_T}$$

with E_x and E_T the binding energy of the exciton and the trion, respectively. M_T is the total mass of the trion, p_F the Fermi momentum and *m* the electron mass. In case of low doping/excitation (Fermi energy E_F smaller than the binding energy) the polaron dispersion simplifies to a case similar to the normal three particle behaviour (trion), otherwise the dispersion has to be seen in the exciton-polaron picture (non-simplified equation). A similar simple dispersion can be found for the biexciton in the low density regime (Klingshirn 2012) assuming the double mass for the biexciton in comparison to the exciton. However, the biexciton is normally observed at high densities, where the interaction with the Fermi sea of carriers cannot be neglected.

Equation 2-29 **| Dispersion of biexcitons**

$$E_{XX}(q) = 2\left(E_g - E_x^b\right) - E_{XX}^b + \frac{\hbar^2 q^2}{4M}$$

The Coulomb interaction and the related oscillator strength related are much smaller for these compounds, such that normally a much smaller coupling can be expected. Note, both the trion and the biexciton dispersion consider the long-range exchange interaction in their model. Thus, in case of strong enough oscillator strength modifications should also occur here.

2.7.3 Exciton-Polaritons

If strong coupling to the light field in a cavity or in vacuum is present due to a relatively high oscillator strength owned by the material, the dispersion of the newly formed hybridized quasiparticle has to be considered. Shortly after their prediction, they were termed "light excitons"(Pekar 1958) attributed to their light mass/ strong dispersion compared to conventional excitons due to the mixing with the light states.

In the following, the models for a bulk crystal will be discussed. The influence of dimensionality is discussed in the next chapter. In the context of classical treatment, the dispersion relation can be obtained as follows, where the light wave gets connected with the polarization:

Equation 2-30 **| Polariton equation.**

$$\frac{c^2k^2}{\omega^2} = \epsilon_b + \sum_i \frac{f_i}{\omega_{0,i}(k)^2 - \omega^2 - i\omega\gamma_i}$$

The polarization, however, is directly coupled to the system's eigenfrequencies, namely the excitons and phonons with their dispersion $\omega_{o,i}(k)$, dephasing rate γ_i and oscillator strength f_i. By solving this implicit equation, one yields the dispersion relations shown in **Figure 3** (a and b). Due to the mixing, the effective mass in Taylor series approximation can reduce several orders into the range of $10^{-3} - 10^{-4}m_e$. The above equation is valid for isotropic media. When dealing with a uniaxial crystal like TMDCs, there is an ordinary and extraordinary polariton, that both fulfill above equation for the corresponding permittivity. For any other incident angle, mixed longitudinal-transverse modes exist (Hesse et al. 1976), such as that high reflectivity band between the longitudinal exciton and the mixed mode cut-off Ω mode can be observed.

Equation 2-31 **| Mixed mode exciton-polaritons**

$$\Omega^2 = \frac{1}{\epsilon_\parallel(\infty)\sin^2(\alpha) + \epsilon_\perp \cos^2(\alpha)} (\epsilon_\parallel(\infty)\omega_t^2 \sin^2(\alpha) + \epsilon_\perp \omega_l^2 \cos^2(\alpha))$$

This lower cut-off frequency is just given by geometry and renormalizes the oscillator strength according to the projection of the electric field.

2.7.4 Quantum-Well Exciton-Polaritons

The above given equations are valid for a bulk crystal; however, dimensionality greatly effects the occurrence of polaritons. For example, for a quantum well, the dispersion is strongly altered due to confinement effects (Andreani and Bassani 1990; Hanamura 1988; Nakayama 1985; Nakayama and Matsuura 1986). For a bulk crystal (3D), there is translational symmetry in all three directions. Therefore, all wavevector components are conserved and polaritons are formed without radiative recombination (only possible at defects or the surface).

In the contrasting case of a microsphere (0D, $a_B \ll R_0 < \lambda$) with radius R_0 smaller than the wavelength λ of the radiative field but much larger than the Bohr radius a_B, no component of the wavevector is preserved and the polariton effect is negligible (Hanamura 1988). Thus, the energy of an optically allowed state is not given by **Equation 2-30**, but simplifies to the centre of mass motion of the exciton (cf. **Equation 2-26**). At the same time due to the lift of the restrictions, a super-radiant decay can be observed.

In the intermediate case(s) of a quantum well (and a quantum wire) one can expect that the dual merits of coherent nature with a polaritonic effect in the 2D-plane (1D-line) of the quantum well (wire) are preserved, while featuring the super-radiant decay in the out of plane direction. Let us consider a quantum well (Hanamura 1988) with thickness $l \approx a_B \ll \lambda \leq L$ and area L^2. If the wavevector is split into the in-plane component q and the out of plane component k_z, it has been shown that the dispersion (for an isotropic material) can be retrieved by solving the following set of equations:

Equation 2-32 **| Equation of motion for a quantum-well polariton**

$$\omega^2 - \omega_q^2 - 2\omega_q \Sigma_q(\omega) = \omega^2 - \omega_q^2 - \frac{2\omega_q \Sigma_{k_z}\left(2ck\left|A_{qk_z}\right|^2\right)}{\omega^2 - c^2(q^2 + k_z^2)} = 0$$

$$\Re\left(\Sigma_q(\omega)\right) = \begin{cases} A\left[-q\left(\frac{c}{\omega}\right)^2 \pi|\hat{\boldsymbol{e}} \times \hat{\boldsymbol{z}}|^2 + q\left(\frac{c}{\omega}\right)^2 \pi\left|\hat{\boldsymbol{e}} \times \frac{\boldsymbol{q}}{q}\right|^2\right], \omega > cq \\ -\frac{A\left(\frac{c}{\omega}\right)^2 (q^2\pi)}{\left(q^2 - \left(\frac{\omega}{c}\right)^2\right)^{\frac{1}{2}}}|\hat{e} \times \hat{z}|^2 + \cdots, \omega < cq \end{cases}$$

$$A = \frac{16|\mu_{cv}|^2 \omega_q^2}{\pi\hbar c^2 a_B^2}$$

Here $\hat{e}$ is the polarization unit vector of the radiation field, A the radiative decay rate and μ_{cv} the transition dipole moment. In the first equation $\hbar\Sigma_q$ represents the self-energy which accounts for polariton effects. One can see that for normal incidence ($q = 0$), the (real part of the) self-energy indeed vanishes, thus no polaritonic effects are obtained and the longitudinal-transversal splitting is zero. Furthermore, one can see that the self-energy scales linearly for longitudinal components of the radiative field and vanishes for transversal ones. In this case the longitudinal-transversal splitting also grows linearly with q in the small q-Limit ($ql \ll 1$) (Andreani and Bassani 1990).

3. Methods

In the following, the most important techniques used in this thesis will be described. Hereby, I will start by discussing the necessary steps and procedures for producing TMDCs monolayer and heterostructure systems, followed by an overview on the experimental methods used for their characterization.

3.2 Preparation of TMDC Monolayers

Generally, there are several approaches for producing monolayer samples having different advantages and limitations. MLs can be prepared by mechanical exfoliation (Desai et al. 2016; Dong and Kuljanishvili 2017; D. Li et al. 2016; H Li et al. 2014), chemical vapor deposition (CVD) (E.-H. Yang et al. 2018; D. Zhu et al. 2017), physical vapor deposition (Muratore, Voevodin, and Glavin 2019), metal-organic vapor-phase epitaxy (MOVPE) (Marx et al. 2017, 2018), molecular beam epitaxy (MBE) (Alvarez et al. 2018) and liquid-based exfoliation methods (H Li et al. 2014).

While during the time of this study there was tremendous progress in the epitaxial growth, mechanically exfoliated samples still provide superior quality offering high domain sizes and rather homogeneous quality. While, it is clear that this process is inherently hard to scale to industrial scale and thus being mainly of academic interest, recent reports show that an upscaling to waferscale (cm-scale already reached) could eventually be still possible using a gold assisted exfoliation (F. Liu et al. 2020). One the contrary, MOVPE growth offers the most cost-efficient fabrication, but until now often only very small grain sizes can be produced. Here, CVD-growth has established itself as the main growth method as it can deliver acceptable quality good enough for some applications (G. G. D. Han et al. 2017; T. Yang et al. 2017) and still can be produced large scale (E.-H. Yang et al. 2018). Recently, h-BN encapsulated high-quality MoS_2 from CVD crystals have shown 2 meV linewidth close to homogenous linewidth (Edelberg et al. 2019a), showing the advances in CVD growth of TMDCs. Nonetheless, even these high quality CVD grown crystals still show a defect concentration of $7 \cdot 10^{10} cm^{-2}$, significantly higher than in conventional semiconductors (Edelberg et al. 2019a). MBE growth is just at the beginning and potentially will offer superior quality, but by now MBE grown crystals can be already purchased commercially for example at *2D semiconductors*®. Similar to conventional semiconductors the question of scaling MBE growth for large scale industry production arises but the technique could be a useful tool for small scale application, where superior quality is absolutely necessary.

The samples used throughout this thesis have different origins and were obtained through different production methods. In the following, I will describe the procedure used for the samples produced in Marburg and will note differences to the production cycle used for the high-quality samples from the Columbia University. In the end I will give a brief summary of the CVD procedure used by our collaborators at the Stevens Institute of Technology.

3.2.1 Mechanical Exfoliation

In the process of exfoliation, a small part of the crystal is cleaved and transferred to the adhesive tape. First the tape, is closed about five times, whereas the opposing facets should touch different spots on the tape. When opening the attached strips, a “sliding reopening” is used rather than “direct pulling”. Thereafter, the tape is opened and closed repeatedly about 15-20 times more. In this second stage of the preparation process a “faster pulling” is used instead of the slower “sliding reopening”. After these steps, flakes can be either directly transferred to a wafer or to a polymer film such as polydimethylsiloxane (PDMS) (or polymethylmethacrylat (PMMA)).

For these steps, the choice of the tape is crucial and should be reconsidered for every different van-der-Waals material. As the internal adhesion forces of the crystal layers vary between these different

materials, one has to use a tape that fits to the material while leaving a low amount of residue in the transfer process. For example, this is highlighted here in the case of Franziska Wall, a former master student under my supervision systematically tested four tapes of different adhesion for the exfoliation of WS_2. The best tape can increase the reachable monolayer flake size from 8 microns to about 25 microns in lateral dimension compared to the (widely) popular magic scotch tape. However, if the same tape is used for WSe_2 almost no flakes are exfoliated and transferred.

In this thesis, mostly a transfer to PDMS was performed rather than to a substrate wafer piece.

3.2.2 Dry Transfer Method

The procedure used in Marburg was inspired by (Castellanos-Gomez et al. 2014). After the flakes have been transferred to a polymer film, they can be systematically transferred to a wafer in a second step. This has the advantage that stacking of different TMDCs in a controlled manner becomes possible. To do so, the Leica DMR optical microscope was extended by a new, second stage. While the substrate is always fixed to a rotary mount on the main stage, the polymer film is fixed up-side down to a glass plate, which is mounted on a 3-axis Nanomax® (later on a 5-axis device) giving precise control over the staking procedure. The microscope itself gives the opportunity to have an optical control over the stacking process. At the same time, it makes it possible to identify monolayers on the gel film. **Figure 15** shows a schematic of the individual steps used in the transfer process.

***Figure 15* | Schematic Representation of the Steps Involved in Producing Exfoliated Flakes.** First a small part of the crystal is given onto the tape. By opening and closing the tape several times, the bulk material is thinned down. It is then partly transferred to a PDMS gel. In a consecutive step the monolayers are searched under the microscope and followingly the gel is brought into contact with the substrate. When the gel is slowly detached, the flake can be systematically transferred. By repeating the process, stacked vertical 2D-heterostructures can be formed.

In contrast the samples from Columbia University were fabricated using the next generation heat assisted pick-up method (L. Wang et al. 2013) in an inert atmosphere within a glovebox. Therefore, the flakes where exfoliated onto an oxygen plasma treated silicon dioxide wafer. Using a PDMS gel with a spin coated thin film of polypropylene carbonate (PPC) flakes can be picked up at 48°C. The finalized stack can be released to a new substrate at 120°C. Afterwards, the substrate is immersed in chloroform and rinsed with isopropanol (IPA) to remove remaining polymer residues. The main advantage is that the TMDC is not touching the polymer in this case, only the h-BN is touching it. Together with the plasma cleaning contaminations are strongly reduced.

3.2.2 CVD Growth

CVD is currently the most established method to grow TMDC monolayers. While in the initial stage of this investigation, monolayers were still grown in random alignment on the substrate and no reliable growth of vertical heterostructures was possible, all of that became possible (Dong and Kuljanishvili 2017; Tongay et al. 2014; E.-H. Yang et al. 2018) within these few years. Typically, the TMDC is grown in a chalcogen rich atmosphere due to the low diffusivity of the transition metal. For example MoS_2 will only grow under normal pressure if the mole fraction of sulfur is beyond 66% (see P-T and T-x phase diagram in (S. L. Shang et al. 2016)). To achieve layer-by-layer growth and avoid bilayer regions the Mo partial pressure has to kept very low. However, the phase diagram of course depends on the used substrate.

Nonetheless, many challenges are remaining, such as the high defect rate (Rhodes et al. 2019), but also oriented growth. Here, the aligned growth on a crystalline substrate with hexagonal lattice (Dendzik et al. 2015; Tiefenbacher, Pettenkofer, and Jaegermann 2000) as well as between two layers of van-der-Waals materials (Lorenz Maximilian Schneider, Kuhnert, et al. 2019; Yuan et al. 2019) has been addressed. However, only perfect alignment and antialignment can be grown systematically, while other interlayer twist angles can be forced in Stranski-Krastanov growth (Ta et al. 2016), that does not give control over the angle, but provides every angle. Thus, different moiré lattices and the controlled achievement of magic angles besides the high-symmetry alignments cannot yet be grown selectively but must be therefore still stacked by using a dry or wet transfer from exfoliated or grown layers.

Generally, there are different variations of CVD-growth methods. In the following, the contact growth in low-pressure chemical vapor deposition (LPCVD) that is used by our collaborators (E.-H. Yang et al. 2018) will be shortly introduced. First, a thin layer of transition-metal oxide is grown on the substrate (SiO_2 or sapphire) and then brought into contact with the actual substrate at high temperatures. The chalcogen is heated elsewhere in the quartz tube and the vaporized atoms are transported by Ar/H_2 carrier gas to the furnace region. This contact scheme enables a patterned growth, since growth on the actual substrate is just happening, where contact is taking place.

3.3 Optical Characterization

Most of the characterization was done in a conventional confocal optical microscopy and spectroscopy setup, which has been built in a 4f-geometry (see **Figure 16**). It is connected with several excitation sources as well as detectors to enable flexible excitation and detection schemes, for the measurement of PL, Raman, TRPL, reflection contrast, SHG, as well as polarization- and angle-resolved measurements.

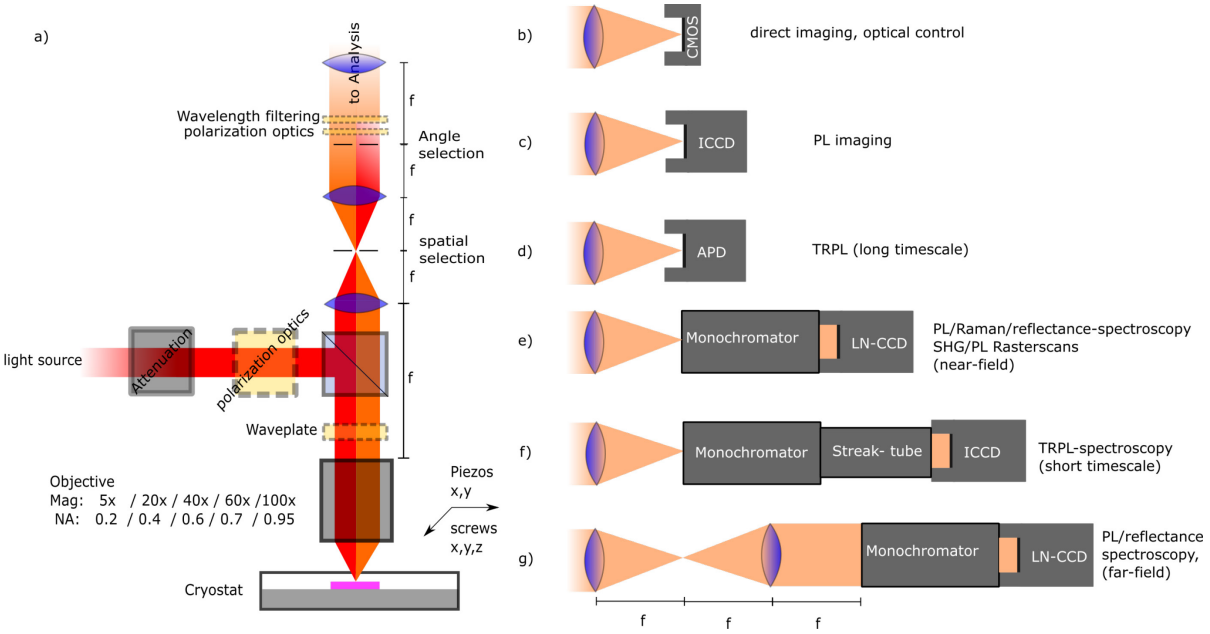

***Figure 16* | Experimental Setup:** (a) Schematic illustration of the versatile and flexibly usable µ-PL setup. Several detection schemes can be used for different experimental schemes (b-g). The yellow setup parts with dashed outlines are optional and are used for a polarization resolved experiments. The detection modes range from optical imaging to time-resolved spectroscopy.

As a light source, either a pulsed (≈ 100 fs) titanium-sapphire (Ti:Sa) laser (Spectra-Physics “Tsunami”) pumped by a frequency-doubled Nd:YAG laser (Spectra-Physics “Millenia”), a continuous-wave (cw) laser as well as white light from a tungsten lamp can be used. CW laser radiation was either provided the Ti:Sa operated in CW-operation, a frequency-stabilized and frequency-doubled Nd:YAG laser or other laser diodes were used to enable different excitation conditions. In case of the Ti:Sa laser the fundamental wavelength can be tuned between 685 and 1000 nm. In a second step, the pulsed Ti:Sa can be frequency-doubled or even tripled by using the “Super Trippler 8315” module from CSK Optronics. It is based on a lithium-triborate (LBO) as well as barium borate (BBO) to create the second and third harmonic. Due to the strong non-linearity in these crystals in the interesting spectral region, a non-linear polarization with double and three times the frequency of the fundamental mode is created. If phase matching as well as proper orientation between crystal axis and laser polarization is fulfilled, this light conversion scheme reaches acceptable efficiency and radiates the photons of these frequency.

The irradiated power and polarization are then modified with regard to the demands in the experiment. For systematic adjustment of the excitation power in pump-density series, a filter wheel featuring discrete neutral density (ND) filters is used. It allows to attenuate the excitation beam between 0.08 to 3 orders of magnitude in steps of about 0.1 ND. The polarization can be changed and analyzed using achromatic quarter- and half-waveplates as well as polarizers. The actual combination of polarization optics varies in the experiment as no combination is available to cover the complete spectrum of relevant TMDCs and excitation lasers.

Following the light beam preparation, the light is focused by a long working distance objective onto the sample which is mounted in the cryostat in high vacuum. Here, several different objectives featuring different numerical apertures, working distances, spectral coverages and magnifications have been used during the thesis. An overview of magnifications and numerical apertures is provided with **Figure 16**. The emitted and reflected light is then collected by the same objective. The following 4-f geometry allows one to confocally select signals in the focal (spatially) and backfocal (angles) plane of the respective projection lens using iris apertures. To block the laser light from the detection path, dielectric longpass filters were used.

Consecutively a selection of detectors can be used for signal acquisiton. For the monitoring and inspection of the sample a scientific CMOS-camera (Blackfly USB U3-2356C-C) is employed in the detection pathway using a flip mirror. It is mainly used to align the laser on to the sample position of relevance. A monochromator (Acton SP2300) with a liquid nitrogen cooled CCD (Roper Scientific LN/CCD-1100-PF/UV) is used for time-integrated measurements. The monochromator has an optical path length of 30 cm and is equipped with two different gratings: One with 300 grooves/ mm and 300 nm blaze for overview measurements and another one with 1200 grooves/ mm and 500 nm blaze for high resolution measurements.

For time-resolved measurements, either a streak camera (Hamamastu C6860) equipped with photocathode S-20) together with another monochromator (Bruker 25015) or an avalanche photo-diode (APD, PicoQuant MPD) are used. The employed streak camera has a theoretical time resolution reaching up to 500 fs. The monochromator attached to the streak camera is equipped with three different gratings with 50, 150 and 300 grooves/mm, respectively. As the signal strength is often close to the detection limit, only the grating with 50 grooves is used in order to not lower the detector counts even further.

For spatially-resolved measurements, either the PL can be directly mapped using an intensified charge-coupled device (ICCD) after appropriate filtering (fluorescence imaging) or a near-field image can be acquired via the array of the LN-CCD camera using the monochromator in imaging configuration.

Furthermore, the setup includes a closed loop piezo system to enable raster scanning of the sample at a maximum scale of 20 x 20 µm.

If another appropriate lens is inserted, to map the backfocal plane to the entrance slit of the detector, an angle-resolved far-field image can be measured, that gives information about the dispersion of the sample as well as the alignment of dipoles related to the relevant transition.

3.4 Theory of Fourier-Space Spectroscopy

The setup employed in Fourier-space spectroscopy can be easily understood in the frame of classical optics. If a plane wave is incident to a lens, it will be focused in the back focal plane. If we assume a light beam incident under angle β being focused at the distance a from the optical axis, $\frac{a}{f} = \tan(\beta) \approx \beta$ holds. Thus an image of the angle dependent intensity distribution is formed in the backfocal plane (N. Le Thomas et al. 2008; Vasista, Sharma, and Kumar 2019), see also (Rahimi-Iman 2020b) and refs within.

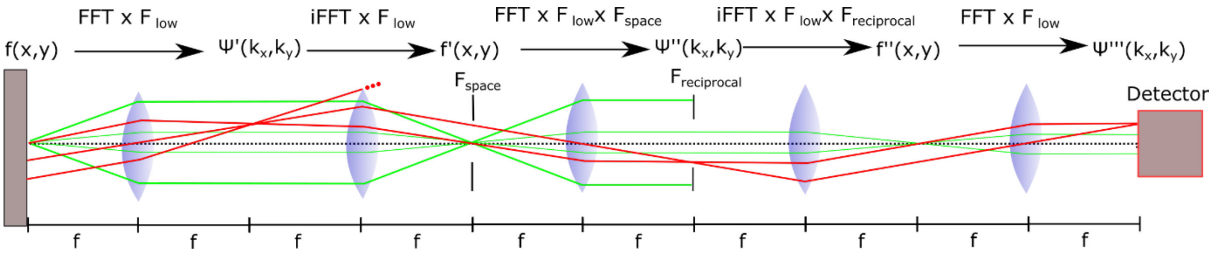

***Figure 17* |Schematic Representation of the 4-f Geometry**. (red) Lines represent the projection for beam under the same angle, while (green) line represent beams from the same point. The dashed line represents the optical axis. On top, the mathematical operations, which are associated to the transformation, are given. Here, FFT correspond to a 2D Fourier transformation. The effect of the iris in the image and Fourier plane are included by two other filter functions.

One can now define the space frequency ν_x, ν_y in the (x,z) and (y,z) plane.

***Equation 3-1* |Space Frequency**

$$\nu_x = \frac{x'}{\lambda z} = \frac{\alpha}{\lambda} = \frac{a}{\lambda f} \quad and \; \nu_y = \frac{y'}{\lambda z} = \frac{\beta}{\lambda} = \frac{b}{\lambda f}$$

In the Fraunhofer approximation, the field distribution in the Fourier plane (back focal plane) can then be calculated as (N. Le Thomas et al. 2008):

***Equation 3-2* | Fraunhofer transformation**

$$\tilde{E}(a,b) = \frac{e^{ikf}}{i\lambda f} e^{\frac{i\pi}{\lambda f}(a^2+b^2)} \int_{-\infty}^{\infty}\int_{-\infty}^{\infty} E(x,y) e^{-2\pi i\left(\frac{a}{\lambda f}x + \frac{b}{\lambda f}y\right)} dxdy$$

In the case, that the original distribution is in the front focal plane, the phase factor is not dependent on a and b, the integral then represents a 2D-Fourier transform (FFT) of the field distribution. However, in a real experiment caused by the limited numerical aperture only small spatial frequency can be resolved that can be included by a low-pass filter T_{filter}, which can also include aberration errors.

***Equation 3-3* | Effect of numerical arperture**

$$I(a,b) = \left|\tilde{E}(a,b)\right|^2 \cdot T_{filter}$$

If one projects this backfocal plane to the detector array, the Fourier transform respectively the angle-dependent emission profile and its spectral components can be analyzed. The technique can be used

for several purposes (Rahimi-Iman 2020a; Vasista, Sharma, and Kumar 2019). As it resolves the PL or reflection intensity as a function of the angle, it can be used to identify the alignment of dipole moments in PL (Schuller et al. 2013), reflection and Raman (Budde et al. 2016) experiments on the one hand and on the other hand, if a dispersion is present in the material, that is linked to the momentum parallel to the interface, it can be retrieved due to momentum conservation caused by translation symmetry (Lorenz Maximilian Schneider, Esdaille, et al. 2019). A fact often used to study polaritons (Rahimi-Iman 2020b; C. Schneider, Glazov, et al. 2018) or photonic crystals (Nicolas Le Thomas et al. 2007).

3.5 Time-Resolved PL-Measurements

In the following section, the basic mechanism behind measurements using the streak camera as well APD based acquisition will be presented. The streak camera offers the overall higher temporal resolution (theoretically as good as 500 fs compared to 20 ps for the APD) but this comes at the cost of a lower sensitivity and higher noise when they are designed for similar spectral regions.

3.5.1 Streak Camera

If the signal is analyzed by the streak camera (Photonics 2018) the signal is first energetically split by a grating spectrometer (cf. **Figure 18**). Its entrance slit selects a vertical line from the image that is projected on it. At the end of the spectrometer an image is formed, where the vertical axis represents position on the slit and the horizontal axis represents wavelength. From this image a second horizontal slit selects a certain line, i.e. a spectrally dispersed spectrum from a single point of the projected image. The size of this slit strongly affects the achievable time resolution. To achieve the specification, it has to be below 25 µm. For very weak signals, however, the slit was open up to 100 µm. This spectrum is then projected onto a photocathode, where the light is converted to an electron beam. The used streak camera has a photocathode of the type: “S-20”. Its sensitivity reaches from about 250 nm to 850 nm. By using electron optics, the electrons are accelerated, and the beam is collimated. The collimated path is then passing through a capacitor featuring an AC-voltage that has been synchronized to the repetition rate of the excitation laser and electrically phase shifted to compensate for optical and electric delays. Due to the AC-field, electrons passing at different times will encounter a different force and therefore the vertical distribution is correlated with the arrival time. Finally, the beam current is amplified with a multichannel plate and converted back to light using a phosphorus screen. The emitted light from the screen is then captured by an ICCD-camera (Hamamatsu C4742-95). The evaluation of the signal can then be analyzed using two different methods. Streak cameras are not limited to record PL, but can in principal also be used to measure transient reflection (Kutta et al. 2013), time-resolved Raman measurements (Tahara and Hamaguchi 1993) and other optical dynamics in this time range.

In case of medium and strong signals, the voltage/counts read from the individual pixels can be directly used as it scales nearly linear with the incoming light. Nonetheless, such measurements always have a background and a noise level that has to be determined separately and has to be subtracted afterwards.

In contrast, if very small signals with small SNR are present, the intensity is analyzed by means of statistical photon counting. For this purpose, thousands of pictures are taken with rather small integration time. In a next step each of these pictures is analyzed. If the counts are above a given threshold they are counted as a single photon otherwise there are neglected as background noise. After building a 2D-histogram of the identified photons, an ideally background free image is obtained. Here, the integration time and the threshold play an important role and have to be chosen carefully. The threshold is chosen in an automized way, that only about 0.02 % of pixels for a measurement with closed shutter are above the threshold.

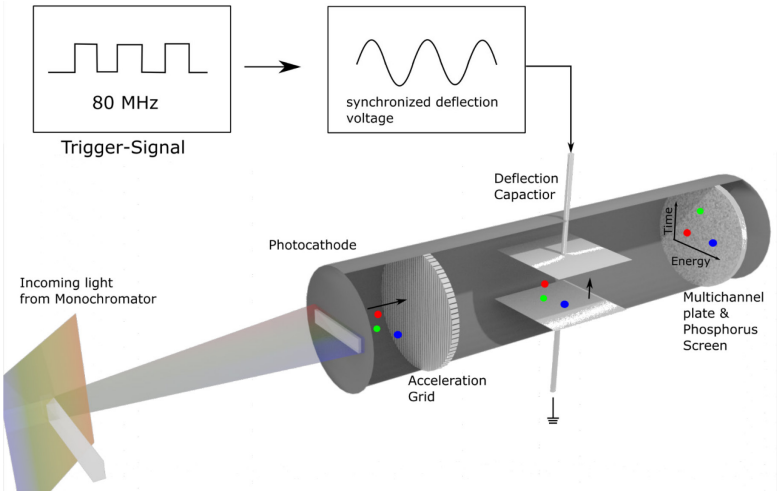

***Figure 18* | Simplified Schematic Drawing of the Streak Camera.** The light is first spectrally dispersed in the monochromator before hitting the second slit in front of the photocathode. Here, free electrons are created and are accelerated to the acceleration grid. The electrons then pass through the capacitor, where a synchronized AC-voltage is applied that deflects them vertically according to their arrival time. A multichannel plate together with a phosphorus screen is used to convert the signal back to light. The screen is then imaged by a conventional ICCD-camera. The streak camera also includes several magnetic lenses (not shown) for collimation and focusing similar to a TEM/SEM, which can be adjusted to reduce astigmatism and other imaging errors. Furthermore, there is a second vertical capacitor which can be used to move the backsweep of the camera.

3.5.2 APD-Based Measurements

An avalanche photo diode (APD) is a diode of high sensitivity that is operated shortly above the breakdown voltage. This means that the current is not anymore linked to the incoming intensity, but instead an avalanche is started, thus it can be used as a very sensitive detector for measuring incoming light. The diodes current in the NIM-type puls itself is not very fast in declining (250ps) but features a fast onset (about 20 ps). The measurement is then based on statistical methods similar to the photon counting with the streak camera. If a rise in current is detected, a single photon is added to the histogram with the temporal delay. The delay is not given by the vertical deflection unit like in the streak camera but by the electronically measured delay of the rising edge of the avalanche with respect to the trigger signal (a fast diode with 250 ps rise time is used). The time resolution of this electronic delay measurement is 4 ps in the here used correlator. Fluorescence lifetime measurement are thereby enabled by building a histogram similar to the streak camera photon counting mode.

3.6 SHG Measurements

Measurements of the second harmonic generation signal are also possible in the presented setup. They are a valuable tool in the field of 2D-semiconductors flake analysis as they can be used to extract the crystal symmetry as well as its crystal axis. In contrast to PL measurements, the fundamental mode of the pulsed Ti-Sa laser is tuned below the resonance (1.38 eV/900 nm) to be able to make virtual excitations using high powers without destroying the sample. In the measurements shown in this thesis, the average power used for SHG measurements is about 30 times more than used for PL-measurements. By using a short-pass filter (Thorlabs SP700) and a band-pass filter (450$\pm$50 nm) the laser light was removed from the detection path and SHG was detected using the liquid nitrogen cooled camera. The setup is generally capable of measuring the crystal axis as well, provided that appropriate polarizers and half waveplate are integrated. Nonetheless, here the polarization sensitivity of the beam splitter and the grating has to be considered as well, which restricted the use in measurements of the total SHG without replacing the beam splitter.

3.7 Raman Measurements

Raman measurements were performed in a separate setup at ambient conditions. The general concept of the setup is very similar besides that a notch filter (Kaiser Optical System 514.5 nm SuperNotch-Plus holographic filter) is used to couple the laser into the confocal microscope (Olympus BX41) as well as to filter it from the signal. Due to this change, the total amount of signal that reaches the detector can be increased compared to a flexible setup based on a beam splitter, used for combining excitation and detection pathways. In the Raman setup, the 514.5 nm laser line of an Argon ion laser (Melles Giot 543-GS-A03) is used for excitation after filtering it by using a laser line filter. For focusing and collection, a 50x / NA 0.75 or a 100x / NA 0.90 objectives are used. In addition, two more 10x objectives are available that are used for optical inspection of the sample using a simple CCD camera (Microsoft Life Cam HD-3000). To achieve sufficient resolution (of about 1/cm relative wavenumbers) this setup employs a spectrometer (Acton SpectraPro 500) with a longer path(50 cm) equipped with a grating of 1200 grooves/mm. Also, here a liquid nitrogen Silicon charge coupled device (Princeton Instruments 7698-0001) is used to detect the signal.

3.8 Scattering-Type Scanning Near-Field Optical Microscope (s-SNOM)

The s-SNOM device presents a rather new type of optical near field microscopes. In contrast to a conventional SNOM, where a sub-wavelength aperture or tapered fiber is scanned over the surface, here the non-linear scattering from the tip is used as a probe (cf. **Figure 19**). This has several advantages as the concept can also be extended to mid or far infrared, where fiber-based concepts are difficult to implement. However, as the linear response (found at the oscillation frequency of the AFM tip) has strong contributions, that are not intrinsic to the material, but just given by the topography of the surface, spectroscopy is limited to non-linear properties. These are obtained by extracting the signal found at higher harmonics of the tip oscillation. Normally, for spectroscopy at least the 3rd harmonic is used to be sure that the signal is not just related to the sample geometry.

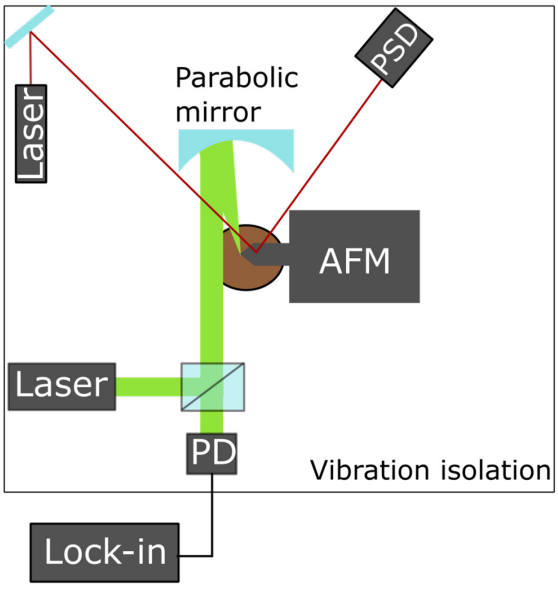

Figure 19 **| Schematic Depiction of the s-SNOM Setup.** Into a home-built AFM, already available in Frankfurt in the group of Prof. Roskos, a new path was added. In addition to the already existing s-SNOM path using 850 nm laser light another one featuring 532 nm irradiance was built. The laser is focused using an off-axis parabolic mirror under 60° to the normal. The scattered signal is collected through the same mirror and measured using a silicon photodiode. The signal is then processed using different lock-in amplifiers, extracting the signal at different harmonics of the AFM tip oscillation.

The s-SNOM used in this thesis within a scientific collaboration on 2D materials belongs to the group of Prof. Roskos at the Goethe University of Frankfurt. It is a home-built s-SNOM using a metallized AFM

tip (ARROW-NCPT, Nanoworld), that achieves about 30 nm resolution. While normally built up for NIR, the setup was modified to include our frequency stabilized Nd:YAG laser also used in the PL measurements. The setup always records the AFM as well as the near field signal demodulated at the first, second and third harmonic of the tip oscillation (260 kHz). The s-SNOM does not only measure the local field intensity but at the same time also measures the changing scattering efficiency and chemical composition (Huber et al. 2007). Both can only be disentangled if a pseudo-heterodyne detection is used, which is available in the setup, but was not used during this study.

4. The Influence of the Environment

The 2D van-der-Waals materials studied in this dissertation comprise very different phenomena compared to a two-dimensional electron gas (2DEG) used in conventional semiconductor quantum wells due to their extreme low height. In conventional semiconductors quantum well thicknesses of several nm are common, thus a microscopic (finite) periodicity in the crystal can be still found perpendicular to the layer. As the quantum well still involves tens or hundreds of unit-cells, several subbands are forming, that lead to a complex dispersion of excitons in these quantum wells (Siarkos 1966). While in conventional QW these confinement effects can be treated in the approximation of the envelope function from the bulk, in monolayers of van der Walls materials the band structure itself is changing dramatically leading to a qualitative not only quantitative change (Stroucken and Koch 2017). Further, in conventional semiconductors heterostructures normally no atomically sharp, but interdiffused interfaces are found (Beyer et al. 2016), while in contrast in van-der-Waals materials , sharp interfaces are in principal possible (Rooney et al. 2017; Withers et al. 2015) as no chemical bonds are necessary between adjacent layers. Furthermore, no reciprocal space is defined perpendicular to the layer for the monolayer case and the bands are only analyzed according to their in-plane momentum. The above cited TEM investigations of vdW-materials show sharp interfaces with corrugated layers (about 1 Å as measured by STM in (H. Yu et al. 2017)), nonetheless the thickness of the interface region – here the height of corrugation – is reduced compared to conventional semiconductors and offers (almost) atomically sharp interfaces.

In the case of monolayers, the difference goes even further, while in conventional quantum well systems the areas of surface physics and semiconductor physics can be easily separated, this is not possible for a monolayer. From this it is immediately clear that common questions of surface physics, like the influence of the roughness of the surface (Decker et al. 2011; Rhodes et al. 2019), adsorbents (Tongay et al. 2013), carrier screening (Ajayi et al. 2017; Konabe 2016; Y. Lin et al. 2014; Stier, Wilson, et al. 2016; Stroucken, Grönqvist, and Koch 2011), mirror charges (Rhodes et al. 2019; Yifei Yu et al. 2016), microscopic quality of the interface (J. Park et al. 2019; Rooney et al. 2017) and similar question will also directly affect the common characteristics of the semiconductor physics such as exciton binding energy (Gerber and Marie 2018a; Raja et al. 2017), strain (Desai et al. 2014; Rhodes et al. 2019), doping (Chae et al. 2017), electrical mobility (W. Han et al. 2018) and with that of course also to their dynamics. This often is displayed with the pictures of an exciton whose wavefunction penetrates deeply in the surrounding (cf. **Figure 10**). While this also happens for the wavefunctions in a quantum well, the fraction is substantially larger for exciton in TMDC monolayers especially if the excitons are in excited states, leading to a bigger modification by the surrounding material (Chernikov et al. 2014).

Some of these questions traditionally asked by surface physics are relevant for almost any application of van der Waal materials in semiconductor devices, mainly the influence of the substrate as well as the influence of stacks with 2D insulators especially h-BN which now is commonly used in many applications (Y. Liu et al. 2016; Withers et al. 2015). In the first year of this investigation mainly the influence of the substrate as the most important of these questions was investigated. To provide generalized interpretations several substrates and production methods for the monolayer were used. This also gave the chance to compare mechanically exfoliated monolayers with CVD-grown flakes under different growth parameter sets. This early work was mainly done together with equal contribution from Sina Lippert and me. In addition, some contributions of Jan Kuhnert are also present. Note this study has been performed in 2016, thus before most of the literature above was published.

Later on, the influence of the environment was studied by analyzing the emission and dynamics in differently arranged h-BN/WSe_2 heterostructures on different substrates. This work has been mainly done together with Jan Kuhnert, again with basically equal contributions. As most of the results of this

studies are already discussed in the dissertation of Sina Lippert (Lippert 2018) and Jan Kuhnert (Kuhnert 2018) respectively, this chapter will in general rather review the most important results than explain the details of these findings. However, some aspects, which are complementary or instructive for other parts of the thesis especially the angle resolved chapter, will be discussed in more detail. For more details the interested reader is referred to the aforementioned dissertations.

4.1 The Influence of the Substrate

To study the influence of the substrate, several exfoliated WSe_2 samples on different substrates were prepared (cf. **Figure 20** a-e). For comparison, also a CVD-grown sample was included in the sample set. In fact, all types of samples were prepared more than once and showed similar behavior. Followingly, µ-PL, Raman-spectra and PL-dynamics were acquired at room temperature as well as at helium temperature and analyzed carefully. In conclusion the different intensity ratios between the arising excitonic complexes as well as spectral features and decay times show that a careful choice of the substrate is indeed crucial to obtain an intrinsic, low linewidth sample, which matches the expectations from ab-initio calculations. As this is discussed in detail in the dissertation of Sina Lippert (Lippert 2018) and our paper (Lippert, Schneider et al. 2017), here just the main findings are illustrated at the power dependent PL-spectra (cf. **Figure 20** a-e).

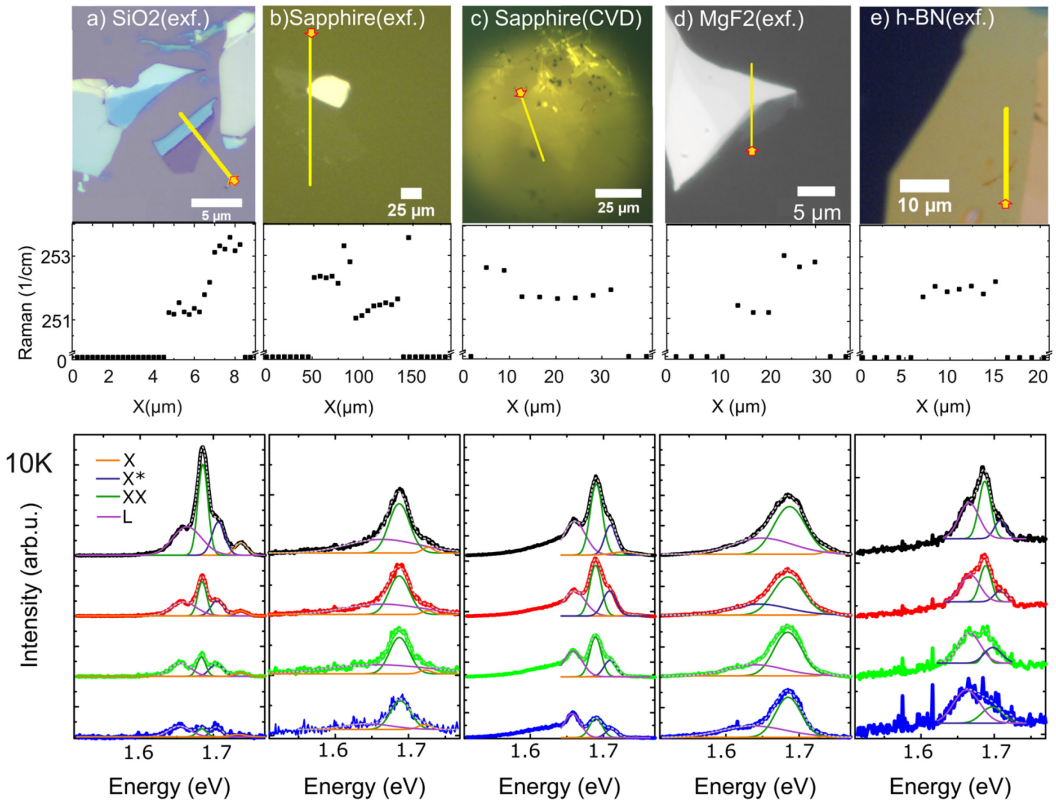

***Figure 20* | Comparison of the PL-Spectra of WSe_2 Monolayers on Different Substrates.** Column (a-e) show the characterization of WSe_2 flakes on different substrates, namely microscopic picture (upper row), Raman peak position along the line given in the microscopic picture (middle row) and density series of PL emission at helium temperature (10K) (lower row). For the power series the time averaged power density was adjusted between 0.34 kW/cm² and 3.4 kW/cm². The signal with the lowest power is multiplied by four and the second lowest power by two for clarity. In addition, the spectra are presented with a constant offset. The excitation took place strongly off-resonant at 2.75 eV using a pulsed laser focused by an 20x objective. In contrast for Raman measurement a 100x objective with high numerical aperture was used. In both cases a confocal selection was used to decrease the area of signal collection even further compared to the spot size. Thus, a resolution of about 1 µm is achieved. The figure has been adopted with changes from (Lippert et al. 2017) under the Creative Commons Attribution 3.0 license.

To confirm that indeed monolayers are present confocal Raman linescans have been performed. The peaks positions of the main optical phonon are shown as function of the position (cf. **Figure 20 a-e**). One can clearly distinguish between mono- and bilayer from the optical images as well the Raman signals.

While here mainly the results taken at 10 K will be discussed, the results at room temperature are shown in the appendix A2. The shown data resembles a power series ranging from 0.34 kW/cm^2 to 3.4 kW/cm^2 and have been acquired with the 20x long working distance objective. The spectra where analyzed by careful fitting with the sum of gaussians peaks. While some clearly show four features, some just show three distinguishable peaks. The number of gaussian was then reduced to not increase the number of free parameters unnecessary.

While the energetically highest peak, which is identified as the neutral exciton of the A-exciton series similar to previous reports (Desai et al. 2014; Moody et al. 2015; You et al. 2015), of course roughly is found at the same energy (1.73 eV), the line shape and the quantum mechanical species found in its vicinity are considerably changing. Some samples show three and others four clearly distinguishable features. Power dependent linearity analysis of the PL-emission (data shown in Appendix A3) as well as polarization-resolved measurements have been used to identify the excitonic species in agreement with literature (Godde et al. 2016; J. Huang, Hoang, and Mikkelsen 2016; You et al. 2015) (cf. **Table 2**). Here, the linearity factor has been used to get evidence for exitonic (linear), biexitonic (quadratic (You et al. 2015)) and localized states (sublinear (Brener et al. 1992)), while additionally the polarization anisotropy gives indication if the species stem from excitonic features where polarization is expected (positive for exciton and trion (Mak et al. 2012; Schaibley et al. 2016b), negative for biexcitonic feature (Nagler et al. 2018) or localized states or defect, where no or less circular polarization anisotropy is expected).

In general, the peaks can be grouped in to five different classes. Two linear features, that are attributed to the neutral excitonic and trionic emission. For the samples on silicon oxide, h-BN as well as the CVD-grown flake a super-linear feature is observed, that has been attributed to a biexcitonic species. While formerly attributed to the neutral biexciton similar to (You et al. 2015), recent publications (Barbone et al. 2018; S.-Y. Chen et al. 2018) and the measurements at the high quality sample presented in chapter 6.8 suggest, that indeed the luminescence peak at 1.687 eV belongs to the charged biexciton. This feature is absent in the other two samples. Instead, a second sublinear feature is found in addition to one, which is present in all samples. This strongly redshifted emission at 1.67 eV has been often attributed to localized emission from defects (J. Huang, Hoang, and Mikkelsen 2016), but can be also explained due to phonon assisted recombination (Brem et al. 2020; M. He et al. 2020) from the dark exciton present in WSe_2-samples.

Furthermore, different ratios between the intensity of neutral and charged as well as between excitonic and localized features are observed. At the same time the linewidth of these species is quite different, suggesting different inhomogeneous and homogenous broadening for the individual monolayer samples. If repeated on the same substrates (cf. the dissertation of Sina Lippert (Lippert 2018)) almost similar results are obtained, suggesting a systematic influence of the substrate.

Table 2 **| Extracted Features and the Linearity of their Emission as well as their Degree of Circular PL-Polarization.**

Feature		*SiO_2 (exf.)*	*Sapphire (exf.)*	*Sapphire (CVD)*	*MgF_2(exf.)*	*h-BN (exf.)*
Exciton	Energy (eV)	1.739	1.727	1.739	1.736	
	Linearity /Polarization	1.2 / 0.19	1.1 / 0.27	1.3 / 0.44	1.1 / 0.27	
Trion	Energy (eV)	1.706		1.710		1.705
	Linearity /Polarization	1.1 / 0.42		1.1 / 0.30		0.4 / 0.06
Biexciton	Energy (eV)	1.685		1.689		1.687
	Linearity /Polarization	1.5 / 0.37		1.2 / 0.24		1.2 / 0.03
Grey Exciton	Energy (eV)		1.689		1.687	
	Linearity /Polarization		0.8 / 0.21		0.6 / 0.05	
Localized State	Energy (eV)	1.660	1.664	1.662	1.642	1.667
	Linearity /Polarization	0.8 / 0.02	0.6 / 0.13	0.7 / 0.08	0.7 / 0.08	0.5 / 0.03

The different intensity ratios between neutral and charged species, especially between neutral exciton and trions, indicate a different doping level in the monolayers. As the exfoliated monolayers are produced in a comparable way, the intrinsic level of doping from the source crystal is expected to be of comparable magnitude. This suggests a modification of the doping level due to the substrate. This can be understood due to dangling bonds of some substrates at the interface which act as dipoles and locally modify the charge carrier density in the monolayers (Rhodes et al. 2019). For this reason, inert, unipolar (hydrophobic) surfaces such as h-BN are the preferred substrates for the usage with monolayers of TMDCs. The results and interpretation are in line with other investigations using liquids (Y. Lin et al. 2014) and other common substrates (Yifei Yu et al. 2016) of different dielectric constants.

The observed linewidth of the samples investigates here (30 meV FWHM for the neutral exciton) is still dominated by inhomogeneous broadening, suggesting a substrate mediated potential due to strain and interface impurities and inhomogeneities. The Raman line scans taken for these samples (cf. **Figure 20**) show a small shift between the samples and small energetical fluctuations on the µm-scale. This could be due to local variation of strain from the atomically rough surfaces. For h-BN were a flatter surface is expected, the fluctuations are reduced, however still present. As other AFM images (cf.

Figure *69* and **Figure 70**) taken during this thesis show, this is not surprising as mechanically exfoliated samples often encounter bubbles and wrinkles alternating with flat areas. They thus feature strain variation not only on the microscopic scale but also on the mesoscopic sample.

Other articles investigating the substrate induced doping and strain by means of STM and AFM (Decker et al. 2011; Shin et al. 2016) also reveal a considerable local deviation in the carrier-density as well as bandgap if placed on common SiO_2-wafer compared to suspended or h-BN supported monolayers. Both papers compare with the measured topography indicating that the microscopically flat h-BN indeed reduces the local strain variation compared to amorphous silicon oxide.

As the 2D-material hexagonal boron nitride is atomically flat, it can be used as a buffer layer to decrease microscopic strain fluctuations and therefore reduces inhomogeneities. Together with being an inert surface, it is now established as the common barrier material in TMDC heterostructures. If used on both sides inhomogeneities can be strongly reduced and the homogenous linewidth can be nearly reached as shown in literature (Ajayi et al. 2017; Cadiz et al. 2017) as well as our own study (Lorenz Maximilian Schneider, Lippert, et al. 2018). Furthermore, by being compatible with silicon-

based technology, it can serve as an intermediate layer to combine TMDCs with established technologies.

A biexcitonic feature was only observed in samples with low linewidth, respectively, low local inhomogeneous broadening and a sufficient helicity. The latter one indicates a low rate of intervalley scattering. As these dephasing processes are mediated by either carrier-carrier, exciton scattering, phonon mediated processes or scattering at defects, samples with low doping and low coupling to substrate phonons will favor biexciton formation.

4.2 Mechanical Exfoliated vs CVD Grown Flakes

In addition, to investigating the influence of the substrate environment, we also analyzed the PL emission and dynamics of CVD grown samples with different growth parameters in comparison to mechanically exfoliated flakes. While often neglected the comparison between exfoliated samples, which can reach the intrinsic lifetime and thus have a small number of defects, and CVD samples, which often show bigger inhomogeneities, is useful to judge if an prototype device can be scaled to industrial size with the currently achievable CVD quality. In fact, for introducing TMDCs in real application on large scale, only growth by (MO-)CVD or MOVPE represent a realistic path. Therefore, at this early stage of research it was fruitful to systematically compare both production types in order to judge on the limitations.

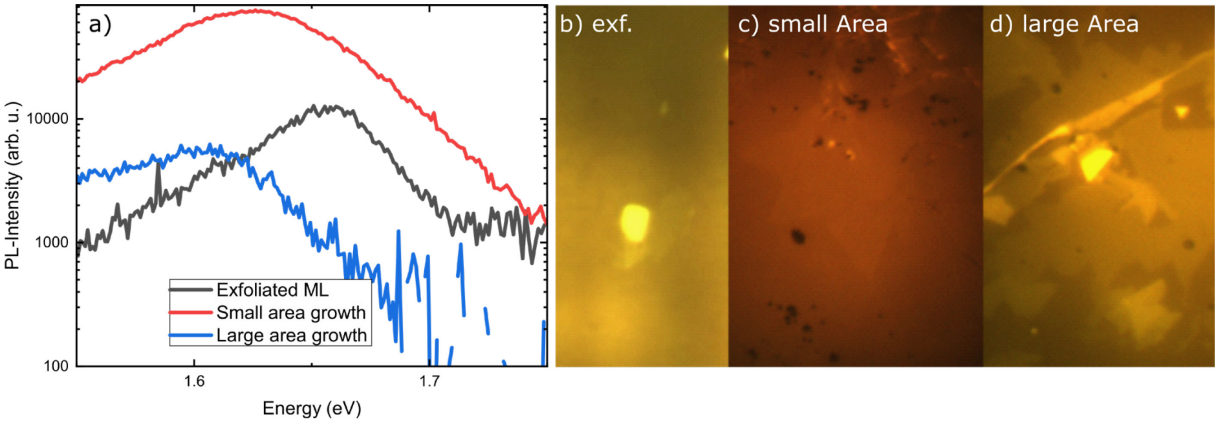

***Figure 21* | Comparison of Exfoliated and CVD-Grown Samples.** (a) PL-spectra at room temperature using an excitation power of 870 µW at 450 nm excitation wavelength under pulsed irradiation. Microscopic picture of the investigated exfoliated (b) and CVD grown samples with parameters for small area (c) and large area (d) growth on sapphire substrates.

Generally, there are two different growth regimes of layer-by-layer growth (Kang et al. 2015; S. L. Shang et al. 2016; E.-H. Yang et al. 2018) for CVD growth of TMDCs. One yields a small number of growth sites resulting in isolated, relatively big and flakes up to about 250 µm length and another growth type with a high number of seed showing either many small sized flakes or, if grown until these are touching, even wafer-scale films. To change in between both growth types the flow of the H_2-carrier gas is changed and with that the growth speed. A high flow leads to many crystal seeds while low flow to big crystal domains (Kang et al. 2015).

Samples of both types have been studied and their optical properties have been compared to a sample fabricated by mechanical exfoliation. For these samples PL spectra and dynamics were analyzed both at room temperature as well as at helium temperature at several sample spots. As a detailed discussion of the data can be found in the dissertation of Sina Lippert (Lippert 2018), the main finding will be described at a central graph. The PL-spectra at room temperature as well as microscopic picture of the samples can be found in **Figure 21**. Already from the microscopical picture one can see, that especially for the large area growth several initial growth sides are formed. As mentioned above these crystals' growth until they meet each other, forming the shown polycrystalline thin film. Furthermore, one can

see that not all angles are multiples of 60° - as expected for aligned growth –, suggesting many different grain boundaries and related defects. In addition, also some bilayer islands are easily found. However, the sample grown under parameters for small scale growths shows nearly only angles, which are multiples of 60°, suggesting a better alignment of the crystal domains and followingly less defects caused by grain boundaries. For the exfoliated monolayers, often large domains or even monocrystalline phases are expected (Hsu et al. 2014) mainly depending on the source crystal.

The measured PL spectra for the CVD samples is redshifted and broadened compared to the exfoliated one. Furthermore, this effect is stronger for the large area grown monolayers compared to the small area growth. The shift is most likely due to bigger strain compared to the monolayer. The increased inhomogeneous broadening can be understood keeping the aforementioned polycrystallinity in mind. In the large area samples the domains are generally smaller often only reaching 1 to 2 µm in diameter (Karvonen et al. 2017; Zimmermann, Mette, and Höfer 2016). Thus, at this early stage of growth research the exfoliated samples still showed superior quality especially compared to wafer-scale samples. This indicates the necessity of improvements before ideas and concept shown on exfoliated samples can be scaled to automatized small scale or eventually even industrial scale production.

4.3 Encapsulation and h-BN/TMD Heterostructures

As the discussion in chapter 4.1 has shown hexagonal boron nitride resembles an ideal substrate for TMDCs monolayers. Therefore, an in-depth study of the influence of h-BN in several heterostructure composed of TMDC monolayers as well as h-BN buffer layers has been performed. Here, several sample sets were employed. While as of now, the effect is rather well understood (Gerber and Marie 2018b; L Meckbach et al. 2018; Lars Meckbach, Stroucken, and Koch 2018b) and encapsulation is common (Rhodes et al. 2019), this study has been performed in parallel to the first works (Ajayi et al. 2017; Cadiz et al. 2017; Wierzbowski et al. 2017) using h-BN encapsulation to reach samples close to the homogenous linewidth. In addition, as it became clear that h-BN is a suitable barrier material, the influence is important for future devices. These most likely will be based on a multi quantum well design (Withers et al. 2015) composed of h-BN as the barrier and TMDCs monolayers as the active material similar to conventional devices. Therefore, the following sample sets were investigated:

1. An *in-situ* measurement of a h-BN encapsulated WSe_2 ML (cf. **Figure 22 a**)
2. Different stacking configuration featuring substrate supported, capped, supported and encapsulated WSe_2 ML (cf. **Figure 22 b,c**)
3. WSe_2 monolayers on various bare substrates and isolated with a h-BN buffer layer
4. Encapsulated and supported WSe_2/$MoSe_2$ heterobilayers (cf. **Figure 22 b,c**)

For these samples sets different phenomena were compared, namely: the effect of the dielectric surrounding on 1. energetics and inhomogeneous broadening and 2. polarization anisotropy, 3. electron-phonon coupling, 4. exciton-exciton annihilation and diffusion and 5. electron-hole plasma formation. Here, especially point 3. to 5. have been studied more extensively compared to the other reports mentioned.

4.3.1 Effects on Energetics and Sample Quality

To investigate the effect of encapsulation, on the one hand a sample was measured at each step of the process of encapsulation to exclude flake to flake variation, on the other hand a sample of each type has been produced on silicon as well as sapphire substrate for in depth analysis of their properties.

Already during the process of encapsulation (cf. **Figure 22 a**), the usual behavior can be observed. The peaks have been fitted with a gaussian to extract the peaks energy and linewidth. When an annealing process is performed, a clear redshift (10 meV) can be observed compared to the h-BN supported case. Furthermore, if the encapsulation is achieved, an increased PL-emission (here a factor of 3) as well as

linewidth shrinking (from 40 meV to 30 meV at room temperature and even less FWHM at low temperature) as well as a small additional shift (3 meV) can be observed. This behavior is typical and has been found in parallel by other groups (Ajayi et al. 2017; Cadiz et al. 2017). It is found in the second sample set with individual samples with different stacking (cf. **Figure 22 b**), too.

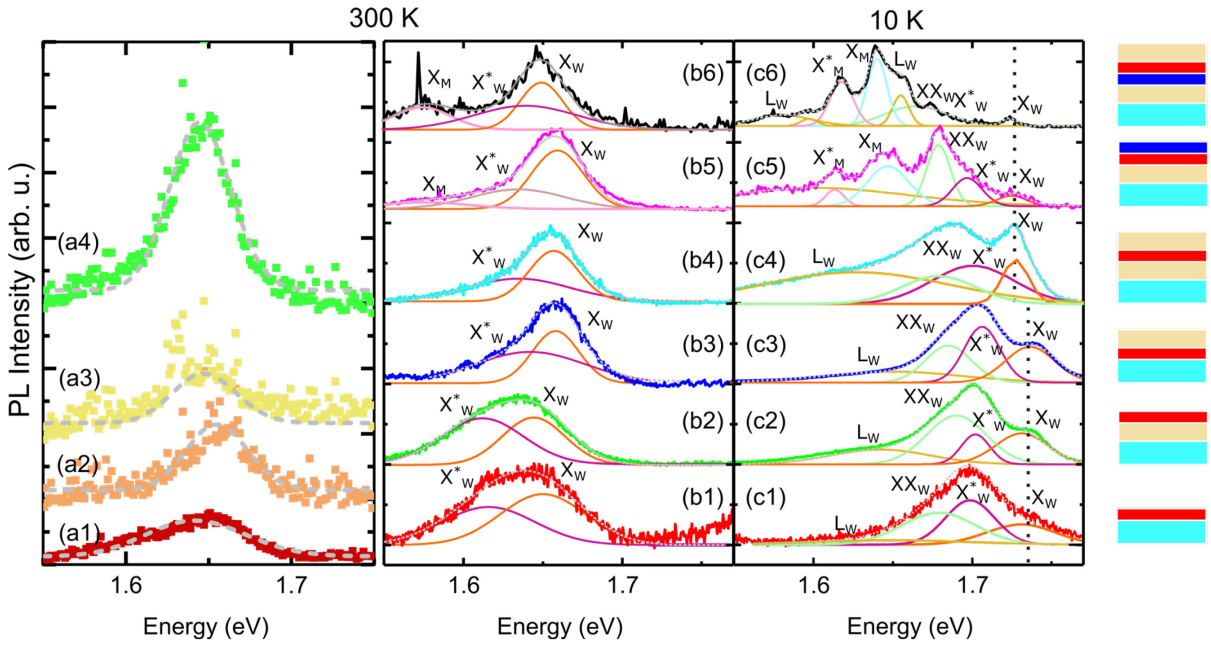

***Figure 22* | PL Spectrum for Different h-BN/TMD Heterostructures.** (a1-4) shows the evolution of a WSe_2-ML during the encapsulation compared to bare monolayer on substrate. From bottom to top: reference monolayer, ML on h-BN, annealed ML on h-BN and h-BN encapsulated ML measured at room temperature under pulsed non-resonant excitation at 2.7 eV with 0.3125 $mJcm^{-2}$ energy density per pulse. PL-spectra of different h-BN/TMD Heterostructures at 300K (b1-b6) and 10K (c1-c6). The stacking configuration is shown schematically on the right (dark grey for SiO_2/Si-substrate, light gray for h-BN, red for WSe_2 and blue for $MoSe_2$). Adopted with permission from (Lorenz Maximilian Schneider, Lippert, et al. 2018).

At the annealing temperature used in the in-situ measurements (200°, 2h in UHV), no relevant annealing of the crystal itself is taking place. However, adsorbents on the top and in between the layers are evaporating, respectively, accumulate by diffusion (Wierzbowski et al. 2017) in big bubbles in an Oswald ripening like process. This increases the area of direct contact, where no fluctuations in strain are present and strong electric coupling can in principle take place.

Nevertheless, if direct coupling with h-BN is considered, only weak effects are expected at the A-exciton resonance of WSe_2 as there are no electric states in h-BN present at this energy. Nonetheless, a Moiré pattern supercell is forming (Gerber and Marie 2018b). Furthermore, even when only the mean response of the dielectric environment is considered, drastic changes in the electronic screening having impact on the bandgap as well as the excitonic energies (Lars Meckbach, Stroucken, and Koch 2018b) are found. Due to the direct contact after annealing compared to the case were small bubbles from air and adsorbents are still present, the screening due to mirror charges h-BN is increased and becomes more homogenous.

Remarkably, if capped by a single layer of $MoSe_2$ an almost similar energy shift of the emission peak is observed (see encapsulated sample compared to the one just capped by $MoSe_2$), suggesting an almost similar screening effect. As $MoSe_2$ also has a comparably high refractive index, an increased screening is also taking place in this case. However, it is surprising that a monolayer of $MoSe_2$ almost shows the same magnitude of screening than capping with few-layer or bulk h-BN. This shows that the out-of-

plane screening is happening in the direct surrounding and only the very next layers are important for the amount of carrier screening.

Similar to the previous chapter 4.1, under pulsed, non-resonant excitation exciton, trion, a biexcitonic and a sublinear feature can be observed in the different stacks of h-BN and WSe_2 at helium temperature (cf. **Figure 22 c**), while at room temperature (cf. **Figure 22 b**) only emission from the exciton and trion peak can be found. Again, polarization and power dependent measurements have been used to identify the different spectral features. The power dependent measurements will be discussed in the chapter 4.3.2.

As these effects are well understood and already discussed in the thesis of Jan Kuhnert (Kuhnert 2018), here I want to focus on the exciton-phonon coupling as well as annihilation and diffusion. In order to ensure comparability, Raman measurements (cf. **Figure 23**) have been performed to extract strain in the different samples. The samples containing only WSe_2 and h-BN show very similar Raman peak position suggesting a comparable strain situation over the laser spot size. The samples on sapphire and the one involving $MoSe_2$ show a different strain situation probably deviating from the other samples on SiO_2/Si substrate. To extract the approximate amount of strain, the positions of the Raman modes were extracted by using Gaussian fits. The resulting energetic differences between both optical modes have been compared to theoretical predictions (Sahin et al. 2013).

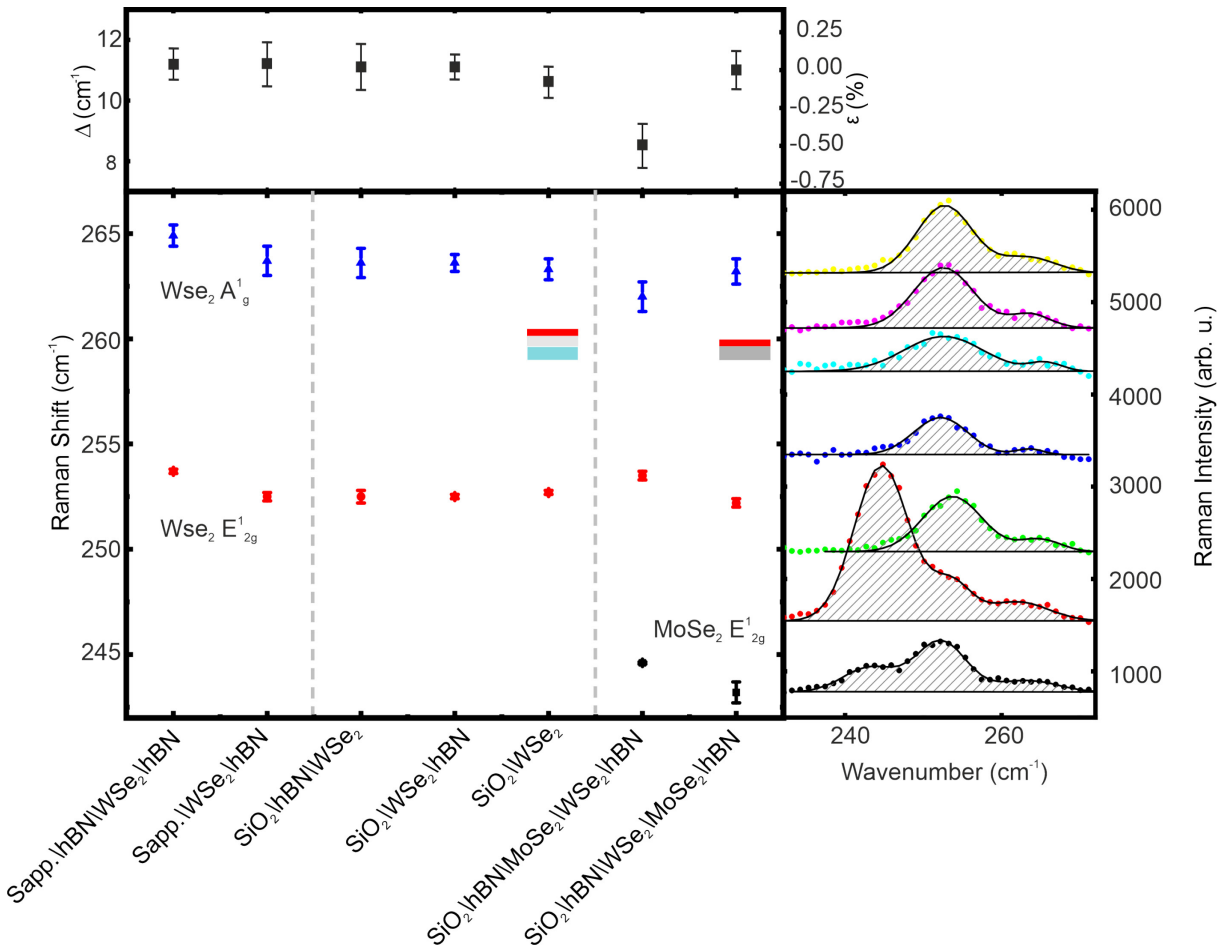

Figure 23 **|Raman Measurements for Different h-BN/TMD Heterostructures.** The (right panel) shows the Raman spectra with a fitted sum of gaussian peaks used for extraction of the center energy. The (main panel) shows the extracted Raman modes for the different samples. The (upper panel) denotes the extracted mode splitting together with the related strain value as predicted by (Sahin et al. 2013).

4.3.2 Electron/Exciton-Phonon Coupling

The coupling of electron, respectively, excitons with the lattice affects many properties important for application e. g. heat generation, amount of non-radiative recombination and many more. It is obvious that the out-of-plane modes are directly affected by encapsulation. But also, for the in-plane components changes arise as the screening of phonon-assisted polarization by the surrounding is changed. Additionally, the local fluctuations of strain are reduced in h-BN supported, capped or encapsulated monolayers. Thus, a change of the electron-phonon, respectively, the exciton-phonon coupling can be expected. In this chapter a detailed analysis of temperature dependent measurements is presented with the aim of analyzing the influence of the different dielectric environment.

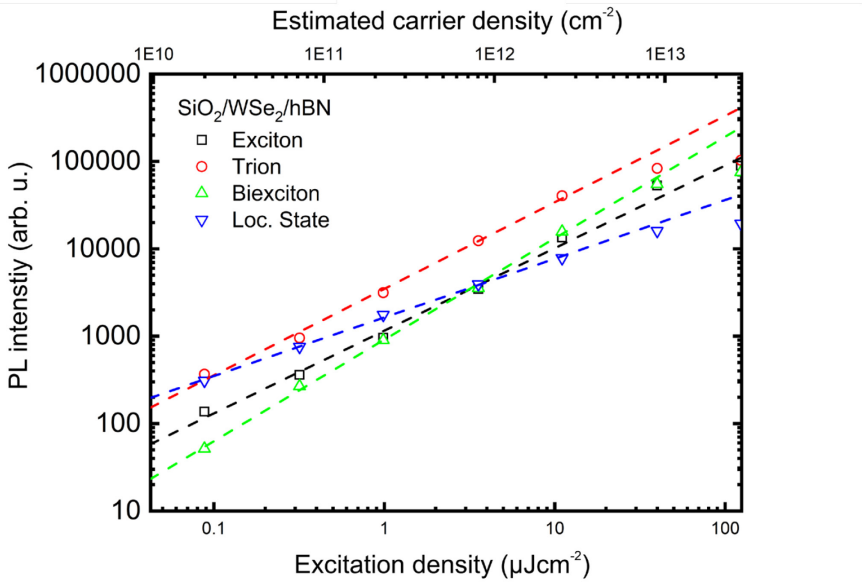

Figure 24 **| Power Dependent PL Intensity and Linearity.** The Graph shows a double logarithmic plot of the PL-intensity of the different peaks as function of the excitation density for the example of a capped WSe_2-ML at 10 K. In addition, an estimated carrier density is given assuming 10 % of absorption. The lines shown are fitted power laws which are used to extract the linearity of the peak intensity.

First of all, a power dependent measurement at 10 K (cf. **Figure 24**) has been performed, in order to verify the attributed species as well as to verify that the measurement has been done in the linear regime. The graph clearly shows two nearly linear features that have been attributed to trion and exciton. Furthermore, a sub- and superlinear feature has been found. These are attributed to localized and biexcitonic emission. Above 10 µJ/cm^2 a clear saturation behavior can be found deviating from the linear regime.

Consequently, all comparisons between the different stackings must be done below this threshold, to exclude density dependent effects. To study the effect of encapsulation to the exciton-phonon coupling, temperature and power dependent measurements of the spectral and dynamic properties have been performed (cf. **Figure 25**). The peak positions, linewidth and intensity of all features have been extracted for all temperatures and powers. For the temperature dependent linewidth and center frequency several phenomenological models exist, which give insight into the exciton-phonon coupling of the carriers contributing to this emission.

An exemplary plot for a h-BN capped WSe2 ML, the dependence of the center frequency on the temperature is shown in **Figure 25 a**. The main features are only rarely shifting below 100K and start red shifting considerably at higher temperatures. Qualitatively, the results are similar for all other sample configuration and can be found in the appendix A4.

The datapoints for excitons and trions have been fitted with the model of O'Donnel (O'Donnell and Chen 1991), a phenomenological model that explains the shift due to interaction with optical phonon modes. It relies on two parameter the mean energy of optical phonons $\langle\hbar\omega\rangle$ and a dimensionless coupling constant *S,* the Huang-Rhys factor. The model can explain the data nicely for all samples. Similarly, a fit with the Varshni-equation (Varshni 1967) can also describe the data. However, for the here purpose of discussing the exciton-phonon coupling the model of O'Donnel seems more appropriate.

Equation. 4-1 **| Model of O'Donnel.** $E(T) = E_0(T = 0K) - S\langle\hbar\omega\rangle\left(coth\left(\frac{\langle\hbar\omega\rangle}{2k_bT}\right) - 1\right)$

Quantitatively (cf. **Table 3**), two observations can be made. If comparing exciton and trion, in all samples the interaction of the exciton with the lattice is stronger than in the case of trions. This seems surprising at first sight, as one would expect that the interaction of the charged particle should be stronger, if the vibrations have a dipole moment. However, it seems that few-particle physics must be considered in detail to understand this finding.

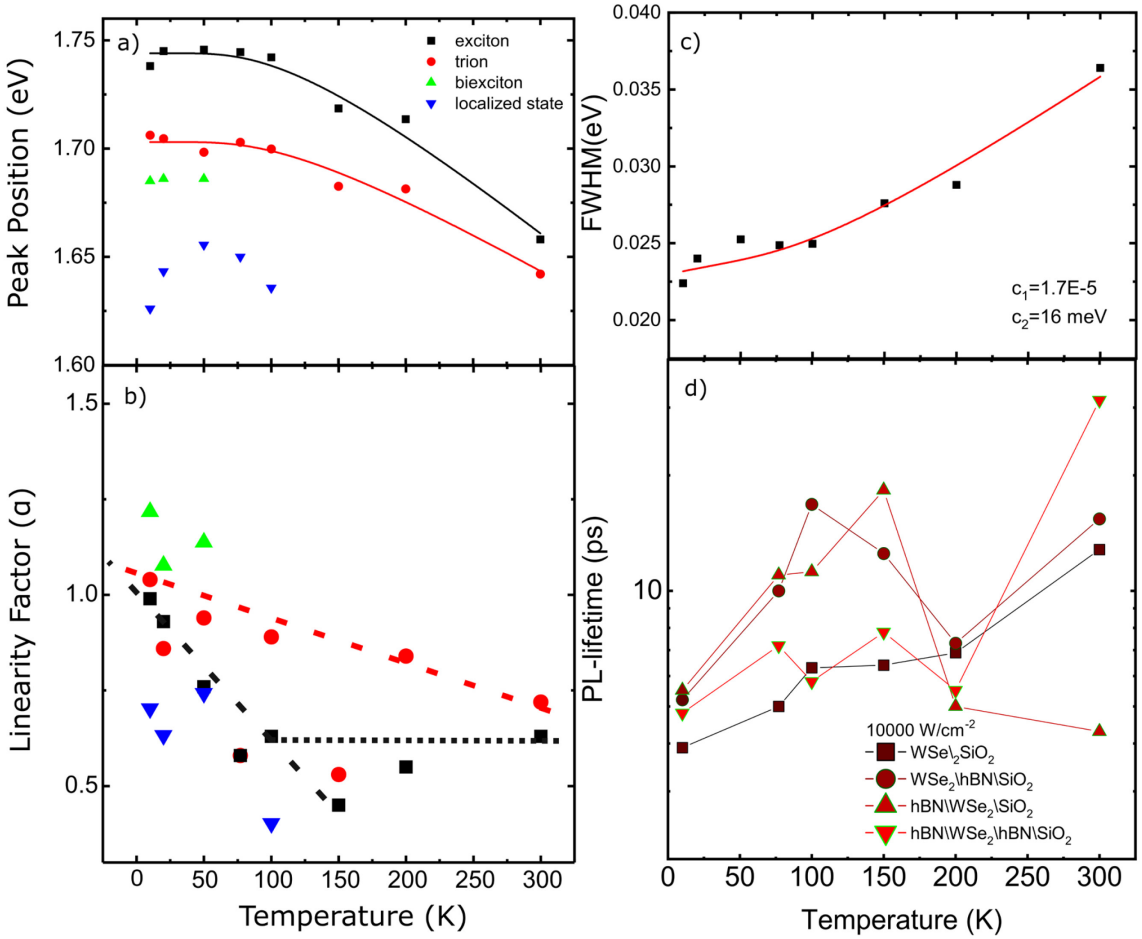

Figure 25 **| Temperature Dependence of the PL Characteristics for WSe_2.** Temperature dependence of the peak positions (a) together with a fit using the model of O'Donnell showing nice agreement between both, exemplary shown for the h-BN capped sample. (b) Dependence of the linearity factor for each spectral feature for the h-BN-capped sample. The dashed lines represent a guide to the eye. (c) Extracted linewidth for the exciton peak fitted with a phenomenological model for the discussion of exciton-phonon coupling for the h-BN encapsulated sample. (d) Shows the temperature dependence of the mean PL-decay time for all samples in a comparison.

Furthermore, from the analysis it can be understood that the interaction with the surrounding and internal phonons can be significantly reduced, if a h-BN buffer layer is used. From this simple model, a reduction of about 15 % in the coupling strength as given by the coupling constant from SiO_2 supported

to encapsulated monolayer is found. This could be due to the change of the exciton radius, which is changing due to different screening or the interaction with the phonon of h-BN instead of SiO_2. Here, a more detailed study, e.g. using resonant Raman or high-resolution photoluminescence excitation spectroscopy to study the coupling to phonon side bands, would be necessary. The value of the coupling constant for the bright A-exciton on bare SiO_2 (S=3.00) is similar to the one observed for bulk GaAs (S=3.00 (O'Donnell and Chen 1991)), while for the encapsulated monolayer a lower exciton-phonon coupling is found for the bright exciton (S=2.55) closer to the behavior of diamond (S=2.31 (O'Donnell and Chen 1991)).

Similarly, to the peaks energy also their linewidth was analyzed. As the encapsulated samples show the lowest inhomogeneous broadening in this sample set, the temperature dependence of the linewidth will be discussed at this example (cf. **Figure 25 c**). The linewidth of the neutral exciton at temperatures below 100 K shows a small peak at 50 K, but on average a linear increase until 100 K is observed. Starting from this temperature a strong increase of the linewidth is found. The linewidth can be described by the following model (Selig et al. 2016a):

Equation 4-2 **| Linewidth as function of phonon coupling**

$$\gamma = \gamma_0 + c_1 \cdot T + \frac{c_2}{e^{\frac{\Omega}{k_B T}} - 1}.$$

Here, γ_0 represents the intrinsic linewidth at 0 K, c_1, c_2 are coupling constants due to acoustic Γ-point phonons and acoustic Λ-point or optical phonons. Ω is the averaged energy of the latter phonons. Here, the same value as used above in O'Donnels model for the central frequency was used. The fit is shown in the graph and describes the overall trend, but it cannot describe the small increase around 50 K. The resulting coupling parameter are $c_1 = 1.7 \cdot 10^{-5}$ meV and $c_2 = 18$ meV with $\gamma_0 = 22$ meV as lower limit of the linewidth. These coupling parameters to acoustic and optical phonons are in the same order as the calculated ones for WS_2 or $MoSe_2$ (Selig et al. 2016b), but still deviate slightly from both.

While the other stacks in general show the same behavior in terms of slope and increase, the clear transition between dominance of coupling to acoustic and optical phonons is not as clearly resolved due to the strong inhomogeneous broadening present in these stacks. The small increase around 50 K could be an indicator for disorder in the analyzed flake. As the extracted linewidth γ_0 has not yet reached the predicted (Selig et al. 2016a) or the experimentally determined intrinsic linewidth (Moody et al. 2015), is it not surprising that a deviation from the model is found, which is not accounting for disorder, which results in the observation of a s-shape (Gies et al. 2014). While the peak at 50 K could be an indication of an s-shape the data is not detailed enough for an in-depth analysis of the disorder in the sample.

Both analyses indicate a significant change of the few-particle physics above 100 K compared to below this threshold temperature. The used mean phonon energy indicate that the change is mainly due to the population of the optical phonons in the system. This is contrasting calculations for WS_2 (Selig et al. 2016a), where mainly the influence of the acoustic phonons at Λ-point is present. However, this is not surprising as the phonon energies in the sulfide-based material are a factor 1.5 larger than in the investigated selenide-based TMDC. The strong carrier-phonon interaction observed in this analysis makes it likely that optical phonon-sidebands form and the exciton has to be discussed using the polaron picture (as also noted in the context of dispersion measurements in **Chap. 6**).

To further investigate the influence of different stacking orders, the linearity of each feature has been analyzed as a function of temperature under pulsed off-resonant excitation (exemplary for h-BN capped WSe_2 ML in cf. **Figure 25 b**). Similar results are found for all four samples. Their data is shown in the appendix A4. At 10 K a linear increase for exciton and trion, a superlinear for the biexciton and a sublinear increase for the redshifted feature is found. With increasing temperature, a linear decrease

of the linearity factor is extracted for the exction and trion peak in the temperature range below 100 K, where the model by O'Donnel predicts an interaction with acoustic Γ-phonons. Hereby, a stronger decrease is found for the exciton compared to the trion in agreement with the bigger Huang Rhys factor indicating stronger phonon interactions.

When the optical or acoustic phonon states at $\Lambda-$ and **K-**point are occupied above 100 K, a slowdown of the decrease or even a constant linearity factor is observed. This finding indicates an increased non-radiative recombination compared to the situation at 10 K. As the decrease of linearity is not amplified above 100 K, it is most likely related to the interaction with acoustic phonons.

Furthermore, the effects of the electron-phonon interaction have been investigated by measuring the time- and temperature dependent photoluminescence decay (cf. **Figure 25 d**). Surprisingly, the decay slows down for all samples when the temperature is increased from 10 to 100 K. Normally, an increase of the decay rate would be expected due to the additional recombination pathways made possible by the phonon occupation. However, the acoustic phonon population at **K** and Λ, that are relevant for intervalley scattering, make a pumping of the bright states in the light cone from momentum indirect excitons (**K-K'** or **K-**Λ) possible, and therefore could slow down the depletion of the bright states in the light cone.

Above 150 K again a decrease of the PL-lifetime of the exciton is found. This could be due to non-radiative recombination or the onset of exciton-exciton annihilation, as diffusion of exciton becomes likely (the process of annihilation will be discussed in detail in the next section). The prediction made later on by (Brem et al. 2020) confirms that phonon assisted recombination from dark, momentum-indirect exciton states 100 meV below the bright exciton indeed weakens at about 50 K when the acoustic phonons starting to get available, making the mentioned pumping scenario reasonable.

Shortly, after this study was published more detailed predictions and experimental evidence have been published, confirming the claim of pumping of the bright exciton from momentum forbidden states as well as the significant formation of phonon side bands of both the bright and the dark exciton (Brem et al. 2018, 2020; Chow et al. 2017; Christiansen et al. 2017).

Table 3 **| Exciton-Phonon Coupling.** Parameters used for fitting equation (5) to data of different samples with SiO_2 substrate containing WSe_2 and h-BN. Reprinted from (Lorenz Maximilian Schneider et al. 2017).

	$E_{0,x}(0K)$	S_x	$E_{0,x^*}(0K)$	S_{x^*}	$< \hbar\omega >$
SiO_2/WSe_2	1.742	3.00	1.706	2.48	30.1
SiO_2/h-BN/WSe_2	1.745	3.01	1.706	2.82	30.1
SiO_2/WSe_2/h-BN	1.744	2.79	1.703	2.19	30.1
SiO_2/h-BN/WSe_2/h-BN	1.730	2.55	1.692	2.25	30.1

4.3.3 Power Dependent Dynamics and Annihilation

The time-dependent photoluminescence has been measured as a function of incident power up to the intermediate and high excitation power density (up to $1 \cdot 10^{12} cm^{-2}$). A strong nonlinear response of the decay has been found that significantly shortens, if the power is increased. This behavior has been reported before by several groups (Kumar et al. 2014; Poellmann et al. 2015; D. Sun et al. 2014; Yuan and Huang 2015) and has been attributed to exciton-exciton annihilation. However, no systematic study on the influence of the environment as well as the underlying mechanism was published at that time.

If the density of excitons is high enough and diffusion is possible, excitons can interact with each other similar to an Auger-process (Kulig et al. 2018). As this interaction is clearly dependent on the exciton Bohr-radius and the diffusion constant - both being influenced by the dielectric environment (Stier, McCreary, et al. 2016) - a study was performed to examine the influence of different substrate and stacking configurations to the annihilation behavior. The study has been performed once using a streak camera probing the influence on the initial decay in few picoseconds and once with an APD probing the decay on a time scale of tens to hundreds of picoseconds, where the lattice and electron temperature should be already in thermal equilibrium (Ruppert et al. 2017). These timescales intrinsically represent different mean carrier densities, therefore changes in the effective Diffusion constant can be expected. The effects will be shown exemplary for samples on SiO_2, h-BN/Si_3N_4 as well as a complex heterostructure SiO_2/h-BN/$MoSe_2$/WSe_2/h-BN.

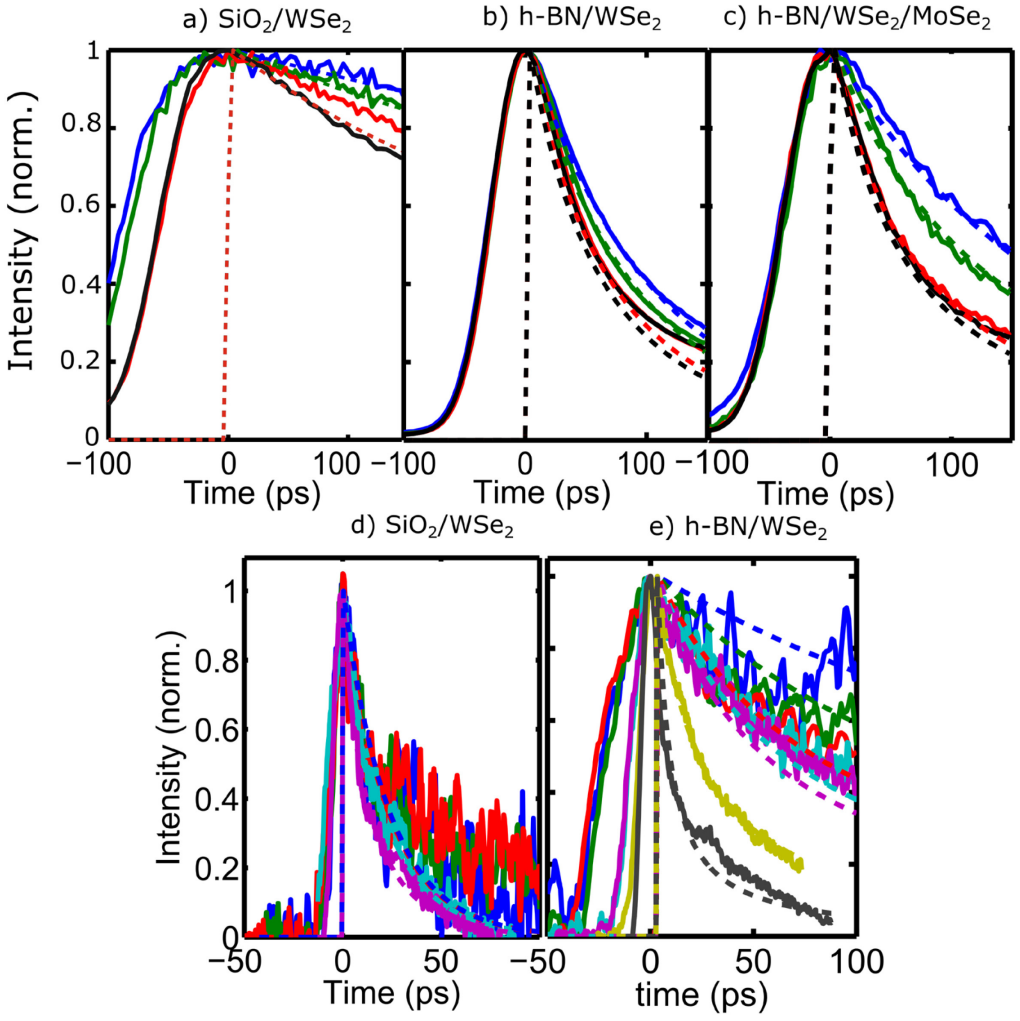

***Figure 26* | Power-Dependent Equilibrium Dynamics and Annihilation.** Transients for a WSe_2 ML on bare SiO_2(a), on a bulk h-BN buffer layer (b) and in an encapsulated heterostructure formed of $MoSe_2$ and WSe_2 (c) as measured with the APD and (e) and (f) as measured with the Streak camera. The used powers are 340, 1000, 3400 and 10000 W/cm² for the measurement with the APD and they are varied from 340 to 34000 W/cm² for the streak camera measurements.

First, the thermal equilibrium regime will be discussed, that was analysed by measuring with the single photon sensitive APD. The power dependent transients are shown in **Figure 26**. On a qualitative level all of these samples show a similar behavior. To analyze the dynamics, a model assuming diffusion as the limiting factor (Daniel et al. 2003; Kulig et al. 2018; Suna 1970) and a model based on limitations set by Förster-energy transfer (Powell 1975; Swenberg and Stacy 1969) were employed:

Equation 4-3 | *Annihilation rate equations*

$$\frac{dN}{dt} = G(t) - \frac{N}{\tau} - \xi N^2$$

$$\xi = \beta_{2D} = -\frac{4\pi D}{\log\left(\frac{1}{2}\sqrt{\frac{1}{Dt}}R_e\right)}$$

$$\xi = \gamma_{2D} = \frac{R_0^2 \pi \Gamma\left(\frac{10}{12}\right)}{\Gamma(2)\zeta^{1/3}t^{1/3}}$$

The first equation represents the general rate equation with a source term *G(t)*, the normal decay with time constant τ and parabolic term with an annihilation rate ξ. This can be modelled either by diffusion (second equation): here D represent the effective Diffusion constant and R_e the radius of exciton in a hard ball model. As an alternative a modelling (third equation) of the annihilation rate a Förster-transfer based model is possible with R_0 representing the Förster radius, the Gamma function Γ and ζ denoting the radiative decay rate without long range Förster interaction.

To reduce the number of free parameters the transient taken at lowest power, where the annihilation should be negligible, was used to determine the decay rate in the linear regime. In addition, the exciton radius determined by (Stier, Wilson, et al. 2016) was used as sphere diameter leaving only the diffusion constant respectively the Förster radius as free parameters in these models. The extracted parameter can be found in **Table 4**. The mean free path $\lambda_{mean} = \sqrt{D\tau}$ is also given for the various samples.

Both models can describe the data, if the monolayer is only surrounded by a dielectric on one side. However, the encapsulated sample can only be well described by the diffusion model, the Förster model here deviates strongly from the experimental transients. The difference in their time dependence – note, the annihilation rates have an explicit time dependence – makes it possible to discriminate between them, as the difference evolves characteristic for both models. Although parameters for the Förster-radius based model have been found which describe the data, they seem unrealistic and are bigger than expected especially if the screening of the surrounding is considered. In conclusion, it can be said that the diffusion model describes the data well and an effective diffusion coefficient could be extracted that is indeed in the expected magnitude.

***Table 4* | Model Parameters Derived from the Annihilation Fit.** The first two row sections represent the extracted parameters from the equilibrium dynamics, while the next row sections (italic) denote the ones derived from the initial fast decay.

Sample	WSe_2/SiO_2	WSe_2/h-BN/Si_3N_4	h-BN/WSe_2/$MoSe_2$/h-BN/SiO_2
$\boldsymbol{D_{eff}}$(nm²/ps)	10	15	50
$\mathbf{R_e}(\boldsymbol{nm})$	1.2	1.5	1.5
$\boldsymbol{\tau}(\mathbf{ps})$	270	111	219
$\boldsymbol{\lambda_{mean}}$ (nm)	52	41	105
$\boldsymbol{R_0}$	420	350	n.A
$\boldsymbol{\tau}$	270	111	n.A
$\boldsymbol{D_{eff}}$*(nm²/ps)*	*15*	*35*	-
$\boldsymbol{R_e}(\boldsymbol{nm})$	*1.2*	*1.5*	-
$\boldsymbol{\tau}(\boldsymbol{ps})$	*243*	*362*	-
$\boldsymbol{\lambda_{mean}}$ *(nm)*	*60*	*112*	-

Furthermore, for this three samples shown here, it seems that the h-BN buffer layer or even h-BN encapsulation can increase the diffusion constant. Reminding of the smoother surface with less local strain variation this seem believable, however, if the all measured samples are considered, some samples combination with and without h-BN buffer layer show almost no change. More statistics and more measurements would be necessary to verify this effect.

In a next step the initial dynamics were analyzed using the streak camera. As can be seen from the graph and the extracted parameter the magnitude is similar besides an increased diffusion coefficient. Shortly after this investigation (Kulig et al. 2018; Zipfel et al. 2019) have measured the exciton diffusion as function of the exciton population directly by using the streak camera in imaging mode. They find a low-density limit for the diffusion constant of 30 nm^2/ps slightly higher but of the same order of magnitude than the value obtained from this analysis in the equilibrium regime. Furthermore, the group found an increase of the effective diffusion constant for higher pump intensities similar to this analysis for the initial decay presented here due to Auger processes. The diffusion constant increases in their study, if a supported in contrast to a suspended monolayer is considered. This can also be seen if other reports of annihilation (Kumar et al. 2014; Mouri et al. 2014; D. Sun et al. 2014; Yiling Yu et al. 2016; Yuan et al. 2017) on different substrates are compared. This comparison further supports the trend that exciton or charge-carrier diffusion is stronger in encapsulated samples compared to supported samples.

4.4 Summary

In this chapter the influence of the substrate, the dielectric environment as well as the production process of TMDC monolayers on their optical properties have been discussed. Generally, it can be concluded that the choice of the substrate, respectively, the dielectric environment, has an influence on many fundamental properties of the monolayers. The study has shown that the choice of the substrate mainly effects the doping of the monolayers, its local strain values as well as the formation of many-body complexes such as biexcitons. This leads to a different markedness of the different excitonic features commonly found in these materials. Here, similarly to other studies (Ajayi et al. 2017; Cadiz et al. 2017; Rhodes et al. 2019) h-BN has proven itself to be an ideal substrate as it provides an inert, atomically flat surface, that leads to a decrease of microscopic disorder in the TMDC monolayer. Thus, it leads to an improved quality in terms of observed quasiparticles, linewidth of the PL emission peaks as well as their polarization degree.

Similar results could also be found in the comparison of CVD grown samples under different parameters with their exfoliated counterparts. Here, the exfoliated flakes still provide the best performance. Nevertheless, small CVD samples, grown with a low number of crystal seeds, can also show a variety of many body features with considerable valley coherence. In contrast, the large area CVD samples, which are grown with many crystal seeds, do not offer high optical quality yet, most likely caused by the many grain boundaries and the small domain sizes typically found in these samples.

Furthermore, the influence of the stacking order in Wse_2 and h-BN based heterostructures has been investigated. Here, the focus was laid on the energetics, the exciton phonon coupling, and diffusion-assisted annihilation of excitons. For the energetics, a redshift of the neutral exciton peak due to encapsulation with h-BN or $MoSe_2$ was found. Interestingly, encapsulating with a ML $MoSe_2$ almost has a similar screening effect than using bulk h-BN. This means that for the increased dielectric screening only very few adjacent layers have to be considered as the screening seems to happen on a microscopic scale. At the same time the biexciton and trion binding energies showed no significant trend within the measurement errors, although they are expected to decrease with higher permittivity of the surrounding (Kylänpää and Komsa 2015). This is not surprising as the expected shift is small against the linewidth of the investigated samples.

To investigate the exciton-phonon coupling the temperature and power dependence of the PL emission and its dynamic has been carefully analyzed. From the polaron shift the coupling strength to optical phonons as well as acoustic phonons at **K**, **M** and Λ–point can be phenomenologically extracted. Two main results were found. Interestingly, the excitons couple stronger to the phonons according to the coupling constant of the model than the trions by about 17%. This is surprising as the charged particle should easily interact with the microscopic polarization created by these phonons and therefore the trion is expected to have one more coupling channel. It seems that the decrease of the oscillator strength is overcompensating the additional monopole coupling. Nevertheless, a detailed many-body calculation would be necessary to understand this counterintuitive finding.

Secondly, it has been found, that capping or encapsulation of the monolayer, decreases the coupling to these kinds of phonons (about 17% for excitons and 10% for trions). This could be either due to a steric change of the involved atoms as they also now have to vibrate against the top layer. Or it could be due to the different screening, which effectively changes the distance in which the interaction between excitons and phonons is mediated by the coulomb force. The strong shift of the peak energy above 100 K indicates the formation of phonon sidebands in agreement with later published theoretical papers (Christiansen et al. 2017; Shree et al. 2018).

From an analysis of the linewidth and the linearity factor of PL-emission evidence for coupling with all phonon types, including acoustic phonons at the Γ-point can be extracted. At the temperatures below the occupation of optical phonons a linear increase of the linewidth, overlaid with a small peak at around 50 K possibly attributed to the remaining disorder in the system, is observed. If a closer look at the power linearity as function of temperature is taken, a strong decrease is already observed before the optical phonons show considerable population. This comparably strong drop in emission linearity at these temperatures, can be explained, if a strong coupling to acoustic phonons at the Γ-point is present. Qualitatively, this behavior has been found for all stacking types of h-BN and Wse_2 and no clear change in the coupling to acoustic Γ-point phonons can be found.

Finally, the effect of the different screening and strain situation as well as the different phonon coupling to the exciton diffusion has been investigated at room temperature. To do so, the diffusion-assisted annihilation, respectively, the Auger-processes have been scrutinized by power dependent measurement of the PL-dynamics up to the intermediate density regime. By fitting a model assuming diffusion assistance the diffusion constant for excitons in monolayers could be extracted (e.g. D=10 nm^2/ps for a monolayer on SiO_2 substrate) for several different stacking types. As a result of these measurements one has to conclude that If a h-BN buffer or even an encapsulated layer is used, an increased diffusion constant is found. Similarly, a higher diffusion constant is found for the initial decay as expected as a dense hot exciton population is found. These findings agree with later works by Chernikov et al. (Kulig et al. 2018; Yuan et al. 2019; Zipfel et al. 2019), which directly probed the diffusion in real space.

5. The Influence of the Stacking Angle and the Microscopic Alignment

As already stated in the introduction to the previous chapter the common properties of semiconductor physics of van-der-Waals materials in general and TMDCs in special are very sensitive to the local environment of the layer. While the previous chapter mostly deals with the influence of the permittivity of the surrounding, and the influence of the roughness at the interface respectively the substrate, both of which cannot model effects that occur due to the microscopic alignment between the TMDC monolayer and its surrounding.

As the stacking of the monolayers of van-der-Waals structures does not need to fulfill a lattice match (Novoselov et al. 2016b; C. Zhang et al. 2017), not only any van-der-Waals material can be stacked on top of each other, but also all twist angle between individual layers can be realized in these material stacks in strong contrast to conventional semiconductors. These new degrees of freedom are opening many new options for stacks with different microscopical alignment and internal symmetry. Nonetheless, this freedom comes with additional phenomena, that have to be considered and understood in order to use them in applications, namely changes in internal crystal symmetry (Puretzky et al. 2016; M. Xia et al. 2015; Van Der Zande et al. 2014) and formation of moiré potentials (Bistritzer and MacDonald 2011; Y. Cao, Fatemi, Demir, et al. 2018; Lei Wang et al. 2019; C. Zhang et al. 2017). While often both phenomena have to be considered, in certain high symmetry stacks of the same material, only the changed symmetry has to be considered as the moiré potential is trivial in this case.

The first part of this chapter will focus on such homobilayers, stacked at different angles of high symmetry. Such highly symmetric stacking of homobilayers allows studying the effects of the symmetry change without the need to investigate the effects of the moiré pattern at the same time. As already briefly discussed in the introductory part (cf. chapter 2.3) these stackings inherit different symmetry properties. As optical selection rules are naturally affected by symmetry, especially parity and rotation symmetry in case of circular polarization, such change will for example affect spin-valley locking and the energetical alignment of bands of the individual monolayers. As in the more complex case of twisted heterostructures high symmetry points in space exist having the same local symmetry (Y. Cao, Fatemi, Demir, et al. 2018; H. Yu et al. 2017) than the stacks investigated in the first part of the chapter, the result are also valuable for this more general case.

The samples used for this investigation are CVD-grown by our collaborators at Stevens Institute of Technology and measurements have been done together with Jan Kuhnert. Theoretical calculation in this subchapter have been provided by Tineke Stroucken, Stephan W. Koch, Ulrich Huttner and Lars Meckbach from the theoretical semiconductors group. Our collaborators at Stevens Institute of Technology have optimized their growth parameters as well as growth substrate to favor one of the minima in phase space (K. Liu et al. 2014), namely the highly symmetric stacking cases AA'(2H) and AB(3R).

The second part of the chapter deals with a preliminary study concerning a twisted heterobilayer composed of monolayered tungsten disulfide and tungsten diselenide, which has been conducted together with my master student Manan Shah. While of course interlayer charge transfer excitons can be expected in this case, in contrast to the results of the homobilayer, also the moiré pattern must be considered. It has been shown that this moiré pattern leads to the formation of a mini-Brillouin zone first observed for van-der-Waals materials in twisted bilayer of graphene (Bistritzer and MacDonald 2011; Decker et al. 2011; Kuwabara, Clarke, and Smith 1990). As this can lead to the emergence of correlated phenomena (Y. Cao, Fatemi, Fang, et al. 2018; Yankowitz et al. 2019), other groups have focused on TMDCs (Y. Cao, Fatemi, Demir, et al. 2018; Jin et al. 2019; Lei Wang et al. 2019) in which

several moiré sub-bands form under small twist angles. Recently, also the emergence of Mott and Wigner crystal states (Mott and Friedman 1974; Padhi, Setty, and Phillips 2018; Wigner 1934; Congjun Wu et al. 2007) in the here investigated type of heterostructure could be confirmed (Regan et al. 2020; Tang et al. 2020). The splitting at γ–point (small Greek letters denote the high symmetry point in the mini-Brillouin zone in contrast to the big letters, which describe the points in the Brillouin zone of the individual layers) leads to the energetic splitting of the intra- and interlayer excitons into several transitions - so called moiré excitons – whose observation can be seen as the spectral fingerprint of the moiré superlattice. The subchapter deals with the preliminary characterization of these newly arising spectral features.

5.1 WS_2 Homobilayers

5.1.1 Samples and Stacking Verification

Several substrates with WS_2 mono- and bilayers grown by CVD under different growth condition (Ghatak et al. 2019) have been examined. The flakes were transferred by a liquid transfer technique (Lorenz Maximilian Schneider, Kuhnert, et al. 2019) unto a bare SiO_2(300 nm)/Si substrate or on a substrate partially covered with bulk h-BN flakes. For comparison some AA' and AB stacks on bare substrate as well as on h-BN buffer were selected (cf. **Figure 27**). Firstly, PL- and SHG raster scans (**Figure 27**) were performed to verify the alignment in between the layers of the individual flakes. While the PL emission gives an indication were the mono- and bilayer parts of the flakes are found (marked in **Figure 27**), as the signal shifts red and the intensity drops significantly at the bilayer areas, the SHG gives evidence about the presence of local inversion symmetry. In the AA' stacked case where inversion symmetry is present, the SHG signal vanishes, consequently only the monolayer parts can be observed. In contrast for the AB-stack were an inversion center is absent, a constructive adding up of both SHG signals from the individual layers is observed giving nearly three times the signal of the monolayer. Note, also on h-BN edges strong SHG signal is observed. Furthermore, PL is also measured from the edges of the underlying h-BN. This indicates that the h-BN may act as a waveguide.

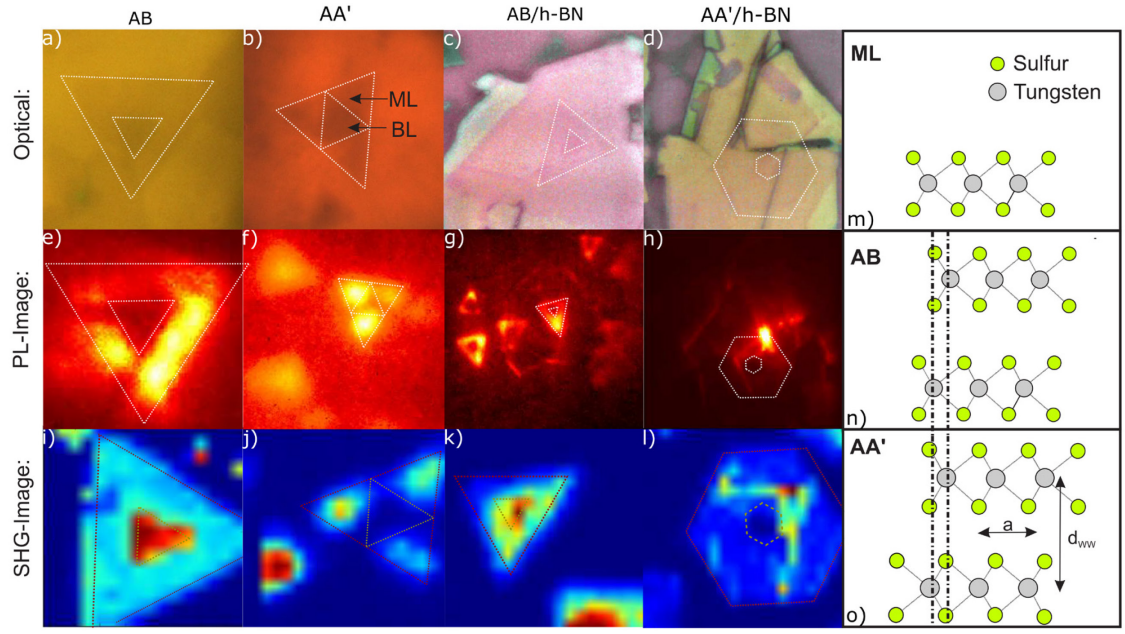

***Figure 27* | WS_2 Homobilayer Samples and Verification of Stacking.** (a-d) microscopic picture of the samples. (e-h) show a false color contour plot of the PL-intensity and (i-l) show the corresponding SHG-signal under illumination at 1.37 eV. (m-o) show the microscopic alignment of the different phases of this WS_2. Adapted with permission from (Lorenz Maximilian Schneider, Kuhnert, et al. 2019). Copyright 2019 American Chemical Society.

The raster scans could verify the assumed alignment in agreement with the TEM high resolution pictures as well as their TEM diffraction pattern taken by our collaborators at Stevens Institute of Technology (not shown, for the diffraction pattern see the Supporting Information of (Lorenz Maximilian Schneider, Kuhnert, et al. 2019)).

5.1.2 Valley- and Layertronics

Due to the different internal crystal symmetry and the consequently changed alignment of the electronic bands, belonging to the individual **K**-points of the monolayers, in the joint band structure, a qualitatively different coupling of valley and spin with the light field was expected for this sample set. In a simplified picture (cf. **Figure 28**), in the case of AB-stacking both **K**-valleys and **K'** valleys of the individual monolayers are (nearly) on top of each other, while in the case of AA' the opposite namely **K** on top of **K'** is realized. This should indeed drastically change the coupling and valley dynamics, where spin-valley locking is only expected for the AB stacks. For the case of AA' stacked bilayers a change of the selection rules compared to AB and the monolayer should be observed.

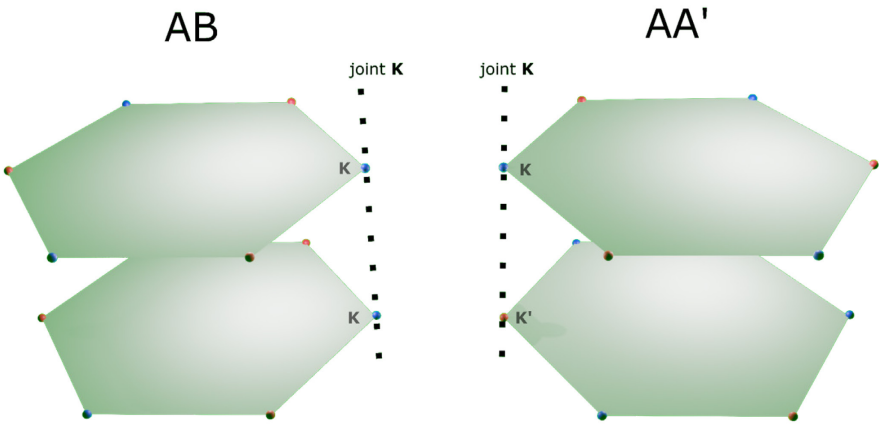

***Figure 28* | Schematic Alignment of the Brillouin Zone in AA' and AB Stacked Bilayers.** The hexagons represent the individual BZ of the monolayer. One can see the alignment of the individual K, K' points. The relevant spins for the A-exciton are depicted by blue (red) spheres at the corner of the BZ corresponding to spin down (spin-up). This simplified scheme neglects the interlayer shift in AB between both layers.

Motivated by this simple reasoning, the polarization of PL-emission was analyzed using a linear as well as a circular basis set (cf. **Figure 29**). Firstly, power dependent measurements were performed, to check if in the investigated range of pump fluxes density dependent changes of the helicity are present. Therefore, the samples have been cooled to 12 K and their emission around the A-resonance has been analyzed using an appropriate combination of half/quarter waveplates and a polarizer for linear/circular polarization measurements.

At first sight surprisingly one finds a pronounced linear and circular anisotropy for all samples, which is not affected by the pump-density. Furthermore, the absolute degree of circular polarization ($\rho_{circ} = (I_{\sigma+} - I_{\sigma-})/(I_{\sigma+} + I_{\sigma-})$) is always a little bit bigger for the AB stack (~35 %) compared to the AA' stack (~25%). Here, $I_{\sigma+}(I_{\sigma-})$ denote the emission intensity with right and left circular polarized light when pumped with right circularly polarized light. Not surprising, however, is the increased polarization anisotropy found for samples on h-BN, that have been isolated from the SiO_2. As shown by our early studies (Lippert et al. 2017; Lorenz Maximilian Schneider et al. 2017) and chapter four, this isolation decreases the doping, due to fewer induced dipoles, and provides a smoother surface. This recently has been verified microscopically by STM to be behind of a decrease of the fluctuations

in strain and local carrier concentration (Rhodes et al. 2019). The increase in helicity is roughly 10 % compared to the SiO_2/Si supported flakes.

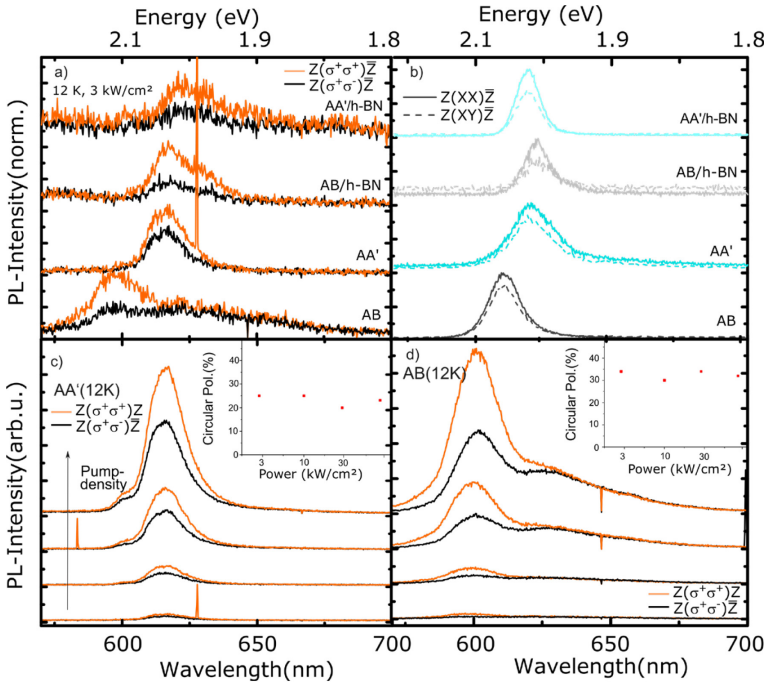

***Figure 29* | Analysis of the Polarization State of the Photoluminescence of WS_2-Homobilayers of Different Stacking Type.** (a) shows helicity resolved PL-measurements while (b) shows the linear polarization anisotropy of the PL at the A-resonance for different stacking configuration. (c &d) are plots of the power dependent PL-spectra in different circular polarization for a different stacking of the bilayers. The insets show the extracted degree of helicity for each power level. All measurements were performed under CW excitation at 2.33 eV excitation energy. Constant offsets have been applied to increase visibility. Adapted with permission from (Lorenz Maximilian Schneider, Kuhnert, et al. 2019). Copyright (2019) American Chemical Society.

The linear polarization anisotropy found is a sign of a sufficiently long coherence time of the valley population compared to the PL-decay rate. For the substrate supported flakes a degree of about 11% is found. On h-BN, where the defects and doping induced dephasing is reduced compared to the SiO_2-supported case, a degree of about 21% is observed for the AA' and 32% for the AB stacked case. Caused by this reasoning it is not surprising that for the sample on h-BN an increased degree of polarization is found for the AB-stacked case. Generally, in AB-stacked bilayers a scattering into the other valley will result in a decrease of the polarization. In the AA'-stacked case, however, in addition a scattering to the other layer in the same valley will result in a loss, too. Due to these increased channels of decoherence a faster decay of the coherent state can be expected.

5.1.3 Reflection Contrast and Energetics

Having verified the alignment of the flakes, a series of reflection contrast measurements has been performed at RT as well as 10K. As the different growth parameters favor but not strictly define a certain growth phase, AA' and AB stacks have been measured under both growth condition. The result for 10 K is shown in **Figure 30**. Sample 2 has been grown with parameters favoring AA' while Sample 3 favors the growth of AB stacked bilayers. Measurements at room temperature can be found in the appendix A5.

If the reflection contrast is compared qualitatively, both substrates show qualitatively similar results, however, sample 2 shows sharper features. When compared to the TEM pictures (not shown), sample 3 probably has a higher amount of disorder. In both substrate pieces the bilayers' A- and B-exciton

resonances are redshifted compared to the monolayer. The AB-bilayer samples though show a bigger shift then the AA'-stacked case. This can be seen easily at the B exciton, furthermore, the energetic separation between A and B exciton series is changing slightly.

If analyzed carefully, also higher order Rydberg states can be seen in the data. The graph shows a zoom-in in the lower inset, where the 2s state of the mono- and bilayers are marked. Furthermore, at close look the reflection contrast reveals a splitting of the 1s-resonance for the bilayers revealing two respectively three features as a fine structure for AA' and AB alignment. The splitting can be easily seen in the upper insets of **Figure 30**.

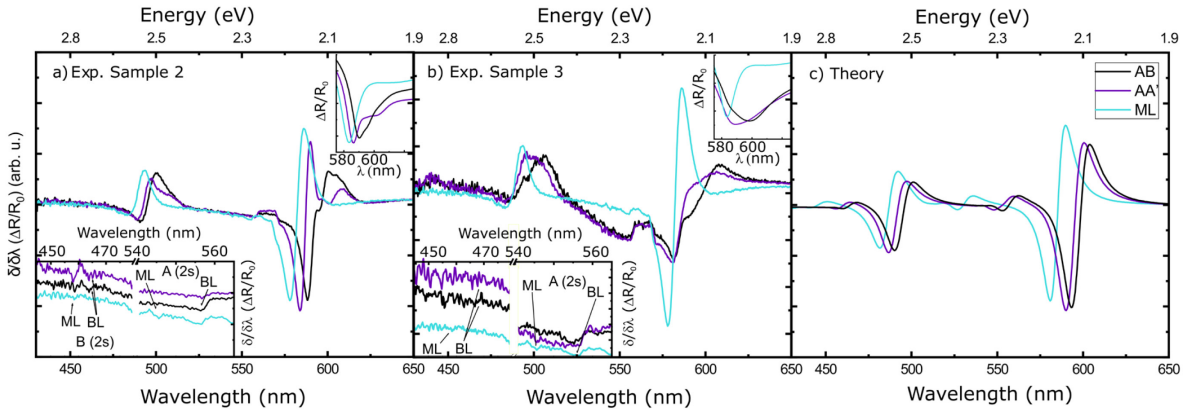

***Figure 30* | Comparison of the Derivative of the Reflection Contrast for Differently Stacked WS_2 Bilayers.** Measurement done on Substrate No.2 and (b) on Substrate No.3. The upper insets show a zoom in to the reflection contrast at the A-resonance. The lower insets depict a zoom-in to the excited states of the A- and B-exciton series. (c) shows a theoretical prediction based on many-body theory assuming a linewidth of 30 meV for the A-exciton and 45 meV for the B-exciton. Adapted with permission from (Lorenz Maximilian Schneider, Kuhnert, et al. 2019). Copyright (2019) American Chemical Society.

5.1.4 Comparison to Theory

In order to understand the observed phenomena many body calculations taking a DFT-bandstructure as input have been performed by colleagues from semiconductor theoretical physics. For computational details the reader is recommended reading our paper (Lorenz Maximilian Schneider, Kuhnert, et al. 2019) and (Lars Meckbach, Stroucken, and Koch 2018b) for the derivation of the underlying gap equations. In short, a DFT-calculation including spin-orbit coupling was performed as implemented in the Vienna ab initio simulation package (VASP) (Kresse and Furthmüller 1996; Kresse and Hafner 1994; Kresse and Joubert 1999; Steiner et al. 2016). The exchange correlation as well as the van-der-Waals forces have been considered by using the Perdew-Burke-Ernzerhof functional with van-der-Waals correction (PBE-D3) (Grimme et al. 2010; Perdew, Burke, and Ernzerhof 1996). The resulting two highest valence and conduction bands are used as input to an additional many body calculation. Here, the anisotropic screening is modelled by an electrostatic model. Then the gap equations and the Dirac-Bloch equations (Horng et al. 2018; L Meckbach et al. 2018; Lars Meckbach, Stroucken, and Koch 2018a) were used to compute the optical linear response. The calculated bands from DFT are plotted in **Figure 31**. This calculation is still not including excitonic effects, however this result from the single-particle calculation already shows the expected change of selection rules and alignment of the bands.

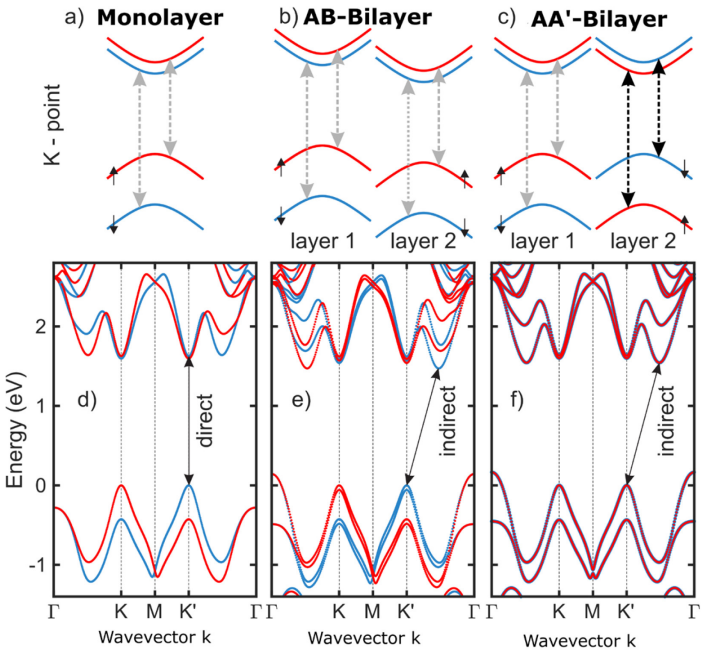

***Figure 31* | DFT-Calculation for a WS_2 Monolayer in Comparison with AA'- and AB-Stacked Bilayers.** (a-c) schematic band alignment for the three cases at the **K**-Point. Red (blue) represents bands with spin up (down). Grey (black) represent allowed transition for right-(left-) circular light. (d-f) show the complete calculated band structure. The calculation has been provided by members of Stefan Koch research group of theoretical semiconductor physics. Adapted with permission from (Lorenz Maximilian Schneider, Kuhnert, et al. 2019). Copyright 2019 American Chemical Society.

As can be seen from **Figure 31** (d-f) the interaction of both layers at **K** and **K'**-points of the joint Brillouin is relatively weak, however states near to the indirect band gap at **Q** pockets (along Λ path) of the bilayers show small effects of hybridization. Nevertheless, as the major experimental findings have concentrated on the emission from the direct band gap at **K/K'**-points of the joint Brillouin zone, a discussion in terms of a superposition of two monolayers with a certain alignment of the high symmetry points of the individual layers is possible in good approximation. Also, the calculated interlayer transition moments are an order of magnitude lower than the intralayer moments, confirming this statement. Interestingly, also the dipole matrix elements (cf. **Table 5**) of the transitions belonging to the direct gap in the bilayer are almost similar to the monolayer.

***Table 5* | DFT Transition Energies and Dipole-Matrix Elements for Differently Stacked Bilayers Compared to a Monolayer.** Note the table shows the results directly taken from the DFT, i.e. before coulomb and excitonic effects have been considered using the gap equations. Adapted with permission from (Lorenz Maximilian Schneider, Kuhnert, et al. 2019). Copyright 2019 American Chemical Society.

	ML	*AA'-BL*	*AB-BL*
X_A *(eV)*	1.627	2.634	1.622 / 1.630
X_B *(eV)*	2.022	2.035	2.017 / 2.025
d_A *(eÅ)*	4.00	3.79	4.01 / 4.00
d_B *(eÅ)*	3.09	2.97	3.09 / 3.09

The upper panel of the calculation (**Figure 31** a-c) shows a schematic zoom in to the relevant **K**-point of the joint Brillouin zone. For the monolayer, the well-known alignment for WS_2 is found with the spin forbidden transition (triplet state) slightly lower than the spin-allowed transition (bright singlet state). Thus, it features the same selection rules for the bright A- and B-excitonic transitions, i.e. both transitions in this valley can only be pumped by one type of circular polarization. Similarly, in the case of AB-stacking, where a broken inversion symmetry and time-reversal symmetry is still present, spin-

valley locking is predicted. In contrast a change of the selection rules for AA'-stacked samples is foreseen. Here, for a given valley, a certain layer can be addressed by choosing the right circular polarization. In simple words, the AB-stacked bilayer behaves very similar to a monolayer not only concerning selection rules, but also in term of transition dipole moments, in contrast AA'-stack - the commonly studied bilayer type -, shows different selection rules and a reduced dipole moment (about 5% reduction).

Furthermore, interestingly a lifting of the degeneracy between the layers in the AB stacked case is present in the DFT-calculation of the suspended bilayer. It amounts for 8 meV for A and B exciton. This is caused by the existence of two different enantiomers. The calculation has been performed for one of them. In case of considering the other enantiomer, the splitting is reversed. Experimentally, this is interesting, as it makes a selective pumping of a certain layer possible if resonant excitation conditions are used.

In the next step the colleagues have included excitonic effects as well as the dielectric influence of the substrate in terms of carrier screening. The resulting energies are summarized in **Table 6** compared to the experimental values and the resulting theoretical predicted reflection contrast is shown in **Figure 30** (c). Generally, the positions of the resonances, the overall shape and the shifts are similar in experiment and theoretical prediction. However, there are small deviations in the position of the higher order resonances.

Table 6 **|Comparison of the Theoretical Predicted and Experimental Resonances for AA' and AB WS_2 Bilayers.** As the sample for the polarized measurement was already degraded, the positions have been taken from the linear measurement. The corresponding energies are written in italic. The energies of Rydberg states are grouped together and separated by a slash. Adapted with permission from (Lorenz Maximilian Schneider, Kuhnert, et al. 2019). Copyright 2019 American Chemical Society.

			A-exciton resonances (eV)			B-Exciton resonances (eV)	
Stacking	layer	gap A (eV)	(theo.)	(exp.)	gap B (eV)	(theo.)	(exp.)
ML	#1	2.467	2.123 / 2.338 / 2.399	2.123 / 2.282	2.940	2.554 / 2.786 / 2.855	2.525 / 2.703
AA'-BL	#1	2.356	2.100 / 2.256 / 2.300	2.103 / 2.247	2.811	2.539 / 2.709 / 2.757	2.507 / 2.694
	#2	2.328	2.089 / 2.234 / 2.275	2.085 / 2.224	2.807	2.533 / 2.695 / 2.742	2.489 / 2.667
AB-BL (σ^+)	#1	2.327	2.082 / 2.223 / 2.275	*2.099 / 2.223*	2.792	2.516 / 2.682 / 2.729	*2.512 / 2.657*
	#2	2.322	2.084 / 2.229 / 2.270	*2.082 / 2.223*	2.780	2.514 / 2.672 / 2.717	*2.512 / 2.657*
AB-BL (σ^-)	#1	2.337	2.091 / 2.242 / 2.284	*2.099 / 2.223*	2.801	2.524 / 2.691 / 2.737	*2.529 / 2.657*
	#2	2.313	2.075 / 2.220 / 2.261	*2.079 / 2.223*	2.777	2.510 / 2.669 / 2.714	*2.509 / 2.657*

The theory also predicts a splitting of the 1s resonance of the A-exciton series due to the asymmetric screening situation (mirror charges in the substrate below the layers, but not in the air above) in agreement with the observation in the experiment. While the splitting of the AA' into 2 peaks can be observed, the splitting of the AB-bilayer into four resonances could not be observed. Caused by the big linewidth of these samples only three resonances could be distinguished. Nevertheless, the experimental observed peaks can be attributed to the band splitting caused by the asymmetric screening. Their observation confirms that for high quality samples and circular polarized pump beam a selective excitation to one of the layers indeed can be realized under resonant condition.

Summarizing the above shows, that both types of bilayers indeed inherit different selection rules, namely spin-valley and spin(-valley)-layer locking. Together with the internal lifting of the degeneracy in the AB-stacked case as well as the external lifting due to the asymmetric dielectric environment, bilayers could be a valuable building block for future valley- and layertronic devices.

The lifted degeneracy makes it possible to excite a certain layer and valley as an initial exciton population. Then external electric fields, which couple to the layer pseudo-spin and magnetic fields coupling to the valley pseudo-spin(Xu et al. 2014), can be used for manipulation of this internal quantum numbers. As in this approach both pseudospins can be defined and manipulated, it potentially offers new capabilities compared to pure valley- or layertronics. Nevertheless, as compared to a monolayer an increased dephasing of the coherent state is expected for the A-exciton, making a fast manipulation time even more important than in the monolayer scenario. One way, to tackle this obstacle for electronic applications would be to use the indirect excitons at **Q** and **Q'** not part of this experimental investigation, that according to the DFT should show comparable selection rules. Caused by their indirect nature the carrier recombination here would be slowed down, so that in high quality samples at low temperatures, where phonon scattering is suppressed, also a longer coherence time can be expected.

5.1.5 Homogeneity of the Samples and Spatial Dependence

In order to verify the findings, not only measurements were taken at one spot, but line scans and raster scans have been performed to check the variations within one flake. First, the fluctuations in PL-emission as well as Raman signals will be discussed, following a discussion of the spatial variation of PL-polarization.

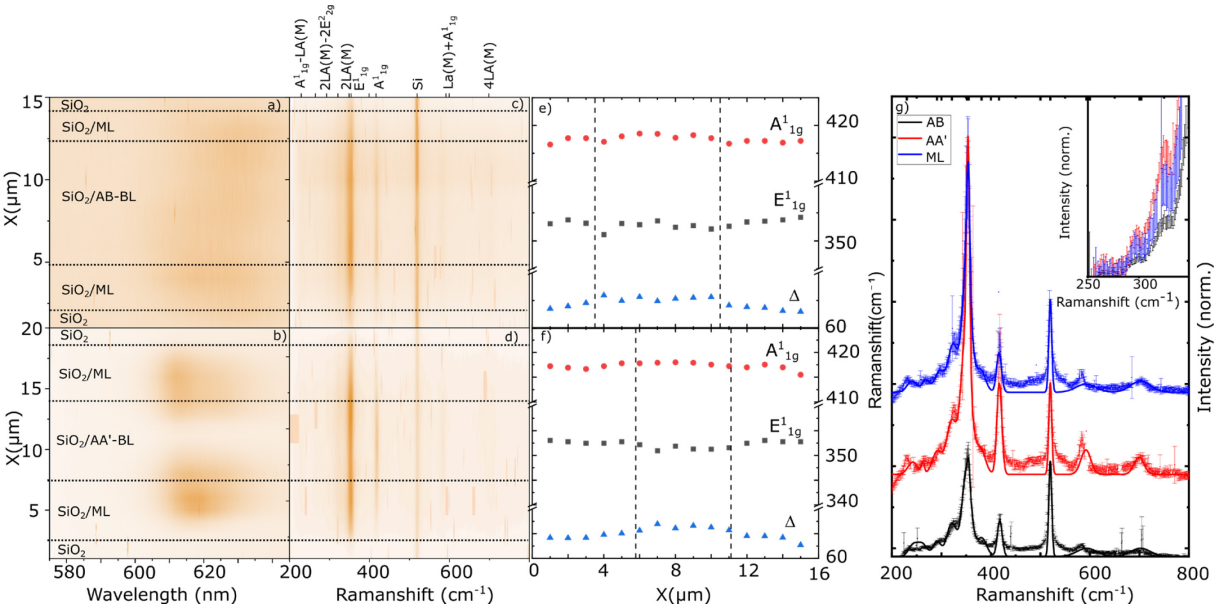

***Figure 32* | Raman Measurements of Differently Stacked Bilayers Compared to a Monolayer.** Line scans of PL for the AB (a) and AA'(b) as well as their Raman signals (c and d) are shown as a contour plot. The dashed lines present a guide to the eye to separate the individual areas as determined by the Raman signal. On the top labels for some of the identified phonon modes are shown according to (Berkdemir et al. 2013). (g) shows the mean Raman signal for the different regions, the error bars show the standard deviation of the mean in these regions. The intensity is normalized to the silicon substrate's Raman signal for better comparison. Interlayer related phonon-modes at the shoulder of the 2LA(M) peak are shown in a zoom in the inset. The extracted peaks over position are shown in (e) and (f) respectively. The data was taken at room temperature using an Ar-ion laser with 1 mW incident power. Adapted with permission from (Lorenz Maximilian Schneider, Kuhnert, et al. 2019). Copyright (2019) American Chemical Society.

The line scans for Raman and PL measurements were performed directly after each other using a confocal µ-PL setup employing a 100x objective with 1 µm steps. **Figure 32** (a,b) and (c,d) shows the resulting PL and Raman spectra as 2D-contour plot, respectively. The dotted lines are separating the ML and BL areas as identified by their Raman signals. The Raman shift of the modes have been extracted for all spectra and our shown in **Figure 32** (f) & (g). One can clearly see the change in the energetic difference between the Raman peaks for different stackings as well as between the monolayer and bilayer region. Furthermore, a correlated shift of the Raman peaks with position can

be seen in the bilayer region, indicating strain variation that are not yet averaged out. As there are still visible at the step size of 1 µm, the strain variation seems to happen not only on a microscopic but also on a mesoscopic scale. The fluctuation is on the scale of one wavenumber, which corresponds to a change in strain of about 0.5% (Chang et al. 2013).

The averages of the Raman-spectra in the respective areas are shown in **Figure 32** (e), the error bars denote the standard deviation over the averaged area. All are normalized with respect to the Raman signal of the underlying SiO_2/Si substrate's Si peak for easier comparison of the signals. As can be seen, not only the common phonon modes ($E^1_{1g}(\Gamma)$ at 355.2 cm^{-1} and $A_{1g}(\Gamma)$ at 417.2 cm^{-1}) but more peaks can be observed at higher Ramanshifts. These peaks have been observed before (Berkdemir et al. 2013), when exciting with the here used Ar-ion laser line at 514.8 nm. According to this interpretation the main strong peak is related to a double resonant process that activates phonon modes at the **M**- (and weakly at the **K**-) point to take part in the process (normally only the Γ-point phonons are involved). Due to that resonant condition other higher order processes involving several phonons become feasible, too. From the measurement it can be concluded that these double resonant Raman processes are stronger in AA' stacked bilayers compared to the AB-stacking type or monolayer systems.

These Raman signatures are of interest as they involve also interlayer Raman modes (E^1_{2g}) on the shoulder of the 2LA(M) peak, that in contrast to the intralayer modes should be more prone to the stacking configuration and the environment. The shoulder including these peaks is shown in the inset of **Figure 32** (e). In order to extract the energy of these vibration and all the others the spectra were fitted with the sum of gaussian. As the higher order phonon peaks can be denoted by their constituents (Berkdemir et al. 2013), constraints have been applied to reduce the number of free parameters, leaving just the four phonon energies involved instead of having a central energy for all peaks. The extracted central Raman shifts are summarized in **Table 7**. The fitting results in a bigger phonon energy for the interlayer mode in case of the AB stack compared to the AA'-BL. While in the graph this seems significant, the fitting errors are too large for a clear indication. Furthermore, a clear change in the intensity ratio between the 2LA and the A^1_g between both stacks and the monolayer is observed. As these phenomena are related to a resonant process, the electronic band structure namely the energetic difference of **K** and **Q** valley as well as the energetic position of the B-exciton necessarily has to be different. The difference at **Q** valley (cf. **Figure 31**) between both stacking types is large and could explain such strong change in the resonance Raman enhancement. Thus, the observation gives experimental evidence that indeed also changes occur at the **Q** valley between the different stackings as predicted by the DFT calculation.

Table 7 **| Comparison of Phonon Modes for Differently Stacked Bilayers.**

SAMPLE	LA(M) (cm^{-1})	A^1_g (cm^{-1})	E^1_{2g}(cm^{-1})	E^1_{1g}(cm^{-1})	Si (cm^{-1})	$\delta\nu$ (cm^{-1})	I(2LA)/I(A^1_g)
ML	175.6 ± 0.5	416.5 ± 0.8	27.5 ± 2.0	354.4 ± 2.0	520	65.3	5.9
AA'	174.8 ± 0.6	417.1 ± 0.6	28.9 ± 2.0	354.0 ± 0.8	520	67.5	2.5
AB	175.6 ± 1.0	418.0 ± 1.0	30.0 ± 4.0	355.1 ± 1.0	520	66.8	3.0

5.1.6 Time-Resolved Photoluminescence of Tungsten Disulfide Bilayers

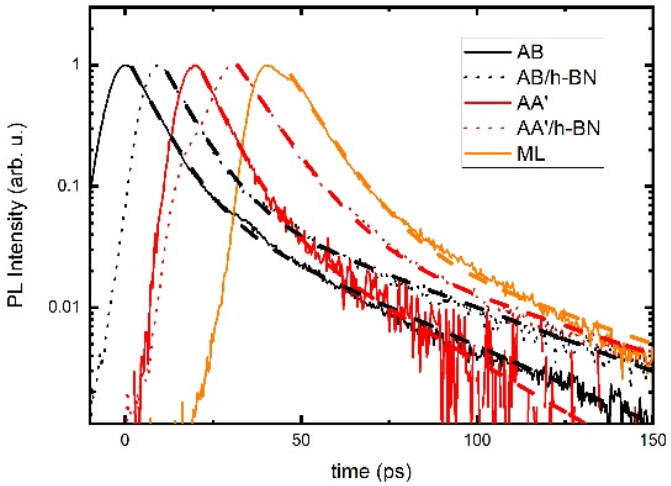

Figure 33 **| Spectrally Integrated Transients of Differently Stacked WS_2 Bilayers.** The graph shows a comparison of the transients at 10 K at a density of 0.25 mJ/cm^2 under non resonant excitation at 2.75 eV. The dashed lines are biexponential fits to the experimental data. The transients are horizontally offset by constant 10 ps for clarity.

In order to check the time dependence of the PL-decay as well as the decay of circular polarization, the samples PL at 10 K have been measured with the streak-camera. First unpolarized measurements at helium temperatures have been executed (cf. **Figure 33**) to check if there is any change in the decay behavior. As can be seen by the graph all of the stackings types as well as the ML behave very similar and can be nicely fitted with a biexponential function. All of them feature a fast decay in the order of 8 ps and a slow decay of about 37 ps. While there is almost no difference in the fast component the slow one is slightly different for the different stackings. This seems surprising at first sight, as one would expect a faster decay of the PL compared to the monolayer as scattering of the excitons to the indirect bandgap opens a new decay channel (Wallauer et al. 2016). Nevertheless, as the transition dipole moments from the DFT for monolayer and both stackings types are nearly similar, furthermore the density of states within one layer should be similar, this finding seems consistent with fermis golden rule, if scattering to the indirect bandgap is slow compared to the radiative decay at these temperatures.

In the next step helicity resolved emission dynamics were studied, therefore, co- and contra polarized measurements were performed. As a small laser jitter (1-2 ps over 20 min measurement time) between consecutive measurements is already leading to huge changes in the overall helicity at zero delay, only spectra integrated over a time range of 10 ps are evaluated. This procedure is in fact reducing the influence of such systematic error. Nevertheless, a measurement using a Wollaston prism and the streak camera would make the simultaneous measurement of both polarization possible and thus could help to eliminate this possible systematic error. A time-resolved waterfall plot of the PL averaged following this procedure is shown in **Figure 34** exemplary for the monolayer. Waterfall plots for the differently stacked bilayer on substrate and on h-BN are shown in the appendix A7. Already from first sight, it is clear that the polarization in the monolayer is stronger under these pulsed off-resonant conditions. Especially, at larger delay, a polarization is absent in the bilayers, while in the monolayer a small amount is still present.

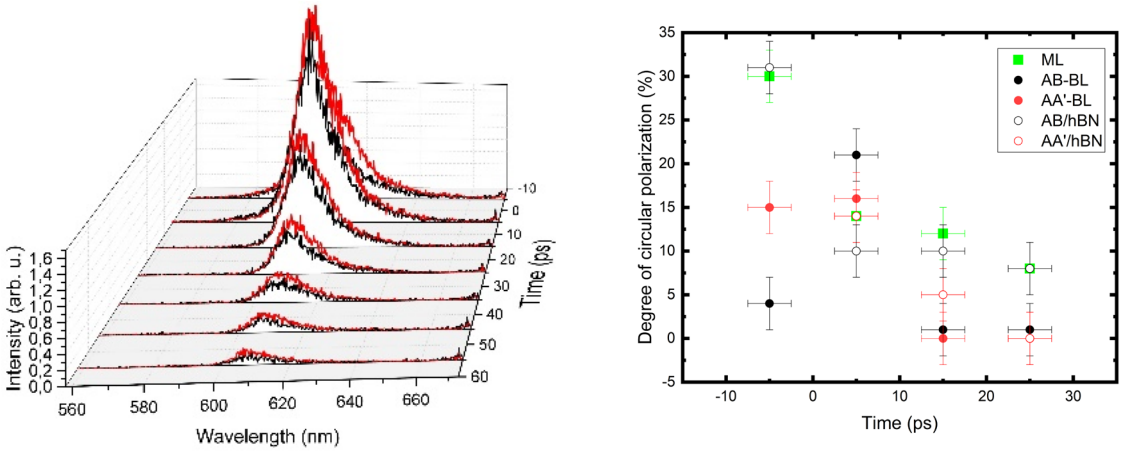

***Figure 34* | Waterfall Plot of the Time- and Helicity-Resolved Photoluminescence for Monolayer and Differently Stacked Bilayers.** Exemplary co- (red) and contra (black) polarized measurement at the example of a monolayer (a) at 10K at a density of 0.25 mJ/cm² under non resonant excitation at 2.75 eV. (b) Extracted Helicity as a function of time for the different stacking types and the monolayer.

To quantify this observation, the amount of helicity was calculated for the shown timesteps for the monolayer as well as all different stacks (cf. **Figure 34**.a). First of all, one can clearly see the improvement, when a h-BN buffer layer is used: The decay gets slower and the initial amount of helicity is bigger. This is expected as the reduced inhomogeneity increases the polarization lifetime.

If AA'- and AB-stacked bilayers are compared, the AA'-stack shows a significantly faster decay of the helicity then the AB stack or the monolayer. This can be understood as in the AA'-stacked case two decay channels, namely scattering to the other layer or valley, while in the AB-BL and monolayer case only scattering to the other valley results in a loss of helicity. Nevertheless, it seems surprising, that the AB stacked bilayer shows a similar helicity lifetime than the monolayer as a scattering to the indirect bandgap in Λ-valley as well as the additional phonon states should naturally increase the dephasing.

5.2 Characterization of a Twisted WS_2/WSe_2 Heterobilayer

In this chapter the optical properties of a WS_2/WSe_2/h-BN/SiO_2/Si structure are discussed. The work has been done together with my master student Manan Shah. The sample was fabricated by mechanical exfoliation in Marburg and was later on annealed at 350° C for four hours in UHV (cf. **Figure 35**). As it is understood (Tongay et al. 2014), that this annealing step will increase the coupling of both monolayers, characterization have been performed before and after annealing. While before annealing often huge numbers of small bubbles of remaining polymer are present, they accumulate during annealing in an Oswald ripening process to form only a few big bubbles. Thus, in the remaining part the layers can get very close, resulting in a strongly coupled system. Unfortunately, the sample got destroyed in one of the last measurements, therefore the important SHG measurement, that was planned to determine the twist angle, could not be obtained. Thus, the study (Shah, Schneider, and Rahimi-Iman 2019) has to be seen as a preliminary study. Nevertheless, the results are promising and show indeed sign of moiré excitons.

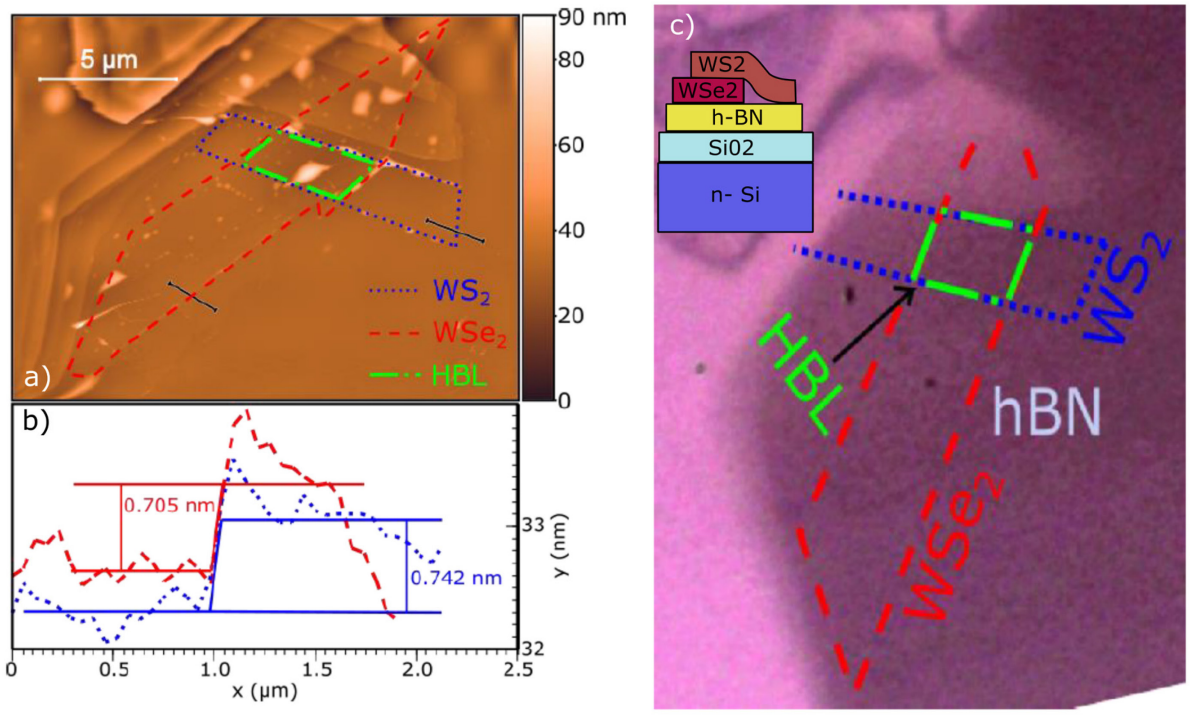

***Figure 35* | Microscopic Picture and Topography of the Sample.** (a) Topography of the sample after annealing as determined by AFM. (b) Height profiles along the lines marked in (a) giving proof that indeed monolayers are present. (c) Microscopic picture of the sample before annealing. The lines in (a) and (c) represents a guide to the eye indicating the borders of the ML. (a) is adapted with permission from (Shah, Schneider, and Rahimi-Iman 2019), Springer Semiconductors, Copyright 2019.

As the SHG could not be performed anymore, the angle between the edges of the flakes have been used to make a guess on the twist angle. This is a reasonable estimate as the monolayers tend to break along a crystal axis. The angle has been measured at all four corners of the heterobilayer region and the average has been calculated. As the picture cannot tell, if the broken edge refers to the zig-zag or armchair direction, such a guess only allows to determine the twist modulo 60°. The result of the estimation thus is either 4° or 56° with an estimated error of about 3°. Particularly, for small twist angle a strong influence of the moiré potential is expected as recent literature shows (Jin et al. 2019).

5.2.1 Properties Before Annealing

In order to investigate the optical properties of the as stacked heterobilayer as function of the position a µ-PL rasterscan (cf. **Figure 36**) using the piezo-stage (step size of 1 µm) of the setup was performed. Before annealing, only a weak coupling between the layers is expected due to remaining residues of the transfer process between the layers, that act as a spacer. The raster scan is plotted for different energy regions (1.55- 1.68 eV / 1.87 – 2.10 eV /1.55 -2.10 eV) corresponding to WS_2, WSe_2 and total intensity in the measured region. The boxes show the extension of the layer as measured in the AFM. One can see, that in the top part the WSe_2 PL is quenched due to the bulk flake WSe_2 on top. Furthermore, one can clearly see, a region of about 2x4 µm, where signals from both monolayers can be found and a weakly coupled heterobilayer is present.

To analyze if there are any spectral shifts present, the spectra along the dashed arrows in **Figure 36** (a-c) where analyzed. The spectra along the green line going from WSe_2 through the heterostructure region ending on WS_2 is shown in (d). One can see a quenching of the PL intensity of both intralayer exciton in the heterobilayer region. This could indicate a charge-transfer. However, the change of dielectric environment causes a change of the band structure (Raja et al. 2017) accompanied with a decrease of oscillator strength (Gerber and Marie 2018b). This effect should be especially noticeable for WSe_2 with gets encapsulated. This effect can be indeed expected as an 8 meV redshift of the WSe_2

intralayer peak can be observed. In contrast no significant shift is present for WS_2. As such the heterostructure has to be not only seen as a vertical heterostructure but also as a lateral one, as the bandgap and exciton binding energy change related to such a transition from a supported to an encapsulated scenario is in the order of up to 100 meV (Raja et al. 2017). Furthermore, a tiny signal between the intralayer peaks can be observed shortly above 1.8 eV in the heterobilayer.

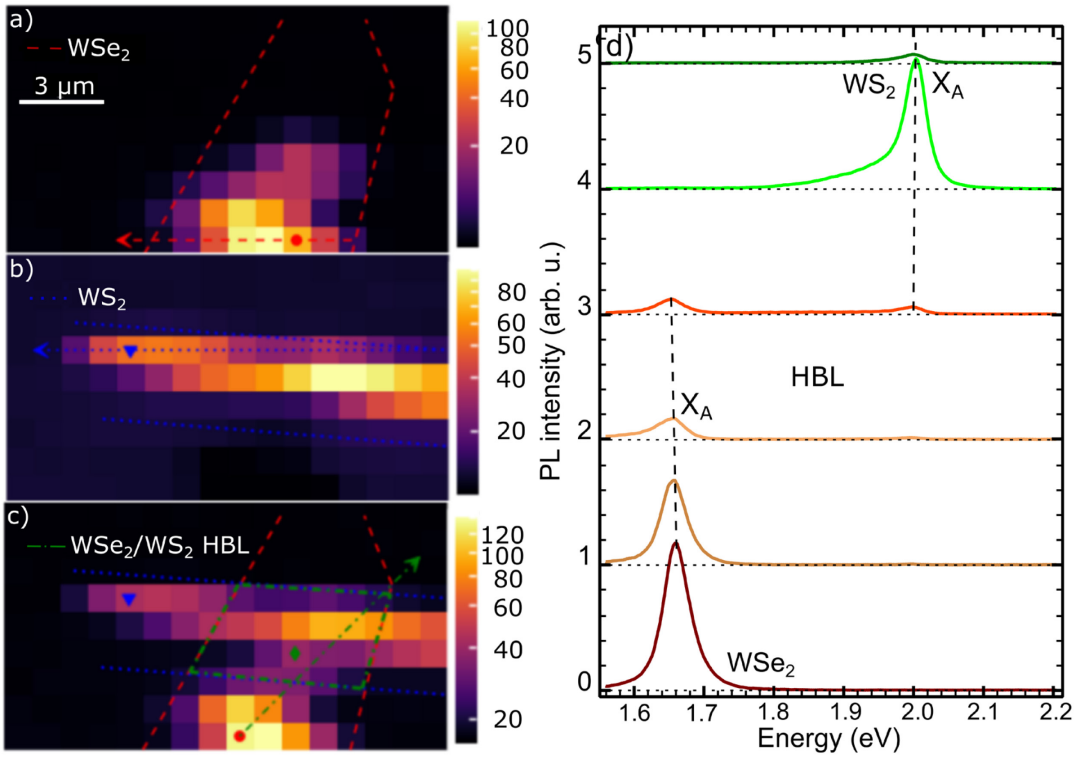

***Figure 36* | µ-PL Rasterscan of the WS_2/WSe_2 Heterobilayer at Room Temperature.** (a, b, c) Spatial maps of the spectrally integrated PL intensity in the energy range of 1.55 – 1.68 eV, 1.87 – 2.10 eV and 1.55 – 2.10 eV corresponding mainly to WSe_2, WS_2 and the whole range. The part where intensity is seen from both layers (green box) can be identified as the heterostructure region. The spectra along the green line are shown in (d). They are shown with constant for better readability. (c,d) are adapted with permission from (Shah, Schneider, and Rahimi-Iman 2019), Springer Semiconductors, Copyright 2019.

In the next step, one PL-spectrum from each region (position marked with symbols in the raster scan) was analyzed in depth together with a reflection contrast measurement taken at the heterostructure region. Both individual intralayer peaks show a weak asymmetry (different from the tiny feature at 1.8 eV) easy visible in logarithmic plotting, that could be related either to defects or phonon assisted recombination (Brem et al. 2020). The theory by (Brem et al. 2020), predicts the phonon side bands from the dark exciton from K-K' or K-Λ transitions to extend approximately 70 meV (LA/TA phonons) below the intralayer resonance of WSe_2 at room temperature. As WS_2 behaves normally similar to WSe_2 a similar extension can be expected.

To analyze the possibility of phonon assisted emission, a Pearson IV distribution was used to fit the neutral intralayer exciton peaks. This distribution effectively describes an energetically asymmetric distributed ensemble of Lorentzian oscillators, which on a phenomenological level nicely can reproduce the inhomogeneous broadening due to acoustic Γ-point phonons (Christiansen et al. 2017; Selig 2018). The distribution reads the following:

***Equation 5-1* | Pearson Type IV Distribution**

$$A(E) = \frac{\left|\Gamma\left(m + \frac{\nu}{2}i\right)\right|^2}{\alpha\beta\left(m - \frac{1}{2}, \frac{1}{2}\right)}\left[1 + \left(\frac{E-\lambda}{\alpha}\right)^2\right]^{-m} \exp\left(-\nu\, arctan\left(\frac{E-\lambda}{\alpha}\right)\right)$$

Here, the first factor is a normalization involving the complex Gamma and beta function. The parameter λ is the center of the peak and $\alpha > 0$ is a scale parameter of the distribution defining the width of the function. The parameter ν dictates the skewness or asymmetry and $m > ½$ describes the general shape of the distribution. For $\nu = 0$, the function turns into symmetric Student's t-distribution and for $m = 1$ the function becomes a skewed version of a Lorentzian. The function tends to a skewed Gaussian as $m \to \infty$.

The distribution can fit the main peak and the asymmetry seen on a linear scale quite good, however, on logarithmic scale there are still visible deviations (cf. **Figure 37**). The asymmetry parameters of the individual layer from the fitting are 0.43 and 0.32. Thus, as expected the phonon coupling is stronger in WSe_2 than in WS_2 similar to previous reports (Christiansen et al. 2017). In the heterobilayer region the asymmetry of the WS_2 peak is increased to 0.46, that could be an indicator for additional states on the low energy side.

In both cases the deviation from the model occur about 70 to 80 meV below the intralayer transition. This is exactly where optical and acoustical phonon sideband from dark exciton are predicted to be located (Brem et al. 2020). As the Pearson function only accounts for one resonance and its asymmetry (or in other words a continuous distribution of resonances arising for example from the interaction with acoustical phonons), it is not surprising, that it cannot model phonon assisted recombination arising from excitonic states related to K-K' or K-Λ transition.

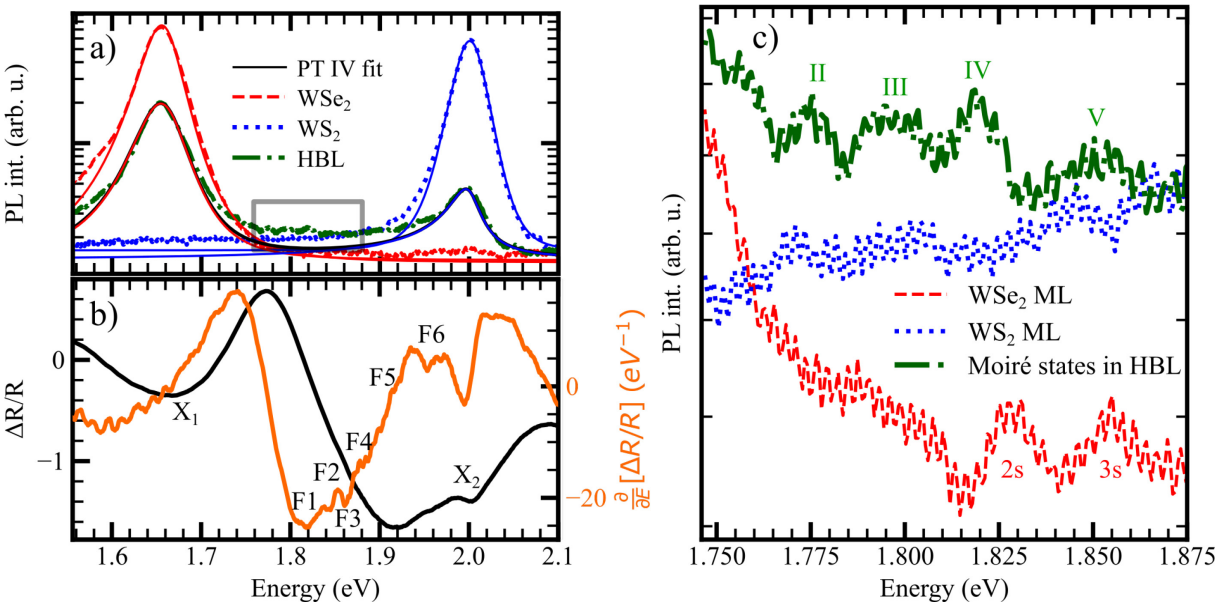

***Figure 37* | Comparison of PL Signatures of the Individual Layers and the Heterobilayer with Reflection Contrast Taken at the Heterobilayer Region.** (a) Overview of the PL spectra in the different regions compared to reflection contrast data and its derivative (b). A Zoom-in to the region between the intralayer peaks marked in (a) is shown in (c). The PL spectra in (a) show asymmetric peaks that have been fitted with a Pearson IV function, that can be used as a simple model to account for acoustic phonon side bands. X1, X2 correspond to intralayer transitions of the monolayers. F1-F6 and II-V are newly arising features in Reflection and PL. F1-F4 and II-V are most likely due to moiré states while F5-F6 are most likely due to phonon assisted recombination or a hybridized state. (a) is adapted with permission from (Shah, Schneider, and Rahimi-Iman 2019), Springer Semiconductor, Copyright 2019.

In order to analyze this spectral overview more deeply, a reflection contrast spectrum has been acquired at the heterobilayer region (cf. **Figure 37 b**). It shows the reflection contrast and it derivative in comparison to the PL emission. One can clearly see the resonance of the neutral excitons intralayer excitons at the same position as in PL. However, two more feature around 1.92 and 1.96 eV (F5 and F6) can be found. Furthermore, the derivative of the reflection contrast reveals four additional features (F1 – F4) hidden in the reflection contrast. The resonances will be discussed in two blocks, namely resonances F1-F4 as well as F5 and F6.

When having a close look to the PL emission in the energetic region between the interlayer peaks, several tiny features can be found at 1.775 eV / 1.797 eV / 1.819 eV / 1.854 eV (labelled II, III, IV, V) in the bilayer region, that are absent in the spectra of the individual layers. These positions roughly match with the resonances F1-F4 found in the reflection contrast. They have been attributed to the higher order moiré exciton states in accordance to (Jin et al. 2019), that find similar peaks (although with slightly smaller spacing) in their small twist angle sample. Similar moiré states have recently also been found in other van der Walls heterobilayers (Seyler et al. 2019; H. Yu et al. 2017). As we still discuss the sample before annealing, we deal with a sample, where the monolayers are at many places still decoupled caused by residues, nevertheless locally some places are already coupled. Therefore, the observation of weak moiré features is not surprising. Nonetheless, the signal at the intralayer transition (X_1, X_2) has strong contribution from the weakly coupled or uncoupled regions and therefore cannot be interpreted as the transition from the lowest moiré miniband.

In contrast F5, and F6 are energetically at the expected position for optical and acoustic phonon side bands from the dark exciton of WS_2 (Brem et al. 2020). However, we observe a surprisingly strong contribution of these peaks to the reflection contrast, that is normally not observed in reflection experiments for dark excitons. This is understood due to the indirect or spin forbidden nature and therefore their small oscillator strength. Similarly, defects seldomly have such a strong oscillator strength. Thus, it could be indeed that the increased intensity originate from a hybridized state similar to the claim of (Kunstmann et al. 2018). They claim that hybridized states between Γ- and K-points with partial charge transfer exists. Caused by the partial wavefunction overlap a bigger oscillator strength is expected compared to interlayer excitons.

When comparing the measurements between samples with a small and a large twist angle in (Jin et al. 2019), they also observe weak signals from transitions in the energetic region around 1.82 eV for a small twist angle arising from even higher moiré bands but do not discuss them. As the dips for F5 and F6 are more pronounced than the one of feature F1-F4, the former origin from hybridized partial interlayer states is more likely, however their definite origin remains unclear.

Note, the additional peaks found in the PL-measurement of WSe_2 (1.829 eV and 1.855 eV) are in agreement with previous reports of the 2s and 3s state of WSe_2 (K. He et al. 2014). While these two peaks are close to feature IV and V, these features cannot be identical as the bandgap and the exciton binding energy renormalize upon encapsulation and thus the position of the higher Rydberg states (Raja et al. 2017) are changing.

5.2.2 Properties After Annealing

To enhance the interlayer coupling an annealing step at 350° C for four hours has been performed. The spatial resolution was gained by taking nearfield images using the focal plane array detector at room temperature (cf. **Figure 38 a**). One can see WSe_2 in the top of the image. In the center of the image WSe_2 is on top of WS_2. Here, strong emission between both intralayer excitonic peaks (1.645 eV for WSe_2 and 2.033 eV for WS_2) can be found (cf. **Figure 38 b**). This strong emission indicates that most likely a large area fraction of the heterojunction is now strongly coupled. Therefore, in contrast to the previous analysis before annealing, the intensity at the energetic position of the common intralayer

transition is most likely arising from the lowest moiré miniband and not the transition of the decoupled layer.

A pump density dependent measurement was performed (**Figure 38 c**), as it allows the separation of the spectral features more clearly. The energies found for the moiré features after annealing (1.645 eV, 1.77 eV, 1.79 eV, 1.82 eV and 1.85 eV) as well as the intra layer peaks (1.46 eV and 1.53 eV) are marked with dashed lines in (c) are at similar energetic position then before annealing. Fitting these moiré states together with the state at 1.93 eV (feature F5) already found in reflection contrast before annealing can nicely reproduce the now dominant PL peak in the center. The fact, that the peak at 1.93 eV indeed gets more pronounced after annealing gives additional evidence, that its emission is related to a hybridized or interlayer state.

A close look at the low energy side of the spectrum shows, that at least two more peak can be found around 1.5 eV, where charge-transfer excitons are expected. This interlayer peak is predicted to also split into four transition (Yuan et al. 2019) caused by the moiré potential which could be experimentally proven for $MoSe_2/WSe_2$ by Tran et al. (Tran et al. 2019). As we here deal with a non-encapsulated sample at room temperature, we can unsurprisingly only resolve two of these peaks. Nonetheless, the observation of the new states and the indication of the split charge-transfer exciton clearly shows, that the moiré potential is not only strongly influencing the WSe_2 (and WS_2) intralayer features but indeed gives rise to a whole plethora of new transitions also affecting the charge-transfer excitons.

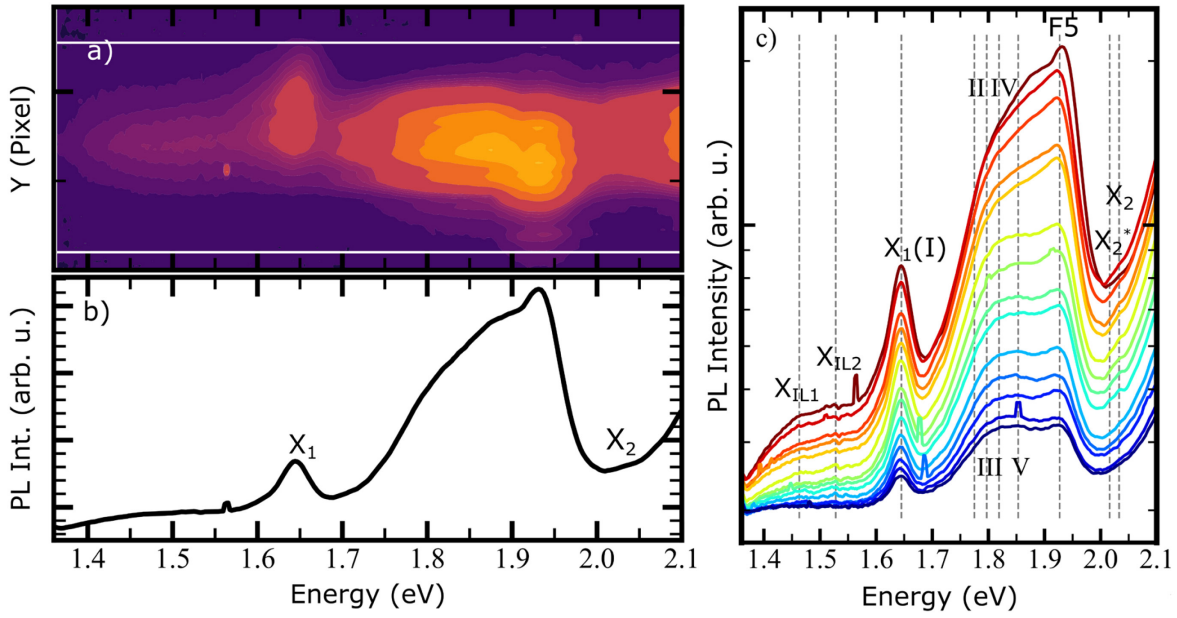

***Figure 38* | Optical Characterization of the WS_2/WSe_2 Heterostructure at Room Temperature After Annealing.** (a) Far-field image of the heterostructure. The y-axis corresponds to a spatial coordinate. (b) Summed spectra over the whole near-field image. (c) Power dependent measurement of the spectra in the heterobilayer region. The excitation was done using the frequency doubled Ti:Sa at 2.77 eV.

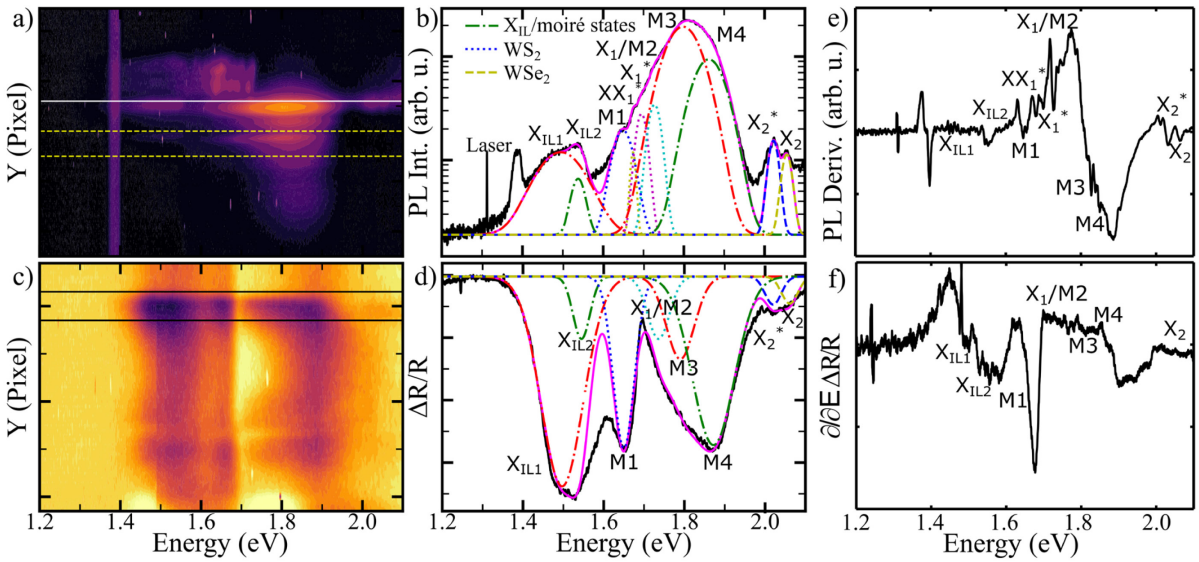

***Figure 39* | Optical Characterization of the WS_2/WSe_2 Heterostructure at 10K.** False color contour plot of photoluminescence (a) and reflection contrast (b). The corresponding spectra from the heterobilayer part (white line in (a), range between black lines in (c)) are shown in (b) and (d). The dashed and dot lines represent the fit for WSe_2 and WS_2 excitonic features, respectively. Likewise, the dash-dot lines represent the fit for the intralayer and moiré features. Both spectra are fitted with the sum of gaussians as inhomogeneous broadening is still dominant. (e) and (f) show the derivative of the PL and the reflection contrast spectrum. The PL was taken with a pulsed excitation at 2.77 eV at 54 μJ/cm² flux density per pulse. (b-d) are adapted with permission from (Shah, Schneider, and Rahimi-Iman 2019), Springer Semiconductors, Copyright 2019.

In a next step the sample's optical property were analyzed at 10 K (cf. **Figure 39**). Again near-field/real-space images were acquired using the nitrogen cooled focal plane CCD-array. Here, easily an area of with PL originating from WSe_2 (top of **Figure 39 a**) and from the heterobilayer (center of **Figure 39 a**) can be identified. Note, the reflection contrast image of **Figure 39 b** just shows the heterobilayer part. For further analysis a part of the heterostructure with strong coupling has been selected from the 2D-images and the spectra is presented in (cf. **Figure 39 b,d**).

At 10 K the peaks get generally, sharper and allow now the clear separation of the charge-transfer exciton from the intralayer transition. Note, while also emission at this low energy is observed for pure WSe_2 due to phonon assisted emission, the counts are clearly enhanced in the heterostructure, indicating that indeed an interlayer feature is present.

As the broad peaks shows several shoulders, the derivative of the PL emission as well as the reflection contrast derivative were plotted (cf. **Figure 39 e,f**), to clearly resolve their position. While both spectra and their derivatives show in general nice correspondence to each other, one has to keep in mind the differences. The PL measurement and its derivative under pulsed excitation will also show higher order exciton complexes and phonon sidebands which normally are barely observable in reflection contrast. Both derivatives reveal a complex fine structure of the broad peak as well as the charge-transfer states with several sub-features with a close spacing of about 30 meV similar to (Tran et al. 2019).

In order to identify the peaks, both spectra are fitted with the sum of gaussians and show nice correspondence between each other. While a shift of the common intralayer feature compared to the bare monolayer can be expected due to the moiré pattern, the binding energies of trions and biexcitons should be not (strongly) affected. Furthermore, higher order exciton complexes in reflection contrast are less visible compared to PL. Similarly higher moiré excitons (Alexeev et al. 2019) are more visible then these excitonic complexes due to higher oscillator strength. With this consideration in mind, the corresponding peaks were identified. The extracted central energies are 2.054 eV and 2.022 eV for the intralayer exciton and trion of WS_2, respectively. Thus only a small shift (about 20 meV

compared to a bare monolayer (Chernikov et al. 2014), (Z. He et al. 2016)) is found for this material similar to (Jin et al. 2019). In strong contrast a large splitting of the moiré band can be expected. The sharp resonance (M1 / 1.66 eV) in the reflection contrast has to belong to the lowest moiré excitonic state of the intralayer exciton as it has the strongest oscillator strength (Alexeev et al. 2019). Nonetheless, also emission from weakly coupled areas is still present, as small shoulders at the common position (1.727 eV, 1.695 eV and 1.674 eV) for the intralayer neutral and charged exciton as well as the charged biexciton of WSe_2 can be found very similar to previous reports (Lorenz Maximilian Schneider, Lippert, et al. 2018; You et al. 2015).

Similar to the room temperature measurements several transition can be found between the main intralayer excitons. For these moiré states 1.66 eV, 1.727 eV, 1.797 eV and 1.861 eV could be extracted as their central energies. While the energetic spacing between the moiré states (including the common A-exciton as second moiré band) is slightly higher (67 meV compared to reported 56 meV for the undoped case) than the one reported by (Jin et al. 2019), their position almost match (1.683 eV, 1.739 eV and 1.776 eV reports by (Jin et al. 2019)). Nonetheless, for a slightly bigger twist angle or doping an increased splitting of the moiré states is expected and was already measured (Jin et al. 2019; F. Wu, Lovorn, and Macdonald 2017). Furthermore, (Alexeev et al. 2019) claim to observe moiré trions comparably to (Jin et al. 2019), that observe a splitting of the moiré peaks at sufficient doping. Thus, the energetics is comparable to these previous reports.

In addition to these rather pronounced states, the derivatives reveal even more transitions between 1.8 eV and 2.0 eV. While in general they could arise from phonon assisted emission from WS_2, they are surprisingly obvious in reflection contrast if they would originate from phonon sidebands. In addition, when comparing with the samples of (Jin et al. 2019) and the SI of this paper, one has to state, that while not discussed by this paper even higher order moiré states in this energy regions can be seen in their spectrum. Nonetheless, the origin is not clear and more measurements with samples of different twist angles are necessary.

Similarly, to the moiré states, 1.495 eV and 1.538 eV could be extracted as the energetic position of the charge-transfer excitons at 10 K. Nevertheless, the shape of the derivatives suggests that the charge-transfer exciton is not only composed of two, but at least four resonances (1.495 eV, 1.538, eV 1.547 eV and 1.578 eV) similar to (Tran et al. 2019). However, the SNR of the derivative in that region is not sufficient such that this four resonances position have to be handled with care. Measurements should be repeated to extract their splitting reliably and understand their origin exactly.

Furthermore, one has to note, that from the reflection contrast measurement the oscillator strength of the interlayer charge transfer excitons seems strongest, indicating a strong coupling between the monolayers. Thus, the preliminary study makes the interpretation of moiré states as well as the guess of small twist angle very likely. Nevertheless, more samples with different twist angles need to be studied to verify the origin of these new optical features.

5.2.3 Time-Resolved Measurements

In order to better understand the dynamics of these new states as well as the transitions itself, time-resolved PL-spectra of the sample at 10 K were taken using the streak camera. Again, an off-resonant pulsed excitation at 2.7 eV was used. Although the signal to noise ratio for this measurement was very low (cf. **Figure 40**), some results could be obtained. For the intralayer excitons a fast-initial decay could be observed, yielding values of (3 ± 1) ps and (6 ± 1) ps for WS_2 and WSe_2, respectively, similar to previous measurements in this thesis and other reports (Korn et al. 2011; Philipp Nagler et al. 2017). Interestingly, one can see a clear redshift of the WSe_2 A-exciton PL in the first 5 ps. The PL-lifetimes were extracted by spectrally integrating the transient intensity in the following energy ranges: 1.95-2.06 eV for WS_2 PL, 1.77-1.86 eV covering the higher moiré states, 1.60-1.76 eV covering WSe_2 and the

lower moiré states, and 1.42-1.49 eV for the interlayer excitons. The resulting transients were fitted with a monoexponentially decay. The signal for the interlayer excitons was very weak and no clear transient although a signature (the time integrated spectrum is very similar to the previous discussed spectra) was detected due to the limited sensitivity of the UV/Vis streak camera in this spectral region.

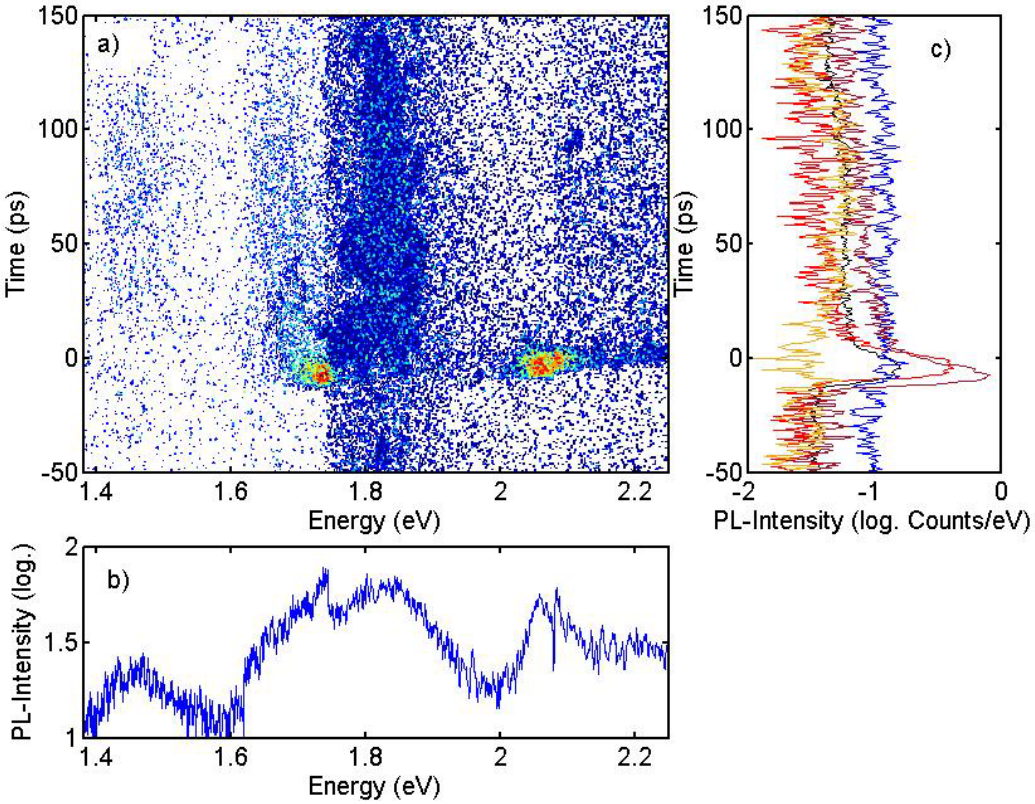

Figure 40 **| Time-Resolved Photoluminescence of the WS_2/WSe_2 Heterobilayer at 10 K.** (a) Contour plot of the stitched streak camera image acquired in photon counting mode. Originally 4 images were acquired. The Intensity is color coded on a logarithmic scale. (b) shows the temporally integrated spectra of the heterostructure and (c) the spectrally integrated transients for the following energy ranges: 1.95 – 2.06 eV (red), 1.77-1.86 eV (blue), 1.60 - 1.76 eV (purble), and 1.42-1.49 eV (orange). In addition, the transient integrated over the whole range is shown in black. The sample was excited using off-resonant condition at 2.7 eV with 54 µJ/cm².

In contrast for the moiré states at about 1.8 eV a very long decay is found. The PL-Intensity is not decayed before the next pulsed arrives. Therefore, it is clear, that is lifetime is beyond 12.5 ns (the time window between consecutive pulses). Similarly, one can only see the onset of the interlayer exciton but due to sensitivity and the long decay time no clear transient time can be extracted. Caused by that it was tried to measure the decay time using a low-repetition rate laser (10 hz) together with an ICCD-camera. Unfortunately, caused by too high flux of the associated laser, the sample got destroyed during that measurement.

The long decay of the hybridized moiré states can be probably explained by two reasons. First, the hybridization at γ-point can give rise to partially space indirect transitions (Alexeev et al. 2019; Kunstmann et al. 2018), that slow down the process due to a reduced wavefunction overlap. Secondly, the moiré states are localized at different points of the Brillouin Zone (cf. **Figure 12** and (Jin et al. 2019; H. Yu et al. 2017)) which have a different associated oscillator strength. Thus, intrinsically the transition at different points in space have a different and possibly slower decay in case of a lower oscillator strength. The last prediction, however, should lead to very different decay times for the different moiré excitons. More measurements with different excitation conditions, longer time windows and more samples are needed to investigate the complex dynamics on the moiré potential even further.

5.3 Summary

The effect of the mutual respective alignment between two monolayers is of central importance for the understanding of homo- and heterobilayer systems of TMDCs. Therefore, CVD-grown bilayers were investigated in the first part of this chapter, while the second part discusses a preliminary study on the effects of the moiré potential on a strongly coupled exfoliated heterobilayer. In the first half of the chapter, mainly the effect of the alignment as well as the coupling on the selection rules and polarization dephasing was the main point of interest. The alignment of the CVD grown bilayers could be verified by SHG measurements as well as Raman measurements of the interlayer modes. In polarization resolved PL-measurements an anisotropy could be found for both stacking types in agreement to older reports on exfoliated (Jones et al. 2014) or artificially stacked samples and could be explained by spin-valley and spin(-valley)-layer locking.

Due to an improved theory also a lifted degeneracy between the layers could be predicted and verified in reflection contrast experiments up to my knowledge for the first time in addition to previous reports. The lifting is either happening due to internal symmetry (existence of enantiomers) or screening by an asymmetric environment. Furthermore, a small shift of about 10 meV of the direct optical bandgap is observed between the different stacking types. This changes in energetics together with the selection rules offer new possibilities, e.g. for the AB stack a certain valley in a specific layer can be addressed selectively. These findings confirm that not only the monolayers but also the bilayers of TMDCs can be valuable building blocks for valley- or layertronics. The new result of the study presented here, that indeed the symmetry breaking due the typically used asymmetric dielectric environment is not negligible but lifts the degeneracy by 5 to 10 meV for common substrates, is remarkable. It maybe can be even increased if other highly polarizing substrates are used. This lifting itself also makes “real” layertronics possible in the commonly occurring AA’ stacks, where in the suspended case a specific layer selectivity is only given for fixed valley.

While polarization integrated dynamics stay almost unaffected by the stacking type, the polarization dephasing is found to be different caused by the additional dephasing channel available for the AA’-stack case, also in line with the theoretical prediction.

In conclusion of this study it can be said that new device concept could arise due to the possibility of selective excitation of both valley and layer. Nevertheless, this study focused only on the direct band gap. A detailed study including the indirect bandgap as well as a study on layer- or valley polarized/resolved photocurrents should be carried out with low linewidth samples to further understand and develop proof of concept devices on these types of stacks. Furthermore, as the degeneracy of the layers is lifted, the homojunction strictly has to be understood as a heterostructure with a band offset in the meV range. Thus if used as a p-n junction, it potentially also radiates THz emission similar to other heterostructures (E. Y. Ma et al. 2019). If stacked similar to a quantum cascade laser, the recombination from this transition in the valence band could be potentially enhanced and used in application. Here MoS_2 would be the natural candidate as it shows stronger interlayer transitions.

In the second part a preliminary study of a WS_2/WSe_2 heterostructure, that is almost aligned (or anti-aligned), was presented. In such a case a strong influence of the moiré potential is expected. To investigate this effect the heterobilayer was investigated before and after annealing, corresponding to a regime of weak and strong coupling between the individual layers, respectively.

A detailed analysis of spatially-resolved PL and reflection contrast measurements in the regime of weakly coupled monolayers, reveals the formation of a lateral heterostructure mainly affecting WSe_2 due to the strong change of dielectric screening in the upper half space similar to (Raja et al. 2017). In addition, weak signals of charge-transfer exciton at the low energy side as well as new features

energetically in between the intralayer excitons could be found. Their energies of the latter ones were very close to recent reports on moiré excitons (Jin et al. 2019), thus likely they are already present in the weak coupling regime (as locally some parts will be already strongly coupled).

After annealing, the sample was analyzed using AFM measurements. As expected, the contaminations between the layers had accumulated in an Oswald ripening, resulting in one part of the heterostructure, that is closely attached and therefore strongly coupled, and another part at the bubble, where coupling should be absent. Using spectrally resolved far-field images, the areas of strong coupling were identified by the presence of sign of charge-transfer excitons and analyzed carefully. The intensity and splitting of the interlayer peaks as well as the features attributed to moiré states show a remarkably increase of their magnitude in the spectra and are clearly visible, as expected. This gives further evidence, that the observed peaks are related to an interaction of both monolayers. While annealing can also increase the number of defects and thus to the observation of red shifted localized states, their strong presence in reflection contrast makes this origin less likely. In addition, time-resolved measurements revealed a very slow decay of these moiré states around 1.8 eV, which can be expected for hybridized states with partial charge transfer.

All of this observation as well as the mostly likely present lateral heterostructure in addition to the vertical band alignment shows that the model of describing a heterobilayer as a “simple” hetero-junction arising in conventional semiconductors is not valid. It neglects the fine structure of the intra- and interlayer caused by the moiré pattern on the order of tens of meV (Jin et al. 2019). The observation of these states similar to recent literature (Seyler et al. 2019; Tang et al. 2020; Tiefenbacher, Pettenkofer, and Jaegermann 2000; Tran et al. 2019; F. Wu, Lovorn, and Macdonald 2017; H. Yu et al. 2017) has huge implication for the use in conventional LED devices and in valleytronics. Furthermore it opens new opportunities if the coupling between the localized excitons are seen as a QD grid (Lei Wang et al. 2019). Thus, additional measurements are necessary to understand the dynamic in the grid as well as the energetics.

In the first application area of LEDs and light harvesting, the dynamics and tuning of these states have to be understood better in order to engineer the transition with the right dynamics and energy differences. Also the influence of the moiré pattern to exciton/charge diffusion, its anisotropy (Yuan et al. 2019) and mobility has to be understood to successfully integrate these heterobilayers in electronics.

For the second topic of valleytronics, interlayer excitons have been long thought to be a solution to achieve long valley coherence and depolarization time while keeping the basic physics. However, the predictions of spatially varying selection rules (H. Yu et al. 2017) as well as the experimental finding of an interlayer moiré fine structure width different selection rules (Tran et al. 2019) render this picture too simplified. Here, further investigation studying the valley dynamics and energetics, when possible using a SNOM to be able to study the different high symmetry points in realspace as function of the moiré potential (i.e. the twist angle), are necessary. The potential outcome could path the way to the usage of twisted heterobilayer system and thier engineering for potential applications.

Thirdly, the strongly coupled grid of localized excitons open the path to new paradigm in TMDCs. It can be used to construct topological excitons (F. Wu, Lovorn, and Macdonald 2017), opening the path to topological photonics, as well as the engineering of exotic quantum phases (Naik and Jain 2018; Regan et al. 2020; Lei Wang et al. 2019; H. Yu et al. 2017) like excitonic Mott insulator and superconductivity, similar to previous demonstration in bilayer graphene (Bistritzer and MacDonald 2011; Y. Cao, Fatemi, Demir, et al. 2018; Y. Cao, Fatemi, Fang, et al. 2018).

6. Fourier-Space Spectroscopy on h-BN Encapsulated Monolayers

Strong coupling between excitons and photons for example in nano- and microstructures can lead to the formation of hybrid quasiparticles called exciton-polaritons. Generally, they can occur either in quantum-wells system with strong oscillator strength in the form of a fundamental excitation (Hesse et al. 1976; Itoh et al. 1981; Klingshirn 2012; Rappel, Feiner, and Schuurmans 1988) or as cavity polaritons in other quantum mechanical systems in which the coupling is enhanced by exploiting optical structures like Fabry-Pérot cavities (C. Schneider, A. Rahimi-Iman et al. 2013; C. Schneider, Glazov, et al. 2018; Weisbuch et al. 1992) and photonic crystals (Bajoni et al. 2009; Fujita et al. 1998; Gogna et al. 2019; L. Zhang et al. 2018). The field is steadily growing (A. Kavokin et al. 2017; Rahimi-Iman 2020c) since the combination of photonic and electronic characteristics in these particles allows not only a dramatic increase of mobility and potentially higher switching and computation speeds (Amo et al. 2010), but also can give easy access to fundamental control of quantum stated or even their sub-cycle manipulation (Colas et al. 2015; L. Dominici et al. 2014; Lorenzo Dominici et al. 2015). Furthermore, exotic physics like condensation (Deng et al. 2002; Kasprzak et al. 2006; Weihs et al. 2003), interaction of a bosonic gas with a degenerate fermi gas (Sidler et al. 2017) and other correlated quantum systems can be studied at higher temperatures.

While the observation of cavity polaritons has been intensively studied in III-V grown integrated system (Byrnes, Kim, and Yamamoto 2014; Deng, Haug, and Yamamoto 2010; Weisbuch et al. 1992), these systems lack sum desirable characteristics. The small binding energies limit the observation of polaritons or even condensates to low temperatures, limiting their significance for applications. Thus, numerous alternative material systems complementing research on the common platforms have been explored and employed for condensation studies, particularly aiming at room-temperature operation (Rahimi-Iman 2020a). At the same time no valley or spin band can be selectively addressed optically or influenced by external electric fields.

In contrast 2D-TMDC's offer superior properties concerning exciton binding energy (300 meV) and oscillator strength of about 1.9 eV^2 (Hill et al. 2015; Yilei Li, Chernikov, et al. 2014b), possibly opening the window for polariton or even polariton condensate-based technology at elevated temperatures up to room temperature (C. Schneider, Glazov, et al. 2018). As the quality of the monolayers increased over time, cavity polaritons have also been shown experimentally for monolayer TMDCs materials up to room temperature (Dufferwiel et al. 2015; X. Liu et al. 2015; Z. Sun et al. 2017). In addition, valley polaritons (N. Lundt, Stoll, et al. 2017; Z. Sun et al. 2017) and exciton-polaritons dressed by the fermi-gas of free carriers (Sidler et al. 2017) could be demonstrated. Nonetheless the study of condensates in TMDCs is at the very beginning with the first signatures found recently (Sigl et al. 2020).

While these effects have been found for cavity supported structures also effects can be expected for h-BN encapsulated samples that show nearly the intrinsic linewidth. In general, the long range electron-hole exchange interaction in 2D-TMDCs has been predicted to lift the degeneracy of the exciton-branches resting in **K** and **K'**-valley (Glazov et al. 2014; Qiu, Cao, and Louie 2015; F. Wu, Qu, and MacDonald 2015; H. Yu et al. 2014), featuring an upper branch with extremely strong and surprisingly linear dispersion instead of the commonly assumed parabolic dispersion for an excitonic branch. This splitting is predicted to be measurable for Fourier-space spectroscopy and also has to be taken into account for the dynamics of dephasing in valley polaritons (Z. Sun et al. 2017). It has to be noted, that the lifting of two degenerate excitons modes forming a linear and a parabolic branch has also been predicted in GaAs and CuCl (Andreani and Bassani 1990), however due to the smaller oscillator strength in these materials the splitting and slope is very small and has no practical relevance. In TMDCs in contrast the higher oscillator strength not only pushes the longitudinal-transverse splitting respectively the slope within the light cone into the meV region but the splitting also corresponds to a

Rabi-oscillation between both, the **K** and **K'**, valleys (H. Yu et al. 2014). In contrast in GaAs the Rabi-oscillations are taking place between both singlet excitons at Γ-point.

Such a splitting can also explained from another viewpoint. As the real part of the permittivity for high-quality samples can get negative due to the strong oscillator strength (DFT calculations of Stefan Koch group and recent experiments (Epstein et al. 2020) show, that negative permittivity is reached), the formation of an exciton-polariton population as fundamental excitation becomes possible. For a bulk crystal this means that the excitons splits into a longitudinal and transversal branch (Klingshirn 2012), if the dephasing rate is not too big. For a quantum well this coherent phenomenon is only seen in the plane thus at the end of the light cone. At normal incidence a longitudinal- and transversal excitation cannot be distinguished anymore, thus the splitting goes to zero due to the interaction with the vacuum field. It has to be noted, that the electron-hole exchange interaction has its origin in the same Coulomb interaction that gives rise to the instantaneous electromagnetic field. Therefore, a microscopic calculation considering the momentum dependent (long-range) exchange interaction should yield the same result as solving the electrostatic Maxwell equations for the interaction of excitons with the electromagnetic field considering the macroscopic excitonic susceptibility, i.e. calculating the polariton modes (Andreani and Bassani 1990). Indeed it has been shown by (Andreani and Bassani 1990; Hanamura 1988) that both formulation are identical and describe to sides of the same coin, thus a linear branch is also found in the description of quantum well polaritons (see 2.7.4 Quantum-Well Exciton-Polaritons).

Both viewpoints respectively formulations, the formation of (valley-) polaritons as well as the hybridization of exitonic states coupling both valleys, lead to a coupling of the center-of-mass motion with the valley degree of freedom (Z. Sun et al. 2017). As a selective excitation of different combination of center-mass-momentum, polarization as well as energy are possible, this phenomenon could be used to establish new excitonic or polaritonic circuits (Amo et al. 2010; W. L. Zhang et al. 2019). Especially, the polaritonic circuits could be of interest, as the offer a dramatically increased mobility compared to their excitonic counterparts. In both cases one could store the information either in the charge for classical computation or in the spin/valley texture for quantum-based computation. Furthermore, condensate-based technologies could be developed (Schmutzler et al. 2015).

This chapter present a systematic experimental study of the emission and reflectivity of several high-quality samples, in the absence of a high Q-factor cavity. In order to extract the radiative pattern and the dispersion of the different excitonic complexes angle resolved measurements have been pursued on h-BN encapsulated monolayers. While mainly WSe_2 has been studied, also $MoSe_2$ has been investigated, as tungsten and molybdenum based TMDC's often encounter different complementary physics due to their different sign of spin-orbit splitting. While physically clear that for such samples two different origins of the dispersion have to be considered namely, the exciton normal mode splitting by electron-hole exchange interaction or the formation of in-plane polaritons due to the high oscillator strength. The influence or dominance of the individual effects is not yet fully clear. Therefore, results and discussion shall be strictly separated. In addition, propagation effects in the multilayer structure that could act as a (bad) cavity were considered as possible source for a curved dispersion, but calculations did not indicate such effect.

First of all, angle resolved reflection contrast and PL-measurements will be discussed in section 6.1 showing the basic observation of dispersion in the spectroscopic Fourier-space data. Here, also a quick discussion of the differences between WSe_2 and $MoSe_2$ is given. Afterwards a more detailed discussion of the dependencies of the dispersion on excitation energy condition (sect. 6.2), temperature (sect. 6.3) as well as excitation density (section. 6.4) is given for the example of WSe_2. As a final step of this initial experimental investigation the angle dependences and energetics of higher excitonic features

and excited states has been investigated (sect. 6.5). After having presented this, a detailed discussion of the three reasonable explanation (sect. 6.6) and their impact is given.

In the next step the coupling of the observed curved dispersion to the valley degree of freedom was investigated. It is accessed optically be analyzing the PL-polarization involved under linear and circular excitation in section 6.7 carefully. The results are discussed in terms of the Maialle-Silva-Sham (Maialle, de Andrada e Silva, and Sham 1993) and the Dyakonov-Perel type mechanism (Dyakonov and Perel 1972).

In the last step (sect. 6.8) the radiation pattern of the different excitonic species will be examined. From this the alignment of the corresponding transition dipole will be extracted as well as the influence of the multilayer structure to the outcoupling of fluorescence emission. Finally, a summary (sect. 6.9) for this chapter is given.

6.1 Experimental Observation of Dispersion

The samples examined in this section have been provided by the group of James Hone, Daniel Rhodes and coworkers at the Columbia University. They provided four WSe_2 (cf. **Figure 41**) flakes that are encapsulated with h-BN on both sides as well as one $MoSe_2$ flake produced by the same procedure. Pictures of the individual stacking steps can be found in the Appendix A8.

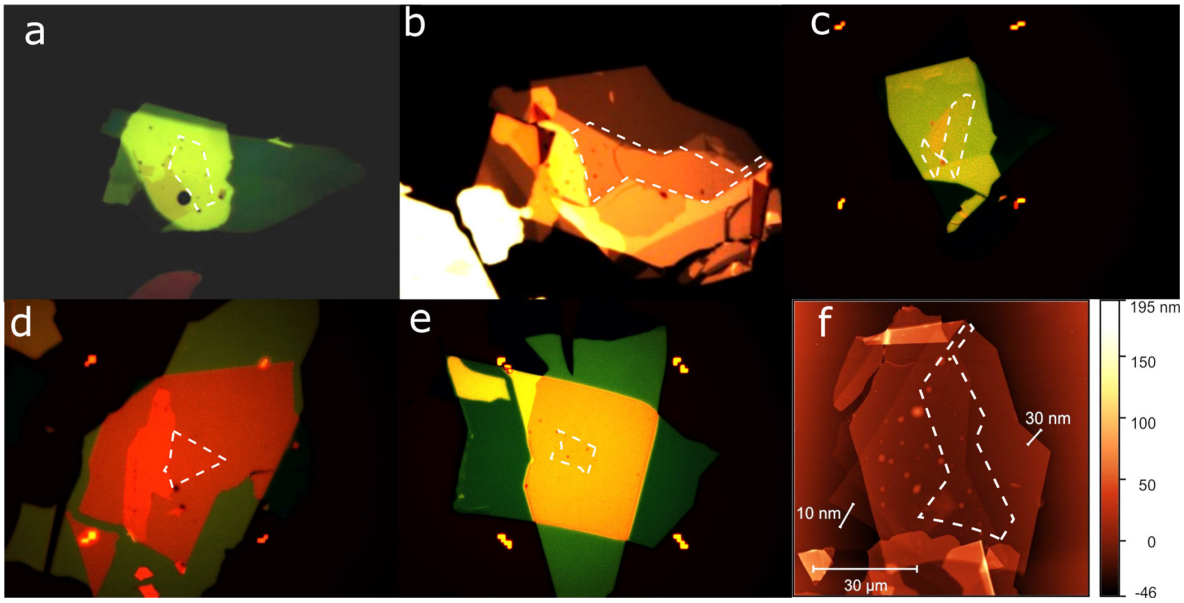

***Figure 41* | Microscopic Pictures of all Samples.** (a-d) microscopic picture of all encapsulated WSe_2 and (e) $MoSe_2$ samples. (f) shows an AFM of the second WSe_2 -sample (b), that was evaluated in detail. For clarity, the areas of encapsulated monolayers are marked with a whited dashed line.

As the signal is strongly affected by the excitation condition, different conditions will be discussed one after the other. Before, the angle-resolved spectrum shall be discussed, the angle-integrated spectrum **Figure 42(a)** will be shown and discussed briefly. The graph shows the spectrum under quasi-resonant and off-resonant excitation. One can see, that while the off-resonant spectrum shows several sharp features discussed later on, the spectrum under quasi-resonant excitation is dominated by the exciton resonance and shows a broad emission band red shifted about 50 meV compared to the exciton. Nonetheless, the derivative reveals that the high-order complexes are still present but their contribution to the spectrum is strongly reduced.

A Voigt-shape (cf. **Figure 42(b)**) was fitted to analyze the lineshape and linewidth of the neutral exciton peak. For this sample a homogeneous linewidth of 2.6 meV and an inhomogenous broadening of 3.7 meV at 10 K is determines by the line fit. However, an asymmetry is found on the higher energy side

of the peak. If this would be neglected in fitting, an even smaller homogeneous linewidth for the main peak becomes reasonable. This very narrow linewidth close to the homogenous linewidth has been found for all of these samples and makes the relatively shallow energy-momentum dispersion measurable. Nonetheless, it easily can be seen, that the Voigt profile does not fit perfectly, as a high energy tail is present. Indeed, the lineshape can be fitted perfectly using an asymmetric Fano-lineshape (Fano 1961) similar to reports on polaritons in photonic crystals (L. Zhang et al. 2018). The origin of this tail are interactions with acoustic Γ-point phonons similar to reports for $MoSe_2$ (Shree et al. 2018) or interactions with the interferences in the multilayer structure (Epstein et al. 2020).

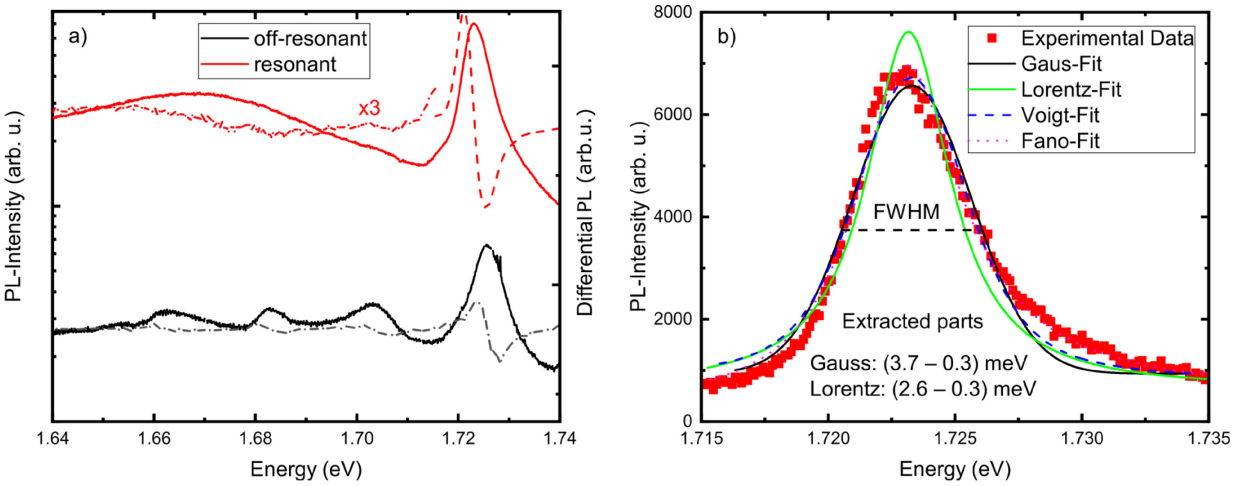

Figure 42 **| Spectrum and Voigt analysis of the Lineshape of the PL emission of the h-BN Encapsulated WSe_2 Sample at 10K.** (a) Comparison of the PL Spectrum at quasi-resonant and off-resonant excitation (lines) as well as their derivatives (dashed dotted lines). The derivative corresponding to the broad emission band has been multiplied for better visibility. (b) Lineshape analysis using different model functions. The standard deviation and linewidth in the picture represent the result from the Voigt profile.

Coming back to angle-resolved data, we will start with the discussion of quasi-resonant continuous wave excitation. First, the angle-resolved reflection contrast and PL-spectra for a representative encapsulated WSe_2 and $MoSe_2$ flake (cf. **Figure 43**) are shown. The graph shows a zoom-in to the A-exciton resonance for both measurements. Generally, the edges of the Fourier-spectroscopy-image represent the maximum numerical aperture of the used objective. By knowing these angles, the respective conserved in-plane momenta can be calculated with the following formula (Rahimi-Iman 2013):

Equation 6-1 **| Relation between emission angle and center-of-mass momentum**

$$k_{||} = \frac{2\pi n}{\lambda_0} \tan\left(arcsin\left(\frac{sin(\theta_0)}{n}\right)\right)$$

Here, λ_0 represents the vacuum wavelength, n the refractive index and θ_0 the measured angle.

Figure 43 shows the PL emission and the reflection contrast spectra as a function of the in-plane momentum for the 1s resonance of the A-exciton for both materials. One can clearly observe a dispersion of this resonance in the measurements, i.e. the energetic position is clearly depended on the in-plane momentum, even for the small momentum accessible within the light cone. Note, no dispersion could be found for other excitonic species like trions under such excitation conditions. Therefore, most of the following sections are just focusing on the 1s-resonance of the neutral exciton. The other encapsulated WSe_2 flakes show qualitatively the same behavior. Fourier-spectra for other similar stacks are shown in the Appendix A9. Qualitatively, the curvature is significantly smaller for $MoSe_2$ compared to WSe_2. Furthermore, Fourier-images at different spots of the sample including the

center and edges of a flake are shown in **Figure A12**. Unsurprisingly, only in the central area the full dispersion can be measured as expected from geometrical consideration of the setup, while on the edges only one side can be observed. Similarly, neither PL emission nor a dispersion can be found on the h-BN or the substrate, i.e. in reflection contrast spectra.

In order to analyze the dispersion quantitatively, each column of the digital Fourier-space spectra (false-color contour maps) representing a $k_{||}$-resolved spectrum has been fitted automatically by the derivative of a Lorentzian lineshape in the case of reflection contrast derivative data or Gaussian peaks for the PL data. Both the reflection contrast as well as the PL could be nicely fitted with this technically motivated assumption.

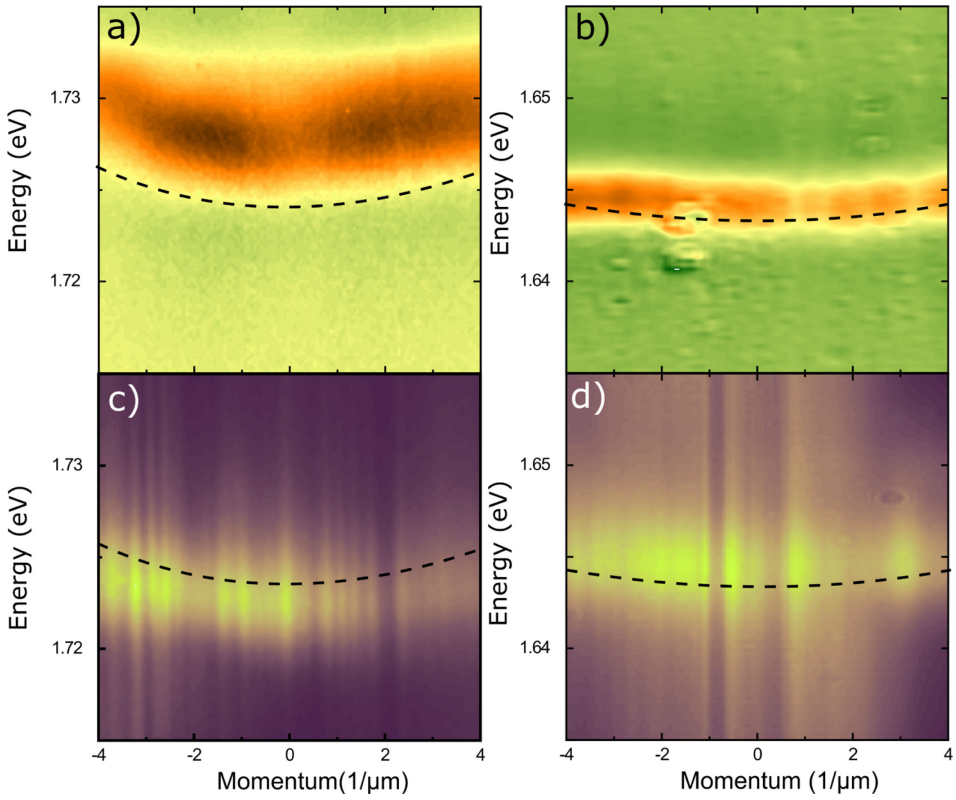

***Figure 43* | 2D Contour Plot of the Angle-Resolved Reflection Contrast and PL Measurement at 10 K under Quasi-Resonant Continuous Wave Excitation comparing $MoSe_2$ and WSe_2:** (a) angle resolved derivative of the reflection contrast of WSe_2 and $MoSe_2$ (b). (c) and (d) are showing the photoluminescence, respectively. For the PL Fourier image a quasi-resonant excitation with 3.6 KW/cm² has been used. The dashed lines represent a guide to the eye.

The A-exciton energy extracted from PL-measurements using the automatic fitting routine is plotted in **Figure 44** (a1-i1) and similarly for the reflection contrast data in **Figure 44** (a2-i2). While there are some deviations between the samples due to fluctuations in stack quality and spot-dependencies in measurability of the features all show clearly a visible dispersion on the order of about 2 meV for WSe_2 and 1 meV for $MoSe_2$ within the light cone. This amounts for an effective mass of (3.6 ± 1.64) $10^{-4}\ m_e$, respectively, (2 ± 1.5) $10^{-4}\ m_e$. This magnitude is a really surprising result, if the order of magnitude is compared with curvatures based on expected common origins, as for a parabolic dispersion from the exciton mass only a dispersion of 100 µeV would be expected. Thus, such a strong dispersion cannot be modeled by the conventional exciton mass but has to have another origin.

On the one hand, for a bare exciton with parabolic dispersion one would expect a value around 0.29 m_e (Gerber and Marie 2018b), orders of magnitude higher than found here. Such high magnitude are expected from the easiest possible model for the exciton mass, as the sum of the effective masses of the electron and hole (Klingshirn 2012). On the other hand considering long-range exchange

interaction between electrons and holes within the same valley and across the valleys yields a leading linear term, (cf. Chapter 2.7 Dispersion of Quasi-Particles) which accounts for a dispersion within the lightcone of about 1.5 meV, predicted for suspended MoS_2 (Qiu, Cao, and Louie 2015). This is still a factor of about two smaller than in experiment for WSe_2 but is very close to our observation on the closer relative $MoSe_2$.

Generally, this could be linked to a different strength of the exchange interaction in WSe_2 compared to MoS_2 or the encapsulation. As WSe_2 has a higher binding energy than MoS_2 arising from the direct Coulomb term and a larger splitting between the bright and dark states resulting from the short-range exchange interaction, a larger long-range exchange interaction can also be expected. On the contrary h-BN encapsulation increases the carrier-screening and thus reduces the long-range exchange interactions. However, the reduced disorder leads to a decreasing observable linewidth and as such a stronger interaction with the light field.
However, as the observed dispersion looks rather parabolic than linear as predicted by (Qiu, Cao, and Louie 2015) other effects like the formation of excitons-polaritons involving h-BN or cavity exciton-polaritons could also contribute. The masses for both phenomena are often observed in the range of 1e-4 m_e (Hauschild et al. 2006; A. Kavokin et al. 2017; Klingshirn 2012; Low et al. 2017; C. Schneider, Glazov, et al. 2018) (cf. Chapter 6.6). Cavity-polaritons however, also are not immediately expected as the multilayer structure including the substrate provides only very weak optical confinement compared to the usual microcavities. Furthermore, the occurrence of dispersion should not be excitation energy dependent as demonstrated below. On the other hand, coupling to the excitation laser is rules out due to the occurrence of strong dispersion even in white-light reflection contrast spectra. Thus, it could be that the argument of (Deilmann and Thygesen 2019) that the screening in an encapsulated sample like here is indeed not strictly 2D but involves mirror charges in the h-BN and therefore a parabolic dispersion should be expected.

The significantly smaller dispersion found for $MoSe_2$ compared to WSe_2 is in agreement with the prediction of (Deilmann and Thygesen 2019) as well as expected from the reduced exciton binding energy. However, compared to other calculations this theoretical paper does not truncate the Coulomb interaction to the 2D-case with the argument that samples on substrate will not face a 2D-interaction. Therefore, they do not find a linear slope but instead an increased parabolic dispersion. Nonetheless, as this paper also includes the short- and long-range interaction one can see that it is indeed weaker for molybdenum-based materials, and a reduced long-range exchange interaction is expected. At the same time the exciton's oscillator strength in these materials is almost similar (Yilei Li, Chernikov, et al. 2014b) while the static permittivity is higher for molybdenum-based ML as such should also lead to slightly smaller dispersion in the light cone from the viewpoint of polaritons.

Coming to the temperature dependence, one can see a clear and comparable decline in the dispersion at elevated temperature for all samples as can be seen from **Figure 44**. This is attributed to the formation of phonon sidebands as will be discussed later on (Chapter 6.3 Temperature Dependence). Having shown, that the results are well comparable in other samples ($\overline{m}^* = 3.6 \cdot 10^{-4} \pm 1.7$) under quasi-resonant condition, in the following the data of sample 2 will be discussed in more detail.

However, as the formation of excitons or excitons-polaritons is strongly influenced by the excitation conditions, this influence on the observed dispersion will be discussed first (cf. Chapter 6.2 Dependence on Excitation Detuning).

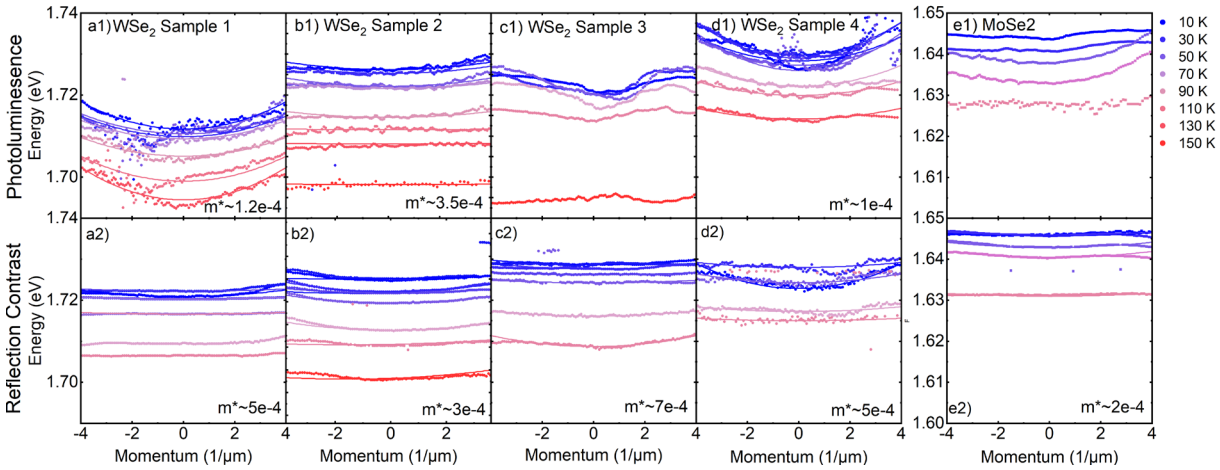

***Figure 44*| Overview of the Temperature Dependence for Luminescence and Reflectance Dispersions in Several Samples.** The measured dispersion is shown for encapsulated WSe_2 (a1-d1) and $MoSe_2$ (e1) in photoluminescence. For comparison the extracted dispersion from the reflection contrast measurements (RC) of the same flake is shown in (a2- e2), respectively. The dots represent the Gaussian (PL) / Lorentzian (RC) fits to the individual spectra, spectra, respectively. The extraction of the center for each pixel line was done automatically. PL and RC spectra have been acquired independently. Thus, spot to spot fluctuation between both series can be expected. Similarly, the material expansion during heating in temperature series shift the laser spot, such that spot to spot fluctuation could not be avoided. Furthermore, due to limited measurement times and helium, temperature steps between different series are not necessarily the same. Nonetheless, all measurements show curvature distributed around a mean value of $(\overline{m}^* = 3.6 \cdot 10^{-4} \pm 1.7)$ for WSe_2. The straight lines represent quadratic fits to the data. The given effective mass m* corresponds to the value at 10K. C1) has not been fitted as a parabolic fit is not well suited. The data in this case follow an almost linear dependence.

6.2 Dependence on Excitation Detuning

To investigate the dependence on the excitation condition, the momentum dependence was analyzed at continuous wave pumping for several excitation energies, i.e. detuning's. The chosen energies (detunings) are 1.784 eV (55 meV), 1.810 eV (81 meV), 1.952 eV (223 meV), 2.330 eV (601 meV), 2.786 eV (1057 meV). Detuning are given with respect to the 1s-energetic level of the neutral A exciton at 10 K. In the following the first and last excitation condition are meant, whenever the terms "quasi-resonant" or "off-resonant" condition are used. A circular polarized excitation was used for pumping. The mean power was held constant at 0.3 mW. In addition, pulsed measurements at quasi-resonant conditions have been performed for direct comparison of the pump schemes. In order to visualize the different photon energies with respect to the different excitonic states as well as the quasi-particle bandgap, the used excitation energies are depicted together with a level scheme in **Figure 45**.

The experimental resulting angle dependence for different detuning's to the A-exciton resonance are shown in **Figure 46** (a-g). As one can see easily the observed dispersion vanishes, if the detuning reaches a critical level (detuning reaching approximately $\Delta E \approx 300$ meV, thus above the quasi-particle band gap and the B-exciton). Furthermore, it can be seen, that the dispersion is significantly suppressed when exciting into higher bound states of the A-exciton (where a weak dispersion is still visible) and its continuum states (where a measurable dispersion is absent). This of course is not surprising as free carriers are not evolving a locking between center-of-mass motion and the emitted photon momentum (cf. Chapter 2.21) (Haug and Koch 2009). It has to be noted, that in the case of pumping above the quasi-particle band gap but below the B-exciton the measurement seems to consist of a curved as well as a flat feature. Here, either the amount of plasma contribution to the emission already reaches a considerable value or that the straight line is originating from an incoherent population fraction of excitons.

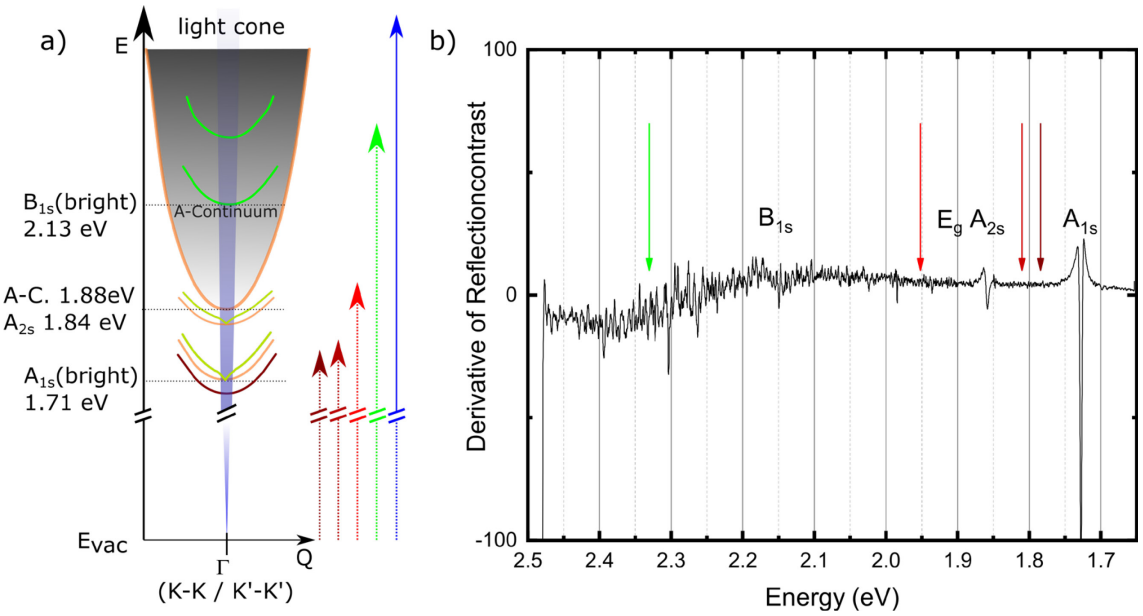

***Figure 45* | Schematic Diagram of the Excitation Conditions for the h-BN Encapsulated Monolayer WSe_2.** (a) The horizontal parabola represent excitonic states (orange for states related to the A-exciton series and green for B-exciton as measured by (M. R. Molas et al. 2019) and calculations by Stefan Koch group) and dark levels are shown in dark red. Horizontal dotted lines mark the lowest energies of the corresponding series. The predicted fine structure is schematically shown by light green lines. (b) Another representation showing the excitation energy (arrows) on top of a line spectrum from an angle integrated Fourier-space spectrum of the reflection contrast derivative.

Nevertheless, if a sufficient percentage of excitons in bound states would form, the occurrence of a measurable dispersion could still be possible. Interestingly, this cannot be observed at non-resonant condition. Most likely, the fraction of coherent excitons is very low in this case. This interpretation is in qualitative agreement with many-body calculation for GaAs quantum wires (Kira and Koch 2006a). There about 80% genuine 1s-excitons are found for resonant pumping at the 1s-resonance, 30% for pumping at the 2s-resonance and only about 2% for off-resonant pumping at the beginning of the continuum. However, as the ratio between exciton binding energies and optical phonon energies are drastically different, it is clear that the role of phonon-assisted polarization and correlations are more important in case of TMDCs than in GaAs.
Another way of explaining it, would be that the excitation induced dephasing is increased at higher detuning, leading to the absence of Rabi-oscillations between the valleys or, if looked from the polaritonic viewpoint, strong coupling to the light field / polarization.

At the same time higher order excitonic features like trions and biexciton as well as phonon sidebands are becoming easily observable (the angle integrated spectra for different detuning's are found in the Appendix A10). It is understood that the phonon sidebands arising from momentum indirect transitions (Brem et al. 2018, 2020) should increase substantially if the excess energy and with this the present phonon population is increased. Furthermore, it is noteworthy that almost no emission from trions and biexcitons can be found for quasi-resonant condition compared to an excitation above the quai-particle band gap, where they are present. This can be understood, as bright biexcitons are always comprised of one exciton resting in K and one in K' (S.-Y. Chen et al. 2018; Alexander Steinhoff et al. 2018) valley. Similarly, for the trion many possible configurations involve both valleys. Hence, the increase of the detuning makes the dephasing into the second valley more likely as well as increases the initial diffusion constant of excitons. Accordingly, with excess pump energy the formation of excitonic complexes becomes more likely.

Further it has to be noted that under pulsed irradiation even under quasi-resonant condition no measurable dispersion is found. This may be attributed to the higher carrier density (initially about 125

times higher than under continuous wave excitation) expected under this pumping scheme that will increase the scattering rate as well as the amount of plasma formed at excitation.

The center peak frequency and its linewidth for different detunings have been extracted by an automatic fitting procedure as done before and are shown in **Figure 46 (g,h)**, respectively. While for the first step, there is nearly no change in the effective mass is observed, both are found around $1 \cdot 10^{-4} m_e$, the effective mass increases to about $7 \cdot 10^{-4}$ m_e if pumped above the quasi-particle band gap, due to a fraction of plasma being present under this condition, which requires additional cooling processes to achieve a exciton population in the 1s-state . This also seem to be visible on the 2D-image, where a straight line from the correlated plasma can be seen on top of the curved line arising from excitonic emission. If the detuning is further increased above the B-exciton, no resolvable curvature (i.e. $m^* > 5 \cdot 10^{-3} m_0$) is found at all.

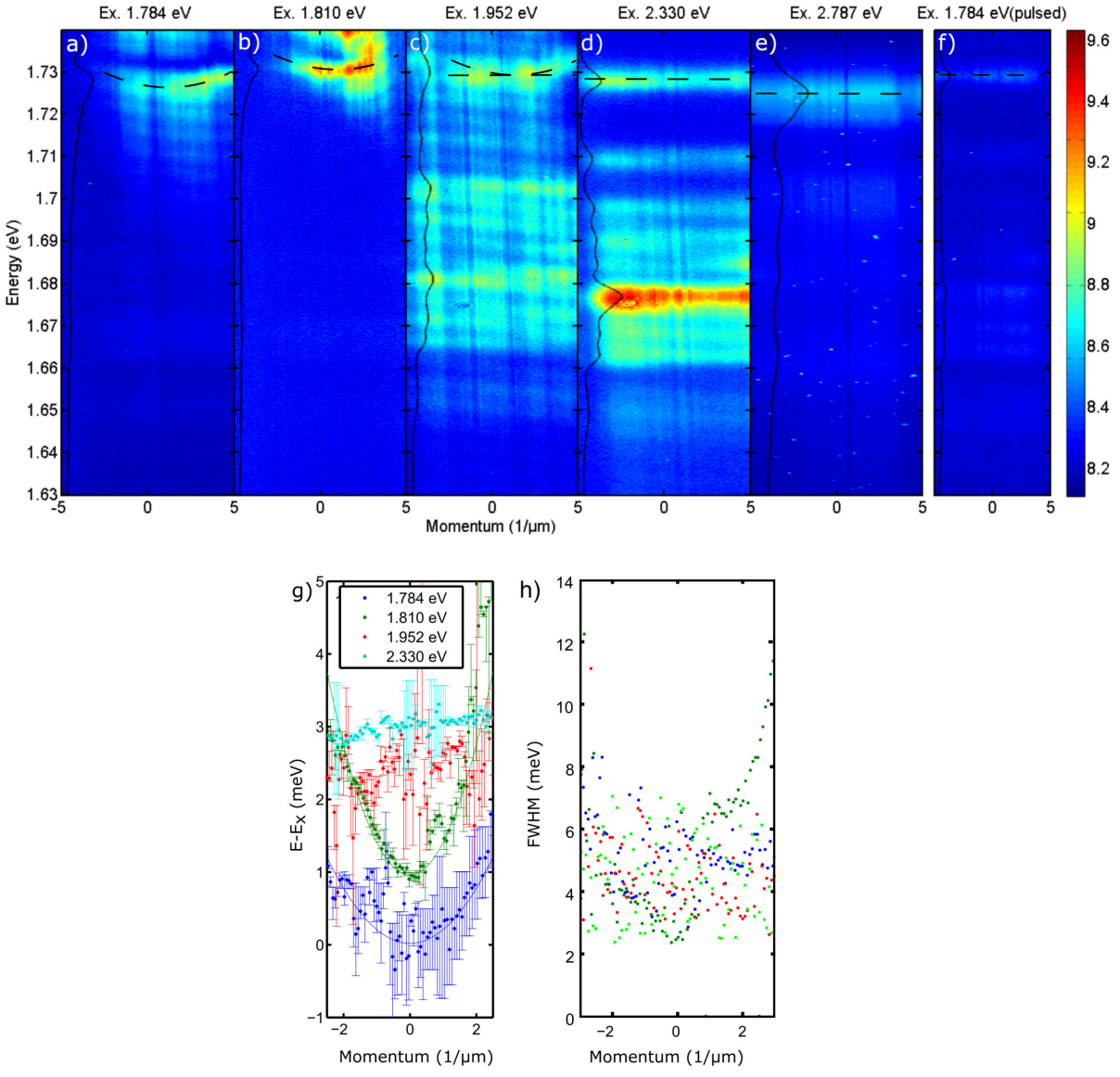

***Figure 46* | 2D- Contour Plots of the Momentum-Dependent Photoluminescence for Different Excitation Conditions at 10K.** (a-e) show the momentum-dependent emission under increasing excitation detuning for continuous wave pumping. (f) show the result for pulsed quasi-resonant pumping as a comparison under the same mean power. The black lines at the side of the contour plots represent an angle integrated spectrum over the shown range. The dashed lines represent a guide to the eye for the observable dispersion. (g) and (h) show the extracted center energy and linewidth from the automatic fitting procedure. The excitation used here is circularly polarized and the total emission is plotted. The errorbars in (g) represent the 1-sigma confidence intervals from the fits. (g) is adapted from (Schneider et al., 2020b) under the Attribution 3.0 Unported (CC BY 3.0) License.

The linewidth shows no systematic relation to the angle or excitation condition. Always a linewidth between 3 and 4 meV is found. This is rather surprising as an increased excitation induced dephasing is often observed with an increased detuning of the laser and thus a bigger linewidth is expected.

6.3 Temperature Dependence

Having analyzed the influence of the detuning at 10 K, the focus will now shift back to the temperature dependence for the smallest and highest detuning. A comparison of the temperature dependent photoluminescence of quasi-resonant and off-resonant excitation is shown in **Figure 47**. The corresponding temperature dependent reflection contrast from a repeated measurement (about 3 months later) is shown in **Figure 48**.

While for the quasi-resonant measurement even at 100 K a clear dispersion is observed (cf. **Figure 47 b**), during the whole temperature series no dispersion can be found at (strongly) off-resonant excitation (cf. **Figure 47 i**). Furthermore, as already noted above, the observed dispersion is vanishing for PL-experiments and decreases significantly in the reflection contrast above 100 K.

This temperature (100K) roughly corresponds to the energy of the optical phonons in WSe_2 (S. Y. Chen et al. 2015) and several theoretical predictions (Brem et al. 2020; Christiansen et al. 2017) and experiments indicate the formation of phonon side bands for the main resonance (for the dark excitons they are observed below that temperature) starting from this particular thermal energy. From the Elliot

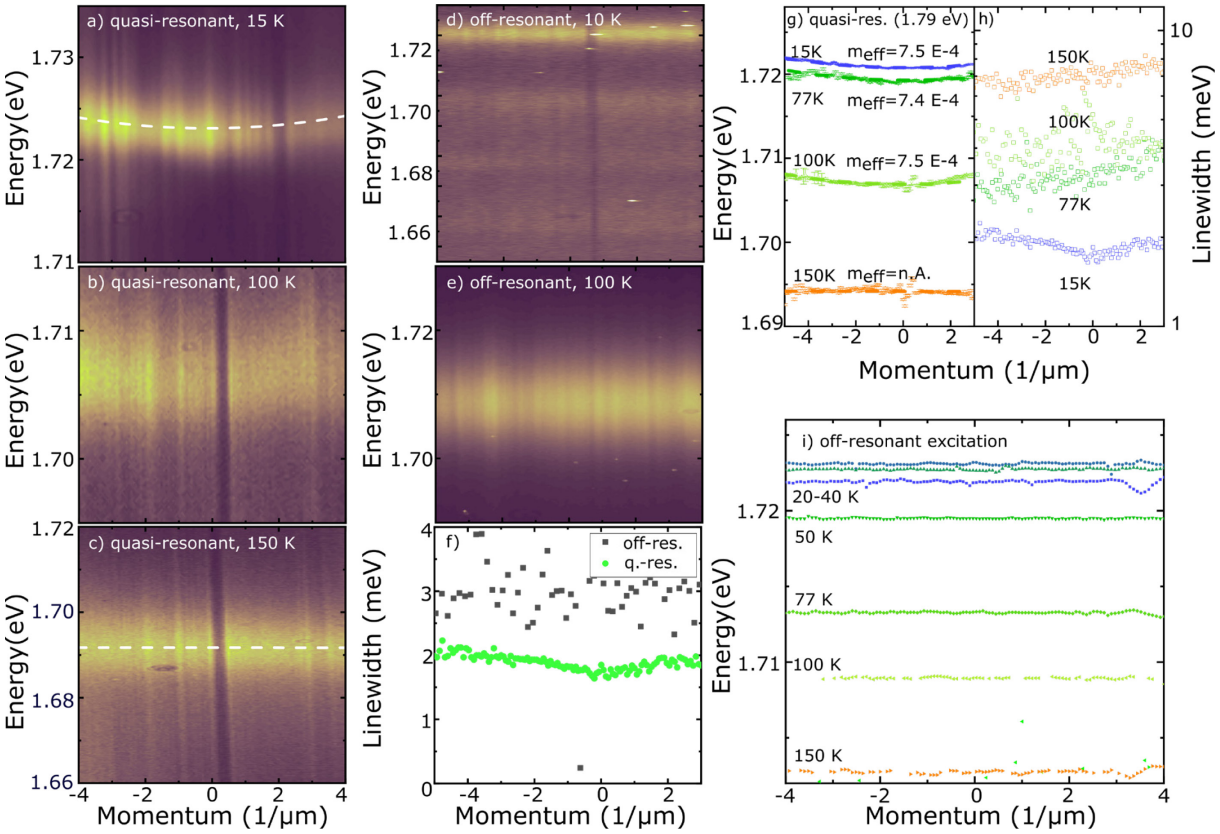

***Figure 47* | Temperature Dependence of the Angle-Dependent Photoluminescence at Quasi-Resonant and Off-Resonant Excitation.** (a, b & c) show exemplary 2D-contour plots for the angle-resolved photoluminescence emission under quasi-resonant condition. (d & e) shows the corresponding angle resolved emission for off-resonant excitation as a false color contour plot. (g & h) show the corresponding extracted peak center and linewidth under quasi-resonant condition at 3.6 kW/cm² and (i) shows the resulting central energy under strongly off-resonant condition at 0.3 kW/cm². (f) shows a comparison of the Gaussian linewidth (σ) for both excitation conditions. Parts have been adapted from (L. M. Schneider, S. S. Esdaille et al. 2020) under the OSA Open Access License.

formula (**Equation 2-12**) it is clear, that the formation of strong phonon sidebands will lift the strict locking between center-of-mass momentum ***Q*** and the photon momentum ***q***. In simple words, the presence of phonon sidebands will smear out the observed photon dispersion, as the sum over all polaron dispersions (Feldtmann, Kira, and Koch 2010) weighted with their occupation factor is measured. Similarly, if looked from the viewpoint of polaritons, the homogenous linewidth is increasing at this point, leading to a weaker coupling between polarization and excitons due to faster dephasing. If the linewidth respectively dephasing is increased enough, the parameter space, where the exciton-polariton formation respectively the splitting between longitudinal and transversal branch in the light cone is possible, is left and only the pure exciton and plasma can be seen.

In the zero-density regime, measured through reflection contrast, lower numbers of the occupation for the phonon modes are expected compared to the pumping with a continuous wave laser. Therefore, it can be understood that even at 150 K a small dispersion is still measured. Similarly, the excitation induced dephasing is smaller in this scenario, so that the formation of exciton-polaritons could be remain observable. Note, while measuring the linear response of a system in general is merely probing the transition probabilities or polarization – an unexcited semiconductor without exciton population still shows excitonic resonances in reflection and transmission –, the PL has a larger contribution of incoherent fractions due to the dynamics involved before recombination.

If one looks at the linewidth at 10K (cf. **Figure 47 f**), a clear trend can be seen towards an increased linewidth observed at higher angles starting from 4 meV close to the intrinsic linewidth of 1.7 meV (Moody et al. 2015). This trend cannot be observed at higher temperatures. The linewidth increases by 0.3 meV, which could be an indication for the predicted k-dependent splitting of the upper and lower branch of the exciton fine structure arising from long-range exchange interaction, here possibly measured as a superposition of both branches.

In order to take a closer look, the line shape of the photoluminescence was analyzed in more detail. therefore, the 1st PL derivative with respect to energy at normal incidence as well as high incident angles has been scrutinized (cf. **Figure 49**). For the higher incident angles, one observes a change in

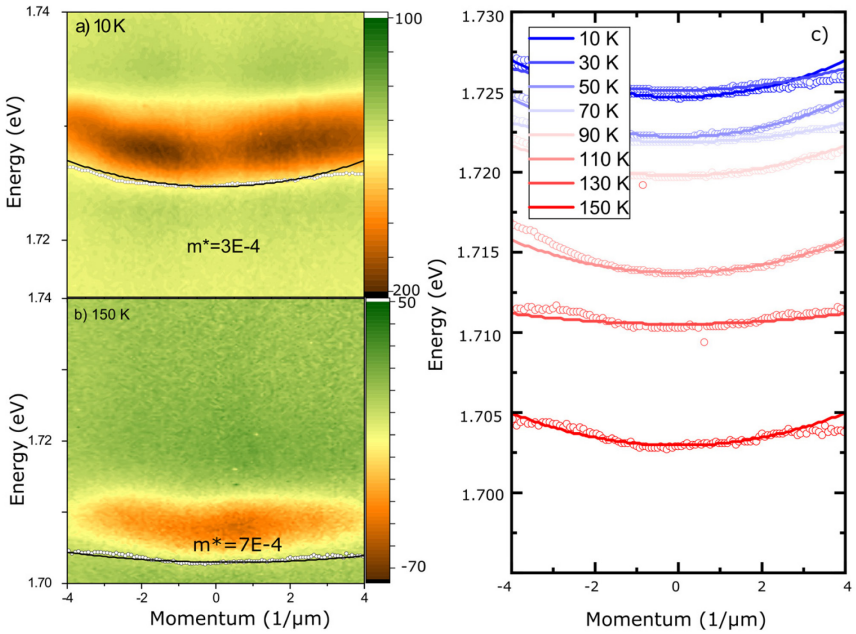

Figure 48 **| Temperature Dependence of the Angle-Resolved Reflection Contrast Derivative.** (a & b) Fourier-space spectra of the derivative of the measured reflection contrast at 10 K and 150 K, respectively, as function of the in-plane momentum. (c) shows the extracted dispersion. The graph has been adapted from (L. M. Schneider, S. S. Esdaille et al. 2020) under the OSA Open Access License.

the line shape, that cannot be nicely modelled with a single Lorentzian, compared to normal incidence where this is possible. If modelled with two Lorentzian a nice agreement can be found. The splitting for both positive and negative angles is found to be 1.9 meV, although different amplitudes for both resonances have to be assumed in the fitting. This splitting measured here for the encapsulated WSe_2 monolayer is bigger than the predicted one by exchange interaction for MoS_2. Nevertheless, this is not surprising as also the splitting between bright and dark exciton states arising from the short range part of the exchange term (Qiu, Cao, and Louie 2015) is bigger for tungsten-based monolayers as well.

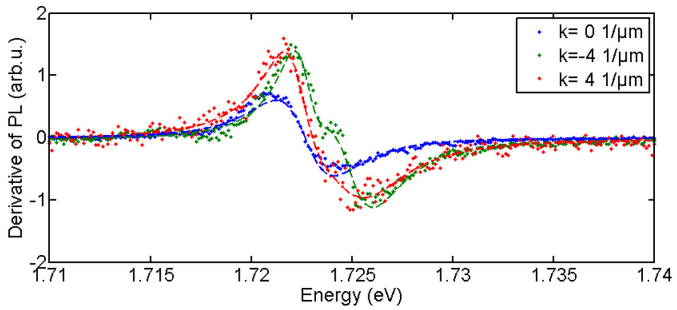

Figure 49 **| Line Shape Analysis of Photoluminescence for Different Emission Angles.** The graph shows the derivative of PL at normal incidence (blue dots) as well as the edge of the possible detection cone (red/green dots). The straight lines correspond to the fitting of the sum of two Lorentzian for high emission angles and a single one for normal incidence. The data is extracted from the quasi-resonant measurement shown in ***Figure 47*** at 15 K.

6.4 Power Dependence

After having discussed the temperature dependence in detail, we will now turn to the power dependence for quasi-resonant excitation. The extracted central energy and linewidth is shown together with exemplary 2D-contour plots of the raw data in **Figure 50**. To estimate the carrier-density from the excitation power densities applied, a simple rate equation model was used. From the chosen power and the photon energy, a photon flux *F* was calculated. It was then multiplied by the absorption α of an encapsulated ML as predicted by (Gerber and Marie 2018) to calculate a creation rate of excited carriers. This prediction does not include the experimentally observed phonon assisted absorption (Chow et al. 2017). One the other hand a mean exciton decay time τ of 10 ps, as determined by TRPL measurements was assumed.

Equation 6-2 **| Rate equation for estimating the charge carrier concentration**

$$\frac{\partial n}{\partial t} = F \cdot \alpha - \frac{n}{\tau}$$

From the numerical solution of such simple rate equation, a steady state carrier density of $n = 3 \cdot 10^8 cm^{-2} - 1 \cdot 10^{10} cm^{-2}$ can be calculated for the lowest and highest power used. Both are in the linear regime and excitation induced dephasing or non-linear effects (starting to be important at an approximate density of n = $10^{12} cm^{-2}$) are not expected to play a major role here (Chernikov, Ruppert, et al. 2015; Moody et al. 2015; L. M. Schneider, Lippert, et al. 2018).

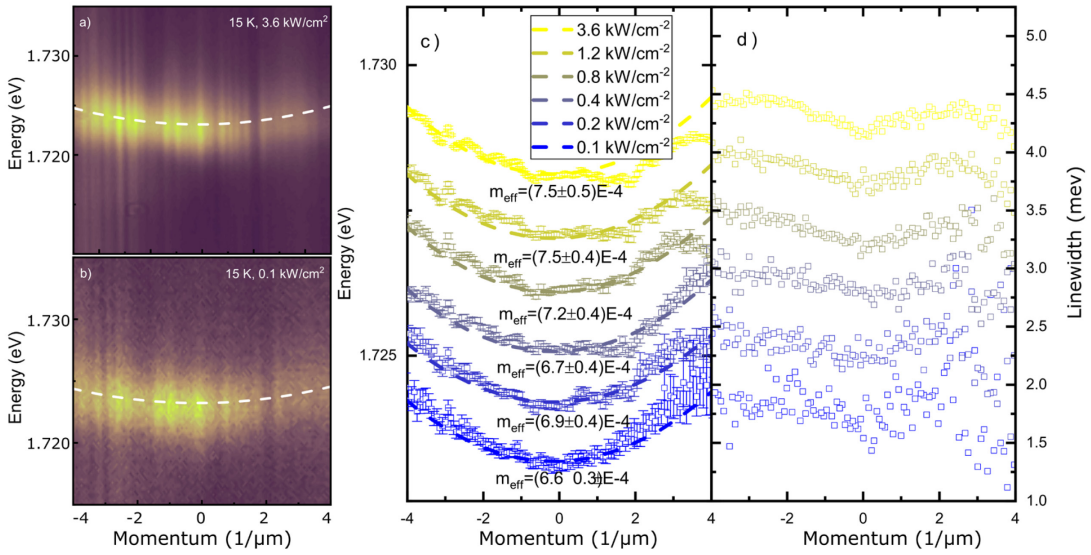

***Figure 50* | Pump Density Dependent Angle-Resolved Measurements for Quasi-Resonant Excitation.** Fourier-space spectra at the lowest investigated power (a) as well as the highest one (b). (c) shows the extracted central energy as a function of the momentum and (d) the related linewidth. The dispersion curves and the gaussian linewidth data have a constant offset of 1.0 meV and 0.5 meV, respectively, for clarity. The graph has been adapted from (L. M. Schneider, S. S. Esdaille et al. 2020) under the OSA Open Access License.

One can clearly observe a curvature over the one and a half orders of magnitude investigated in this power series. If the dispersion is analyzed carefully by fitting a quadratic fit to the data, a small increase of the effective mass with excitation density can be observed. From the Elliot formula (**Equation 2-12**) it is clear, that not only excitons, but also plasma is radiating at the energetic position of the exciton resonance. Similar observations are typical for semiconductors and have been observed before (Chatterjee et al. 2004; Galbraith et al. 2005; Koch et al. 2006). In this mechanism where the correlated plasma radiates from the exciton resonance, that is favored, caused by its high transition dipole moment, the excess energy is given to the rest of the plasma to fulfill energy conservation. The mechanism therefor is only understandable in the many-body picture and would neither occur in the single nor the two-particle picture.

The presence of plasma in ML systems could be proven during the studies of this PhD thesis as the wavelength dependent time resolved dynamics (data not shown see puplication) follow the usual behavior of a hot plasma (Lorenz Maximilian Schneider, Kuhnert, et al. 2018) similar to observations in GaN. However, as the emission angle for plasma is not dependent on the absolute momentum of the hole and the electron, but only on their difference, the sum involved calculating the emission under one specific center-of-mass momentum will have contributions from all single particle momenta. I.e. it will run over all possible energies and no curvature is expected statistically for the ensemble of uncorrelated charge carriers. Effectively, if the fraction of uncorrelated carriers is increasing, one is expecting a flatter dispersion formed by the superposition of the excitonic and plasma dispersion. This could explain the reduced curvature at higher pump powers and the absence of measurable dispersion for strongly off-resonant pumping.

For the off-resonant pumping scenario the laser energy is almost resonant to the C-exciton peak. As discussed in Chapter (2.5.4 Excitonic Properties), the single particle states contributing to this peak are not found directly at the ***K***-point but in the vicinity of the Γ- and ***K***-point. As we continuously inject into these states at CW-pumping, it is understood that many of the charge carriers radiating at the A-exciton resonance will not be correlated but in contrast initially a hot plasma (Ruppert et al. 2017) is expected at large detuning. This hot plasma is cooling in the first few ps (Ruppert et al. 2017).

Clearly, also the linewidth is increasing as a function of the center-of-mass momentum for all powers investigated. This could be either a sign of a splitting of the resonance with higher angles or a faster decay of the population from these states.

6.5 Higher Order Excitonic States

To check the dispersion for higher resonances the energy range of the reflection contrast measurement was increased up to 2.480 eV in order to also include the A-2s and B exciton peak. The results together with an angle integrated spectrum are shown in **Figure 51**. The resonances found are in agreement with theoretical predictions for encapsulated WSe_2 (Gerber and Marie 2018b) and close to the prediction by our theory group based on DFT and the gap equations (cf. **Figure 53**, the computations follows the same rules then described in the first part of chapter 5. For further details see (Lars Meckbach, Stroucken, and Koch 2018a)). A close-up view on to the 2s-resonance is also shown. While almost no curvature is visible at first sight, the automatic fitting procedure indeed extracts a small but measurable curvature. The extracted effective mass is 9.5 $10^{-4}\, m_e$, about one order smaller than the one obtained for the 1s-resonance. While the B-exciton resonance is clearly observed, no significant curvature is present or can be extracted caused by the significantly broader linewidth.

The observed decrease in curvature for the 2s-resonance dispersion is in line with predictions from many-body theory (Deilmann and Thygesen 2019; Qiu, Cao, and Louie 2015). However, for the B-exciton a strong dispersion similar to the A-exciton should be also observed (F. Wu, Qu, and MacDonald 2015) from a theoretical point of view. However, caused by the big linewidth observed in the experiment a large dephasing rate can be expected. This makes it hard to experimentally observe small shifts on the one side, on the other side if looked from the viewpoint of polaritons this will hinder polaritonic effects as a weakened coupling to the light field will occur. As the measurements for the 2s-resonance shows only a very subtle feature, they should be repeated on several samples to confirm their existence and allow a statistically significant extraction.

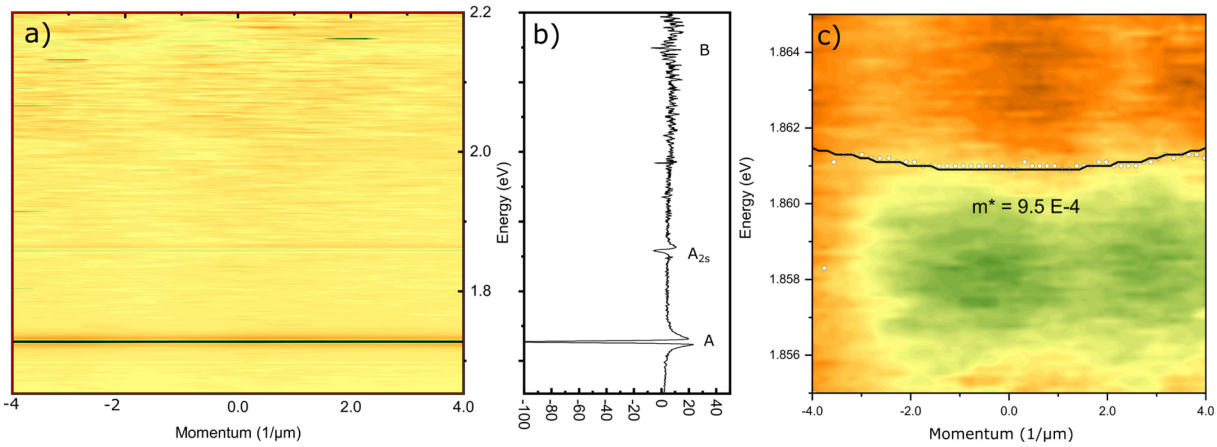

***Figure 51* | Overview over the Fourier Space Spectrum in an Extended Energy Range.** (a) shows a false-color contour plot of the whole angle-resolved data, with the pronounced visible feature representing the A-1s resonance. (b) angle-integrated reflection contrast spectrum, also showing the A-2s and B resonance. (c) shows a zoom in of the contour plot to the A-2s resonance.

6.6 Origins of the Dispersion

Having shown the experimental dispersion, which is at first sight surprisingly strong, the three different mechanisms, which could lead to these interestingly small effective masses, will be discussed: firstly splitting by (long-range) electron-hole exchange interaction, secondly the formation of exciton-polaritons caused by the strong oscillator strength observed for TMDCs. As a third possibility the

influence of propagation effects in the multilayer structure will be discussed. Although the first two models are related, the phenomenon will be discussed form both very different viewpoints.

6.6.1 Exchange-Interaction

While in the literature there is no calculation available for the effect of the long-range exchange interaction (Andreani and Bassani 1990) on the exciton dispersion for an encapsulated WSe_2 monolayer, several ones can be found for suspended MoS_2. However, currently the effects are still under debate as the predictions vary from strong interaction giving rise to Dirac cones and Dirac saddle points (H. Yu et al. 2014), to other findings suggesting an upper, non-analytic, nearly linear exciton dispersion branch together with a lower parabolic one (Glazov et al. 2014; Qiu, Cao, and Louie 2015; F. Wu, Qu, and MacDonald 2015), whereas even others argue that the exchange interaction is negligible (Sommer 2017) for small momenta or just a splitting into two parabolic branches with increased slope could be expected (Deilmann and Thygesen 2019). Nevertheless, most of these theory groups agree that the long-range interaction has to be considered, however, the strength of the coupling and therefore the exact magnitude and functional relation of the dispersion and its splitting into branches remain unclear.

(H. Yu et al. 2014), (Qiu, Cao, and Louie 2015) and (F. Wu, Qu, and MacDonald 2015) all predict a splitting of the degenerate excitonic states in suspended MoS_2 at the light cone border in the order of 1-2 meV, roughly a factor of two smaller than our observation for WSe_2. For WSe_2 or generally tungsten based materials a steeper slope can be expected than for molybdenum based ones (Deilmann and Thygesen 2019). This is also clear from the larger exciton binding energy compared to MoS_2, that indicates a stronger Coulomb interaction. However, the prediction of Deilmann et al. has to be handled with care, as the Coulomb interaction was still treated in a 3D manner ($V \propto 1/Q^2$) (Deilmann and Thygesen 2019) instead of a real 2D interaction ($V \propto 1/Q$) (Cudazzo, Tokatly, and Rubio 2011). Of course, as we deal with an encapsulated not with a suspended monolayer the reality of the truncation of the Coulomb interaction/screening will be found in between these two approaches (Molas et al. 2019). Nonetheless, the permittivity contrast to the surrounding is substantial such as the screening of the layer contributes a considerable share. For the 1s-wavefunction, which is still almost confined to the monolayer, the Rydberg series is still described by a nearly logarithmic potential in contrast to the regular Coulomb potential. Nonetheless, small deviation from the 2D treatment should already occur due to the h-BN encapsulation. For higher order states however a 3D treatment is probably valid. Thus, it has to be concluded that the encapsulation and its material will strongly affect the screening and thereby the functional relation.

While the absolute amount of dispersion predicted within the light cone matches on the order of magnitude to the observed one, most measurements appears to show parabolic dispersion rather than originating from the predicted linear slope. Here sample 3 is an exception (cf. **Figure 44**) as it looks almost linear. The color differences of the samples indicate different thicknesses of the h-BN encapsulation which potentially changes the screening and therefore the exact dispersion shape. Unfortunately, AFM data is only available for one sample, making a quantitative discussion of h-BN thicknesses impossible. Nonetheless for the direct Coulomb term the influence asymptotically saturates at about 3 nm or 10 layers (Gerber and Marie 2018b). Most likely the long-range effect will see the influence of even thicker layers, as the electric field lines then will penetrate deeper into the h-BN.

Although the prediction are made for MoS_2 the calculated branches where projected onto the measurement data (cf. **Figure 52**). Hereby, an offset was applied to match the exciton energy, while the slopes have been not changed. It still matches to a certain extend. Also as shown in **Figure 49**, the spectral shape at high angles compared to low angles indicates a possible underlying splitting of the

resonance, that would also agree with the two-branch explanation (be it linear plus parabolic or merely parabolic). It shows the 1st derivative of the PL-data for quasi-resonant excitation at 10 K with respect to energy. While for large negative angles a clear signature of a second feature can be seen, only a small change of the slope is found at the same emission energy under a large positive angle. The emission under normal incidence, however, can be nicely fitted by only using one Lorentzian. While this analysis provides a hint that a splitting could indeed be present, it is not completely unambiguous (as the magnitude of the features is not completely symmetric in angle), as spatial inhomogeneities could also lead to such observation.

Nonetheless, the parabolic appearance (a comparison of the measurement with a predicted linear slope can be seen in ***Figure 52***) of most of the measurements suggests, that also other effects are present here or that the encapsulation changes the interactions already qualitatively. The graph shows a comparison the prediction with second derivative, too. Here a splitting seems to be observed, however the slope of the MoS_2 prediction is too low to describe the data. If the two minima clearly observed at high negative momentum but only hardly visible at large positive angles, indeed indicate the splitting roughly twice the slope compared to the prediction of MoS_2 would be necessary to describe the data.

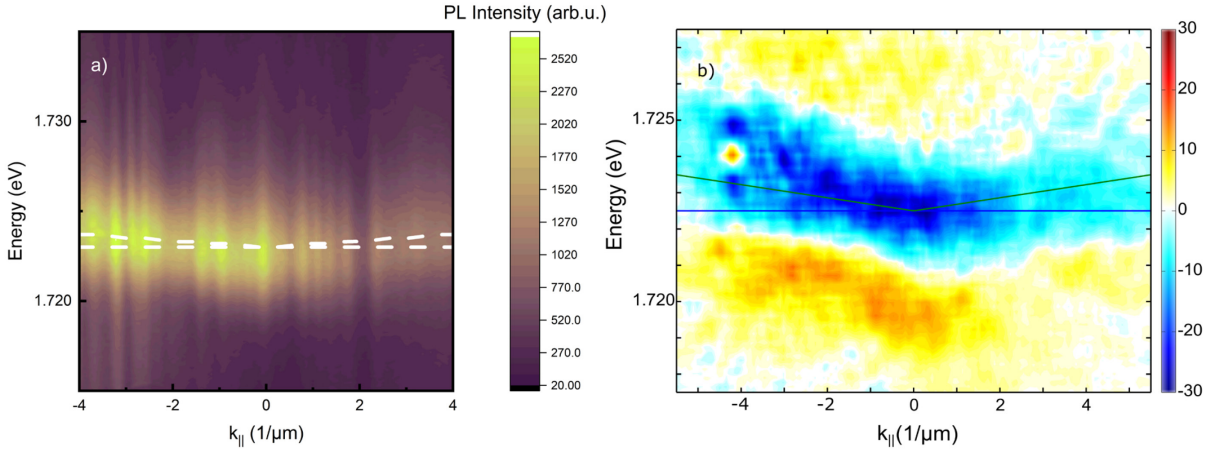

Figure 52 **| Qualitative Comparison of the Prediction with the Observed Dispersion.** (a) The graph shows the measured dispersion at 10 K with the prediction by Qiu et al. for MoS_2 projected onto the contour plot as an overlay in whited dashed lines representing two branches. The prediction has been shifted by a constant energy to enable comparison with WSe_2. (b) the graph shows the same data but this time as the second derivative. (a) has been adapted from (L. M. Schneider, S. S. Esdaille et al. 2020) under the OSA Open Access License.

6.6.2 Exciton-Polariton

In the next step the observation shall be discussed from the viewpoint of (quantum-well) exciton-polaritons formation (Khurgin 2015). To do so, the gap equations were solved by the group of Stefan W. Koch using input from DFT calculations. From this calculation the in-plane complex permittivity of a WSe_2 monolayer could be derived, where the decreased screening due to h-BN encapsulation has been already considered in the electrostatic model of the gap equations. If not states otherwise a homogenous linewidth of 2 meV and Gaussian inhomogeneous broadening of 5 meV has been used for this calculation - values close to the experimental values (cf. **Figure 42**). In the next step, the classical (bulk) polariton equation was used (Klingshirn 2012) to calculate a possible polariton equation.

Equation 6-3 **| Relation between permittivity and dispersion for polaritons in a bulk crystal**

$$Re\{k\} = \frac{Re\left(\sqrt{\epsilon}\right)\omega}{c}, Im\{k\} = \frac{Im\left(\sqrt{\epsilon}\right)\omega}{c}$$

In addition, the Fresnel equation for uniaxial materials (Lekner 1991) were used to calculate the angle dependent and angle integrated reflection for unpolarized light (cf. **Figure 53**). For the out of plane permittivity ($\epsilon_z = 7.5$) the values from (Laturia, Van de Put, and Vandenberghe 2018) were used. Such a calculation does explicitly neither consider effects caused by interference within this multilayer structure nor that the polarization, to which the polariton couples to will also extend into the surrounding h-BN flakes, especially for higher excitonic states. Furthermore, the bulk equation is, of course, not considering the confinement effects relevant for quantum-well exciton polaritons related to a strictly 2D treatment of the Coulomb interaction. Nonetheless, the advantage of the model is that modifications of the dephasing rate, homogenous as well as inhomogeneous broadening and different screenings can be (easily) integrated on a phenomenological level and allows to discuss their qualitative influence.

If one compares the angle-integrated derivative of the reflection contrast (cf. **Figure 53 a**) with the calculated derivative of the reflectivity, the overall shape looks similar, although the predicted peaks are not exactly at the right positions. As the reflectivity of the underlying substrates is nearly flat in region, where there are no Fabry-Pérot resonances, the position of the peaks in reflection contrast are almost not shifted compared to the calculated reflectivity. However, the energetic differences are only about 10 meV. The most striking differences is that the higher excited states as well as the B-exciton are shallower in the experiment. This could be due to small differences in parameters or the partly neglected influence of h-BN in the calculations. If instead of a constant linewidth for all resonances, larger homogenous linewidths are assumed for the exited states, a better agreement can in general be reached (cf. **Figure A 14**). Nonetheless, this calculation enables the clear identification of the observed features and provides useful insight to the expected phenomena on a qualitative level.

Both the calculated dispersion relation and the calculated reflectivity clearly show a dispersion. The calculation of the reflectivity also shows a dispersion for the 2s-resonance and the B-exciton. However, they are hard to resolve due to their small magnitude respectively the broad spectral feature. The amount of energy-shift due to dispersion from such an angle-resolved reflectivity calculation is about 1 meV for the A-1s exciton within the light cone, a magnitude comparable to the experiment. Nonetheless, one has to note that the assumption of using the bulk formula is a strong approximation such that only the order of magnitude but not the actual number can be compared quantitatively.

If one takes a close look the experimental data, a small signature can be found at 1.7 eV. If one follows the argument of (Deilmann and Thygesen 2019), that for an encapsulated flake on substrate the Coulomb interaction cannot be handled strictly 2D in contrast to a suspended flake, a small longitudinal-transversal splitting could maybe present for normal incidence like in bulk polaritons. In this case, the main peak could be identified with the upper polariton branch (longitudinal) and the small signature at 1.7 eV with the lower polariton branch (transversal) similar to the (bulk) model. Nonetheless, the total optical thickness including the h-BN is still smaller than the wavelength and longitudinal and transversal excitation cannot be distinguished by symmetry at normal incidence. Thus, this assignment as lower branch is unlikely to be true, especially as the energetic position of the small signature at 1.7 eV is very close to the position of the dark exciton (1.686 eV) and optical sidebands of the neutral exciton (1.696). As a broad redshifted feature is observed in PL at this energetic position (cf. **Figure 53** a) and is also found a zero angle, the feature at 1.7 eV is most likely phonon assisted emission respectively absorption.

Both the reflection as well as the PL have the common shape found in textbooks for polariton formation in bulk crystals. Thus, a full many-body calculation including the screening and polarization in the h-BN encapsulation and the substrate is needed to answer, which interpretation is indeed valid.

To get an estimate of the effect, that the exciton polariton is also coupling to the polarization induced in the surrounding h-BN, a simple effective medium theory model was employed. It accounts for the volume fraction of the monolayer and h-BN within the Bohr radius and is used to calculate a new effective permittivity by linear combination with this factor. As the comparison between **Figure 53** (d) without including the response of h-BN and (c) from the effective medium theory and the comparison of both dispersion relations (cf. solid and dashed lines in **Figure 53** b) shows that including also the response of the surrounding is influences the energetics and the shape of the main feature. In short, the interaction gets weaker; thus, the main peak is shifted red and the dispersion is slightly weaker. Nonetheless in both cases a curvature of the reflection contrast derivative is predicted. Both calculations were performed assuming 5 meV Gaussian broadening and 2 meV Lorentzian broadening. While such a model can be used to include the h-BN, the model result is strongly depending on the radius considered. Here the approximate Bohr-radius of 1.3 nm was used. While this choice seems natural, also other scales could be used. Indeed, using a convolution of the possible radii with their probability would lead to a better description. As such, the quantitative response should be handled with care. In addition, also a van der Waals gap between the monolayer an the encapsulant (filled with vacuum) could be included, that would further influence the result. As the inclusion of h-BN gives results closer to the experiment, it's likely that response has to be considered more than just including the increased screening already included in the gap equations/DFT. For quantitatively correct results, the h-BN has to be included in the DFT similar to (Gerber and Marie 2018a).

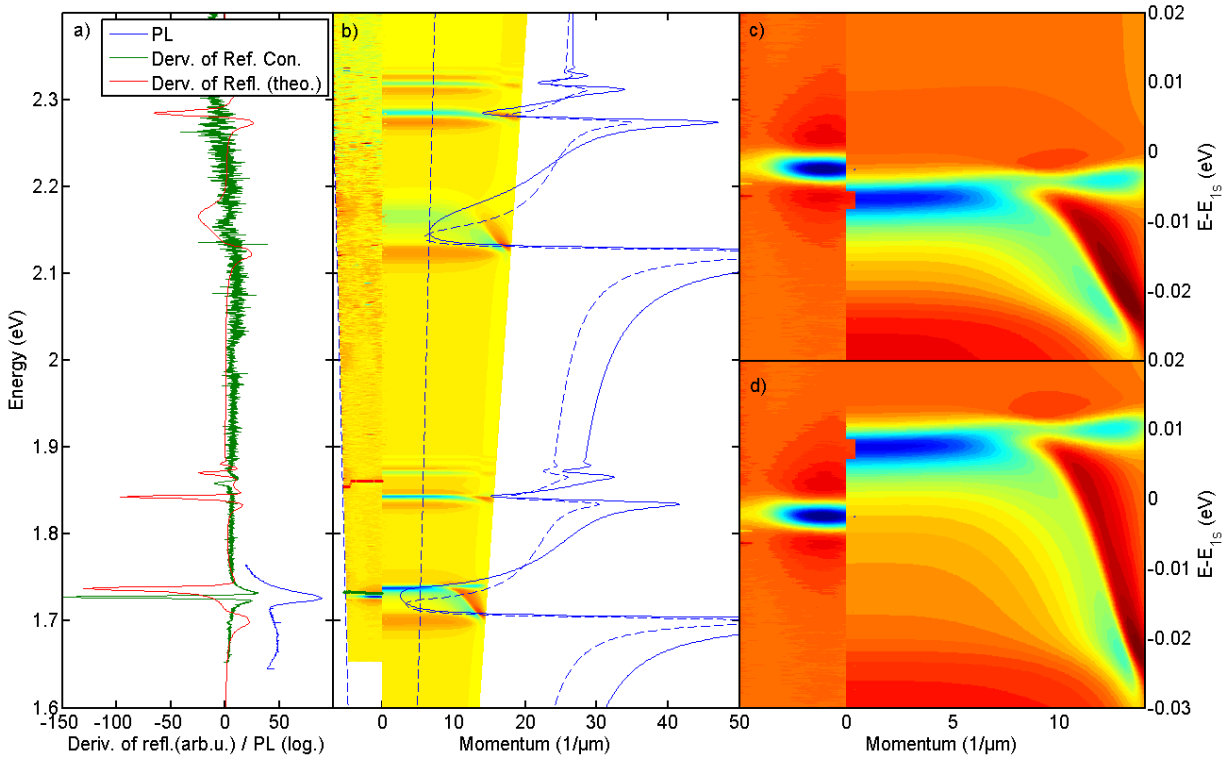

Figure 53 **| Comparison of Exciton-Polariton Model with the Experimental Data.** (a) Experimental derivative of the reflection contrast (green) compared to the calculated derivative of reflectivity neglecting the multilayer structure (red) close to normal incidence. The PL is shown in blue as a complimentary information. (b) Comparison of the derivative of the angle-resolved reflection contrast from the measurement with the calculated reflectivity from the model dielectric function. The blue straight (dashed) line corresponds to the calculated dispersion exciton-polariton dispersion without (with) using the phenomenological effective medium theory. Zoom in to the A-1s exciton for the bare model (d) and (c) for the case an effective medium theory approach was used.

In a next step, the temperature dependence was modelled using a simple model. Therefore, the permittivity was modelled by a Lorentz model. As oscillator strength 1.57 eV^2 was used, as it resembles the dispersion found in experiment. This value is slightly smaller (18%), than the one stated by (Yilei Li, Chernikov, et al. 2014b) (1.9 eV^2). This is expected as the encapsulation decreases the oscillator strength by roughly 20% (Gerber and Marie 2018a). To include a temperature dependence, the dephasing was modelled using the common phenomenological equations (Moody et al. 2015; Selig et al. 2016a) with a linear contribution (60 µeV/K) for Γ-point phonons (value taken from the experimental data of Moody et al.) and exponential term for the phonons at other points as well as optical phonons taken from theoretical predictions (Selig et al. 2016b). Then afterwards again the derivative of the reflectivity was calculated (cf. **Figure 54 a**).

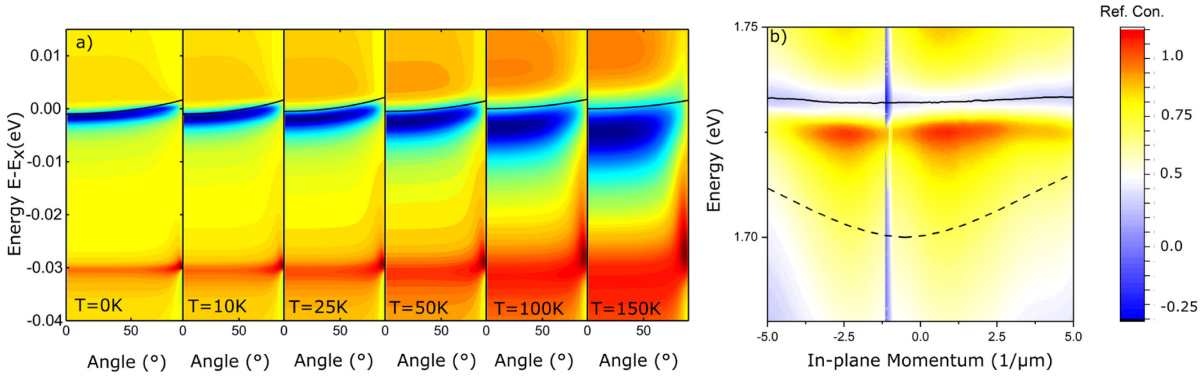

***Figure 54* | Model Comparison for Temperature Dependence of Dispersion and Mixed Modes.** (a) Calculated temperature dependence of the derivative of reflectivity, if the shift of the resonance is ignored and just the change in dephasing rate is considered in the model. The used dephasing rates resulting from the phenomenological treatment (Moody et al. 2015; Selig et al. 2016a) are 1.6 meV, 2.2 meV, 3.1 meV, 4.7 meV, 8.3 meV and 12.4 meV. The lines are parabolic dispersion fits to the calculated reflectivity. (b) Measured reflection contrast of the WSe_2 sample. The straight line is the extracted position of the longitudinal exciton branch and the dashed line is the end of the high reflectivity band as calculated by the mixed mode polariton model (Hesse et al. 1976).

In the case of the homogenous linewidth a strong dispersion curvature in calculated reflectivity's is found. In addition, the flattening of the curvature can be obtained at dephasing rates that correspond to higher temperatures, that are γ=1.6 meV, 2.2 meV, 3.1 meV, 4.7 meV, 8.3 meV and 12.4 meV for *T*= 0K, 10 K, 25 K, 50 K, 100 K and 150 K, respectively. When comparing the result with parabolic dispersions (see **Figure 54a**) one sees that the effective mass approximately drops from 3e-3m_e at 10 K to 5e-3m_e at 150 K. This simple model shows that, even if the interaction with phonons are only included at this phenomenological level, the decrease of the measurable dispersion can be explained. Similarly, if the excitation induced dephasing is modelled as measured by (Moody et al. 2015), a decrease in curvature with carrier density can also be explained. However, also the oscillator strength is changing with temperature (Arora et al. 2019), which should be taken into account.

Up to this point, the anisotropy was only considered in the reflection, but not in the dispersion relation. While the current treatment is correct for the case of normal incidence, in an uniaxial crystal present in the experiment, mixed modes arise between the longitudinal and transversal branch (Fröhlich, Reimann, and Koidl 1982; Hesse et al. 1976) in case of bulk crystals. In case of mixed modes, one can find a band of high reflectivity between the longitudinal and transversal. While this band always has the same high energy cut-off namely the longitudinal branch, the size of the band of high reflectivity is changing. The lower cut-off can be calculated according to the following formula in case of an uniaxial crystal (Hesse et al. 1976).

***Equation 6-4* | Cut off frequency for mixed mode polaritons in an uniaxial bulk crystal**

$$\Omega^2 = \frac{1}{\epsilon_{\parallel}(\infty)\sin^2(\alpha) + \epsilon_{\perp}\cos^2(\alpha)}\left(\epsilon_{\parallel}(\infty)\omega_t^2\sin^2(\alpha) + \epsilon_{\perp}\,\omega_l^2\cos^2(\alpha)\right)$$

The lower limit has been calculated and can be seen in **Figure 54 b** in comparison with the experimental reflection contrast. The results reasonably describe the lower end of the observed high reflectivity band. This is another hint, that the argument of (Deilmann and Thygesen 2019) in favour of a 3D treatment of the Coulomb interaction could be indeed valid.

6.6.3 Influence of Confinement Effects or Light Guiding

Generally, in a multilayer structure like the stack investigated in the experiment confinement effects caused by Fabry-Pérot modes (out of plane) or existing waveguide modes (in-plane) can in principle assist the formation of exciton-polaritons. Thus, both effects were investigated. While at first sight, there seem to be no reasonable cavity, also the weak Fabry-Pérot effects from the multilayer structure especially from the SiO_2 layer could modulate the optical density of states. To investigate the influence of the multilayer structure, electromagnetic simulations have been performed for the bare as well as h-BN covered substrate with and without the WSe_2 monolayer. Without the monolayer only very weak modulation can be found in the simulated reflection spectrum. Nevertheless, there are no signatures of Fabry-Pérot resonances found in the experimental reflection of the substrate or the sample.

In order to search for cavity effects, the cavity with and without WSe_2 was simulated. No confined modes are found between 670 nm and 790nm, i.e. between -128 meV negative detuning and 152 meV positive detuning with respect to the exciton resonance no modes exist. From a simple calculation the out-of-plane confinement mode wavelengths, where the Fabry-Pérot modes are located, can be estimated. From the used SiO_2 thickness of 285 nm one calculates the fundamental and first mode to be at 878 nm and 439 nm. If one includes the h-BN as well, one can estimate 1006 nm and 503 nm. All of these estimates are very strongly detuned. All in all, it can be said, that cavity modes can be neglected as a source of the observed features as confinement will be low and the detuning pretty high.

In addition, simulations for the in-plane guiding of incoming TE and TM waves have been performed using the finite integration solver of CST microwave studio. One can see that a weakly confined mode centered at the monolayer indeed exists but extends over the entire stack including the h-BN. Nonetheless, this mode leaks considerably in a mode provided by the SiO_2-layer. After about 400 nm of travelling the field is almost completely transferred to the substrate mode. While such a weakly confined, leaky mode helps the formation of exciton-polaritons in plane, as reabsorption is assisted, it is unlikely to be the source of such strong dispersion. In contrast for the TM-mode mostly a phase jump, but no guided mode is found. Thus, in conclusion the splitting and the dispersion is very likely coming from long-range exchange interaction.

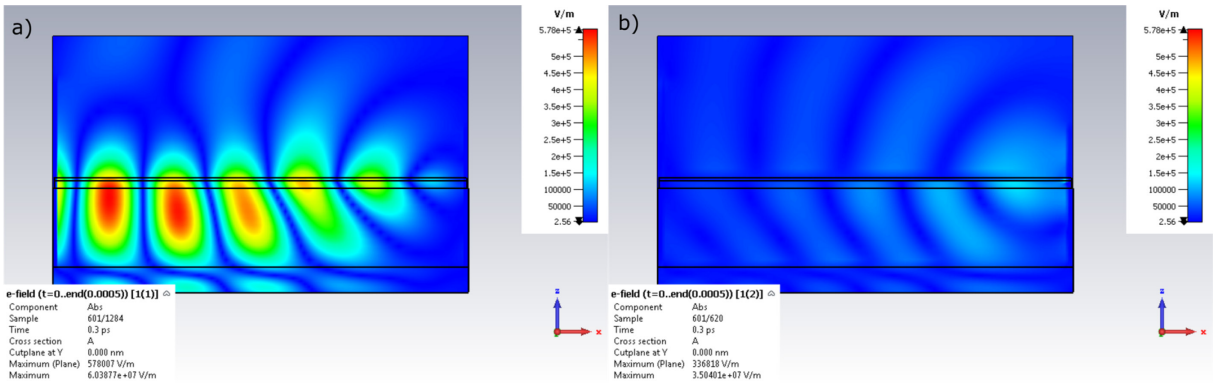

Figure 55 **|Snapshot of the laterally-guided Electric Field profile for the TE and TM Mode.** The wave is travelling from the right to the left. The dimension of the stack along x-direction is 1.6 µm. The simulated flake has dimension of 0.8 x 1.6 µm (in z- and x-direction, respectively). The results after 0.3 ps (200 fs after the source turned off) are shown for incoming TE-(a) and TM-waves (b).

6.7 Valley Physics Analyzed by Angle Resolved Spectroscopy

As in the previous sections a strong dispersion has been presented, that can be either explained from the viewpoint of polaritonic effects or hybridization of the excitonic states, this chapter will focus on its dependence on polarization. Both considered mechanism respectively viewpoints predict to lead to a locking of center-of-mass momentum with the valley-pseudo spin (Qiu, Cao, and Louie 2015; Z. Sun et al. 2017; H. Yu et al. 2014). In the following this statement shall be explained from these different viewpoints.

If discussed from a semiclassical macroscopic viewpoint, the excitation with linear polarized light corresponds to excitation of a certain coherent linear superposition of excitons resting in the K and K' valley, which itself couple to circularly polarized light. The different coupling of the linear superpositions to the radiative field give rise to the different energetic branches (polariton modes) discussed in the previous sections, i.e. for a defined plane of incidence, the energy is coupled to the direction of the pseudo-spin. As polaritons with a different magnitude of center-of-mass momentum have different fractions of excitonic and photonic component, i.e. different dephasing times, a change in linear and circular polarization with center-of-mass momentum can be expected. For example in the vicinity of the exciton resonance, where the excitonic content is still sufficiently high (Dufferwiel et al. 2017; Z. Sun et al. 2017) the spin-valley locking can be preserved.

In contrast, if discussed from a microscopical view, i.e. long-range exchange interactions are considered quantum mechanically, new excitonic eigenstates are formed as coherent superpositions with a more complex pseudospin texture and associated different selection rules (Glazov et al. 2014; Qiu, Cao, and Louie 2015; F. Wu, Qu, and MacDonald 2015; H. Yu et al. 2014). The upper branch couples to the longitudinal part (with respect to the in-plane momentum) of the in-plane projection of the incoming electromagnetic wave, while the lower one couples to the transversal part of the projection. In this treatment the splitting between both branches is understood as a Rabi-oscillation between both spin-valley locked valleys (H. Yu et al. 2014), i.e. an oscillating energy transfer between both valleys within a hybridization of the states. As no splitting is predicted at the quasi-particle's Γ-point, no energy transfer is predicted for vanishing momentum. Similarly, the increased splitting at higher momentum reflects a stronger transfer. Thus, a faster dephasing of the valley coherence is expected.

To investigate this dependence, the degree of circular and linear polarization anisotropy was measured as a function of the emission angle. For this purpose, angle-resolved Fourier-space images have been acquired at different excitation conditions shown in **Figure 45**. First, the helicity shall be discussed. By

using a quarter-wave plate, the excitation was prepared and analyzed together with a polarizer. For each excitation condition the degree of circular polarization is calculated in the usual fashion and is shown in **Figure 56**. The corresponding angle integrated spectra can be found in appendix A10. For small and medium size of detuning a circular anisotropy can be still found for the PL emission.

One can clearly see, how the circular degree is vanishing for increased detuning similar to previous reports (G. Wang et al. 2014) on bare monolayers without angle resolution. Compared to quasui-resonant 1s excitation, the helicity decreases significantly when pumped to higher states of the A-exciton series. Here, probably in the relaxation process lots of phonons are created that faciliate an efficient scattering to the counter polarized valley, thus lowering the degree of polarization. Finally, when pumped above the exciton quasi-particle gap of the A-exciton series, the polarization is finally (almost) completely gone.

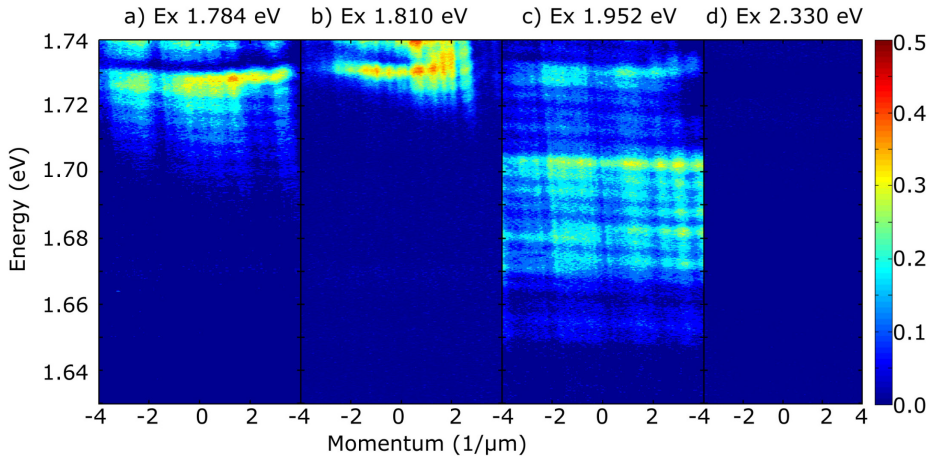

***Figure 56* | Angle Resolved Circular Degree of PL Polarization for Different Excitation Conditions at 10 K.** (a-d) Contour plot of the degree of circular polarization, which is directly linked to the valley polarization. The figure is adapted from (Schneider et al., 2020b) under the Attribution 3.0 Unported (CC BY 3.0) License.

In a next step the angular dependence of the circular anisotropy was evaluated quantitatively, by plotting the maximum degree of circular polarization found at the A-1s neutral exciton resonance as function of the momentum (cf. **Figure 57a**). As can be seen easily, a decrease of the PL helicity is found for increasing angle for small detuning of the excitation energy and becomes flatter for bigger detuning. The drop at quasi-resonant excitation is about 20% in the analyzed region starting from 40% at normal incidence. Angle-dependent helicity has been reported before for exciton-polaritons in microcavities (N. Lundt, Stoll, et al. 2017; Z. Sun et al. 2017) or generally valley-exciton polaritons in TMDC's (Y. J. Chen et al. 2017; Dufferwiel et al. 2017). These publications also present a dependence of the angle-resolved helicity on different excitation energies and cavity detuning.

Generally, in these reports and in models for the valley pseudo-spin S_k an effective magnetic field $\Omega_{eff}(k)$ (K. V. Kavokin et al. 2004; Maialle, de Andrada e Silva, and Sham 1993) driven by the energy splitting of the excitonic branches $\Omega_{ex}(k)$ and the photonic modes is used. In our case the cavity confinement or guiding effects seem to be negligible therefore contribution of the photonic mode splitting is not relevant here. Thus, the following equation of motion has to be considered (Glazov et al. 2014):

***Equation 6-5* | Equation of motion for valley pseudo-spin**

$$\frac{\partial S_k}{\partial t} = Q(S_k) - S_k \times \Omega_{eff}(k)$$

Here, $Q(S_k)$ is the collisional integral that accounts for other valley decoherence channels such as phonon and carrier scattering. In case of a TMDC monolayer the effective field due to the exciton fine-structure has the following form with the excitonic Hopfield constant $|X_k|$, the valley-orbit coupling strength due to the exchange interaction $J_k = A|k|$ and the angle between center-of-mas momentum and photonic momentum ϕ (Z. Sun et al. 2017):

Equation 6-6 **| Effective magnetic field due to the exciton fine-structure**

$$\Omega_{eff}(k) = |X_k|^2 \Omega_{ex}(k) = \frac{|X_k|^2 2J_k(\sin(2\phi_k), \cos(2\phi_k), 0)}{\hbar} = \frac{|X_k|^2 2A|k|(\sin(2\phi_k), \cos(2\phi_k), 0)}{\hbar}$$

Obviously, the effective magnetic field is vanishing at zero center-of-mass momentum such that under the assumption that the collisional integral is independent of the momentum in within the light cone, the total decoherence time τ_{dec} can be split into a k-independent part $\tau_{dec,k=o}$ from other collisions and a k-dependent part from the long-range exchange interaction $\tau_{dec,EI}$. If one assumes that the spin decoherence takes place within the framework of the Maialle-Silva-Sham mechanism (Maialle, de Andrada e Silva, and Sham 1993) similar to reports with TMDCS in cavities (N. Lundt, Stoll, et al. 2017; Z. Sun et al. 2017), the decoherence time can be denoted as follows using the momentum relaxation time τ_{relax}:

Equation 6-7 **| Decoherence time using the Maialle-Silva-Sham framework**

$$\frac{1}{\tau_{dec}(k)} = \frac{1}{\tau_{dec,k=0}} + \frac{1}{\tau_{dec,EI}(k)} = \frac{1}{\tau_{dec,k=0}} + \Omega_{eff,||}^2(k)\tau_{relax}$$

While (Glazov et al. 2014; Schmidt et al. 2016) assume that the loss happens due to the Dyakonov type mechanism (Dyakonov and Perel 1972) , the loss in both mechanism is based on a motional narrowing, such that the equation stays valid for both assumptions. The k-independent part can be extracted from the experimental helicity at normal incidence (k=0) using the following simple model (Glazov et al. 2014):

Equation 6-8 **| Simple model for extraction of the spin coherence time**

$$P_c = \frac{P_0}{1 + \frac{\tau_{rec}}{\tau_{dec,k=0}}}$$

When assuming strict selection rules for the excitation ($P_0 = 100\%$) and a PL-relaxation time of $\tau_{relax} = 5 \pm 0.5\ ps$) (Glazov et al. 2014; N. Lundt, Stoll, et al. 2017; Lorenz Maximilian Schneider et al. 2017), one can determine the k-independent part of the decoherence time from the experimental observation (cf. **Figure 57d**).

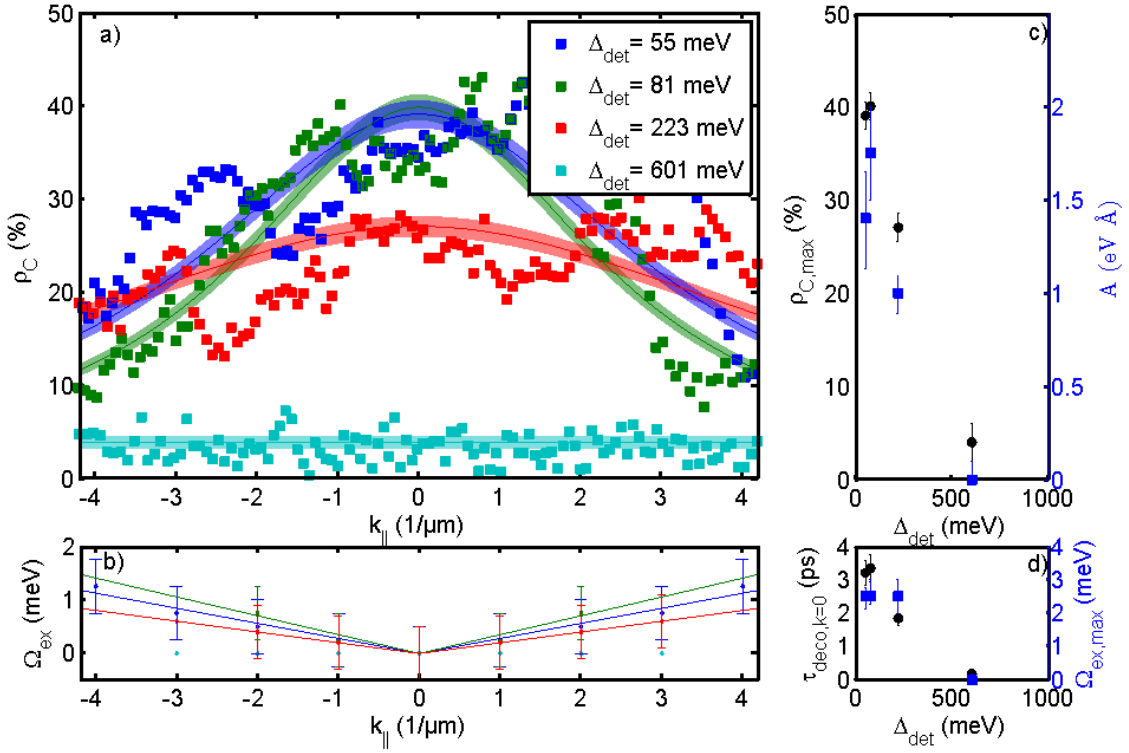

***Figure 57* | Comparison of the Experimental Helicity as Function of the Center-of-Mass Momentum with Calculated Values from a Phenomenological Model.** (a) Experimental Helicity (triangles) in comparison with the calculated result (lines with error bars). The error bars denote the calculated propagated uncertainty from the input parameters. (b) Estimated splitting from the experimental data (triangles) together with a linear fit so extract the slope *A*. (c) Maximum observed helicity as a function of detuning (black, left axis) and slope of the splitting *A* (blue, right axis). (d) Extracted k-independent decoherence time (black, left axis) and approximated maximum value of the fine-structure at the edge of the light cone. The figure is adapted from (Schneider et al., 2020b) under the Attribution 3.0 Unported (CC BY 3.0) License.

In order to extract the splitting between the two branches necessary for the model, the derivative of the Fourier-spectra where plotted as they allow a clearer view on the subtle fine-structure. They show a flat onset for the negative slope, while the minimum of the negative slope values shows a curvature similar to ***Figure 52*b**. Thus, the approximated position between lower and upper branch was readout manually and is shown in **Figure 57c**. It was fitted linear ($\Delta E = 2A|k|$) to extract the slope of the linear branch. One has to note that (Qiu, Cao, and Louie 2015) predict a saturation of the splitting outside of the numerical aperture accessible with this objective. From the qualitative comparison with their prediction the here observed splitting should be roughly 2/3 of the maximum one. This suggests a splitting of 2.0 - 2.5 meV for the here investigated sample.

Assuming a pure exciton gas ($|X_k| = 1$) and a momentum relaxation time of $\tau_{relax} = \frac{2\hbar}{\Gamma} = 241$ fs, one can calculated the helicity. Indeed, a reasonable agreement between experiment and model can be found. It shows that an excitonic splitting of this magnitude can explain the drop of helicity and the loss most likely originates from the long-range exchange interaction due to the Silva-Maialle-Sham mechanism. Furthermore, the decline of decoherence time at normal incidence shows that this process is only dominant if the detuning is low. Otherwise other decoherence channel such as carrier-carrier scattering in a hot plasma or phonon scattering are more important.

In a second step, the results of measurements of linear anisotropy should be discussed briefly as well. The spectra together with a zoom-in to the neutral exciton of the A-exciton series are shown in **Figure 58**. The pump was p-polarized (polarization in the plane of incidence) and oriented parallel to the in-

plane direction momentum resolution. One can see that in the co-polarized emission, still a small curvature seems to be superimposed by some flat feature, which can be attributed to decoherence effects. Nonetheless, it is not as clearly visible as in the circular polarized measurements. The signal appears to be dominated by the linear feature, in total giving a different picture than in the other measurements, where no selection of a linear polarization was made. Interestingly, a flat response is visible in the contra-polarized emission, which reflects decoherent emission from excitons or plasma.

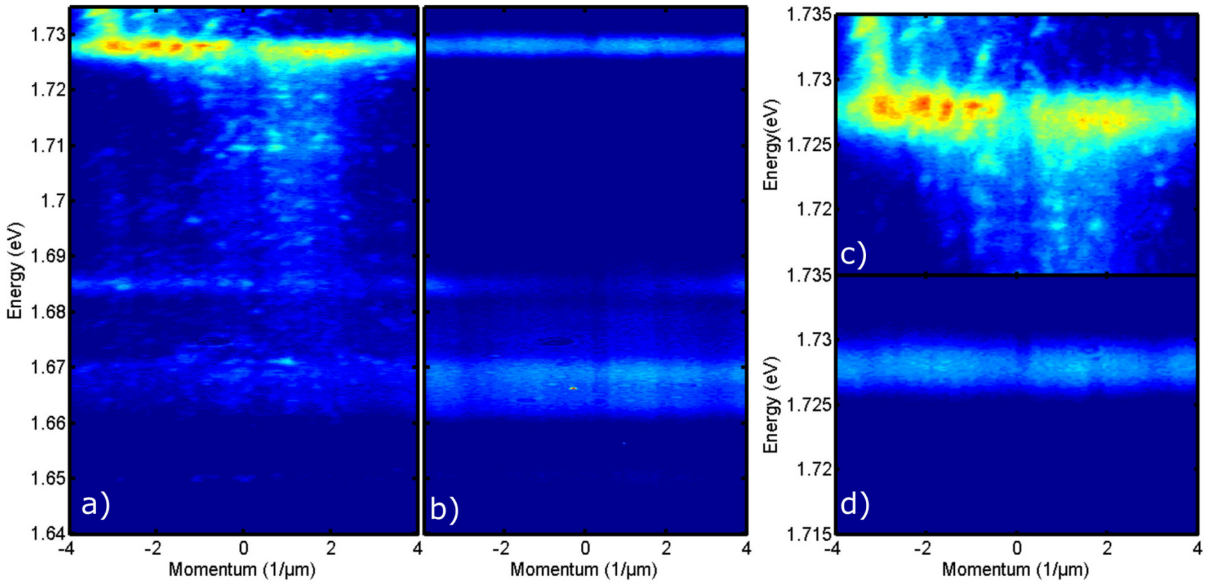

***Figure 58* | Linear Anisotropy of the Angle-resolved PL Emission under P-Polarized CW-illumination.** Co- (a) and contra polarized (b) emission from the encapsulated WSe_2 monolayer at 10 K. (c) and (d) show a zoom-in to the A-exciton resonance, respectively. The pump is p-polarized and corresponds to the direction of projected momenta.

Both observations fit to the prediction (Glazov et al. 2014; Qiu, Cao, and Louie 2015; H. Yu et al. 2014), that the upper exciton branch couples to the longitudinal (p-polarized) light and the lower branch couples to the transversal (s-polarized) part of the excitation. The fact that emission from a flat feature is present in both s- and p-polarized direction of the angle-resolved emission strongly hints at decoherence, i.e. a redistribution of emitters from the initially populated upper branch (coherent excitons) into states representing microscopic polarization (incoherent excitons or uncorrelated plasma). If no dephasing is present, both branches (longitudinal and transversal) should also emit with this polarization (p- and s-polarization, respectively). Also, in the language of exciton-polaritons this phenomenon can be explained. A dispersion should only be present, if a macroscopic polarization is indeed present. If the valley coherence is lost and emission is coming from the perpendicular direction, no macroscopic dipole-moment is present. In conclusion, one can say both the observation – the dependence of helicity to center-of-mass momentum as well as the different dispersion for the linear polarization – is agreement with the expectation from both viewpoints. Nonetheless, measurements should be repeated also including an s-polarized pump for a deeper understanding an easier comparison with the experiment.

6.8 Radiation Pattern and Dipole Alignment

In a second step of analysis not only the peak energetic location and linewidth were evaluated, but instead the focus was turned to the amplitude. These amplitudes are directly linked with the radiation pattern of the excitonic dipole moments and allow the analysis of their alignment. This is particular interesting for TMDCs as they are uniaxial crystals with exitonic transition associated with aligned dipoles. While it is clear, that the dipole alignment can have a huge influence in application like LED, Lasers, polariton quantum optics or coupling with other photonic structures, there are only very few reports dealing with the radiation pattern or the dipole alignment (Robert et al. 2017; Schuller et al.

2013; G. Wang et al. 2017b). Nonetheless, if the possible excitonic states, arising from the coupling of the bands in both valleys by short-range exchange interaction, are analyzed by group theory interesting states arise (Robert et al. 2017).

As the crystal symmetry at the K-points is described by C_{3h} (3-fold rotational symmetry), also the Hamiltonian commutes with wavefunctions of this particular symmetry. By constructing the exciton wavefunction in this way, the resulting states can be categorized (Dery and Song 2015; Glazov et al. 2014; Robert et al. 2017; Song and Dery 2013; G. Wang et al. 2017a, 2017b). As the exchange interaction has to be included, also states formed from coherent superposition of both valleys are present. There are two $\Gamma 6$-states, that are bright and are predicted to mix into the linear and parabolic branch (cf. Chapter 6.1) if inter- and intravalley long-range exchange interactions are considered. In addition there are two $\Gamma 5$ states, that are spin- and momentum forbidden states and are located at K-point of the quasi-particle momentum space. Interestingly, there are also $\Gamma 3$ and $\Gamma 4$ states. One of them is both spin and dipole forbidden, while the other one is still dipole allowed in-plane in contrast to the $\Gamma 6$, which are allowed out of plane. This particular difference of dipole alignment (cf. **Figure 59**) is expected to be revealed by analyzing the radiation pattern.

The data analyzed in this section have been taken under pulsed quasi-resonant condition, where all of the excitonic complexes are nicely resolved as can be seen from **Figure 60**. The angle-integrated spectra have been fitted assuming Lorentzian lineshape for each resonance. The energetic position found for the resonances are in agreement with other samples of comparable high quality (e.g. (Barbone et al. 2018; S.-Y. Chen et al. 2018)). While some of the spectral features were still not understood respectively not discussed in these papers, they quantitatively agree with the prediction of phonon-assisted sideband from the bright and dark excitons (Brem et al. 2020). In order to verify this a temperature series has been performed (see **Appendix A12**). The results are in good agreement with the predictions made by (Brem et al. 2020). The results of the fitting procedure are summarized in **Table 8**. It has to be noted that although 14 peaks have been considered, the features are so sharp that leaving out one of the resonances will make a good representation of the spectrum not anymore possible. From the identification of the resonances, the splitting Δ between bright and dark states resulting from spin-orbit coupling and short-range exchange interaction as well as the splitting δ between dark and grey exciton solely originating from the short-range exchange interaction can be determined. They are $\Delta = (43 \pm 2)$ meV and $\delta \approx (5 \pm 3)$ meV. To estimate the latter one, the phonon band structure as determined by (Terrones et al. 2014) and the identified phonon sidebands was used to calculate the position of the dark exciton. In literature, (Robert et al. 2017) they are

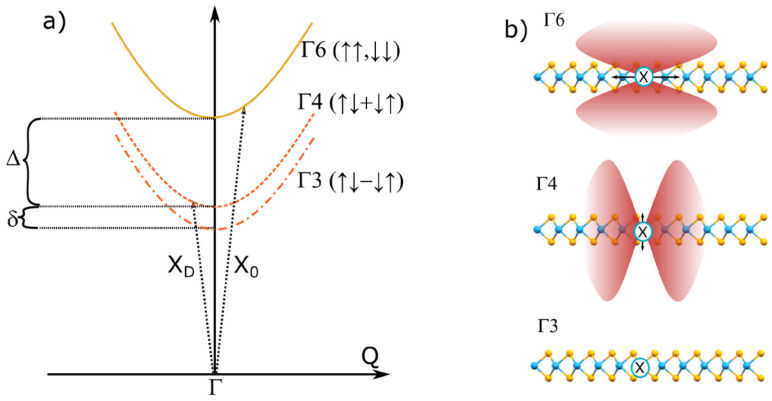

***Figure 59* | Dipole Alignment in TMDC Monolayer.** (a) Sketch of the different excitonic states after considering the short-range exchange interaction. (b) Sketch of the expected radiation pattern for in-plane, out-of-plane dipole as well as dipole forbidden transitions. Reused under the Creative Commons Attribution CC BY 4.0 International License (Commons 2020) from (Lorenz Maximilian Schneider et al. 2020).

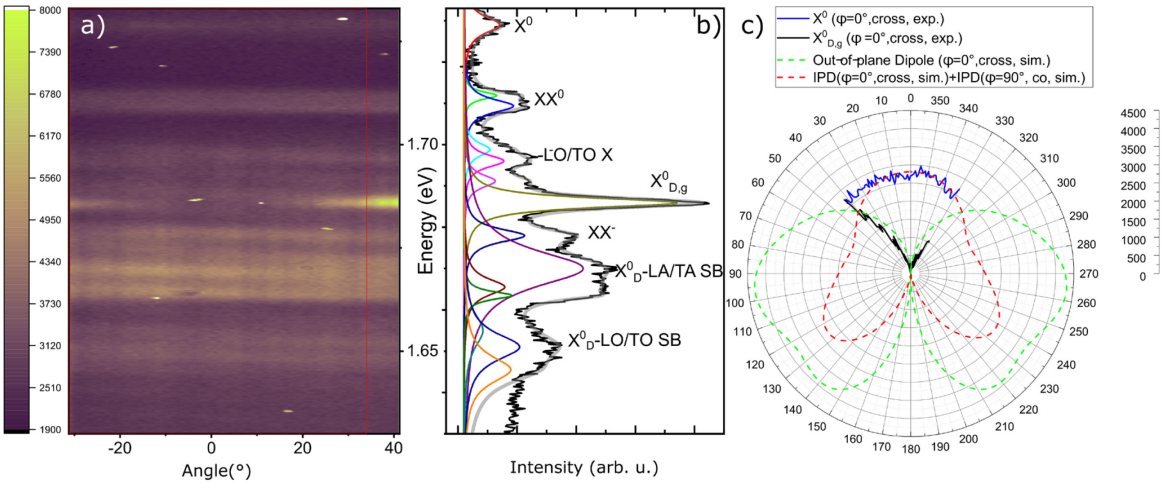

***Figure 60* | Angle-Resolved PL-Intensity under Pulsed Excitation and Emission Pattern.** (a) Angle-resolved photoluminescence under quasi-resonant pulsed excitation under cross-polarized detection. (b) Angle-integrated spectra showing several emission peaks. They have been fitted with a sum of Lorentzian peaks shown underneath. (c) Comparison of the experimental radiation pattern for the neutral bright and the neutral exciton in the z-mode to the simulated results. Dashed lines correspond to the simulations. For the in-plane dipole due to decoherence the comparison is made with the average of parallel and perpendicular alignment of the dipole with respect to the excitation. Adapted under Creative Common CC BY Attribution 4.0 License (Commons 2020) from (Lorenz Maximilian Schneider et al. 2020).

determined to be $\Delta = 40$ meV and $\delta = 0.6$ meV. Both are comparable with the here determined value, although the fine-structure splitting of the dark exciton is overestimated. This could be due to need the use of calculated phonon energies, that still often have some errors, compared to the direct approach using a magnetic field used by Robert et al.

When considering the PL-Intensity as function of the emission angle, one feature behaves strikingly different than the other observed resonances (cf. **Figure 60**). While for most resonances an almost flat response with a slight decrease to the side is present, the resonance attributed to the grey exciton (cf. **Figure 9**, **Figure 60**) exhibits a steep increase of emission intensity towards higher angles. While indeed the presence of the grey exciton has been predicted (Robert et al. 2017) and indirectly confirmed (G. Wang et al. 2017b), the here shown measurement is up to my knowledge the first direct measurement of its radiation pattern confirming the predictions made by group theory.

It is clear, that the intrinsic radiation pattern of the excitons will be modified by the multilayer structure, especially by encapsulation with h-BN. In order to study this effect, electromagnetic simulations using CST microwave studio have been performed for an in-plane as well as out-of-plane dipole present within the layer. Similarly to calculations discussed above in section 6.6.2 a Lorentz model was employed to model the in-plane permittivity of the WSe_2 monolayer, while the out-of-plane

***Table 8*| Extracted Parameters of the PL Peaks obtained under Quasi-Resonant Pulsed Excitation.** A multi-peak fit with Lorentzian line profiles yields the following central energies of different excitonic (X) species and their full width at half maxima (FWHM). Adapted under Creative Common CC BY Attribution 4.0 License (Commons 2020) from (Lorenz Maximilian Schneider et al. 2020).

Peak	X^0	XX^0_1	XX^0_2	X^-_{inter}	X^0 *op.SB*	X^-_{intra}	$X_{D,g}$	XX^-	X_D *(K-K′ TA)*	X_D *(K-K′ LA)*	X_D *(K-Λ TO)*	X_D *(K-Λ LO)*	X_D *(K-K′ TO)*	X_D *(K-K′ LO)*
Energy (eV)	1.729	1.712	1.709	1.699	1.696	1.691	1.686	1.678	1.670	1.666	1.663	1.655	1.651	1.646
FWHM (meV)	5.0	2.2	4.0	4.0	3.7	3.9	3.0	4.0	11.0	5.0	2.4	10.0	8.0	8.0

permittivity ($\epsilon_z = 7.5$) was taken from (Laturia, Van de Put, and Vandenberghe 2018) and the anisotropic permittivity of h-BN ($\epsilon_z = 2.56, \epsilon_{xy} = 4.84$) was taken from (Segura et al. 2018). Firstly, to check if an in-plane dipole could also lead to such pattern at the dark exciton's energy or an out-of-plane dipole at the bright exciton's energetic position both scenarios are simulated as well (cf. **Figure 61**).

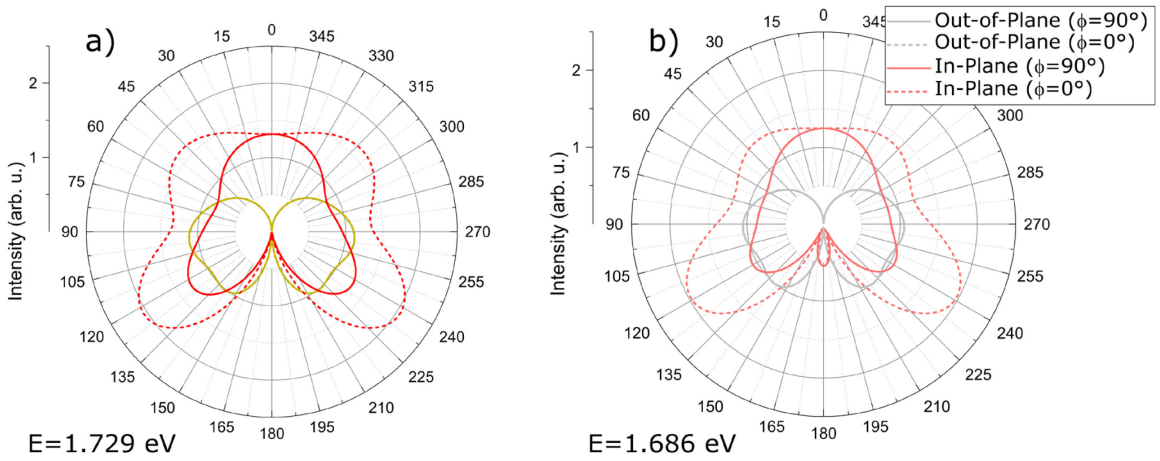

Figure 61 **| Simulated Radiation Pattern at the Bright (a) and Grey Exciton's (b) Energetic Position.** The polar coordinates represent the emission direction, with the plane of the monolayer oriented along the 90-270° line. The redish colored lines depict the situation for in-plane dipole orientation, whereas the lighter colored curves represent the out-of-plane dipole radiation pattern. The angle ϕ represents the orientation of the plane of angle-resolved radiation with respect to the dipole alignment in the plane. In fact, no difference occurs for out-of-plane dipole orientations with respect to the two-dimensional profiles perpendicular to the monolayer plane. Adapted under Creative Common CC BY Attribution 4.0 License (Commons 2020) from (Lorenz Maximilian Schneider et al. 2020).

Although there are some modifications of the radiation pattern by the multilayer structure, the result clearly shows, that only the interpretation of the "grey" exciton feature as a z-mode, respectively, and the bright exciton as an in-plane mode agrees with the experimental observations. In the next step, the outcoupling was analyzed for different states of linear polarization. The far-field approximation was therefore projected according to the Ludwig III convention, to extract the co- and cross-polarized parts of emission (cf. **Figure 62**) (Ludwig 1973; Zinka 2007). This convention projects the spherical wave onto the spherical unit base vectors ($\hat{\phi}, \hat{\theta}$) not on the cartesian unit vectors, as the former are orthogonal to the wavevector of the outgoing wavefront at this angle.

Equation 6-9 **| Ludwig III convention**

$$\hat{u}_{ref} = sin\phi\hat{\theta} + \cos\phi\ \hat{\phi}$$

$$\hat{u}_{cross} = cos\phi\hat{\theta} - sin\phi\ \hat{\phi}$$

The polar plots (cf. **Figure 62**) show the emission for an in-plane dipole at the bright exciton position as well as an out-of-plane dipole at grey exciton position. Both show the analysis of polarization in an emission plane parallel to the alignment of the dipole (ϕ=0°, similar to the experiment) as well as perpendicular (ϕ=90°).

For the grey exciton a modified torus shaped radiation pattern is found. According to the projection convention this gives cross-polarized emission for ϕ=0° and co-polarized emission for ϕ=90°.

For the perfectly aligned in-plane dipole the simulation predicts mostly co-polarized emission in both detection planes. Nonetheless, in the experiment – due to quantum dephasing soon after excitation –

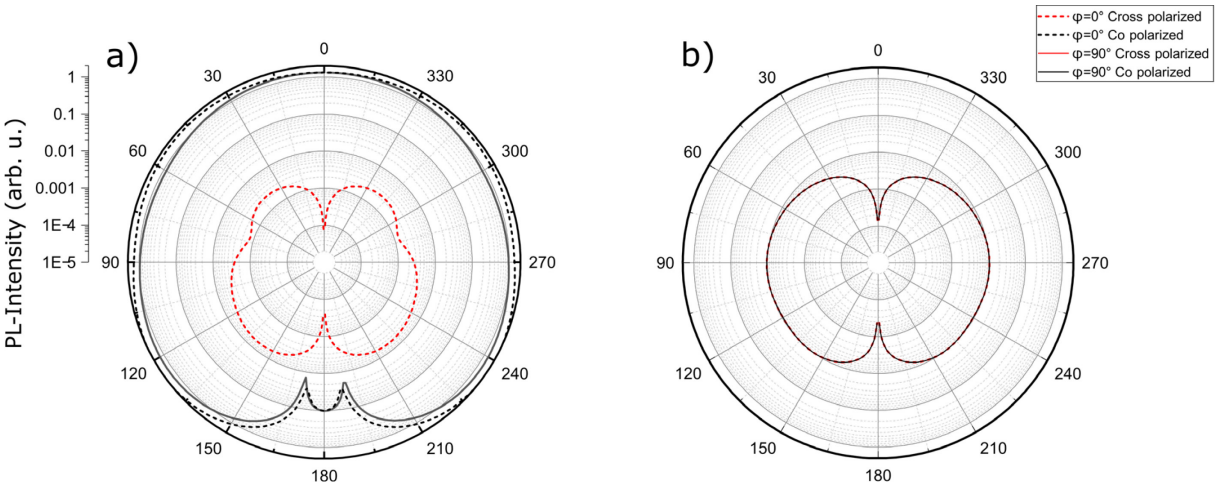

***Figure 62* | Polarization Analysis of the Simulated Radiation Pattern for In-Plane Bright (a) and Out-of-Plane Grey (b) Exciton at their Respective Energetic Position.** For the projection of the radiated field onto the polarization the Ludwig III convention is used. Adapted under Creative Common CC BY Attribution 4.0 License (Commons 2020) from (Lorenz Maximilian Schneider et al. 2020).

one gets a distribution of dipole alignments with only a small peference for the direction of the exciting laser. This dephasing is not included in the simulation and a weighted average over both directions has to be taken when comparing model data with the experiment (red dashed line in **Figure 60**).

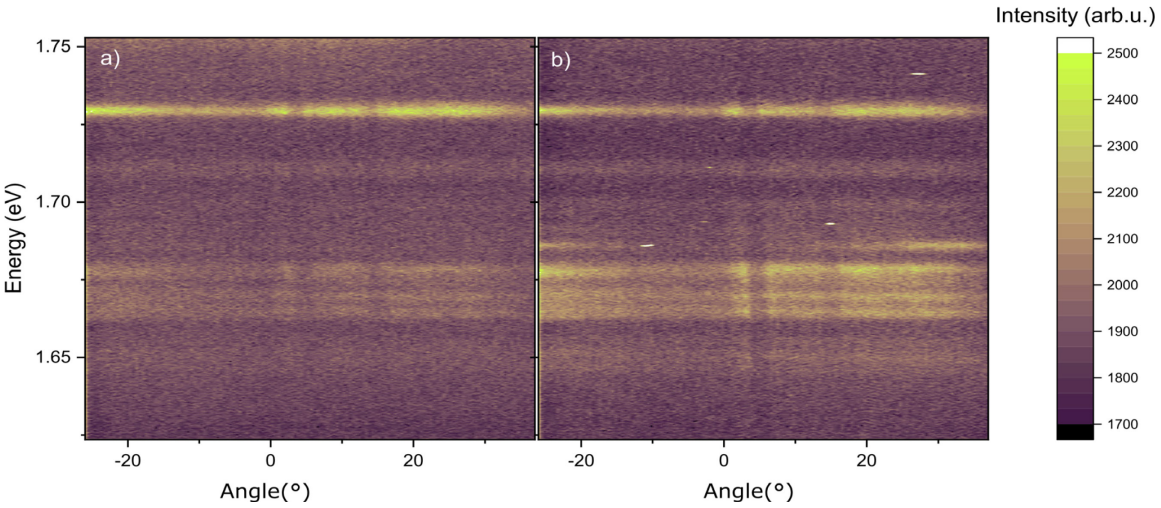

***Figure 63* |Experimental Analysis of the Polarization of the Radiation Pattern.** The 2D-images show co-polarized emission (a) and contra-polarized emission (b). Adapted under Creative Common CC BY Attribution 4.0 License (Commons 2020) from (Lorenz Maximilian Schneider et al. 2020).

The experimental analysis for ϕ=0° of the polarization is shown in **Figure 63**. This second measurements shows comparable results to the initial measurement. For the neutral exciton the angle-dependent emission profile is almost identical to the calculated behaviour as expected, if dephasing is considered. For the grey exciton almost only emission in cross polarization is found as predicted by the simulation. Furthermore, slightly more PL (degree of linear polarization degree about -8%) is found in cross polarization for the charged biexciton and the phonon sidebands from dark exciton states compared to the small positive intensity difference (degree of linear polarization about +3%) for the neutral exciton. For circular polarization, it is known that a negative degree of polarization is found for the charged biexciton (S.-Y. Chen et al. 2018; Nagler et al. 2018). This is understood, as the dark exciton involved is residing in the other valley.

6.9 Summary

This chapter discussed the investigation of the angle-dependent emission of h-BN encapsulated WSe_2 monolayers. Remarkably, a comparably strong dispersion was found for the exciton resonance, when set in relation to the ordinary exciton effective mass in semiconductors. In order to understand the origin and ways to alter this pronounced dispersion with respect to the in-plane momenta, temperature- and power-dependent measurements were performed for several samples.

A slight reduction of dispersion curvature at increasing pump power in the linear regime was observed, which most likely is related to the increasing role of a plasma fraction in the emission mode (or excitation inducing dephasing). Similarly, a sudden flattening of the energy-momentum dispersion relation was observed shortly above 100K, which is attributed to the increased phonon scattering due to the formation of phonon sidebands.

The origin of the dispersion has been discussed using three different viewpoints, (i) the microscopic view where the exciton mode splits due to long-range exchange interaction forming a linear as well as a parabolic branch, (ii) coupling of the polarization to the exciton branch due to the strong oscillator strength leading to the formation of exciton-polaritons, as well as (iii) propagation or waveguide effects of the structure that could lead to the formation of cavity-polaritons.

While a comparison with predictions from the microscopical models using the long-range exchange interaction show a little bit smaller curvature then observed in experiment, some features do not match the prediction exactly. For example, the dispersion seems to be rather parabolic not linear as expected from microscopic theories with 2D Coulomb potential (Qiu, Cao, and Louie 2015). Similarly if treated strictly 2D also from the viewpoint of macroscopic electrodynamics a linear branch (Andreani and Bassani 1990) would be expected. However, in case of an encapsulated monolayer, a 3D treatment of the screening could be necessary (Deilmann and Thygesen 2019). Interestingly, a comparison with calculation based on the 3D bulk equations indeed can used to explain some aspects of the findings on a qualitatively level. The origin based on cavity effects could be excluded by simulations since only a leaky weakly confined mode is present. While it is clear that the dispersion has to arise from exchange interaction, respectively, coupling to the induced polarization and radiative field, the effect on the dispersion due to the screening by the surrounding and thus the treatment (strictly 2D with linear branch or 3D with parabolic branch with increased slope) in an encapsulated monolayer is still not clear.

In a second step, the circular and linear anisotropy has been investigated as function of the emission angle. Here, a decrease of helicity with the angle respectively the center-of-mass momentum is found, similar to some reports that deal with valley cavity polaritons (N. Lundt, Stoll, et al. 2017; Z. Sun et al. 2017). Putting the result of this measurement in other words, the valley pseudo-spin is coupled with the center-of-mass motion. The dependence of valley polarization on the center-of-mass momentum is in general a complex interplay of the dephasing mechanisms in the photonic and excitonic/electronic system as well as the relaxation and redistribution between both systems (N. Lundt, Stoll, et al. 2017; Z. Sun et al. 2017). While in cavity-based systems the dephasing mechanism due to the TE and TM mode splitting is believed to be the dominant contribution (Z. Sun et al. 2017), here it could be due to the predicted mode splitting of the excitonic system (Rabi oscillations between K and K' valleys due to hybridization of states) as only weak cavity effects seem to be present. Therefore a phenomenological model based combining the spin-relaxation mechanism developed by (Maialle, de Andrada e Silva, and Sham 1993) with the linear dispersion predicted by (Andreani and Bassani 1990; Qiu, Cao, and Louie 2015; Tassone, Bassani, and Andreani 1992) was employed. The found decline in helicity is in agreement with the model prediction and proves that the helicity loss with momentum is caused by the exchange interaction based pseudo-spin decoherence.

In addition, the dispersion is merely found in the linear polarization parallel with the excitation. This perfectly matches with the theoretical prediction with the expected degeneracy lifting for a longitudinal and transversal exciton branch and the loss of coherence of the states in the picture of macroscopic polarization (i.e. exciton-polaritons). Nonetheless, additional, more experiments with a more detailed analysis of the linear polarization are necessary for better comparison with the theoretical predictions. Furthermore, a strong influence of the excitation detuning on the observation of the meV-strong curved dispersion within the light cone was observed. The vanishing of an observable curvature at increased detuning is attributed to the increased decoherence due the influence of hot charge carriers in an increasingly electron-hole-plasma plus incoherent-exciton configuration which predominates the emission and replaces the emission from coherent excitons.

In a third step, the radiation pattern of such a high-quality encapsulated monolayer stack was analyzed under pulsed excitation conditions. One can clearly differentiate between in-plane modes e.g. the bright exciton and z-modes that have an out-of-plane dipole orientation. Moreover, it was shown that the measured angle-resolved emission pattern, respectively, dipole orientations matches nicely with electrodynamic simulation taking into account the anisotropy of both h-BN and WSe_2.

7. Integration of 2D-TMDCs into Photonic Structures

As the field of 2D-TMDCs started to mature in the second phase of this thesis, new questions concerning the integration of TMDCs into photonics structures and circuits have been raised. Therefore, the community started to study the integration of monolayer and bilayer systems as saturable absorbers (Du et al. 2014; Z. Luo et al. 2016; K. Wu et al. 2015), active material (Yongzhuo Li et al. 2017; J. Shang et al. 2017; S. Wu et al. 2015; Y. Ye et al. 2015) in laser science or on waveguides (Blauth et al. 2018; H. Chen et al. 2017; Wei et al. 2015), cavities (X. Liu et al. 2015; Nils Lundt et al. 2016; Z. Sun et al. 2017), nano-resonators (Castellanos-Gomez et al. 2013) as well photonic crystals (Noori et al. 2016; S. Wu et al. 2014) in the area of integrated photonics (F. Xia et al. 2014).

Generally, van-der-Walls materials are a very promising material for this purpose, as in contrast to the integration of III-V materials on silicon, the lattice mismatch does not result in a big obstacle. A transfer/deposition of flakes on another material is generally often possible. Nevertheless, if a crystalline substrate is used, a moiré-pattern will be formed, and the dielectric constant of the substrate and its polarity will affect the optical properties of the layer as seen in chapter four and five.

With this motivation, two investigations in collaboration with master students Oliver Mey and Franziska Wall co-supervised by me within this thesis project as well as our co-workers, such as Frederik Wall from the Roskos-group in Frankfurt, and others from the Fang-group at the Zhejiang University in Hanzghou, China, have been performed. One featured the integration of a 2D-material on a circular Bragg cavity inscribed in a substrate. This approach can enhance the outcoupling of the PL, as demonstrated in our study, and should increase its directionality, which is still the subject of ongoing characterization via Fourier-space imaging and spectroscopy. Especially, for the usage of 2D-materials in LED devices or the integration of 2D materials as polarization sensitive element in integrated photonics, this proof of principle concept could be useful.

In the other study, a combination of TMDC's with polarization selective mirrors or substrates were envisioned, designed and tested. This concept could possibly enhance the already existing valleytronic properties of these materials, leading to a possible integration of 2D materials into valley selective nanophotonics possibly even up to the strong and ultrastrong coupling regime (Forn-Díaz et al. 2019). Both studies and direction were promoted by Dr. Arash Rahimi-Iman, who co-supervised these projects based on his initial ideas. Other valuable initial ideas in the project such as using evolutionary algorithms for design optimizations, proof-of-principle in THz regime using the 3D-printer were promoted from my side.

As the achievement of chiral mirrors has not yet reached a mature status, this chapter will focus on the development and test of a circular Bragg grating for efficient in- and outcoupling. For the preliminary results for the chiral mirrors the interested reader can find the details in the master thesis of Oliver Mey. Furthermore, the overall study in this chapter was also performed to identify general problems and challenges arising in the integration of 2D-materials to photonic structures.

7.1 Concept of the Circular In-Plane Distributed Feedback Optical Microcavity

The design consists of two parts: the in-plane confinement of light is achieved using a circular in plane distributed Bragg reflector based optical microcavity (CIDBROM) (C. Wu et al. 1991) ,while the out-of-plane confinement is based on a simple interference approach. As the concept is based only on edges parallel and perpendicular to the plane of the TMDC, the in- and out-of-plane confinement can be considered and optimized separately using 1D-simulations. Only at the end full 3D simulation of some relevant parameter pairs have been performed using the time-domain solver of CST microwave studio. Here, the concept for the in-plane confinement will be discussed first, followed by the discussion of the out-of-plane direction.

WS_2 has been selected as the exemplary material as it has the strongest light-matter interaction of the common four semiconducting TMDCs (Yilei Li, Chernikov, et al. 2014a) and comparably big flakes can be achieved by exfoliation. Nevertheless, the concept in principal can be easily adopted for other TMDC's, when sizes are changed according to the changed wavelength of the A-exciton.

For the in-plane confinement of light a circular in-plane distributed Bragg reflector based optical microcavity (CIDBROM) was designed matched to the A-1s resonance of WS_2. It is based on a circular $\lambda/2$-cavity in the middle surrounded by seven pairs of Gallium Phosphide and air – each of them having the thickness of $\lambda/4n$, n being the refractive index and λ the wavelength of the A-exciton –, where GaP has been selectively removed by focused ion beam milling (FIB). In order to achieve high reflectivity for both in- and out of plane confinement, gallium phosphide was used as a substrate, as it has a comparably high refractive index. For the in-plane confinement this is important as the high refractive index contrast decreases the total number of quarter-wavelength layer pairs needed to reach the necessary high reflectivity. By this the overall size of the cavity can be reduced to about 3.5 µm in diameter. By using a dielectric with even higher refractive index such as TiO_2 a further miniaturization of the design for example for designing micro- or nano-LEDs could be feasible. Furthermore, a rather strong reflection is present at the interface to air, again due to the high refractive index contrast, that is beneficial for out-of-plane confinement.

Generally, CIDBROM-desings are well known and have been shown as the base of low-threshold distributed feedback lasers for several other emitter types like quantum dots (Scheuer et al. 2005; Scheuer and Yariv 2004), dyes (Y. Chen et al. 2009; Turnbull et al. 2005), conventional quantum wells (Olson et al. 1998; C. Wu et al. 1991) and many more. As the system is in principal well understood, it presents a good testbed for integration. Nevertheless, here we show up to our knowledge the first extensive study of integration of 2D-materials into a CIDBROM also featuring s-SNOM measurements. SNOM here brings the advantage that local features and properties such as topography, electrice-field properties, bending and strain etc. can be identified.

A transfer-matrix method was employed to calculate the stopband of the ideal mirrors (cf. **Figure 64 a**). As can be seen by the calculation, the mirror design features a wide stopband, that covers all the four relevant TMDCs and is centered at the WS_2 resonance. To investigate the spatial confinement of the proposed structure the standing wave pattern (cf. **Figure 64 c**) at the design frequency as well as the transmission (cf. **Figure 64 b**) have been calculated using Meep (Oskooi et al. 2010), an open source finite difference time domain solver (FDTD), developed by the M.I.T. , U.S.

One can see a strong confinement of the electric field as expected. From such a 1D simulation an effective mode volume of only 2.44 µm can be extracted. The in-plane mode volume V_{eff}^N has been calculated using the following formula (Kristensen and Hughes 2014):

Equation 7-1 **| Effective mode volume**

$$V_{eff}^N = \int_V \frac{\epsilon(r)|E(r)|^2}{\epsilon(r_c)|E(r_c)|^2}$$

Here, $\epsilon(r)$ presents the permittivity as function of position, E the electric field and r_c the center of the cavity, where the maximum field is observed. To estimate the in-plane *Q* factor the transmission through the cavity was simulated. Once with a broadband excitation to map the hole stopband and lower resolution and once using a narrow band excitation around the expected resonance with higher resolution (see. **Figure 64b** inset). From a linewidth analysis of this calculated transmission the *Q* factor of the proposed design is at least 500. However, as a time domain solver is used, the maximum resolvable *Q* factor from linewidth analysis is directly linked to the simulation time by the principle of

the FFT. The current result is still exactly limited by the simulation time, suggesting that this value has to be seen as a lower bound.

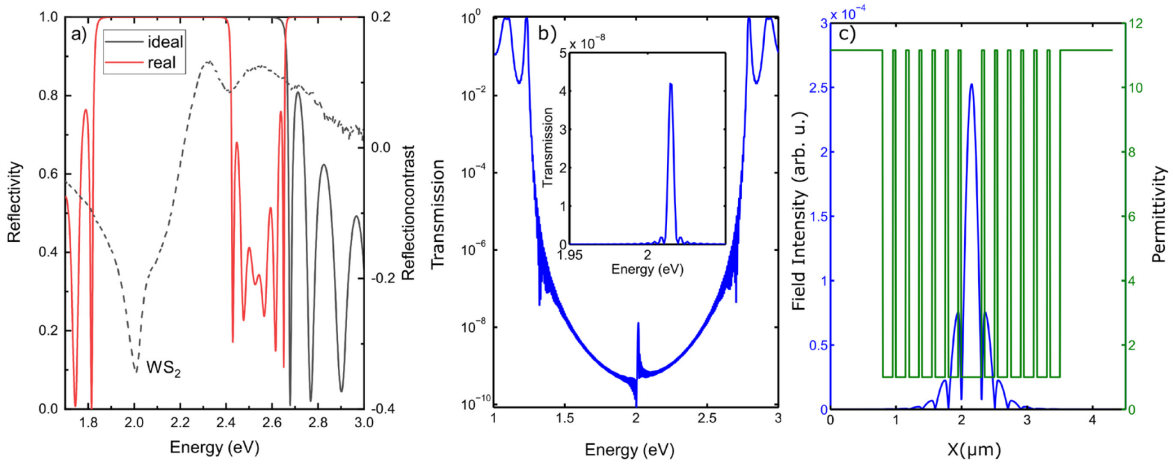

***Figure 64* | Calculated Field Distribution and Stopband for the CIDBROM.** (a) Calculated reflectivity for the ideal (black) structure as well as the realized structure (grey) together with the reflection contrast data for WS_2. (b) Transmission of the cavity as calculated by Meep (Oskooi et al. 2010). The inset shows a simulation with higher precision but lower bandwidth nicely showing the cavity resonance. (c) Standing wave pattern (blue) in the ideal structure as calculated by the finite difference time domain solver Meep (Oskooi et al. 2010) together with the refractive index profile (green) in the background for better legibility. The electric field distribution shown is the equilibrium situation one ps after excitation, where the electric field distribution reached the steady stat distribution. (a) has been adapted with permission from (Mey et al. 2019). Copyright 2019 American Chemical Society.

In conclusion one can say that this structure shows a reasonably goof in-plane optical confinement. As the stopband is quite wide also small errors in the production discussed later on are not leading to an immediate loss of optical confinement, although it can lead to a detuning of the cavity with respect to the monolayer emission or to a reduction of the experimental quality factor.

The out-of-plane design is, however, based a different approach. Here, the field strength at the monolayer is tuned by varying the etching depth as well as the h-BN-support in order to optimize the interference of the incoming respectively emitted with the reflected field. An additional h-BN support has been introduced, as surprisingly the GaP has quenched the PL if used without h-BN buffer layer. This is unexpected as the GaP bandgap is drastically larger and no states are expected in the relevant region. Nevertheless, the band offsets are not known, and a transfer could be still possible. The introduced h-BN layer effectively isolates the monolayer from this quenching and restores the emission of PL. Nonetheless, in realistic applications it is very likely that encapsulated monolayer would be used anyway caused by their superior optical quality (i.e. narrower linewidth and less non-radiative decay).

The multiple reflection model (Lorenz Maximilian Schneider et al. 2020; H. Zhang et al. 2015) (short MRM) is used to calculate the incoupling efficiency for the laser light as well as the outcoupling efficiency for the PL. It is based on Fresnel equations and considers all possible internal reflection in the air and h-BN layers underneath the WS_2 (cf. **Figure 65** for a schematic). It is assumed that the light gets absorbed in the thick GaP sample, so no reflection from the backside of the substrate have to be considered here.

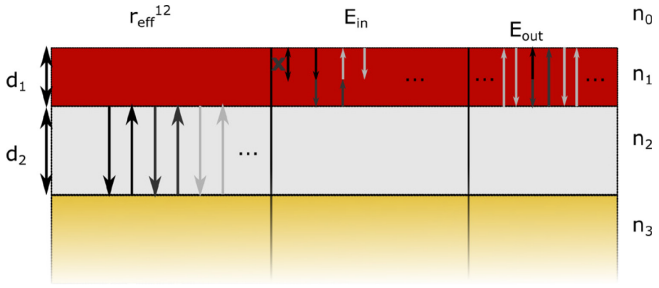

***Figure 65* | Schematic Representation of the Multiple Reflection Model.** (left) the reflection and interference in the second layer are combined into a new effective reflection coefficient. This effective refractive index is used to calculate the in- (middle) and out-coupling efficiency (right). The first term is depicted in black, the second in dark grey and the third on in light grey.

The multiple reflections in a lower layer are summarized in a new effective reflection (and transmission coefficient) (H. Zhang et al. 2015).

***Equation 7-2* | Effective reflection amplitude according to the MRM**

$$r_{12}^{eff} = a_1 + \sum_{n=0}^{\infty} a_2\left(r_{21}e^{-2i\beta_2}r_{23}\right)^n = a_1 + a_2/(1 - r_{12}r_{23}e^{-2i\beta_2})$$

Having done this, the efficiency for in- and out-coupling can be derived the following.

***Equation 7-3* | In- and out-coupling efficiency according to the MRM**

$$E_{in} = \sum_{n}^{\infty} b_n = \sum_{n}^{\infty} b_{2n+1} + b_{2n+2} = \frac{b_1 + b_2}{1 - r_{12}^{eff} r_{10} e_1^{-2i\beta_1}}$$

$$E_{out} = \frac{c_1 + c_2}{1 - r_{12}^{eff} r_{10} e_1^{-2i\beta_1}}$$

Here r_{ij} are the regular reflectivity's as given by the Fresnel equations and β_i is the phase shift due to the propagation in the material. a,b, and c are amplitudes given by the Fresnel equation and depend on the selected situation. In both cases the result of the geometric sum is used to simplify the result. In case of additional layers, the effective reflectivity can be recursively defined, thus the model can be generalized to more complex structures. Having derived the in- and outcoupling coefficients, a total enhancement factor can be defined:

***Equation 7-4* | Enhancement factor according to the MRM**

$$F = \frac{1}{N}\int_0^{d_1} |E_{in}(x)E_{out}(x)|^2 dx$$

For two different thicknesses of the h-BN buffer layer the total enhancement factor *F* compared to a monolayer on bare substrate or h-BN buffer layer, respectively, has been calculated (cf. **Figure 66**). One can clearly see the drop of the enhancement, if a thick h-BN buffer layer is used. For a thin layer an enhancement of about 100 times can be reached in the ideal case. In order to achieve this the optimum etching depth is predicted to be 104 nm. If the excitation wavelength is changed, even higher values close to 130 can theoretically be achieved. In the following discussion these ideal vales will be used.

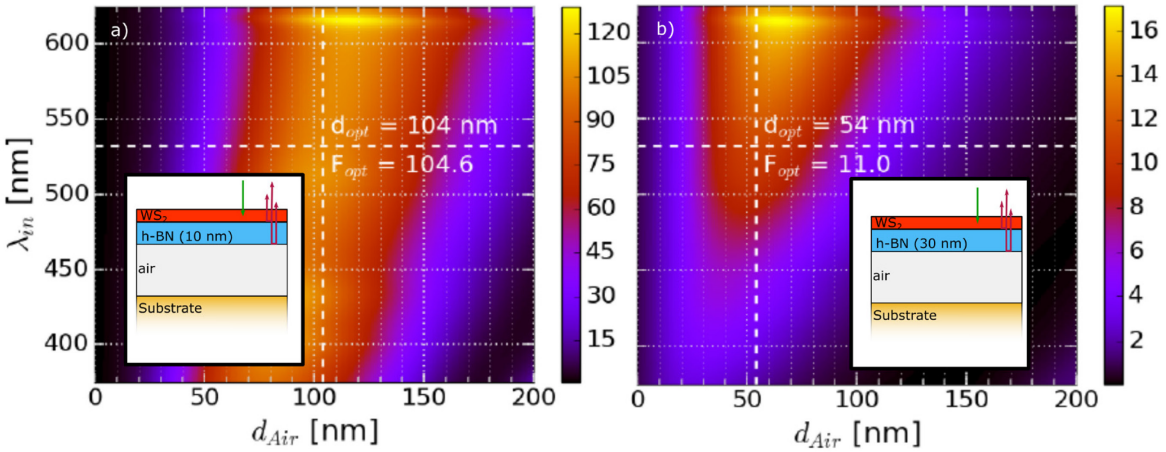

***Figure 66* | Calculation of the Out-Of-Plane Enhancement Factor Comprising the Incoupling of the Excitation as well as the Outcoupling of the Photoluminescence.** The calculation is shown for h-BN of 10nm (a) and 30 nm (b) thickness. The enhancement is given with respect to a reference sample with no additional air gap. Adapted with permission from (Mey et al. 2019). Copyright 2019 American Chemical Society.

Now, as the ideal parameters of the design have been fixed, a three-dimensional simulation using the finite integration technique solver (FIT) of CST microwave studio has been used to calculate the steady state field after excitation. In contrast to the FDTD used for the 1D simulation, FIT solves the Maxwell equation in their integral form, not in the differential form. **Figure 67** shows the field at timepoint t=75 fs – the initial excitation is gone after 25 fs –, where the excitation energy has already decayed by 80 dB and is only slowly decaying compared to the initial field energy. Similarly, to the previously discussed 1D- and 2D-calculation the full 3D-simulation has been performed with two different h-BN buffer thicknesses, namely 10 nm and 50 nm. In the case of the thin h-BN, a suitable confinement can be seen while no strong confinement can be seen for the thick h-BN buffer layer. Thus, the simulation confirms that the confinement reduces drastically if the used h-BN thickness is too large. Note that the mode is not found in the position of the dipole excitation, rendering the simulation believable although the simulation time is rather short. For the thin h-BN layer the mode is roughly confined within 0.02 μm^3 giving an estimate on the achievable mode volume. Note, the definition of the mode volume of a leaky cavity has to be handled with care (Kristensen and Hughes 2014), as for a leaky cavity the normal definition will necessary diverge.

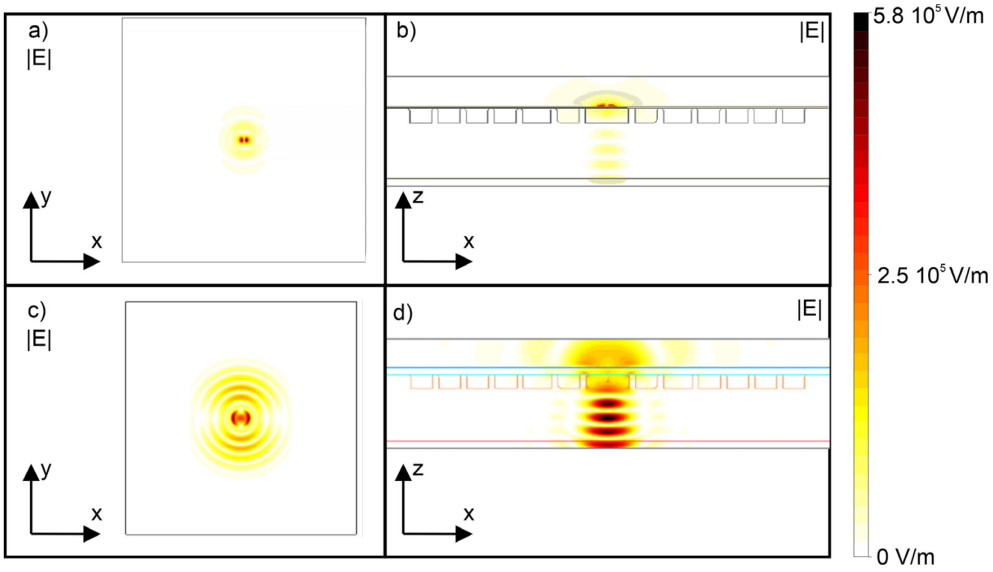

***Figure 67* |Simulated Steady State Field in the CIDBROM after a Broadband Excitation by a Dipole Located in the Cavity for Different Capping h-BN Thicknesses.** Absolute electric field strength for a 10 nm h-BN (a,b) and 50 nm h-BN (c,d) buffer is plotted. Adapted with permission from (Mey et al. 2019). The position of the dipole emitter was set below the h-BN in the middle of the central hole. Copyright 2019 American Chemical Society.

Furthermore, not surprisingly the confinement within the plane is indeed stronger than the out-of-plane concept. Nonetheless, a strongly localized field can be found for this idealized structure. In the next step the in- and out-of-plane component of the electric field where analyzed separately (cf. **Figure 68**) for the structure involving a thin h-BN buffer layer. In can be seen, that the out of plane component is stronger localized than the in plane electric fields. This is not surprising, as a DBR in general is designed for those electric waves travelling perpendicular to the alternating quarter wavelength pairs, i.e. E-field parallel to the DBR interfaces.

Here the design could be optimized, as the dipoles related to the bright A-exciton resonance lie in plane, therefore the confinement of the in-plane field component is indeed more important than the confinement of the out-of-plane field. Nevertheless, also a confinement for the in-plane field is found, that will lead to an enhancement of the electric field.

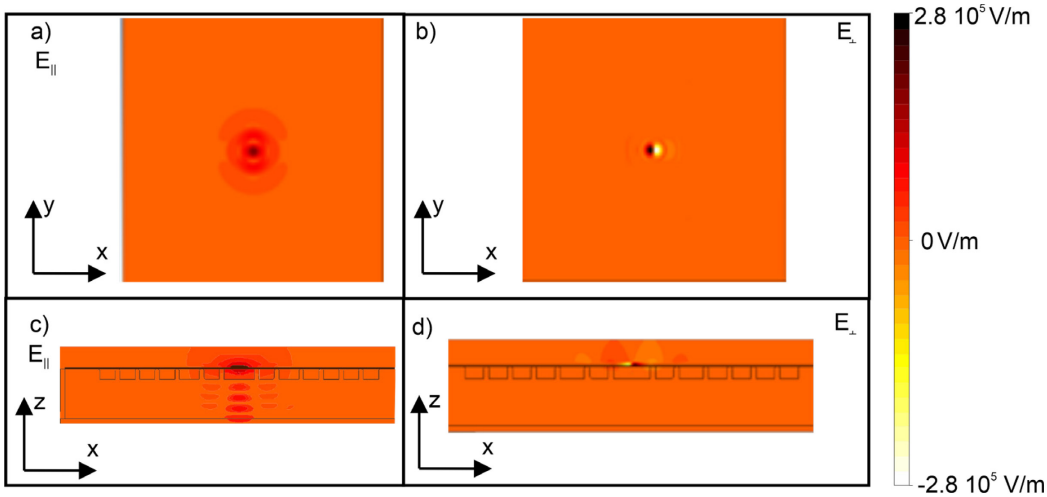

***Figure 68* | Simulated Field Distribution in the CIDBROM for In- and Out-Of-Plane Components.** Intensity of in-plane components (a,c) as well as out of plane components (b,d). Adapted with permission from (Mey et al. 2019). Copyright 2019 American Chemical Society.

7.2 Realization of the Cavity

The cavity as well as a reference was realized by milling into the GaP substrate by using a focused ion beam. As a reference structure a hole of same diameter and depth is used, to disentangle the cavity effects from the effects of suspending the layer. Nevertheless, the optimized back-reflections also take place in the out-of-plane direction in this structure, whereas the in-plane confinement is absent. Followingly, h-BN and WS_2 were transferred onto both of them. In the next step, the topology of the uncovered and covered reference and cavity have been analyzed by taking SEM and AFM pictures (see **Figure 69**).

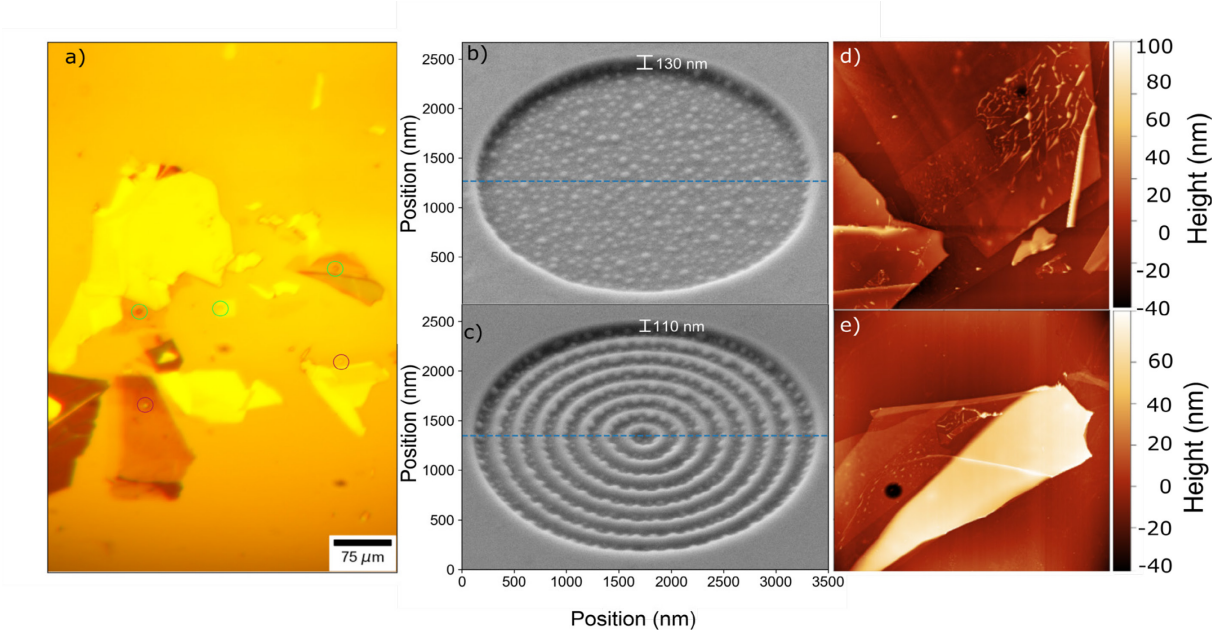

Figure 69 |Morphology of the CIDBROM and the Reference Structure. (a) Microscopic picture of the sample area featuring three reference structures as well as three cavities. The green circles mark the cavities and the red ones the reference structures. (b & c) Exemplary SEM data of the reference structure as well as the realized cavity before capping with vdW-materials. (d & e) AFM picture of the capped reference as well as CIDBROM structure. Adapted with permission from (Mey et al. 2019). Copyright 2019 American Chemical Society.

From the SEM the realization of the pattern could be proven. However, there are small deviations from the designed structure. The depth was measured to be around 110 nm for the cavity and about 130 nm for the reference structure. Both values are slightly bigger than the optimum value. However, the calculation (cf. **Figure 66**) shows still a rather high expectable enhancement of the in- and outcoupling of laser and PL respectively. In addition, the GaP walls are having a round shape rather than steep walls and furthermore, there is a slight deviation in thickness of the etched lines. Nevertheless, they are still tolerable as the recalculated stopband (cf. **Figure 64a**) still includes the A-exciton resonance, however the deviation possibly leads to a detuning of the cavity in respect to the PL emission frequency.

From the AFM of the capped reference (d) and hole(e) a h-BN thickness of 20 nm respectively 12 nm was extracted. Both are slightly bigger than the optimum, nevertheless an enhancement of more than an order of magnitude can be still expected. Furthermore, wrinkles and small bubbles in the monolayer part can be observed, which is not uncommon for the outcome of such van der Waals stacking procedures. In addition, however a considerable bending on the order of 30-40 nm of the sample into the hole can be found (cf. **Figure 71**). As the initial produced depth was slightly too big, this can be even beneficial for the here discussed samples. While in the center it is nearly flat, a strong curvature is found at the edges of the hole, which should lead to a locally strained 2D-stack at these positions. Interestingly almost no periodic pattern in the bending are found in case of the CIDBROM. Caused by

the bending, changes of PL linewidth, position and intensity are not only expected at the center but also at the edges (Brotons-Gisbert et al. 2018; Conley et al. 2013; Roldán et al. 2015).

7.3 Optical Properties of the Monolayer on the Cavity

In the next step the optical properties of both, the reference as well as the sample, were analyzed by means of µ-PL and reflectance contrast on the one hand and scattering type scanning field optical microscope (s-SNOM) on the other hand. Here, firstly the near-field results (cf. **Figure 70**) shall be discussed. As the PL near-field signal was too weak to be detected, the near-field signal at the design excitation wavelength (532 nm) as well as outside the stopband (850 nm) has been probed with a laser. The scattered signal was detected at 2ω and 3ω with respect to the tip frequency ω. By doing this, the nonlinear response of the underlying material can be probed locally with a maximal resolution of about 30 nm (Walla et al. 2018).

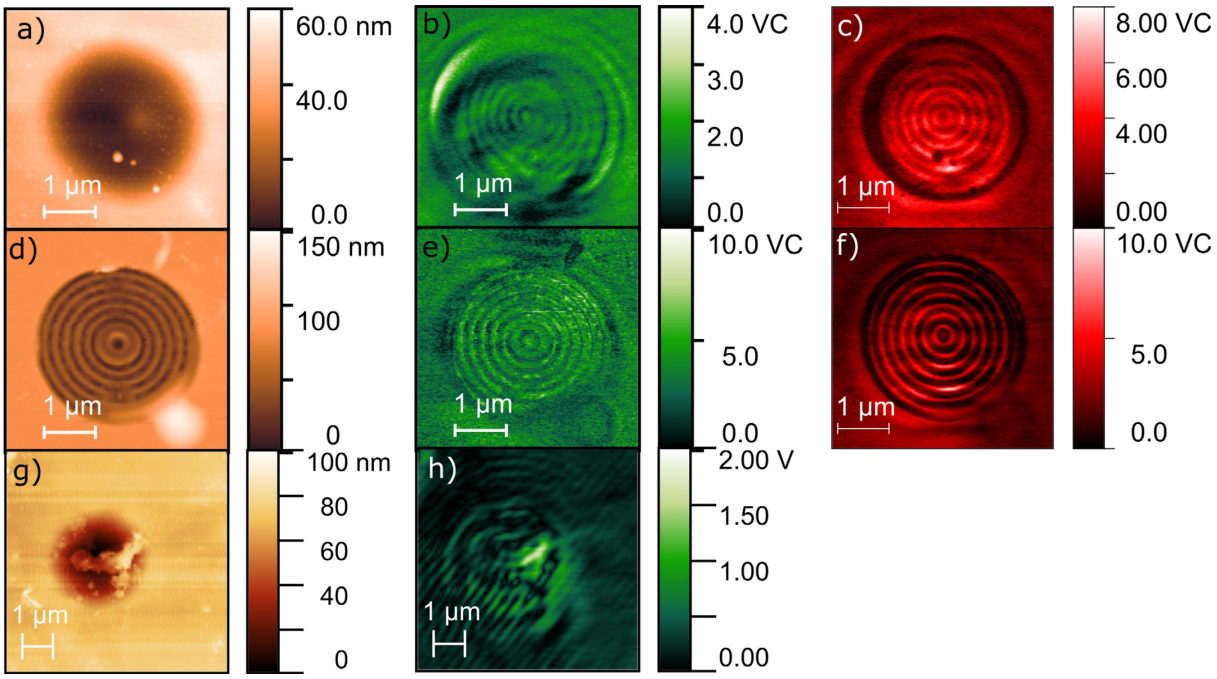

***Figure 70* |Comparison of the Topology and Experimental Near-Field Signal for the Capped and Uncapped Cavity.** false color AFM images of the capped (a), uncapped CIDBROM (d) and the capped reference structure (g). Near-field images at 532 nm from the 3rd harmonic signals are shown in (b), (e) and (h). The signal at 850 nm outside the stopband is shown in (c) and (f). Again, both are shown in false colors. Adapted with permission from (Mey et al. 2019). Copyright 2019 American Chemical Society.

This also helps to minimize topography effects to the near-field signal, that mostly induce a linear scattering change.

In the near-field measurements at 532 nm of the uncapped CIDBROM the standing wave with the enhancement in the center can be seen easily. As 532 nm is in the stopband but not at the designed cavity resonance the enhancement is not striking, but nevertheless a confinement to the center is found. The signal is roughly 1.5 times stronger in the center compared to the bare substrate and 25% stronger than in the other etched areas. In the reference an enhancement can be found close to the edges with a drop of the signal to the substrate level at the center of the structure.

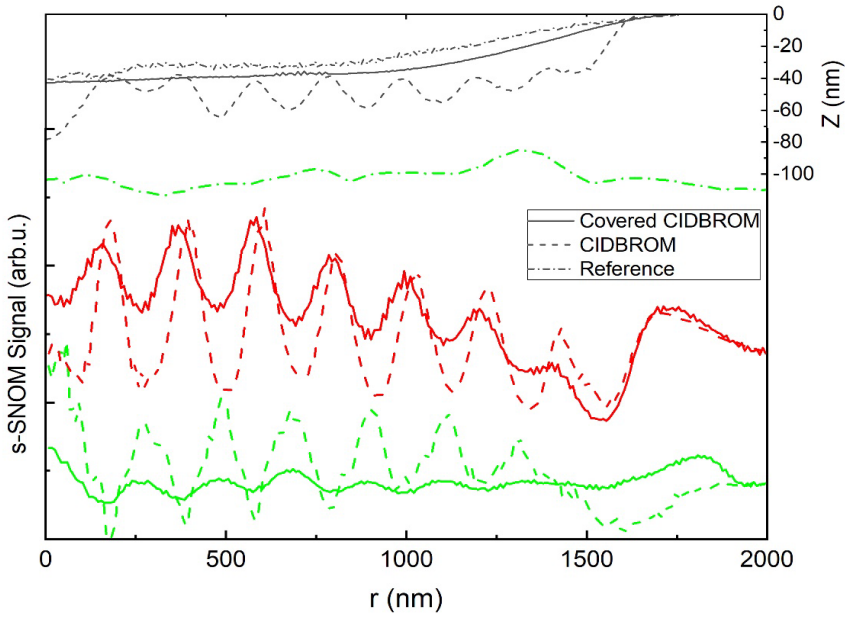

Figure 71 **|Comparison of Topographic Information and Near-Field Signal in the CIDBROM and the Reference Structure.** (top right axis) Topography as determined from the AFM taken simultaneously with the near-field data (bottom left axis). The comparison is shown for the open and covered cavity as well as the covered reference. For the CIDBROM also measurement at different excitation wavelength are shown namely, 532 nm (green lines), which is the excitation laser within the stopband, and 850 nm (red lines), which is outside the stopband. The near-field signal has been normalized to the value on the substrate and each type is offset for clarity.

As the standing wave can also be seen in the capped CIDBROM, the design consideration could be proven experimentally. However, it seems a little distorted. This has several reasons, firstly surface wave starting from the cavity can also be observed, secondly the bending that induces strain and changes the dipole alignment of h-BN as well as WS_2 in the bended regions with respect to the lab coordinate system complexifies the structure even further. This tilt of the dipoles of the bright excitons allows a direct radiative coupling with the out-of-plane electric field.

For the case of near-field measurement of the cavity at 850 nm, interestingly, we find an anti-aligned pattern, where strong field and a depletion of the signal in the center are found on the GaP, not on the etched parts, instead. This strong contrast has to be discussed carefully, as s-SNOM always measures the field as well as the nonlinear scatter efficiency of the material simultaneously (Brehm et al. 2006; Huber et al. 2007; von Ribbeck et al. 2008). It is likely that in the 532 nm measurement the signal is dominated by the standing wave contribution, while in the measurement at 850 nm could be dominated by the different scattering efficiency. A pseudo-heterodyne detection of the s-SNOM signal together with a careful analysis could help in principle to disentangle these two effects leading to a better understanding of the monolayer integrated to this stucture and similar nanophotonic devices.

To further quantify the difference, the cylindrical symmetry of the structure was used to calculate radial profiles (cf. **Figure 71**). This angular averaging decreases the influence of local changes and therefore provides a cleaner analysis compared to linear profiles. The CIDBROM shows a nice increase of the near-field signal at the center of the structure both for the covered and the uncovered one. However, the field modulation is weakened by the coverage (34% in contrast to 300% compared to the signal outside the structure). The reference in comparison shows almost no modulation, but a small increase at the edges of the hole can be found.

In the next step the PL was investigated by means of confocal measurements (cf. **Figure 72**) as well as using the spectrometer in imaging mode (cf. **Figure 73**). For spectral analysis the PL of the structure, respectively, the emission next to it on h-BN, was selected by the confocal iris and is plotted in **Figure**

72. Also here, an increase of the emission is found. Furthermore, a blueshift of the emission and reflection dip can be observed. The occurring blueshifts (up to ten meV) can be expected as we deal now with a flake with periodically different screening scenarios, only thin h-BN or h-BN and substrate. This changes the screening and will lead to a blueshift. For the enhancement on average a factor of ten in peak intensity can be found for the CIDBROM and 3.5 for the reference. When we want to compare to the multiple reflection model, we have to account just for the suspended areas of the stack (referred as $A_{eff,CIDBROM}$) were the considered interference in MRM takes place.

Equation 7-5 **| Experimental enhancement factor**

$$R_{Exp} = \frac{F_{exp.,CIDBROM}}{F_{exp.Ref.}} = \frac{10}{3.5} = 2.9$$

$$R_{MRM} = \frac{F_{MRM,CIDBROM}}{F_{MRM,Ref}} \frac{A_{eff,Ref}}{A_{eff,CIDBROM}} = \frac{68}{32} \frac{8.4\ \mu m^2}{5.7\ \mu m^2} = 3.1$$

Generally, when corrected in this way a nice agreement between the prediction and the experimental findings can be found. This confirms that the out-of-plane confinement indeed can be observed.

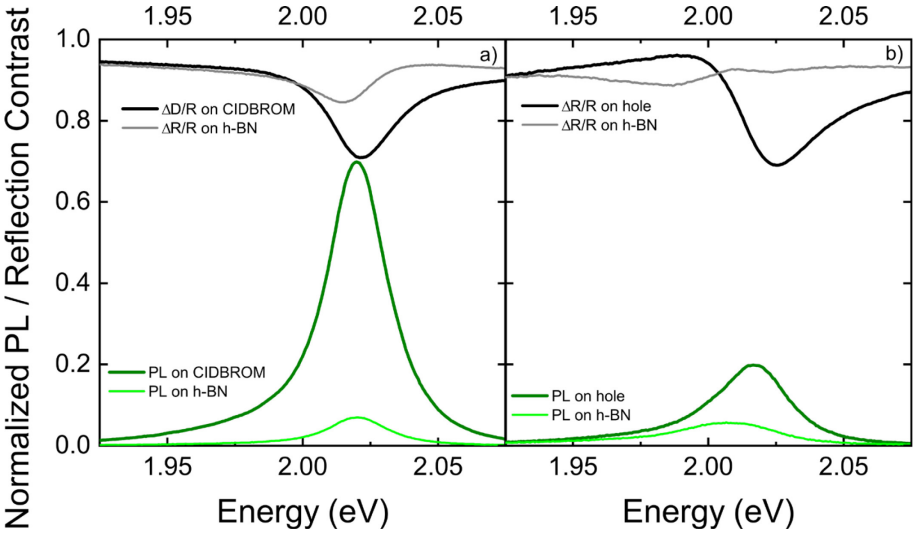

Figure 72 **|PL- and Reflection Contrast Spectra of the Covered CIDBROM as well as the Reference Compared to the h-BN Supported Case in the Surrounding.** (a) shows the CIDBROM and (b) the reference. Adapted with permission from (Mey et al. 2019). Copyright 2019 American Chemical Society.

In order to further investigate the in-plane confinement the spectrometer was used in imaging mode. The resulting PL images are shown in **Figure 73 a** and **b**. The shape of the flake as well as the structure can be easily identified in these pictures, by the circular-shaped region of emission enhancement. Profiles have been extracted in different directions through the structures. In the CIDBROM enhancement of the PL emission is found at the edges of the structure as well as a small increase exactly in the center similar to the s-SNOM measurement. However, caused by the resolution no fringes can be found in the interior as they are averaged out by the optical resolution in these experiments. Similarly, for the reference enhancement is found at the edges. In addition, an artifact caused by a wrinkle on top of the reference causes a drop of the intensity along a line. The local enhancement compared to the h-BN supported surrounding is shown in **Figure 73 e-g**.

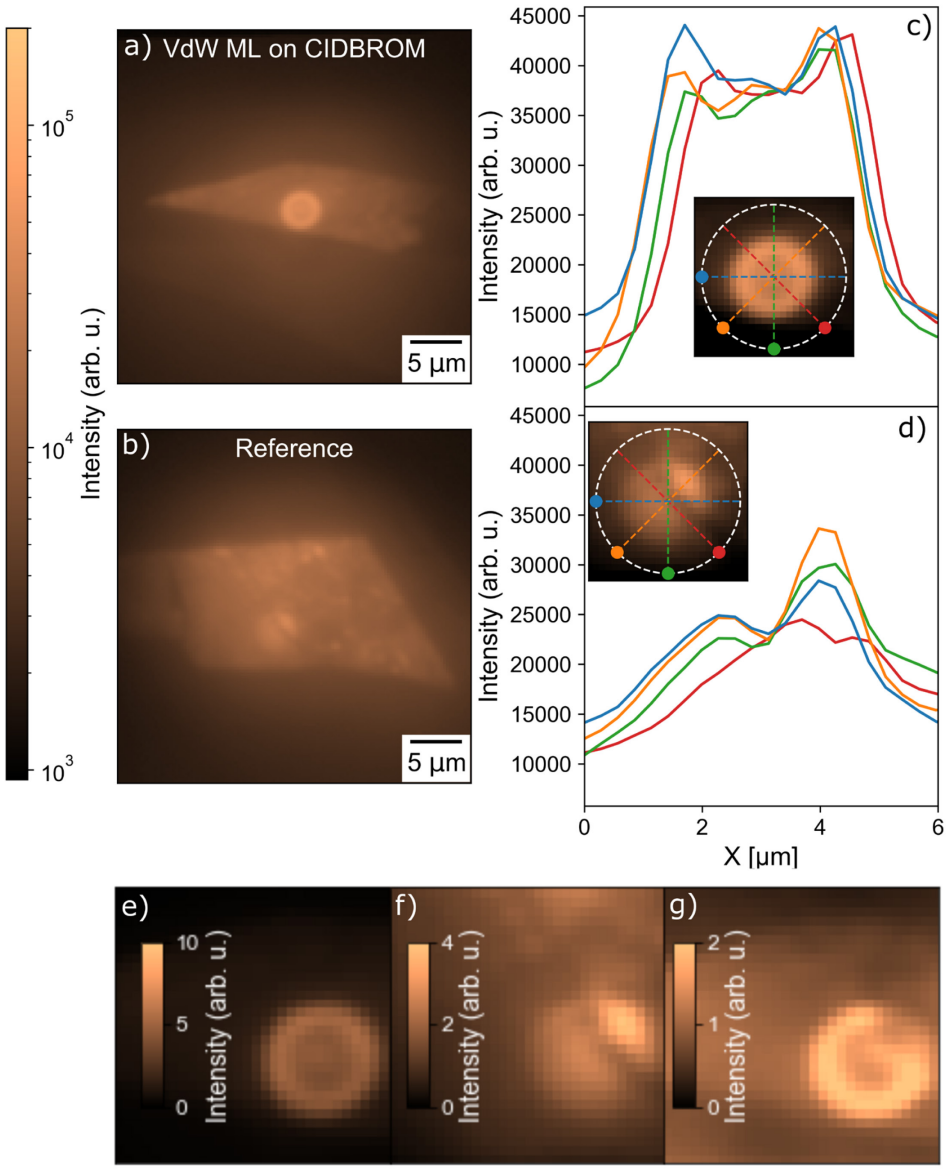

***Figure 73* | Spatial Analysis of the Enhancement as Calculated from the PL-Images.** (a) and (b) show the PL images depicting the CIDBROM and reference, respectively. (c) and (d) show profiles taken through the structures for in depth analysis. (e) Enhancement of the PL of the covered CIDBROM compared to the flake on h-BN in the surrounding, and a similar analysis for the reference case is shown in (f). (g) shows the ratio between both measurements. Adapted with permission from (Mey et al. 2019). Copyright 2019 American Chemical Society.

One can again nicely see the local behavior of the enhancement. It locally varies from four to about nine in enhancement factor for the CIDBROM while only about 1.8 times maximum enhancement can be seen for the reference. The CIDBROM locally shows about 1.7 to 2 times more detected emission confirming the design as well as the in-plane confinement.

7.4 Summary

In this chapter the challenges arising when integrating monolayered TMDCs into photonic structures have been investigated for a prototype photonic structure etched into a substrate by a focused ion beam. In general, the proposed structure generates a local field enhancement or in other words a nano-focus in the in-plane direction. Furthermore, the in- and outcoupling of the excitation and emission is improved by optimizing the interferences from the trenches, i.e. their depth. While such structures could be useful in several areas like enhancing the light matter coupling for detectors or making use of nonlinear effects as well as µ-LED approaches, here we studied the general applicability of such a structure to 2D-materials and the challenges arising for this class of materials.

The integration itself can be established comparably easy compared to conventional semiconductors by a dry transfer and no restrictions are arising from the lattice constant mismatch. Nonetheless, bending of the layered system occurs, that causes several additional effects due to the introduced strain, different alignment of the transition dipole moments with respect to the design and a spatially modulated screening of charge carriers. Furthermore, a quenching of the PL due to the substrate can occur with can be countered by isolating the ML using a h-BN buffer. In that case, however, the performance of the structure is especially sensitive to the thickness of the used buffer layer.

The here investigated structure has been fabricated by a focused ion beam (FIB) and a dry transfer method. Even though, the above-mentioned additional effects were not taken into account, the experiment could show that the in- and out-of-plane confinement indeed work. Nevertheless, also an enhancement at the edges is found for of the proposed structure, that could be either due to strain of the monolayer or efficient scattering from these edges. Other obstacles that arise easily by such a production process are the development of wrinkles on top of the structure, which easily disturb such structure and reduce the overall efficiency.

In conclusion, the study in this chapter shows, that indeed monolayered TMDC material can be easily integrated into a CIDBROM structure similar to other approaches like photonic crystals (Noori et al. 2016; Shiue et al. 2019), whispering gallery mode resonators (Salehzadeh et al. 2015) and others. In addition, it shows that if the photonic structure does not have a plane surface, bending of the ML occurs at the edges of the structures which should be carefully taken into account in the design, as strain and light matter coupling are changed. Nonetheless, this study paves the way to integrate monolayers in more complex structures or extending the concept for increasing the nonlinear response of monolayer systems.

8. Summary and Outlook

In this final chapter of this thesis, a brief summary of experimental results is provided and their importance to applications will be outlined. In recent years van-der-Waals materials have emerged as a new field of semiconductor physics bridging the world of conventional inorganic and molecular semiconductors. On the one hand, they have drawn tremendous attention due to the many exciting possible material combinations which are not limited by lattice or rotational mismatch of the crystal structure. On the other hand, this material class offers easier access to exotic physics such as spin-valley locking or strongly correlated quantum phases like the excitonic Mott insulator. When one considers the electric field lines related to the excitonic Coulomb interaction of such quantum material system, which remarkably extends into the surrounding of the single layer, it becomes immediately clear that the interactions with the environment are at the heart of understanding the optoelectronic properties of such systems and possibilities for designing those. Having this in mind, this thesis first briefly discusses the role of the environment before addressing other aspects that affect the properties of TMDCs, such as the stacking configuration and twist angle in homobilayers or heterostructures. Thereafter, optical dispersion measurements based on high-quality h-BN encapsulated monolayers are discussed, and in a final chapter, a nanophotonic concept for the enhanced outcoupling of photoluminescence from monolayers is analyzed.

Chapter 4 summarizes prominent interactions of 2D materials with the environment. First, the influence of mesoscopic properties of the surrounding environment, such as its dielectric constants, its interface roughness, strain and charge inhomogeneity, on the PL and emission dynamics are discussed at the example of WSe_2. By carefully analyzing the PL and TRPL spectra of monolayers on different substrates shown in this part, signs of substrate-induced strain as well as doping could be found. Here, the induced doping can be identified for different samples relative to each other by an observable change of the exciton/trion ratio. This changing ratio is in line with studies e.g. (Chernikov, Van Der Zande, et al. 2015), where doping is created artificially by gating the sample. Different strain situations mainly manifest themselves in an increased linewidth and a larger emission fraction from red-shifted localized states. These features were observed as expected mainly on substrates, where a microscopic roughness was known to be present. Furthermore, if substrate-induced doping or strain are present, a decline of the PL-helicity due to a faster valley dephasing is observed, as anticipated. Only if small valley dephasing and low doping is present, biexcitons and other higher many-body complexes can be observed. Summarizing this study one can state that an atomic flat, clean substrate, with no dangling bonds, is one key element for observing low linewidth emission showing higher excitonic complexes. This conclusion was verified by other groups later on with improved high quality samples (S.-Y. Chen et al. 2018).

Furthermore, some indication of a systematic peak shift with the refractive index of the substrate could be found in the investigation presented here. This indication is in line with theories from several groups (Lars Meckbach, Stroucken, and Koch 2018b; Raja et al. 2017) published later, which concluded that a proper treatment of the screening is crucial for the description of the monolayer. While the influences seemed subtle at first sight as the band renormalization and the change in excitonic binding energy almost cancel out each other's energy changes, the substrate itself and the resulting interface with the 2D material is crucial for the achievement of high-quality samples. The here presented experimental study shows that h-BN is a good substrate as it provides an ideally flat substrate without dangling bonds and now is commonly used by many groups (Ajayi et al. 2017; Cadiz et al. 2017; S.-Y. Chen et al. 2018; Rhodes et al. 2019). In addition, to tackle the substrate-induced doping even further, electrostatic gating is now often used to reach an intrinsic sample.

Therefore, in the second part of **Chapter 4**, the influence of h-BN in several different h-BN/WSe_2 heterostructures is addressed, namely h-BN supported, capped and encapsulated samples. This investigation was performed in parallel to other groups (Ajayi et al. 2017; Cadiz et al. 2017; Wierzbowski et al. 2017). The conclusion from our study is in agreement with their main finding, that h-BN encapsulation is a viable route to better optical sample-quality reaching almost intrinsic broadening.

Our investigation also involved a detailed analysis of electron-phonon coupling as well as investigations of annihilation and diffusion. These parts are absent in the above cited studies. By comparison of the different stacking in this study a systematic change could be found. When capped or encapsulated – even if just a single layer of $MoSe_2$ is used on top of WSe_2 – a red-sift of the WSe2's A-exciton PL-peak as well as a noticeable linewidth reduction can be found. Our study showed that this originates from a decreased inhomogeneous broadening from disorder compared to SiO_2 and changes in carrier-screening, as was proven by parallelly published theories (Stroucken and Koch 2016). As capping by a single layer results in a similar shift, it can be concluded, that the carrier-screening is indeed influenced only by the very next layers. The observed improvements by h-BN encapsulation in terms of disorder and the subsequently reduced non-radiative recombination are essential such as almost any application will benefit if not even require it.

As such change in carrier-screening should affect the electron-phonon coupling, temperature- and power-dependent measurements of PL and TRPL have been performed. Generally, this work finds a rather strong exciton-phonon interaction for WSe_2. By modeling the emission energy and linewidth with phenomenological equations, one can extract a comparably robust interaction with optical and non Γ-point acoustic phonons, which leads to the formation of phonon sidebands above 100 K. Similarly, also a qualitative change in the very same temperature range can be seen in the dynamics and PL-linearity providing additional evidence for this interpretation. By comparing samples in different environmental settings this study could find systematic changes. Therefore, it must be concluded that the environment also affects the interaction with phonons. For encapsulated samples, the coupling to phonons is for example about 15 % lower than for samples on bare SiO_2. Thus, the change cannot be neglected. Furthermore, the applied models also extract a stronger exciton-phonon coupling for excitons than for trions. This could be due to a different oscillator strength, which changes the coupling to phonon-assisted polarizations. Nonetheless many-body calculations are necessary to understand this finding in detail.

The last part of **Chapter 4** deals with exciton-exciton annihilation by analyzing power dependent TRPL measurements. Here, for the first-time systematic changes in exciton diffusion for different stacking environments were found. To understand these changes, two models were employed; one based on Förster-transfer limited annihilation and another one limited by particle diffusion. It could be concluded that the Auger-like annihilation is limited by diffusion, thus allowing the extraction of the exciton diffusion constant for different stackings. The study shows an increased diffusion of excitons for h-BN supported and encapsulated samples compared to substrate supported ones. Nonetheless, the change in annihilation rates are not only arising from different diffusion constants but also from a change in the exciton Bohr radius due to different screening. The main contribution to the increased diffusion constant comes most likely from the smoother surface with less disorder, that allows for efficient diffusion. The here extracted diffusion constants (in the range $D = 10\ nm^2/ps$) could be verified in other reports (Kulig et al. 2018) published one year later than (L. M. Schneider, Lippert, et al. 2018) (online 2017), which extracted the diffusion by direct time-resolved measurements in real space. The observed increased diffusion and the consequently reduced Auger-processes are beneficial for light-harvesting and laser application as they promise higher efficiencies. Thus, from the here presented investigation one can conclude that the surrounding has a strong influence on the mean

free path in general and h-BN encapsulation specifically offers a way to increase it compared to SiO_2 for many applications.
To investigate the diffusion even further, time-resolved SNOM could be a valuable tool to probe the local origins of differences in exciton diffusion behavior. Here, especially the influence of crystal defects and disorder (Rhodes et al. 2019) are potential candidates for investigations. This is especially interesting for heterobilayers forming a moiré potential, where a non-trivial flow of carriers is found (Yuan et al. 2019).

While **Chapter 4** has dealt with the mesoscopic influence of the surrounding, **Chapter 5** discusses the effect of the microscopic alignment in high-symmetry homobilayers and twisted heterobilayer systems. While in the first case, only the symmetry and selection rules are changed, the case of an arbitrarily twisted heterobilayer involves the formation of a moiré supercell with spatially varying energetics and optical selection rules, especially for small twist angles.

Therefore, in the first part of **Chapter 5**, selectively-grown aligned (AB) and anti-aligned (AA') homobilayers have been scrutinized. It was expected that the change in inversion symmetry should restore the spin-valley polarization, which is absent in the regular inversion symmetric bilayer type. Nonetheless, circular and linear PL-anisotropy has been surprisingly observed in the measurements for both types. Ab-initio calculation from our theory colleagues could show anisotropy for both cases originating from a change of the selection rules from spin-valley to spin-(valley)-layer locking, i.e. for a given valley the layer can in principle be selectively addressed.
Furthermore, the internal breaking of inversion symmetry in the AB-stacked bilayer leads to a lifting of the degeneracy between the bands of the layers. In addition, the external breaking of symmetry due to different half spaces, one comprised of the substrate and the other one filled with air, leads to an additional energetical splitting for both types of stacks. This enables selective excitation for each combination of valley and layer index in the AB-stacking, and for the energetically lowest state even a selective excitation becomes possible. In the AA'-stack on substrate, the degeneracy lifting is smaller but in generally also enables a preferred excitation for high-quality stacks (i.e. narrow-linewidth absorption).
An indication of these splittings could be found in measurements in agreement with these calculations. Especially, the mechanism leading to an external symmetry breaking by the dielectric environment in contrast to external fields is interesting, as the concept does not only apply to the studied material but also to other 2D-materials. Thus, the study show in summary that all semiconducting aligned or anti-aligned van-der-Waals homobilayers on substrate can in principle be used in layertronics (Jaskólski et al. 2018), whereas AB-stacks qualify for layer- and valleytronics (Mak, Xiao, and Shan 2018; Schaibley et al. 2016a) and are in fact heterojunctions.

These findings raise several interesting questions and motivate additional experiments. Potentially the amount of degeneracy lifting can be tuned by changing the permittivity contrast between both half spaces for example by exchanging the substrate to a high k-material such as TiO_2 or $SrTiO_3$ ($\epsilon_{TiO_2} = 80, \epsilon_{SrTiO_3} = 2000$ (Robertson 2004)). This could increase the magnitude of the splitting to values more feasible for applications. Also, layer-selective photocurrent measurements could be valuable to judge on the use in future applications. Or if viewed from an academic perspective, the lifting of degeneracy makes time-resolved optical studies possible, which can separately resolve the dynamics in each layer / valley combination for AB stacks or layers for AA'-stacked cases.

The second part of **Chapter 5** shows a preliminary study of a twisted heterobilayer of WS_2 and WSe_2 close to one of the high symmetry alignments, commonly giving rise to moiré patterns due to the small inter-lattice twist. The structure was characterized before and after annealing corresponding to the regime of weak and strong layer coupling, respectively. Using spatially-resolving techniques, new

features could be found in both cases, although in different magnitude. The newly arising features on the low energy side were attributed to charge-transfer states, while the states in between both intralayer peaks could be attributed to hybridized moiré exciton states similar to (Jin et al. 2019). Although the sample still showed considerable inhomogeneous broadening, a fine structure of the charge-transfer exciton similar to high quality samples (Tran et al. 2019) could be found, which is most likely related to the moiré potential landscape. Time-resolved measurements revealed a long decay time in the ns-range of the moiré states compared to the intralayer excitons, most likely due to to their indirect nature as a consequence of hybridization.

The observation of moiré states with a splitting of several tens of meV's and their quite different dynamics in this work are important, because of their implications for potential applications: 1. optoelectronics, 2. valleytronic and 3. the construction of excotic matter states. For the optoelectronic the different energetics and dynamics play the key role, while the spatially varying selection rules have consequences for their use in valleytronics. The third application is even only possible due to the moiré potential. It leads to a strong localization of charge carriers, which allows the construction of flat bands. Thus, an exciton Mott insulator similar to twisted bilayers of graphene can be constructed from such a heterobilayer. In any case the spatial and temporal dynamics of charge carriers necessarily must be understood to optimize potential devices.

This show that as a next step, a study of the dynamics is needed, including one which investigates the implications on valley decoherence and depolarization by time-resolved photoluminescence or Kerr-rotation. This should be performed in combination with a SNOM-based technique or a nano-ARPES to be able to resolve the spatially varying dynamics in the moiré landscape. Here, especially the influence of the moiré potential, which can be tuned by the twist angle, strain and material combination, should be scrutinized to allow the engineering of moiré exciton bands to the applications' needs.

Until here, all discussed measurements where performed without the selection of certain certain emission, respectively, incidence angles. However, a lot of information is lost when angle-integrated spectra are acquired. The Fourier-space spectrum contains valuable information about on emitters' radiation pattern, the in- and out-coupling efficiency of the Fabry-Pérot structure and it's angle-dependent mode profile. Furthermore, information about the in-plane center-of-mass dispersion are available due to momentum conservation. **Chapter 6** discusses angle-resolved PL and reflection contrast measurements performed at high-quality h-BN encapsulated flakes of WSe_2 and $MoSe_2$ flakes for the first time. A remarkably strong dispersion was measured in both reflection contrast (RC) and PL at cryogenic temperatures and quasi-resonant condition (PL). Angle-dependent energy shifts amount to about 2 meV within the collected light cone, corresponding to an extracted effective mass of about $4 \cdot 10^{-4}$ m_e for WSe_2 and about 1 meV or approximately $2 \cdot 10^{-4}\, m_e$ for $MoSe_2$.

To further investigate this effect, temperature- and power-dependent measurements have been carried out. A slight decline of curvature with power can be found, attributed to a smearing out of the center-of-mass dispersion at higher charge-carrier densities owing to an increasing fraction of electron-hole plasma. At elevated temperatures above 100 K, no dispersion can be extracted from the Fourier-space PL spectrum anymore. This originates from linewidth broadening and the increasing role of polaron formation for PL resonances. In contrast, the dispersion feature remained visible in RC but considerably weakened. In addition, the careful evaluation of RC data indicates a very weak dispersion for the 2s resonance. Here, measurements on additional samples are necessary for confirmation and reliable extraction.

To understand the dispersion and it dependencies, the observations were discussed in the context of predictions, which consider the (long-range) exchange interaction from a microscopical view on the

one hand, as well as polaritonic models, i.e. the coupling of the macroscopic dipole moment to the radiative field, on the other hand. Note that polaritons due to cavity effects by the Fabry-Pérot structure of the stack on substrate have been ruled out as no confined but only a leaky mode could be found in simulations. In the case of the other models many of the observed features can be explained, however, predicting weaker dispersions. The reduction of dispersion with temperature can be easily modelled by integrating the increase of dephasing due to phonons at the phenomenological level into the common semiclassical polariton model. Similarly, the carrier density dependent decrease of curvature in PL-measurements very likely can be explained by the presence of correlated plasma together with the excitons, as the former does not show a locking between center-of-mass momentum and emission angle in contrast to excitons. Or when expressed in terms of the polariton picture, the oscillator strength reduces with increasing excitation densities, weakening the light-matter coupling.

In summary, the experimental observation of the strong dispersion is in agreement with the predictions for 2D excitons (Qiu, Cao, and Louie 2015; H. Yu et al. 2014). Indeed, it proves that a strong and unusual dispersion is found for the exciton resonance at low center-of-mass momenta with possibly even quasi-linear dispersion. Thus, the common view that almost no dispersion can be obtained for excitons within the light cone must be withdrawn for such samples. While looking rather parabolic, which would agree with the argument of Deilmann (Deilmann and Thygesen 2019) that the Coulomb interaction in an encapsulated monolayer cannot be treated strictly two-dimensional, the observation with limited extraction precision cannot fully exclude a linear dispersion. Interestingly but not surprisingly, the measurable dispersion clearly vanishes if the excitation is detuned. This can be seen as a signature of uncorrelated electron-hole plasma instead of the formation of an exciton population or very low coherence time of such population.

The calculations from many-body theory result in a complex pseudo-spin texture, therefore in the second part of **Chapter 6**, the circular and linear anisotropy have been investigated as function of the emission angle. Here, a drop of helicity from about 45 % to 20% to higher emission angles was found for quasi-resonant excitation in the measurable Fourier-space range. Comparable observation are reported for valley cavity-(exciton-)polaritons (Z. Sun et al. 2017). In other words, a coupling of the center-of-mass motion to the valley pseudo-spin is clearly evidenced by the here presented investigation. The observed decline of the PL-helicity can be modeled using a phenomenological model based on the Maialle-Silva-Sham mechanism (Maialle, de Andrada e Silva, and Sham 1993) taking the lifted degeneracy as the source of an effective magnetic field. Thus, at higher in-plane momenta, the increasing hybridization of modes (H. Yu et al. 2014) trough intervalley exchange interaction can be understood to cause a faster dephasing. In contrast, the helicity decrease with increasing excitation detuning is attributed to other scattering events of the electronic system.

The remarkable observation of the dispersion motivates several follow up investigations. As the dispersion of 1s and 2s states can be seen, it would be interesting if in a pump-probe experiment the relaxation dynamics within the light cone can be measured, similar to the model-based prediction in the literature (Brem et al. 2018). While this report suggests measuring the relaxation with optical pump MIR/FIR probe without angle resolution, such angle-resolved measurements could give complimentary information.
In addition, as the splitting of the exciton branches towards higher momenta correspond to the Rabi oscillation (H. Yu et al. 2014) between both valleys, a polarization-resolved coherent detection similar to (Colas et al. 2015; L. Dominici et al. 2014) could indeed directly map this coherent oscillations and therefore directly access the valley dynamics as function of center-of-mass momentum providing a deep understanding of valley depolarization in monolayers at the quantum level.

For cavity-based (valley) polaritons (Colas et al. 2015; L. Dominici et al. 2014; W. L. Zhang et al. 2019) and monolayers (Z. Ye, Sun, and Heinz 2017) it already has been shown that control over the valley polarization is possible by external fields or employing appropriate sequences of optical pulses. If repeated for our structures, the decoherence at different magnitude of the Rabi-splitting could be evaluated for both branches.

Besides this dispersion analysis, angle-resolved PL measurements were used to analyze the radiation pattern as shown in the final part of **Chapter 6**. Here, clearly the emission between bright and dark states could be distinguished due to their different dipole alignment, in agreement with theoretical considerations in the literature for these species. The patterns directly show that the transition dipole moment is in-plane for the bright exciton and out-of-plane for a certain dark exciton species.

The successful extraction of dispersions and radiation pattern motivates to move forward to type-II heterostructures with moiré and interlayer states. It could also be used to investigate nanophotonic structures which optimize the outcoupling of type-II emission perpendicular to the plane. This would be valuable as the expected in-plane radiation is not beneficial for some optoelectronic application and hinders the use of multi quantum well designs.

The final investigation presented in **Chapter 7** deals with the integration of a TMDC monolayer to a nanophotonic structure for optical outcoupling. Here, a circular Bragg grating was designed, and a monolayer was integrated by a dry transfer step. By means of PL-mapping and s-SNOM/AFM, the working principles were confirmed experimentally. Besides small deviations from the actual design, a nano-focus and an enhanced PL-extraction could be achieved. We related the deviations to the bending of the monolayer at the edges of the structure which introduces strain, changes the alignment of the transition dipole with respect to the field and also affects the interferences that are designed for efficient in- and outcoupling. One has to conclude, that while the performance was still surprisingly close to the prediction and the integration of the Monolayer can be achieved easily, similar effects will generally occur in many nanophotonic structures and should be considered in the design in order to reach the expected performance.

The facile integration motivates consecutive designs. Here especially, it is not immediately clear how the different transition dipole alignment will affect the integration if designed for a type II exciton. Furthermore, the proposed structure creates a nano-focus without any selectivity for polarization. During the time of this PhD study some initial chiral design and fabrication concepts have been discussed and created, which theoretically favor a certain helicity and therefore could link nanophotonics to valleytronics. Nonetheless, the simplicity of integration in this more basic pattern motivates to further work on this approach to realize potential building blocks linking nanophotonics, especially based on silicon photonics, to TMDC and valleytronics.

In addition, as 2D materials are knowingly very sensitive to the environment, the FIB-based structures generally also allow the spatial modulation of the band structure for example to design QDs or imprint artificial moiré patterns to the TMDC monolayer.

9. Zusammenfassung und Ausblick

In diesem letzten Kapitel möchte ich die experimentellen Ergebnisse nochmal kompakt darstellen und ihren Einfluss auf zukünftige Anwendungen erläutern. In den letzten Jahren haben sich van-der-Waals Materialien als eine neue Teildisziplin der Halbleiterphysik zwischen dem Studium klassischer anorganischer Halbleiter einerseits und molekularen Halbleitersystemen andererseits etabliert. Aufgrund der Möglichkeit, jegliche Van-der-Waals Materialien zu Heterostrukturen kombinieren zu können, ohne hierbei durch die Größe der Einheitszelle oder den Drehwinkel zwischen zwei Monolagen limitiert zu sein, wurde ihnen großes Interesse zu Teil. Darüber hinaus bietet diese Materialklasse aber auch die Möglichkeit exotische Physik oder quantenmechanischen Phasen, wie zum Beispiel Spin-Tal Kopplung oder stark korrelierten exzitonischen Mott-Isolatoren, unter deutlich einfacheren Bedingungen zu realisieren und zu untersuchen. Da sich das elektrische Feld der Coulomb Wechselwirkung innerhalb von Exzitonen in diesem Quantenmaterial nicht nur auf die Monolage selbst beschränkt, sondern sich auch in dessen Umgebung erstreckt, ist es offensichtlich, dass die Umgebung einen großen Einfluss auf die Coulomb-Wechselwirkung und damit auf die elektronische Bandstruktur hat. Um die optoelektronischen Eigenschaften solcher Materialien sowie Möglichkeiten ihrer Manipulation besser zu verstehen, ist es von herausragender Bedeutung diesen Einfluss der Umgebung systematisch zu untersuchen. Aufgrund dieser Tatsache befasst sich diese Arbeit zunächst mit dem Einfluss der Umgebung, bevor sie sich anderen Aspekten, welche die Eigenschaften von TMDCs beeinflussen, wie die relative Anordnung und den Drehwinkel zwischen zwei Monolagen in Homobilagen und Heterostrukturen. Daran anschließend werden optische Dispersionsmessungen an hochqualitativen in h-BN gekapselte Monolagen diskutiert, und abschließend ein nanophotonisches Konzept vorgestellt und analysiert, welches die Auskopplung von Photolumineszenz von Monolagen erhöht.

Kapitel 4 fasst wichtige Wechselwirkungen von 2D-Materialien mit ihrer Umgebung zusammen. Zunächst werden der Einfluss der mesoskopischen Eigenschaften der Umgebung wie die dieelektrische Konstante, Rauigkeit, Verspannung und Ladungsinhomogenitäten auf die Photolumineszenz und deren Dynamik am Beispiel von WSe_2 dargestellt. Durch gründliche Analyse der PL-Spektren und ihrer Dynamik auf verschiedenen Substraten in diesem Teil der Arbeit konnten Anzeichen von substrat-induzierten Verspannungen sowie lokaler Dotierung gefunden werden. Die verschiedene Dotierung der Proben kann hier durch eine relative Änderung des Intensitätsverhältnisses von trionischer und exzitonischer PL identifiziert werden. Diese Änderung des Intensitätsverhältnisses stimmt mit anderen Studien (Chernikov, Van Der Zande, et al. 2015) überein, in denen durch Anlegen eines externen Feldes die Dotierung gezielt beeinflusst wird. Verschiedene Verspannungen zeigen sich hingegen in den diskutierten Spektren durch eine Vergrößerung der Linienbreite und eine verstärkte Emission aus rotverschobenen lokalisierten Zuständen. Solch spektrale Eigenschaften konnten wie erwartet insbesondere bei der Verwendung von nicht atomar glatten Substraten beobachtet werden. Es konnte ebenfalls eine Verringerung der zirkularen Anisotropie durch substratinduzierte Dotierung oder Verspannungen beobachtet werden. Nur in Fällen prägnanter Helizität der Emission bei gleichzeitig niedriger Dotierung können exzitonische Moleküle und andere höhere Vielteilchenkomplexe beobachtet werden. Zusammenfassend muss daher ein möglichst atomar flaches, sauberes Substrat, welches eine geringe Polarität aufweist, als ein Schlüssel für die Beobachtung niedriger Linienbreiten und exzitonischer Komplexe angesehen werden. Diese Schlussfolgerung wurde später von anderen Forschergruppen bei Messungen an Proben mit verbesserter Qualität (S.-Y. Chen et al. 2018) bestätigt.

Darüber hinaus konnte in der hier vorgestellten Arbeit zwar kein klarer Trend jedoch Indizien für einen Zusammenhang zwischen der Verschiebung der zentralen Wellenlänge exzitonischer Emission mit dem Brechungsindex des Substrates gefunden werden. Dieser Befund fügt sich nahtlos in spätere

theoretische Vorhersagen mehrerer Arbeitsgruppen (Lars Meckbach, Stroucken, and Koch 2018b; Raja et al. 2017) ein, welche die richtige Modellierung der Ladungsträgerabschirmung als Schlüssel sehen, um eine zutreffende Vorhersage für Monolagen zu treffen. Obwohl der Einfluss des Substrats zunächst subtil erscheinen mag, da sich die Bandkanten Renormalisierung und die Änderung der Bindungsenergie einander nahezu aufheben, so ist doch das Substrat und die sich bildende Grenzschicht von herausragender Bedeutung für die Herstellung hochqualitativer Proben. Die hier durchgeführten Untersuchungen zeigen, dass hexagonales Bornitrid (h-BN) ein ideales, flaches Substrat für geschichtete Übergangsmetalldichalogenide ist, da es keine ungesättigte Bindungen besitzt und wird nun bereits routinemäßig von vielen Gruppen (Ajayi et al. 2017; Cadiz et al. 2017; S.-Y. Chen et al. 2018; Rhodes et al. 2019) verwendet. Zusätzlich wir nun meist ein Gate verwendet, um verbleibende substratinduzierte Dotierung auszugleichen.

Daher wird im zweiten Teil von **Kapitel 4** der Einfluss von h-BN in verschiedenen Anordnungen mit WSe_2 untersucht. Hierbei wurde WSe_2 auf, unter bzw. zwischen zwei mehrlagigen Stücken aus h-BN als Probe verwendet. Diese Untersuchung wurde zeitgleich mit anderen Forschungsgruppen (Ajayi et al. 2017; Cadiz et al. 2017; Wierzbowski et al. 2017) durchgeführt. Das Ergebnis der hier vorgelegten Studie stimmt mit den genannten insofern überein, dass die Einkapselung von Monolagen in Bornitrid die optische Qualität deutlich erhöht, d. h. es ermöglicht intrinsisch verbreiterte Proben zu erhalten. Dennoch gibt es auch Unterschiede.
Die hier vorgestellte Studie hat ihren Fokus auf der Kopplung zwischen Gitterschwingungen und Exzitonen sowie der Untersuchung der Ladungsträgerdiffusion, welche in den anderen Studien nicht abgedeckt werden. In den hier vorgestellten, systematischen Messungen konnte gezeigt werden, dass es bei Einkapselung oder Abdeckung der Monolage – interessanterweise genügt hier bereits eine einzige Lage $MoSe_2$ –zu einer Verschiebung und deutlichen Schmälerung der A-Exziton Resonanz kommt. Es konnte geschlussfolgert werden , dass die Verschiebungen einerseits auf eine Verringerung der Inhomogenitäten in der Probe, andererseits auf die Veränderung der Ladungsträgerabschirmung zurück zu führen sind, wie in zeitgleichen theoretischen Publikationen bestätigt wurde (Stroucken and Koch 2017). Da bereits die Abdeckung durch eine einzelne Lage Verschiebungen ähnlicher Größenordnung hervorruft, kann geschlossen werden, dass die Ladungsträgerabschirmung tatsächlich vor allem durch die wenigen direkt anliegenden Lagen beeinflusst wird. Die beobachteten Verbesserungen durch h-BN-Einkapselung in Bezug auf verringerte Unordnung und reduzierter nichtstrahlender Rekombination sind essentiell, da fast alle Anwendungen zumindest von ihnen profitieren, wenn nicht gar benötigen.

Da eine solche Veränderung die Kopplung zwischen Phononen und Elektronen beeinflussen sollte, wurde die Photolumineszenz und deren Dynamik in Abhängigkeit der Anregungsdichte und der Temperatur untersucht. Es kann generell eine starke Kopplung von Gitter und Elektronensystem in WSe_2 beobachtet werden. Durch die Modellierung der Emissionsenergie und deren Linienbreite mittels phänomenologischer Formeln, kann insbesondere eine vergleichsweise starke Kopplung mit optischen Phononen und akustischen Phononen abseits des Γ-Punktes festgestellt werden, welche sich durch die Formation von Phononenseitenbanden oberhalb von 100 K zeigt. Gleichfalls kann in diesem Temperaturbereich auch eine qualitative Veränderung in der Dynamik und PL-Linearität beobachtet werden. Durch einen Vergleich von Proben in unterschiedlicher Umgebung konnte diese Studie zeigen, dass in der Tat die dielektrische Umgebung einen systematischen Einfluss auf die Exzitonen-Phononenkopplung hat. Die erhaltenen Parameter zeigen, dass sich für eingekapselte Proben die Wechselwirkung mit Phononen fernab des Γ-Punktes um 15% gegenüber Proben auf SiO_2 abschwächt. Diese Änderung ist daher nicht vernachlässigbar. Darüber hinaus zeigen die angewandten Modelle, dass die Exzitonen-Phonon Kopplung stärker ist als die für Trionen. Dies könnte auf eine schwächere Oszillatorstärke zurückzuführen sein, welche die Wechselwirkung mit phononen-

assistierter Polarisation verringert. Nichtsdestotrotz sind Vielteilchen-Rechnungen nötig, um die genaue Ursache dieses Befundes zu verstehen.

Im letzten Teil von **Kapitel 4** wird die Annihilation zwischen Exzitonen durch leistungsabhängige TRPL Messungen analysiert. Hier konnten zum ersten Mal systematische Änderungen der Diffusionskonstante aufgrund der Stapelumgebung gefunden werden. Um das Phänomen genauer zu beleuchten, wurden die Daten sowohl mit Vorhersagen eines Modells, welches eine Förster Wechselwirkung zu Grunde legt, als auch eines zweiten Modells verglichen, welches eine einfache Diffusion mit anschließendem Auger Prozess vermutet. Es konnte geschlussfolgert werden, dass diffusionslimitierte Annihilation vorliegt, sodass ein Rückschluss auf die exzitonischen Diffusionskonstanten möglich wird. Die Studie zeigt, dass in Proben auf bzw. zwischen h-BN Schichten eine erhöhte Exzitonendiffusion im Vergleich zu Proben auf Siliziumdioxid vorherrscht. Die Änderung der Annihiliationsraten wird nicht nur durch unterschiedlich Diffusion, sondern auch durch einen vergrößerten Exziton Bohrradius beeinflusst. Die deutlich homogenere Grenzschicht mit weniger Unebenheiten und Unordnung ist wahrscheinlich die Hauptursache der erhöhten Diffusion. Die hier bestimmten Diffusionskonstanten (im Bereich von $D \approx 10\, nm^2/ps$) konnten durch spätere unabhängigen direkten Messungen der zeitabhängigen Ladungsträgerverteilung anderer Gruppen (Kulig et al. 2018) bestätigt werden. Die beobachtete erhöhte Exzitonen Diffusion und die entsprechend gesenkte Auger-Rekombination sind insbesondere für Photovoltaik und Laseranwendungen hilfreich, da sie deren Effizienz steigern. Es muss daher aus den hier vorgestellten Messungen geschlossen werden, dass die Umgebung generell einen großen Einfluss auf die Diffusion hat und h-BN Einkapselung im Speziellen als ein Werkzeug zur Erhöhung der mittleren Diffusionslänge gegenüber Siliziumdioxid und somit zur Optimierung in vielen Anwendungen benutzt werden kann.
Um die Diffusion und die mikroskopische Ursache der Unterschiede und den Einfluss von Kristalldefekten und Unordnung (Rhodes et al. 2019) zu verstehen, könnten zeitaufgelöste SNOM Messungen ein wertvolles Werkzeug sein. Dies gilt insbesondere in Moiré-Übergittern, da hier ein nicht trivialer Ladungsträgerfluss zu erwarten ist (Yuan et al. 2019).

Während **Kapitel 4** die mesoskopischen Einflüsse der Umgebung diskutiert hat, so befasst sich **Kapitel 5** mit dem Einfluss der exakten mikroskopische Anordnung zweier Monolagen in hochsymmetrischer angeordneten Homobilagen sowie in leicht verdrehten Heterobilagen. Während sich im ersten Fall nur die Auswahlregeln und die interne Symmetrie ändern, so bildet sich im zweiten Fall ein Moiré-Übergitter aus mit lokaler, sich periodisch ändernder Energetik und optischen Auswahlregeln, welches insbesondere für kleine relative Rotation zwischen den Lagen von Bedeutung ist.

Daher werden im ersten Teil von **Kapitel 5** selektiv gewachsene ausgerichtete (AB) und entgegengesetzt ausgerichtete (AA') Homobilagen untersucht. Im Fall gebrochener Inversionsymmetrie wurde eine Wiederherstellung der Talpolarisation erwartet, die in der üblicherweise untersuchten Bilage nicht vorherrscht. Interessanterweise kann trotzdem in den Messungen beider Proben sowohl zirkulare als auch lineare Anisotropie beobachtet werden. Ab-Initio Rechnungen konnten die Anisotropie in beiden Fällen zeigen, jedoch aufgrund einer anderen mikroskopischen Ursache, da eine Änderung der Auswahlregeln von einer festen Korrelation von Spin-Tal zu Spin-(Tal)-Lage stattfindet. Demnach kann für eine gegebenes Tal nun eine spezifische Lage angeregt werden.
Darüber hinaus führt die interne Brechung der Symmetrie in der AB-Bilage zu einer Aufhebung der Entartung der Zustände zwischen den Lagen. Ebenfalls konnte gezeigt werden, dass für eine Flocke auf einem Substrat in der Tat, durch die Brechung der Inversionssymmetrie der Umgebung, ebenfalls die Entartung leicht aufgehoben wird. Auch diese Vorhersage konnte in dieser Arbeit durch

Reflektionskontrast Messungen bestätigt werden. Diese Aufhebung der Entartung ermöglicht die selektive Anregung eines bestimmten Tales in einer ausgewählten Lage in einem AB-Stapelung. Im Gegenzug ist dies auch in einem hochqualitativen AA'-Stapel möglich, sofern sich die Probe auf einem Substrat befindet, jedoch ist die Aufspaltung kleiner. Auch dies konnte in der hier vorgestellten Studie bestätigt werden. Insbesondere der Mechanismus, die Entartung durch ein Substrat aufzuheben, ist im Gegensatz zu anderen externen Möglichkeiten wie elektrischen und magnetischen Feldern interessant. Denn der Mechanismus ist nicht nur für das untersuchte Material gültig, sondern sollte generell für jede Van-der-Waals Bilage gültig bleiben. Daher kann als Fazit dieser Studie geschlussfolgert werden, dass alle hochsymmetrischen VdW-Bilagen auf Substrat generell als ein Baustein im Paradigma von „Layertronics" (Jaskólski et al. 2018) verwendet werden können, während ein AB-Stapel sowohl in „Layer- " als auch in „Valleytronics" (Mak, Xiao, and Shan 2018; Schaibley et al. 2016b) eingesetzt werden kann. Beide Stapelmöglichkeiten auf Substrat müssen darüber hinaus aufgrund der Aufspaltung tatsächlich als Heterostrukturen angesehen werden.

Hieraus ergeben sich mehrere interessante Fragestellungen und weiterführende Experimente. Höchstwahrscheinlich kann die Stärke der Aufspaltung der Entartung durch die Änderung des Permittivitätskontrasts zwischen oberen und unterem Halbraum beeinflusst werden, z.B. durch die Ersetzung des verwendeten Siliziumdioxids durch ein „high-k" Material wie TiO_2 or $SrTiO_3$ ($\epsilon_{TiO_2} = 80, \epsilon_{SrTiO_3} = 2000$ (Robertson 2004)). Dies könnte die Aufspaltung erhöhen, sodass diese für Anwendungen nützlicher wird. Auch lagenabhängige Photostrommessungen könnten wertvolle Einblicke ermöglichen, um die Nutzbarkeit in der Anwendung besser einschätzen zu können. Andererseits ermöglicht die Aufhebung der Entartung zeitaufgelöste, optische Messungen in denen die Dynamik der Bandstruktur-Täler und Lagen getrennt vermessen werden kann.

Der zweite Teil von **Kapitel 5** untersucht in einer vorläufigen Studie eine leicht verdrehte Heterobilage aus WS_2 und WSe_2, in der üblicherweise ein Moiré Übergitter beobachtet wird. Die Probe wurde sowohl vor als auch nach einem Ausheizschritt untersucht, um die Eigenschaften bei schwacher und starker Lagenkopplung zu erforschen. Durch örtlich aufgelöste Messungen der Photolumineszenz bzw. des Reflektionskontrastes konnten neue spektrale Merkmale im Bereich der Heterostruktur identifiziert werden. Im Regime starker Kopplung sind diese deutlich ausgeprägter, können jedoch bei genauer Analyse auch im Fall schwacher Kopplung beobachtet werden. Die neuen Merkmale im niederenergetischen Bereich wurden als Typ-II Exzitonen identifiziert, während die Spektrallinien zwischen den Intralagen Exzitonen hingegen vermutlich auf hybridisierte Zustände aufgrund des Moiré-Übergitters zurückzuführen sind, ähnlich wie bei Jin (Jin et al. 2019). Obwohl die verwendete Probe noch deutlich inhomogene Verbreiterung aufweist, konnte eine Feinstruktur des Typ-II Exzitons beobachtet werden, vergleichbar mit Messungen an hochqualitativen Proben (Tran et al. 2019). Diese dürfte ihren Ursprung ebenfalls in der Ausbildung eines Moiré-Potentials haben. Darüber hinaus konnten zeitaufgelöste Messungen eine deutlich verlängerte PL-Abklingzeit (im zweistelligen Nanosekundenbereich gegenüber dem einstelligen Pikosekundenbereich) gegenüber jener der Intralagenexzitonen für diese hybridisierten Zustände feststellen. Dies deutet auf teilweise indirekte Übergänge aufgrund der Hybridisierung hin.

Die Beobachtung solcher Moiré-Zustände mit Aufspaltung von einigen 10 meV's sowie deren deutlich veränderte Dynamik in dieser und anderen Arbeiten zeigen bereits die große Bedeutung des Effektes für potentielle Anwendungen in 1. Optoelektronik, 2. „Valleytronic" und 3. der Konstruktion exotischer Materie. Für die Optoelektronik ist die veränderte Energetik und Dynamik ausschlaggebend, während es für die „Valleytronic" die örtlich sich ändernden Auswahlregeln sind. Das dritte Anwendungsgebiet wird überhaupt erst durch das Moiré-Übergitter möglich. Es erlaubt aufgrund der starken Lokalisation

der Ladungsträger, die Konstruktion sehr flacher Bänder. Daher wird die Untersuchung exotischer Quantenzustände wie exzitonischen Mott Isolatoren (Lei Wang et al. 2019), ähnlich zu den Beobachtungen an Graphenebilagen (Y. Cao, Fatemi, Demir, et al. 2018), möglich. In jedem Fall ist es nötig, die zeitliche und örtliche Dynamik besser zu verstehen, um sie für potenzielle Bauteile zu optimieren und nutzen zu können.

Als nächster Schritt sollte daher die Dynamik, insbesondere die Mechanismen der Tal-Dekohärenz sowie Depolarisation, durch zeitaufgelöste Messungen der Photolumineszenz oder Kerr-Rotation untersucht werden. Hier ist insbesondere der Einfluss des Moiré-Potentials von Interesse, welches durch Verdrehwinkel, Verspannung sowie Materialkombination kontrolliert werden kann, um das gezieltes Design von Moiré-Exzitonen zu ermöglichen. Hierzu könnten SNOM basierte Techniken oder (spinaufgelöstes) nano-APRES verwendet werden, um die lokale Abhängigkeit des Moiré-Übergitters sowie die lokale Ladungsträger-Dynamik erfassen zu können.

Bis hier wurden alle diskutierten Messungen winkelintegriert durchgeführt, d.h. ohne Selektion von Einstrahl- bzw. Emissionwinkel. Jedoch gehen dadurch wichtige Informationen verloren. Fourier-Raum Spektren enthalten viele wertvolle Informationen bzgl. der Abstrahlcharakteristik des Emitters, der Ein- Auskopplungseffizienz der Fabry-Pérot Struktur und des winkelaufgelösten Modenprofils. Darüber hinaus können aufgrund der Impulserhaltung Informationen über die Schwerpunktsdispersion innerhalb der Lage gewonnen werden. **Kapitel 6** diskutiert daher zum ersten Mal winkelaufgelöste Messungen der Emission und des Reflektionskontrastes an hochqualitativen, von h-BN eingekapselten Monolagen aus WSe_2 bzw. $MoSe_2$. Bei tiefen Temperaturen und quasi-resonanter Anregung konnte sowohl für PL-Messungen als auch Messungen des Reflektionskontrastes eine bemerkenswert starke Dispersion beobachtet werden. Innerhalb des Messbereichs wurde eine winkelabhängige Blauverschiebung von circa. 2 meV entsprechend einer effektiven Masse von ungefähr $4 \cdot 10^{-4}$ m_e für WSe_2 gemessen bzw. 1 meV oder $2 \cdot 10^{-4}\ m_e$ für $MoSe_2$.
Um das Phänomen eingehender zu untersuchen, wurden sowohl temperatur- also auch leistungsabhängige Messungen durchgeführt. Im Fall der Variation der Anregungsdichte, konnte eine leichte Abschwächung der Dispersion festgestellt werden. Dies wird höchstwahrscheinlich durch einen größeren Anteil von freiem Elektron-Loch Plasma im Gegensatz zu Exzitonen hervorgerufen. Hingegen wurde in temperaturabhängigen PL-Messungen ein komplettes Verschwinden der Dispersion oberhalb von 100 K gefunden. Dies wird zum einen durch eine erhöhte Linienbreite verursacht, aber auch durch den stärkeren Einfluss von Polaroneffekten wie Phononenseitenbanden. In Reflektionskontrastmessungen hingegen konnte nur eine Abschwächung festgestellt werden, zusätzlich erlaubte dies auch die Dispersion der 2s-Resonanz zu studieren. Hier konnte eine sehr schwache Dispersion beobachtet werden, jedoch sind weitere Messungen an zusätzlichen Proben nötig, um dies zu bestätigen und eine zuverlässige Bestimmung zu ermöglichen.

Um die Ursache der Dispersion und ihrer Abhängigkeiten zu erörtern, wurde die Krümmung zum einen mit einer Vorhersage einer mikroskopischen Theorie, welche lang-reichweitige Austauschwechselwirkungen als Ursache annimmt, zum anderen mit makroskopischen Polaritonmodellen, welche die Kopplung mit dem makroskopischen Dipolmoment beschreiben, verglichen. Die Bildung von Kavitätspolaritonen konnten ausgeschlossen werden, da keine stark eingeschlossene Mode gefunden werden konnte. Die beiden anderen Modelle können zwar viele der beobachteten Zusammenhänge erklären, allerdings sagen beide eine etwas schwächere Dispersion als beobachtet voraus. Die Abnahme der Dispersion mit der Temperatur kann bei phänomenologischer Integration der von Phononen hervorgerufene erhöhte Dephasierung modelliert werden. Gleichfalls kann ein erhöhter Anteil an Plasma bzw. anregungsinduziertzer Dephasierung eine Abnahme der

Dispersion in der leistungsabhängigen Messung erklären, da für freie Ladungsträger keine Korrelation zwischen Schwerpunktsimpuls und Abstrahlwinkel besteht.
Als Resultat der Studie muss festgehalten werden, dass der experimentelle Befund der starken Dispersion die Vorhersagen für 2D Exzitonen von (Qiu, Cao, and Louie 2015; H. Yu et al. 2014) zum Teil bestätigt und sogar eine lineare Dispersion möglich erscheinen lässt. Daher muss das herkömmliche Bild der verschwindend geringen Dispersion innerhalb des Lichtkegels für diese Proben revidiert werden. Obwohl die Messungen noch eher parabolisch erscheinen, was mit dem Argument von (Deilmann and Thygesen 2019), dass die Coulomb-Wechselwirkung in einer eingekapselten Monolage nicht strikt zwei-dimensional behandelt werden kann, übereinstimmt, so kann eine lineare Dispersion durch die Messungen jedoch nicht völlig ausgeschlossen werden. Nicht überraschend verschwindet die messbare Dispersion, wenn die Anregung stark blau verstimmt wird. Dies kann durch mehr Plasma bzw. deutlich kürzere Kohärenzzeiten erklärt werden.

Die Vorhersagen sprechen ebenfalls von einer komplexen Pseudo-Spin Textur. Daher wird im zweiten Teil von **Kapitel 6** die zirkulare und lineare Anisotropie als Funktion des Abstrahlwinkels diskutiert. Hier konnte eine Abnahme der zirkularen Anisotropie von 45% auf 20% mit höherem Winkel bei quasiresonanter Anregung festgestellt werden, vergleichbar mit einigen Veröffentlichungen zu Tal-Kavität-Polaritonen (Z. Sun et al. 2017). Mit anderen Worten es wurde eine Kopplung der Schwerpunktbewegung und des Tal-Pseudo-Spins festgestellt. Die Abnahme der Helizität der PL-Emission kann durch ein phänomenologisches Modell, basierend auf dem Maialle-Silva-Sham Mechanismus mit der Aufspaltung der Exzitonenbandstruktur als Quelle des effektiven magnetischen Feldes, beschrieben werden. Daher muss die stärkere Hybridisierung bei größeren Impulsen (H. Yu et al. 2014) aufgrund der Austauschwechselwirkung als Grund für die stärkere Tal-Dephasierung angesehen werden. Im Gegensatz dazu ist die abnehmende Helizität mit der Anregungsenergie durch andere Streuprozesse bestimmt.

Die bemerkenswerte Beobachtung der Dispersion motiviert neue Experimente. Die Beobachtung der Dispersion höherer angeregter Zustände in Reflektionskontrastmessungen sollte eine zeitaufgelöste Messung des Aufbaus und der Relaxation des Exciton-Polariton in einem Anrege-Abfrage-Experiment ermöglichen, ähnlich zu dem Vorschlag von (Brem et al. 2018). Die dort vorgeschlagene Messung in einem optischen-Anrege THz-Abfrage Experiment ist jedoch schwer mit Fourier-Spektroskopie zu verbinden, sodass ein solches Experiment komplementäre Resultate liefern könnte. Da die Aufspaltung einer Rabi-Oszillation (H. Yu et al. 2014) zwischen beiden Tälern entspricht, könnte eine polarisationsaufgelöste Messung mit kohärenter Detektion vergleichbar mit (Colas et al. 2015; L. Dominici et al. 2014) die direkte Messung der Oszillationen und somit der Tal-Dephasierung als Funktion der Scherpunktimpulses ermöglichen.

Für Kavitätsbasierte Tal-Polaritonen (Colas et al. 2015; L. Dominici et al. 2014; W. L. Zhang et al. 2019) und Monolagen (Z. Ye, Sun, and Heinz 2017) konnte bereits gezeigt werden, dass die Helizität durch äußere Felder oder optischer Pulsfolgen kontrolliert werden kann. Durch eine Wiederholung dieser Experimente an einer hochqualitativen Probe, in der die beiden Exzitonenäste klar zu beobachten sind, könnte die Talkohärenz als Funktion der Rabi-Aufspaltung vermessen werden und somit eine tieferes Verständnis der Wechselwirkung zwischen den beiden Tälern erlangt werden.

Neben der Vermessung der Dispersion konnten die Winkelabhängigen Messung auch genutzt werden, um die Abstrahlcharakteristik der Proben zu untersuchen, wie im letzten Teil von **Kapitel 6** gezeigt. Hierbei konnte ein klarer Unterschied zwischen optisch hellen und dunklen Zuständen festgestellt

werden. Während den hellen Zuständen ein in der Ebene liegender Dipol zugeordnet werden muss, korrespondieren bestimmte dunklen Zustände zu einem aus der Ebene zeigendem Dipolmoment.
Diese erfolgreiche Bestimmung motiviert das Konzept für Typ-II bzw. Moiré-Zustände zu verwenden, in denen ebenfalls eine andere Ausrichtung des Übergangsdipolmoments erwartet werden kann z.B. senkrecht zu den Lagen für Typ-II Exzitonen. Da dies für die meisten Anwendungen nicht günstig ist, könnte die Methode ebenfalls zu Optimierung photonischer Strukturen benutzt werden, um die Licht Auskopplung gezielt zu optimieren. Außerdem könnte eine Messung der Dispersion in diesen Fällen ebenfalls interessante Einblicke liefern.

Die letzte in **Kapitel 7** vorgestellte Studie befasst sich mit der Integration von TMDC Monolagen in eine nanophotonische Strukturen zur optimierten Auskopplung der PL. Im vorliegenden Fall wurde eine zirkulare Bragg-Struktur entworfen und die Monolage durch einen trockenen Transferprozess integriert. Durch örtliche Auflösung der PL und SNOM/AFM Messungen wurden die theoretischen Überlegungen experimentell bestätigt. Trotz kleinerer Abweichung konnten der Nanofokus und die erhöhte Extraktion der PL als Ziele erreicht wurden. Die Abweichungen konnten auf die Krümmung der Monolage, welche Verspannungen induziert und gleichzeitig die Ausrichtung des Dipols bzgl. des Feldes ändert, zurückgeführt werden. Darüber hinaus beeinflusst eine solche Biegung der Monolage auch die Interferenzen, welche die Ein- bzw. Auskopplung optimieren. Obwohl die erreichte Erhöhung der Auskopplung bemerkenswert ist, so ist doch klar, dass die eben beschriebenen Probleme in vielen nanophotonischen Strukturen, die mit TMDC kombiniert werden, auftreten können und werden. Es kann also schlussgefolgert werden, dass die Integration zwar im Prinzip relativ einfach zu bewerkstelligen ist, die zu erwarteten Biegungen der Monolage sollten jedoch bereits bei dem Design der Struktur berücksichtigt werden, um ein optimales Ergebnis zu erhalten.

Auch hier bieten sich direkt Folgeexperimente aufgrund der recht einfachen Integration von Monolagen in solche Systeme an. So wäre es interessant wie sich, der veränderte Dipolmoment eines Typ-II Exzitons auf die Funktion der Struktur auswirkt. Darüber hinaus wäre es von Interesse die Struktur in derart zu modifizieren, dass sie eine zirkulare Polarisation bevorzugt und somit als ein verstärkender Faktor für „Valleytronics“ eingesetzt werden kann. In der Zeit der Dissertation wurde hierzu bereits erste selektive Strukturen entworfen und hergestellt. Eine Weiterentwicklung derselbigen könnte die Bereiche der Nanophotonik und der Valleytronic verbinden und neue Anwendungsszenarien erschließen. Bei der Verfeinerung dieser Designs sollte insbesondere auf Möglichkeiten der Integration in Silizium basierte Photonik geachtet werden.
Generell könnte ein solches künstlich strukturiertes Substrat auch genutzt werden, um künstlich ein Moiré Übergitter oder Lokalisation der Ladungsträger zu erreichen. Auch hier wurden bereits erste Versuche unternommen.

Appendix

A1 Materials

A complete list of chemicals used throughout the thesis is given in Table 9. If possible, additional information given by the company like common defect concentration, purity, known dopants and similar things are also stated. The given defect rates are to be understood as the one of the bulk crystals. The process of exfoliation, oxidation and reaction with adsorbates and so on can of course significantly increase the defect rate achieved in a monolayer system (Edelberg et al. 2019b; Rhodes et al. 2019). For the tapes the adhesion is specified if possible.

Table 9 List of chemicals and raw crystals used during the thesis

Chemical	Company	Information
WSe_2	Manchester Nanomaterials	Grade A
h-BN	Manchester Nanomaterials	Grade A
PDMS	Gel Pack	
Magic Scotch tape	Scotch	Adhesive 22 µm Synthetic Acrylic, 2.5 N/cm Adhesion to Steel
RAPGARD TDS F6F Tape	Nitto	
SPV 5058A5 Tape	Nitto	Adhesive 50 µm Synthetic Acrylic, 35 cN/cm Adhesion to Steel
n-Si/SiO_2 (300nm)	IDB Technologies Ltd	
n-SI/SiN_x (75 nm)	IDB Technologies Ltd	
Sapphire	Plano	
Aceton	Sigma Aldrich	Optical Quality
Isopropanol	Sigma Aldirch	Optical Quality
Deionized Water	n.A.	

A2 Substrate Influence at Room Temperature

In this section the influence of the substrate on the PL-spectra at room temperature (cf. **Figure A1**) will be shown for the samples discussed in Chapter 4. Compared to the measurements at low temperatures the effect is more subtle, nonetheless small changes in the trion/exciton ratio indicating different induced doping levels as well as linewidth changes that indicate different levels of inhomogeneity in the samples.

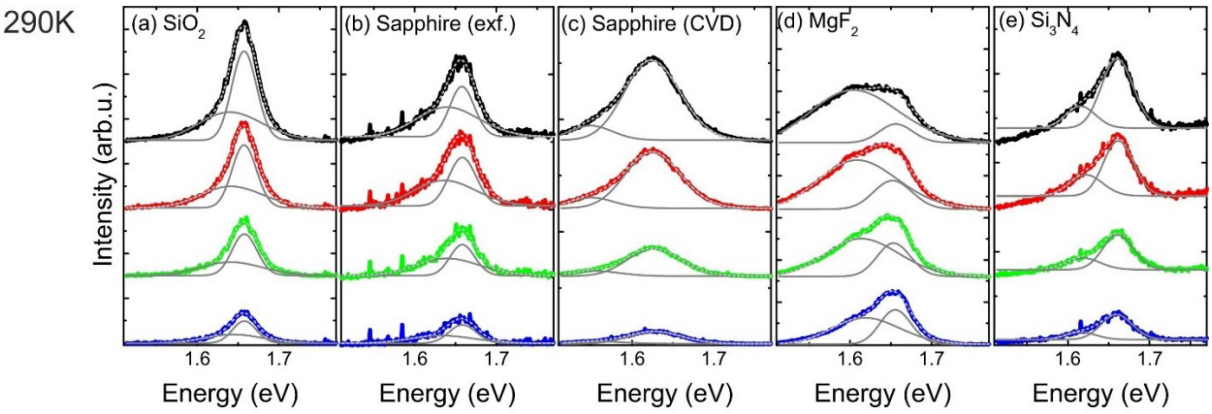

***Figure A1* | Comparison of the Power Dependent Spectra for Different Substrates at Room.** The PL-spectra were taken with average power densities of 0.34 kW/cm$_2$ to 3.4 kW/cm^2 at pulsed excitation with 2.75 eV. The PL was collected with a 20x objective. The figure has been adopted with changes from (Lippert et al. 2017) under the Creative Commons Attribution 3.0 license.

A3 Linearity Analysis of PL Emission for Flakes on Different Substrates

This appendix shows the linearity analysis at 10 K that has been used to assign the different peaks to excitonic, biexciton and localized/trap states. Similarly, also the peaks at room temperature were analyzed. The intensity was taken from the Gaussian fits, which have been used to extract the peaks energy, and plotted on double logarithmic scale. In a second step a pseudo-linear fit ($I_{PL} = I_{pump}^{\alpha}$) was performed to extract the linearity α of the different excitonic species. Here excitons and trion should ideally have a linearity of one (Brener et al. 1992; Chiari et al. 1998), states that are localized due to defects or disorder are normally observed at lower values close to 0.5 (Brener et al. 1992) and biexciton and plasma emission at a linearity of two (Hader, Moloney, and Koch 2005; You et al. 2015). However, as this reasoning is coming from simple rate equations, deviations due to additional recombination and pumping channels can occur. The different behavior can be clearly seen for all samples most strikingly for the sample on SiO_2 and h-BN. Nonetheless, due to additional relaxation channels that are not considered in these simple rate equations, linearity factors slightly smaller than 1 still can be identified as exciton or just clearly distinguishable as superlinear (<1.2) can be also identified as biexcitons.

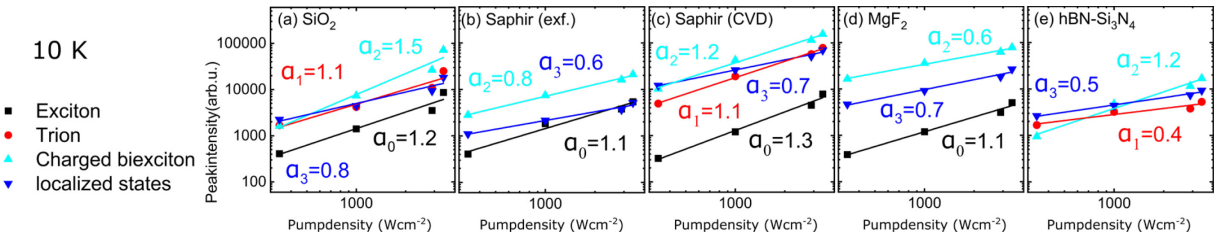

***Figure A2* |Linearity Analysis of the Different Excitonic Complexes Observed for WSe_2 Samples on Different Substrates.** (a-e) double logarithmic plot of the peak intensity of the different excitonic species on different substrates. A power-law has been fitted to the data to extract their linearity. The figure has been adopted with changes from (Lippert et al. 2017) under the Creative Commons Attribution 3.0 license.

A4 Analysis of Temperature Dependent Spectra and Dynamics for Other Stacks of h-BN and WSe_2

As already stated in chapter 4.3.1, temperature dependent analysis has also performed for the other stacks discussed in this chapter. In this appendix the temperature dependent shift (cf. **Figure A3**) as well as another example of the linearity analysis (cf. **Figure A4**) is shown. In all of them the same trend than discussed in chapter 4.3.1 can be observed.

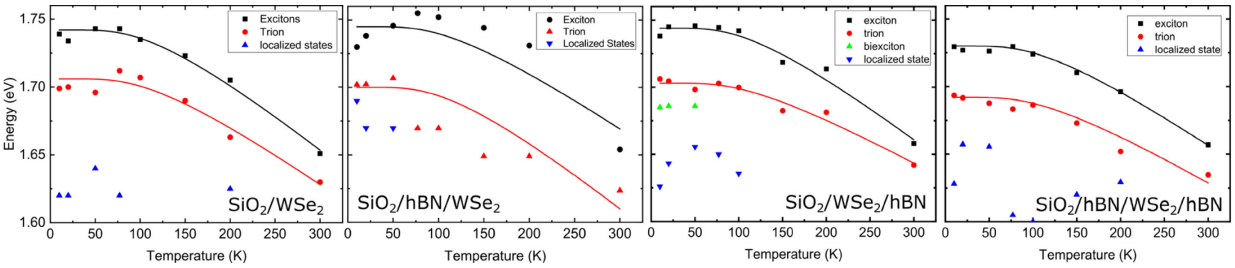

Figure A3* | Comparison of the Temperature Dependent Shifts for Different Stackings of h-BN and WSe_2.** Extracted Peak positions of the different excitonic features: exciton (black), trion (red), biexciton (green) and localized states (blue). The lines represent a fit with the phenomenological equation of O'Donnel ***Equation. 4-1.

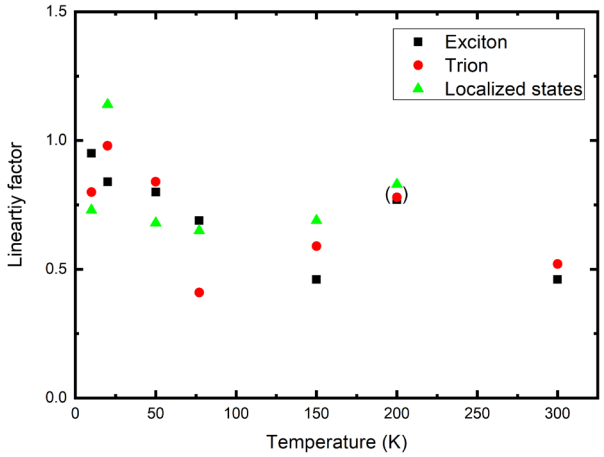

***Figure A4* | Temperature Dependent Analysis of the Linearity for the Encapsulated Sample used in Chapter 4.** The graph shows the linearity factor extracted from power dependent measurement series as function of temperature.

A5 Reflection Contrast Measurements of Differently Stacked Bilayers of WS_2 at Room Temperature

Similar to the spectra shown in chapter 5 also reflection contrast measurements were performed also at room temperature **Figure A5**. As one can see similarly to cold temperature a clear shift of the A-exciton, which is different for both cases. Interestingly, in contrast to low temperature almost no shift is observed at the B-exciton. Furthermore, interestingly the absorption of higher order states of the A-exciton series is surprisingly strong.

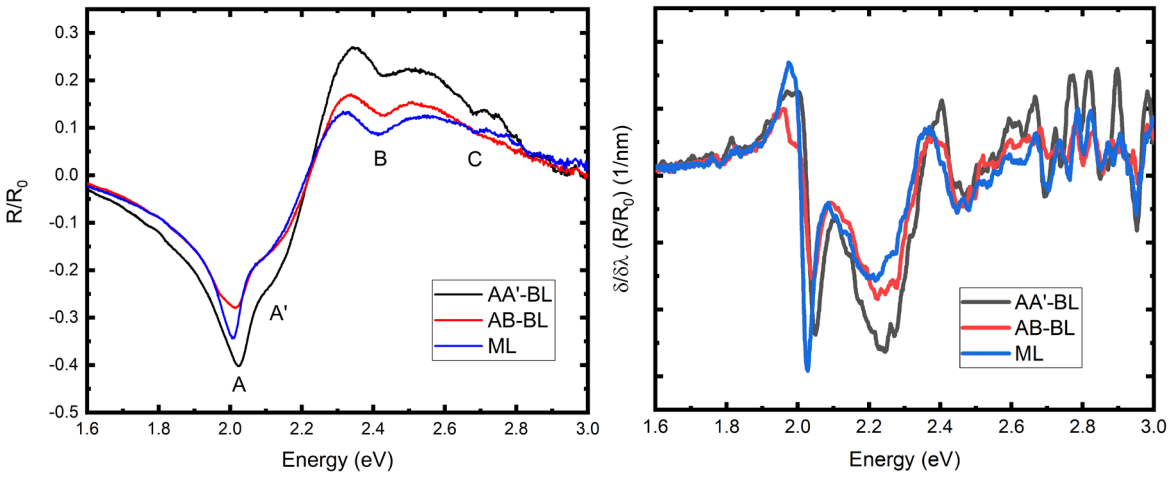

***Figure A5* | Comparison of Reflection Contrast and its Derivative for a WS_2 ML as well as AA' and AB Stacked Bilayers at Room Temperature.** A' denotes the excited states of the A-exciton.

A6 Spatial Homogeneity and Polarization Analysis of AA' and AB Stacks on h-BN.

Similar to **Figure 32** the Raman, PL and helicity was analyzed by means of linescans as well as PL imaging. For the helicity analysis two linescans respectively two images have been taken with different polarization. The results are shown in **Figure A6** and **Figure A7** for the AA' and AB stacked bilayers on h-BN buffer. To distinguish mono- and bilayer parts the spectral position of the peak and its lineshape has been used. One can clearly see the shift/drop in intensity between monolayer and bilayer regions. Furthermore, the amount of average helicity of the bilayer region is always reduced (5-10% less) compared to the monolayer region. Nonetheless, in both regions local fluctuation in the helicity can be observed that are a little bit smaller than the difference between mono- and bilayer parts. Moreover, the big influence of h-BN steps or cracks becomes evident from the analysis of AA' stacked sample and can also be seen in the fluorescence images. If the drop of helicity between mono- and bilayers is analyzed spectrally, the drop is not distributed equally over the region of PL-emission, but instead drops more significantly at the low energy side of the bilayer.

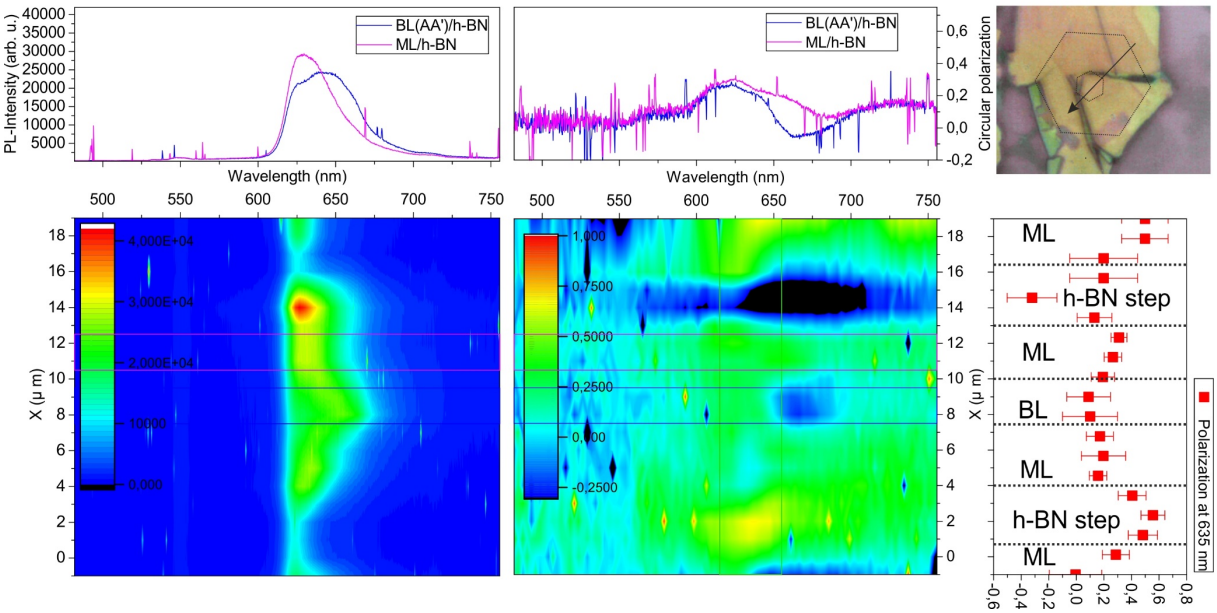

Figure A6 **|Spatial Analysis of CVD Grown AA' Stacked WS_2 Flake on h-BN.** The left panel shows a contour plot of the PL linescan along the path shown in the microscopic picture shown in the top right corner. The spectra at the top show integrated spectra in the marked boxed. By using two linescans performed under different circular polarization the helicity was calculated as function of position and wavelength. The result is plotted in the central panel. Again, the integrated results for the ML and BL region is shown in the corresponding upper panel. The right scatter plot shows the helicity (i.e. the degree of circular polarization) as function of the position on the path evaluated at the peak (635 nm). The error bars indicate the standard deviation within the marked box in the right panel.

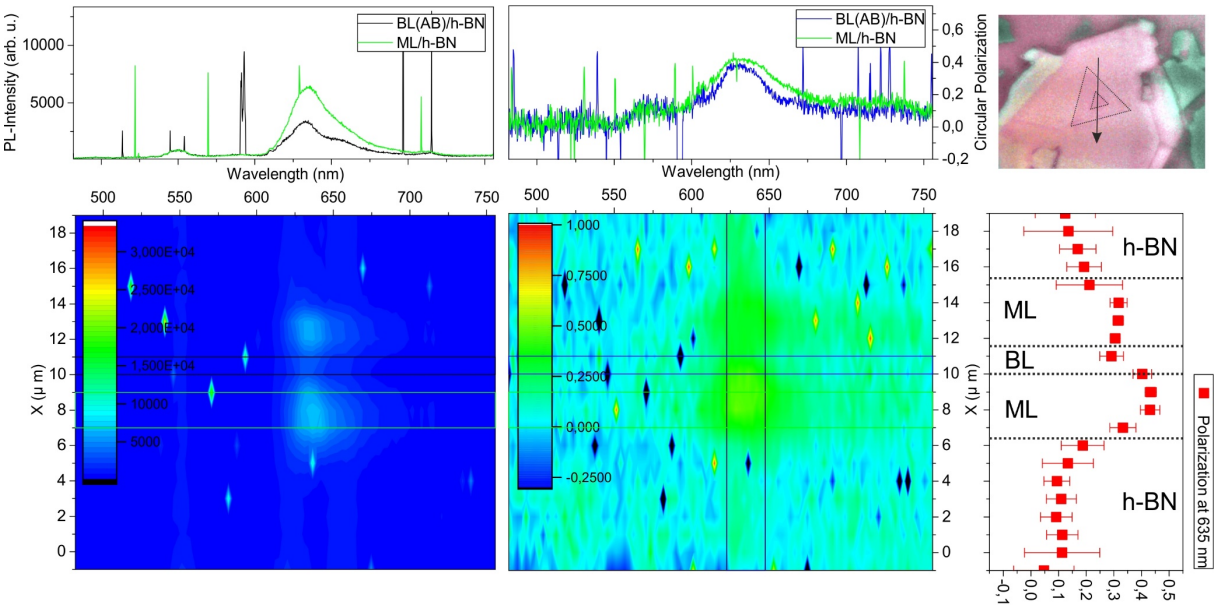

Figure A7 **| Spatial Analysis of CVD Grown AB Stacked WS_2 flake on h-BN.** The presentation is similar to ***Figure A6***.

A7 Helicity and Time-Resolved Photoluminescence Measurements for AA' and AB Stacks

Similar to the helicity and time resolved photoluminescence of the monolayer shown in **Figure 34** also measurements have been performed at AA' and AB stacked bilayer grown by CVD and transferred to SiO_2/Si substrate. The decay of co- and contra polarized emission is shown in **Figure A8**. While noisy, a small amount of polarization can be found in the emission for small times after the excitation. For example, the polarization of the AB stack has decayed after 20 ps. In contrast for the AA' stacked case a longer dephasing time is found for these samples on bare substrate.

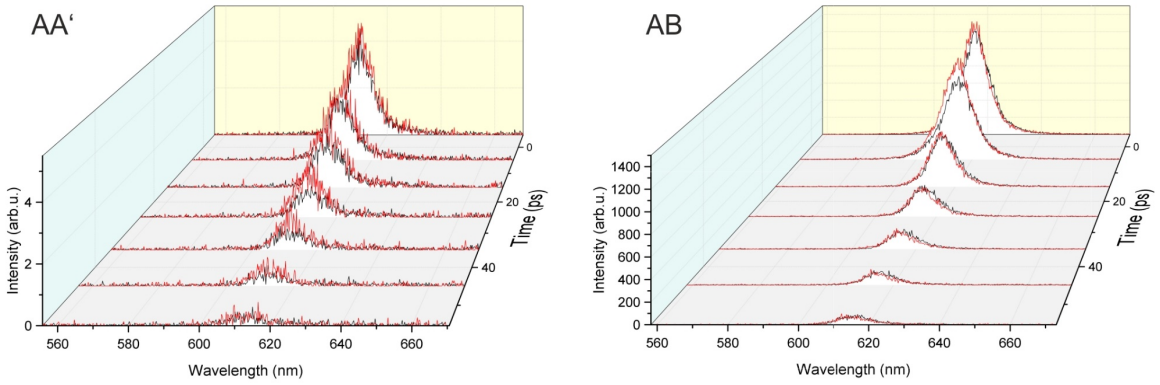

***Figure A8* | Waterfall Plots of the Polarization and Time-Resolved Measurement of Photoluminescence of AA' and AB Stacked Bilayers.** The measurement is performed at 10K at a pump density of 0.25 mJ/cm^2 under non resonant excitation at 2.75 eV.

A8 Microscopic Pictures of the Layers Comprising the High-Quality Stack

The flake mostly discussed in chapter 7 has been assembled by a dry stacking method by our collaborators at the Columbia university. Pictures of the individual parts are shown in **Figure A9**.

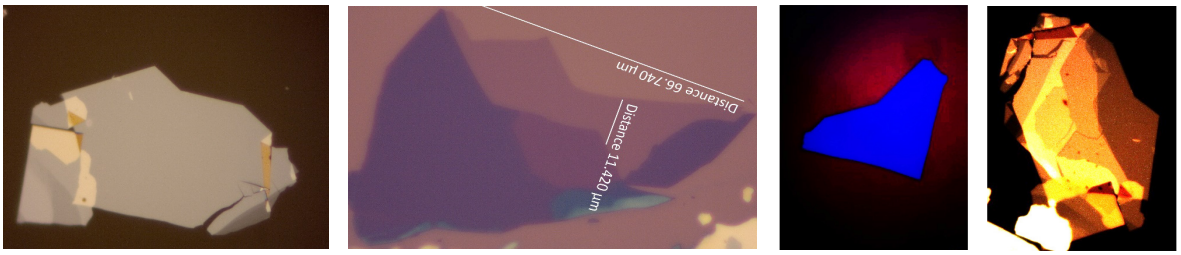

***Figure A9* | Microscopic Pictures of the Individual Parts of the Sample discussed in Chapter 7.** From left: bottom h-BN, WSe_2 flake with ML part, upper h-BN flake and competed stack

A9 Fourier-Space Spectra of the Control Samples, Repeatability and Spatial Dependence of Dispersion

To judge on the reproducibility and the fluctuations between different flakes, the temperature and power series for angle dependent measurements have been carried out on four samples. The corresponding PL (cf. **Figure A10**) and reflection contrast (cf. **Figure A11**) Fourier image as used in the temperature series is shown at the example of 10K. For all samples a measurable dispersion can be found.

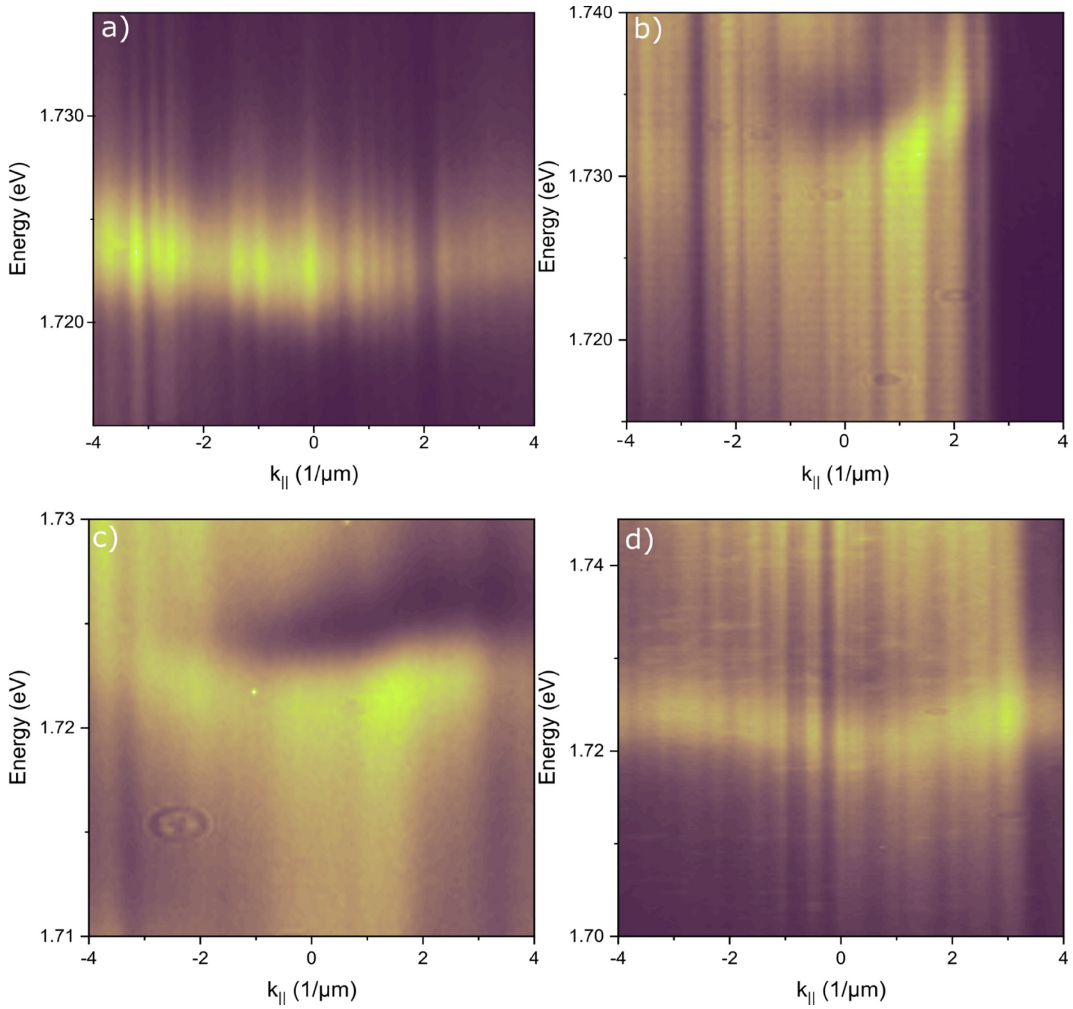

Figure A10 **| Fourier Images of PL-emission of other High-Quality Encapsulated WSe_2 Samples at 10 K.** All show almost the same amount of dispersion. The measurements have been performed at quasi-resonant condition similar to the measurements presented in chapter 6. The graph has been adapted from (L. M. Schneider, S. S. Esdaille et al. 2020) under the OSA Open Access License.

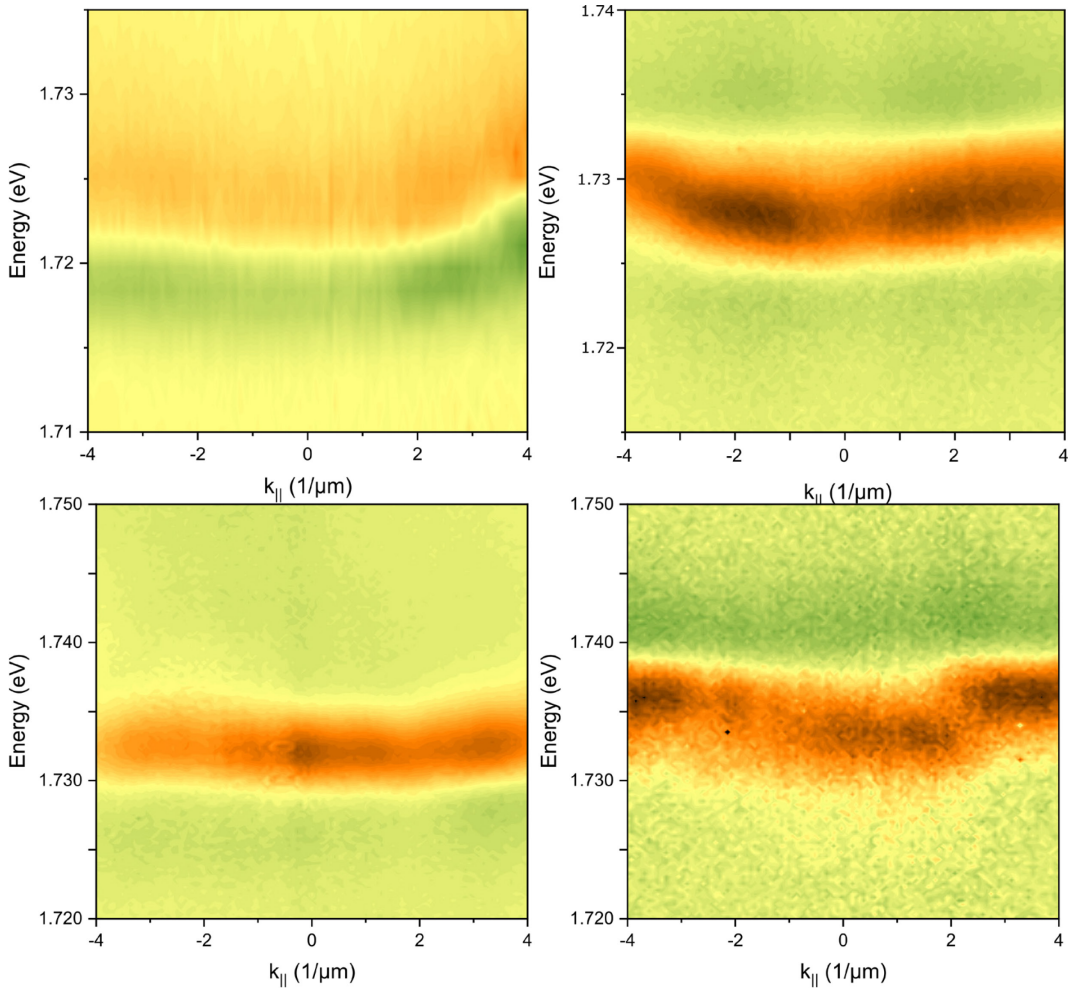

Figure A11 **| Fourier Spectra of the Reflection Contrast Derivate for all Four High Quality Encapsulated WSe_2 Samples.**

In addition to measuring several samples also the spatial homogeneity of the signal was investigated. Therefore, Fourier images were acquired at different spots of one of the samples (cf. **Figure A12**). For measurements in the center area of the flake (spot 3 and 6) a symmetric picture is found. For measurements taken on the samples edge (spots 1,2 and 5) only a faint signature of a half arm is found. As the light from one side cannot arrive under high angles this is not surprising but expected. At spots outside the layer (4, 7 and measurements spots on the SiO_2 substrate) no signature is found.

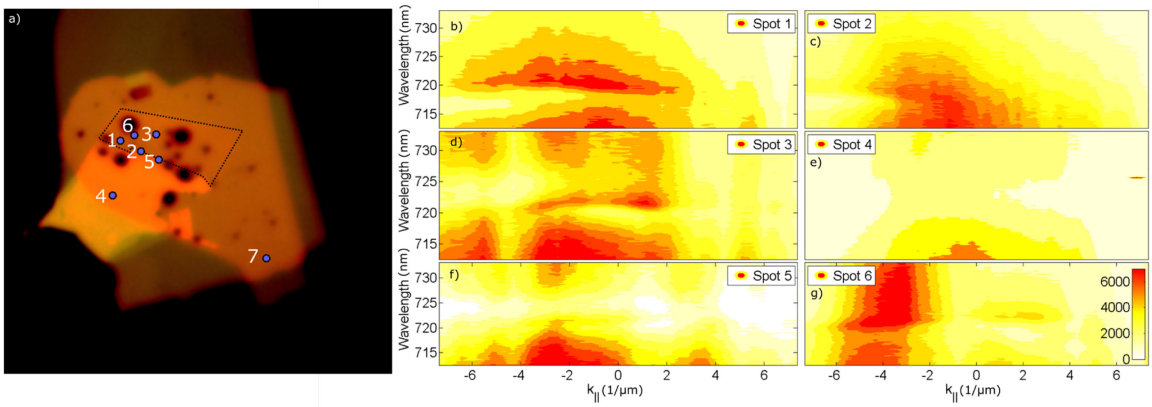

Figure A12 **|Spatial Dependence of Measured Fourier-Images.** (a) Microscopical picture with enhanced contrast. The dashed line represents a guide to the eye marking the position of the WSe_2 monolayer. The numbered dots are the investigated measurement points. (b-g) Acquired Fourier-space-spectra at these spots.

A10 Angle Integrated Spectra for Different Detunings

In order to analyze spectral changes for different excitation wavelength, angle integrated spectra where calculated from the angle resolved measurements. In order to correct for small spatial inhomogeneities, the spectra are plotted with respect to the exciton energy (cf. **Figure A13**). As already mentioned in the main text, starting from pumping above the 2s state biexcitonic features can be observed. The grey exciton and its phonon sidebands in contrast can be observed at all detuning, although they are more prominent at large detunings. Interestingly, in the spectra with the lowest detuning periodic sidebands can be observed. They have an approximate spacing of 4.5 meV. They are most likely arising from phonon emission during recombination similar to (Chow et al. 2017; Maciej R. Molas et al. 2017). If the lineshape of the neutral exciton for higher excitation detuning is examined, one can also see a shoulder or an asymmetrie at the very same energetic position of the first sidebands. Nonetheless, there are less pronounced, indicating that the surplus energy of the excitation is relaxed by other processes most likely Auger processes. This would also explain the different magnitude of trion emission in the spectra.

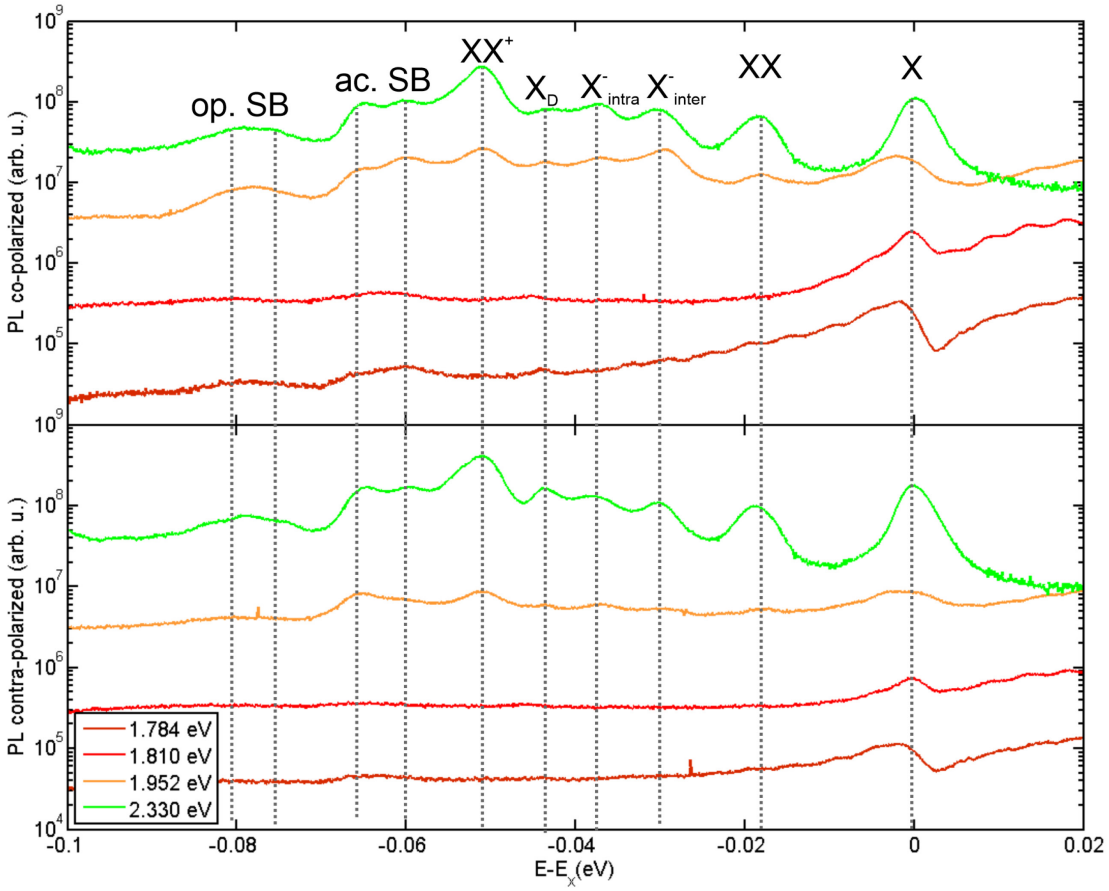

Figure A13 **|Angle Integrated Spectra for Helicity-Resolved Spectra for Different Laser Excitations.** The spectra are horizontally offset by one order of magnitude for clarity. The dashed lines are a guide to the eye indicating the approximate position of the individual features. Op. SB and ac. SB denote the sidebands of the dark exciton. The figure is adapted from (Schneider et al., 2020b) under the Attribution 3.0 Unported (CC BY 3.0) License.

A11 Dispersion Calculation Assuming Different Linewidths

In order to reach a better agreement between the calculated reflection and the experimentally observed reflection, a stitched permittivity assuming different homogenous linewidth (2 meV for A_{1s}, 5 meV for the excited states of the A exciton series, 3 meV for the B-exciton and 5 meV for the excited states of the B-excitons series) for different resonances was created and was used for a calculation similar to **Figure 53**. The stitching was done in a region where the background contribution dominates in order not to introduce new features.

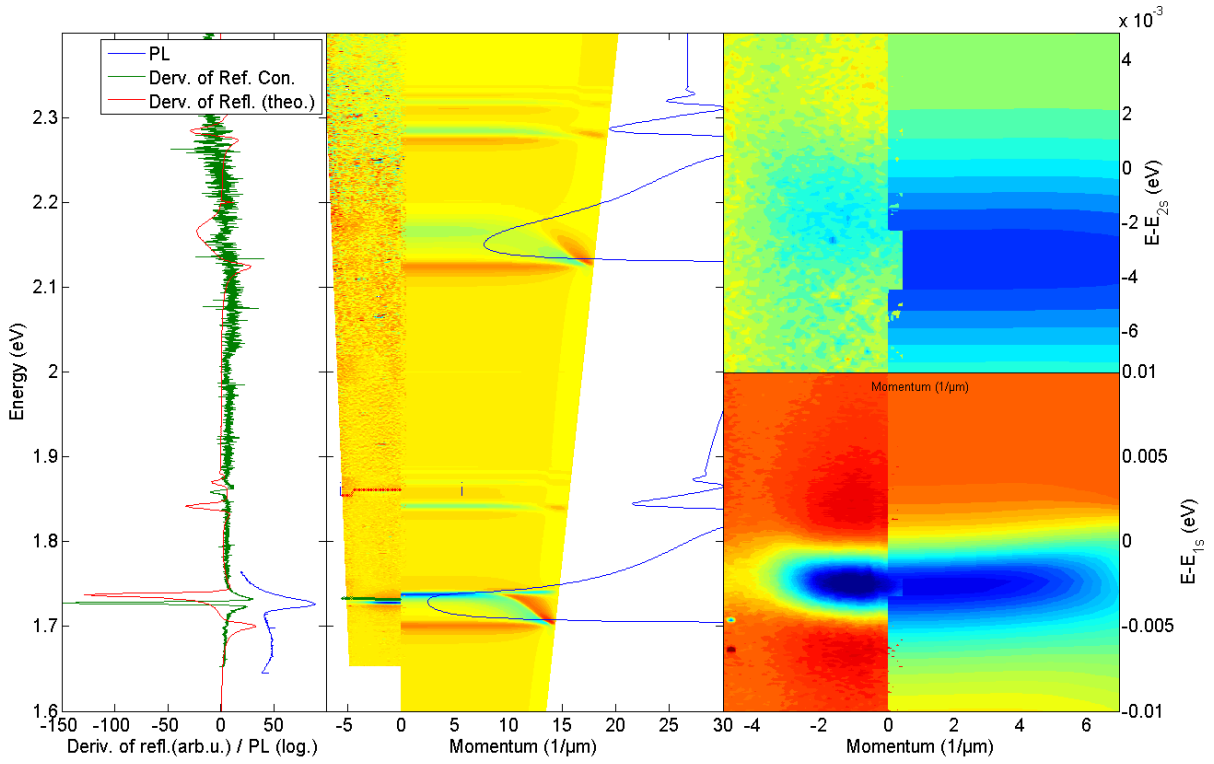

Figure A 14 **| Comparison of Experiment and Exciton Polariton Using Different Homogenous Linewidth for the Different Resonances.** In the insets an individual offset is applied to remove the not exactly matching theoretically binding energy. (left panel) angle integrated derivative of the reflection contrast spectra (green) in comparison with the calculated derivative of the calculated reflectivity (red). In addition, the experimental PL spectra is shown for quasi-resonant excitation. (main panel) angle resolved experimental spectra (left part) together with the calculated one (right part). The blue linear shows the polariton dispersion and the green on the extracted dispersion. The right panels show a zoom in to the 1s and 2s-resonance in calculation and experiment for comparison.

A12 Temperature Dependence of Phonon Sidebands

A temperature dependent measurement of the PL-Spectra of the h-BN encapsulated sample discussed in the section 6.8 has been performed under pulsed excitation. The spectra match the predictions of (Brem et al. 2020) nicely. The peaks at 1.65-1.66 eV, thus can be identified as the phonon sideband of the dark exciton.

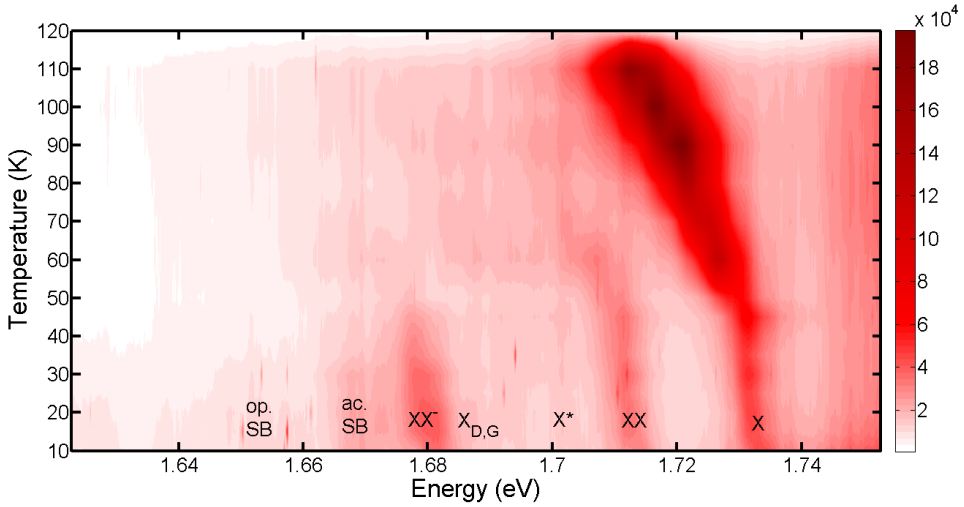

***Figure A 15* | PL-Temperature Series of a h-BN encapsulated WSe_2 Monolayer.** The excitonic species are marked as usual. Reused under the Creative Commons Attribution CC BY 4.0 International License (Commons 2020) from (Lorenz Maximilian Schneider et al. 2020).

References

Ajayi, Obafunso A et al. 2017. “Approaching the Intrinsic Photoluminescence Linewidth in Transition Metal Dichalcogenide Monolayers.” *2D Materials* 4(3): 031011.

Alexeev, Evgeny M. et al. 2019. “Resonantly Hybridized Excitons in Moiré Superlattices in van Der Waals Heterostructures.” *Nature* 567(7746): 81–86.

Alvarez, Carlos J. et al. 2018. “Impact of a van Der Waals Interface on Intrinsic and Extrinsic Defects in an MoSe2 Monolayer.” *Nanotechnology* 29(42): 425706.

Amo, A. et al. 2010. “Exciton-Polariton Spin Switches.” *Nature Photonics* 4(6): 361–66.

Anasori, Babak, Maria R. Lukatskaya, and Yury Gogotsi. 2017. “2D Metal Carbides and Nitrides (MXenes) for Energy Storage.” *Nature Reviews Materials* 2(2): 16098.

Andreani, Lucio Claudio, and Franco Bassani. 1990. “Exchange Interaction and Polariton Effects in Quantum-Well Excitons.” *Physical Review B* 41(11): 7536–44.

Arora, Ashish et al. 2019. “Excited-State Trions in Monolayer WS2.” *Physical Review Letters* 123(16): 167401.

Bajoni, D. et al. 2009. “Exciton Polaritons in Two-Dimensional Photonic Crystals.” *Physical Review B* 80(20): 201308.

Band, Yehuda B. 2006. 1 *Light and Matter: Electromagnetism, Optics, Spectroscopy and Lasers*. John Wiley & Sons.

Barbone, Matteo et al. 2018. “Charge-Tuneable Biexciton Complexes in Monolayer WSe2.” *Nature Communications* 9(1): 3721.

Beal, A. R., and W. Y. Liang. 1976. “Excitons in 2H-WSe2 and 3R-WS2.” *J. Phys. C. Solid State Phys.* 9: 2459–66.

Berghäuser, Gunnar et al. 2018. “Mapping of the Dark Exciton Landscape in Transition Metal Dichalcogenides.” *Physical Review B* 98(2): 020301.

Berkdemir, Ayse et al. 2013. “Identification of Individual and Few Layers of WS2 Using Raman Spectroscopy.” *Scientific Reports* 3(1): 1755.

Berkelbach, Timothy C., Mark S. Hybertsen, and David R. Reichman. 2013. “Theory of Neutral and Charged Excitons in Monolayer Transition Metal Dichalcogenides.” *Physical Review B* 88(4): 045318.

Beyer, Andreas et al. 2016. “Pyramidal Structure Formation at the Interface between III/V Semiconductors and Silicon.” *Chemistry of Materials* 28(10): 3265–75.

Bhimanapati, Ganesh R. et al. 2015. “Recent Advances in Two-Dimensional Materials beyond Graphene.” *ACS Nano* 9(12): 11509–39.

Bistritzer, Rafi, and Allan H. MacDonald. 2011. “Moiré Bands in Twisted Double-Layer Graphene.” *Proceedings of the National Academy of Sciences of the United States of America* 108(30): 12233–37.

Blauth, M. et al. 2018. “Coupling Single Photons from Discrete Quantum Emitters in WSe2 to Lithographically Defined Plasmonic Slot Waveguides.” *Nano Letters* 18(11): 6812–19.

Bordas, J., and E. A. Davis. 1973. “Electromodulation Spectroscopy of Excitons: High Field Regime.” *Surface Science* 37(C): 828–35.

Born, M., and R. Oppenheimer. 1927. “Zur Quantentheorie Der Molekeln.” *Annalen der Physik* 389(20): 457–84.

Brehm, Markus, Thomas Taubner, Rainer Hillenbrand, and Fritz Keilmann. 2006. “Infrared Spectroscopic Mapping of Single Nanoparticles and Viruses at Nanoscale Resolution.” *Nano Letters* 6(7): 1307–10.

Brem, Samuel et al. 2020. “Phonon-Assisted Photoluminescence from Indirect Excitons in Monolayers of Transition-Metal Dichalcogenides.” *Nano Letters* 20(4): 2849–56.

Brem, Samuel, Malte Selig, Gunnar Berghaeuser, and Ermin Malic. 2018. “Exciton Relaxation Cascade in Two-Dimensional Transition Metal Dichalcogenides.” *Scientific Reports* 8(1): 8238.

Brener, I. et al. 1992. “Particle Localization and Phonon Sidebands in GaAs/AlxGa1-xAs multiple quantum wells.” *Physical Review B* 46(12): 7927–30.

Brotons-Gisbert, Mauro et al. 2018. “Engineering Light Emission of Two-Dimensional Materials in Both the Weak and Strong Coupling Regimes.” *Nanophotonics* 7(1): 253–67.

Budde, Harald et al. 2016. “Raman Radiation Patterns of Graphene.” *ACS Nano* 10(2): 1756–63.

Byrnes, Tim, Na Young Kim, and Yoshihisa Yamamoto. 2014. “Exciton-Polariton Condensates.” *Nature Physics* 10(11): 803–13.

Cadiz, F. et al. 2017. “Excitonic Linewidth Approaching the Homogeneous Limit in MoS2-Based van Der Waals Heterostructures.” *Physical Review X* 7(2): 021026.

Cao, Ting et al. 2012. “Valley-Selective Circular Dichroism of Monolayer Molybdenum Disulphide.” *Nature Communications* 3(May): 885–87.

Cao, Yuan, Valla Fatemi, Ahmet Demir, et al. 2018. “Correlated Insulator Behaviour at Half-Filling in Magic-Angle Graphene Superlattices.” *Nature* 556(7699): 80–84.

Cao, Yuan, Valla Fatemi, Shiang Fang, et al. 2018. “Unconventional Superconductivity in Magic-Angle Graphene Superlattices.” *Nature* 556(7699): 43–50.

Castellanos-Gomez, Andres et al. 2013. “Single-Layer MoS2 Mechanical Resonators.” *Advanced Materials* 25(46): 6719–23.

———. 2014. “Deterministic Transfer of Two-Dimensional Materials by All-Dry Viscoelastic Stamping.” *2D Materials* 1(1): 011002.

Chae, Woo Hyun et al. 2017. “Substrate-Induced Strain and Charge Doping in CVD-Grown Monolayer MoS2.” *Applied Physics Letters* 111(14).

Chang, Chung Huai, Xiaofeng Fan, Shi Hsin Lin, and Jer Lai Kuo. 2013. “Orbital Analysis of Electronic Structure and Phonon Dispersion in MoS2 , MoSe2 , WS2 , and WSe2 Monolayers under Strain.” *Physical Review B - Conde* 88(19): 195420.

Chatterjee, S et al. 2004. “Excitonic Photoluminescence in Semiconductor Quantum Wells: Plasma versus Excitons.” *Physical Review Letters* 92(6): 067402.

Chen, Haitao et al. 2017. “Enhanced Second-Harmonic Generation from Two-Dimensional MoSe2 on a Silicon Waveguide.” *Light: Science & Applications* 6(10): e17060–e17060.

Chen, Shao-Yu et al. 2018. “Coulomb-Bound Four- and Five-Particle Intervalley States in an Atomically-Thin Semiconductor.” *Nature Communications* 9(1): 3717.

Chen, Shao Yu, Changxi Zheng, Michael S. Fuhrer, and Jun Yan. 2015. “Helicity-Resolved Raman Scattering of MoS2, MoSe2, WS2, and WSe2 Atomic Layers.” *Nano Letters* 15(4): 2526–32.

Chen, Xi et al. 2017. “Optical Control of Spin Polarization in Monolayer Transition Metal Dichalcogenides.” *ACS Nano* 11(2): 1581–87.

Chen, Yan, Zhenyu Li, M. David Henry, and Axel Scherer. 2009. “Optofluidic Circular Grating Distributed Feedback Dye Laser.” *Applied Physics Letters* 95(3): 2007–10.

Chen, Yen Jung et al. 2017. “Valley-Polarized Exciton-Polaritons in a Monolayer Semiconductor.” *Nature Photonics* 11(7): 431–35.

Chernikov, Alexey. 2011. “Time-Resolved Photoluminescence Spectroscopy of Semiconductors for Optical Apllications Beyond the Visible Spectral Range.” Philipps Universität Marburg.

———. 2014. “Exciton Binding Energy and Nonhydrogenic Rydberg Series in Monolayer WS2” *Physical Review Letters* 113(7): 076802.

Chernikov, Alexey, Arend M. Van Der Zande, et al. 2015. “Electrical Tuning of Exciton Binding Energies in Monolayer WS2.” *Physical Review Letters* 115(12): 126802.

Chernikov, Alexey, Claudia Ruppert, et al. 2015. “Population Inversion and Giant Bandgap Renormalization in Atomically Thin WS2 Layers.” *Nature Photonics* 9(7): 466–70.

Chiari, A et al. 1998. “Temperature Dependence of the Photoluminescence in GaAs-GaAlAs Multiple Quantum Well Structure.” *Physica Status Solidi (B)* 147(1): 421–29.

Cho, Yeongsu, and Timothy C. Berkelbach. 2018. “Environmentally Sensitive Theory of Electronic and Optical Transitions in Atomically Thin Semiconductors.” *Physical Review B* 97(4): 041409..

Chow, Colin M. et al. 2017. “Phonon-Assisted Oscillatory Exciton Dynamics in Monolayer MoSe2.” *npj 2D Materials and Applications* 1(1): 33.

Christiansen, Dominik et al. 2017. “Phonon Sidebands in Monolayer Transition Metal Dichalcogenides.” *Physical Review Letters* 119(18): 187402.

Colas, David et al. 2015. “Polarization Shaping of Poincaré Beams by Polariton Oscillations.” *Light: Science and Applications* 4(11): e350.

Commons, Creativ. 2020. “Creative Common Attribution 4.0 License.” http://creativecommons.org/licenses/by/4.0/.

Conley, Hiram J. et al. 2013. “Bandgap Engineering of Strained Monolayer and Bilayer MoS2.” *Nano Letters* 13(8): 3626–30. ht

Crasto de Lima, F., Gerson J. Ferreira, and R. H. Miwa. 2018. “Quantum Anomalous Hall Effect in Metal-Bis(Dithiolene), Magnetic Properties, Doping and Interfacing Graphene.” *Physical Chemistry Chemical Physics* 20(35): 22652–59.

Cudazzo, Pierluigi, Ilya V. Tokatly, and Angel Rubio. 2011. “Dielectric Screening in Two-Dimensional Insulators: Implications for Excitonic and Impurity States in Graphane.” *Physical Review B* 84(8): 085406.

Daniel, Clément et al. 2003. “Exciton Bimolecular Annihilation Dynamics in Supramolecular Nanostructures of Conjugated Oligomers.” *Physical Review B* 68(23): 235212.

Decker, Régis et al. 2011. “Local Electronic Properties of Graphene on a BN Substrate via Scanning Tunneling Microscopy.” *Nano Letters* 11(6): 2291–95.

Deilmann, Thorsten, and Kristian Sommer Thygesen. 2019. “Finite-Momentum Exciton Landscape in Mono- and Bilayer Transition Metal Dichalcogenides.” *2D Materials* 6(3): 035003.

Dendzik, Maciej et al. 2015. “Growth and Electronic Structure of Epitaxial Single-Layer WS2 on Au(111).” *Physical Review B* 92(24): 245442.

Deng, Hui et al. 2002. “Condensation of Semiconductor Microcavity Exciton Polaritons.” *Science* 298(5591): 199–202.

Deng, Hui, Hartmut Haug, and Yoshihisa Yamamoto. 2010. “Exciton-Polariton Bose-Einstein Condensation.” *Reviews of Modern Physics* 82(2): 1489–1537.

Dery, Hanan, and Yang Song. 2015. “Polarization Analysis of Excitons in Monolayer and Bilayer Transition-Metal Dichalcogenides.” *Physical Review B* 92(12): 125431.

Desai, Sujay B. et al. 2014. “Strain Induced Indirect to Direct Bandgap Transition in Multilayer WSe2.” *Nano letters* 14(8): 4591-4597.

———. 2016. “Gold-Mediated Exfoliation of Ultralarge Optoelectronically-Perfect Monolayers.” *Advanced Materials* 28(21): 4053–58.

Ding, Yuan Li et al. 2015a. “Jarosite Nanosheets Fabricated via Room-Temperature Synthesis as Cathode Materials for High-Rate Lithium Ion Batteries.” *Chemistry of Materials* 27(8): 3143–49.

———. 2015b. “Rapid and Up-Scalable Fabrication of Free-Standing Metal Oxide Nanosheets for High-Performance Lithium Storage.” *Small* 11(17): 2011–18.

Dominici, L. et al. 2014. “Ultrafast Control and Rabi Oscillations of Polaritons.” *Physical Review Letters* 113(22): 25005.

Dominici, Lorenzo et al. 2015. “Vortex and Half-Vortex Dynamics in a Nonlinear Spinor Quantum Fluid.” *Science Advances* 1(11): e1500807.

Dong, Rui, and Irma Kuljanishvili. 2017. “Review Article: Progress in Fabrication of Transition Metal Dichalcogenides Heterostructure Systems.” *Journal of Vacuum Science & Technology B, Nanotechnology and Microelectronics: Materials, Processing, Measurement, and Phenomena* 35(3): 030803.

Du, Juan et al. 2014. “Ytterbium-Doped Fiber Laser Passively Mode Locked by Few-Layer Molybdenum Disulfide (MoS2) Saturable Absorber Functioned with Evanescent Field Interaction.” *Scientific Reports* 4(1): 6346.

Dufferwiel, S. et al. 2017. “Valley-Addressable Polaritons in Atomically Thin Semiconductors.” *Nature Photonics* 11(8): 497–501.

Dufferwiel, S et al. 2015. “Exciton–Polaritons in van Der Waals Heterostructures Embedded in Tunable Microcavities.” *Nature Communications* 6(1): 8579.

Duong, Dinh Loc, Seok Joon Yun, and Young Hee Lee. 2017. “Van Der Waals Layered Materials: Opportunities and Challenges.” *ACS Nano* 11(12): 11803–30.

Dyakonov, M I, and V I Perel. 1972. “Spin Relaxation of Conduction Electrons in Noncentrosymmetric Semiconductors.” *Soviet Physics Solid State, Ussr* 13(12): 3023–26.

Edelberg, Drew et al. 2019. “Approaching the Intrinsic Limit in Transition Metal Diselenides via Point Defect Control.” *Nano Letters* 19(7): 4371–79.

Efimkin, Dmitry K., and Allan H. MacDonald. 2017. “Many-Body Theory of Trion Absorption Features in Two-Dimensional Semiconductors.” *Physical Review B* 95(3): 035417.

Epstein, Itai et al. 2020. “Highly Confined In-Plane Propagating Exciton-Polaritons on Monolayer Semiconductors.” *2D Materials 7(3)*: 035031.

Fano, U. 1961. “Effects of Configuration Interaction on Intensities and Phase Shifts.” *Physical Review* 124(6): 1866–78.

Fei, Z. et al. 2016. “Nano-Optical Imaging of WSe2 Waveguide Modes Revealing Light-Exciton Interactions.” *Physical Review B* 94(8): 081402.

Fei, Zaiyao et al. 2017. “Edge Conduction in Monolayer WTe2.” *Nature Physics* 13(7): 677–82.

Feldtmann, T., M. Kira, and S. W. Koch. 2009. “Phonon Sidebands in Semiconductor Luminescence.” *physica status solidi (b)* 246(2): 332–36.

———. 2010. “Theoretical Analysis of Higher-Order Phonon Sidebands in Semiconductor Luminescence Spectra.” *Journal of Luminescence* 130(1): 107–13.

Ferrari, Andrea C., and Denis M. Basko. 2013. “Raman Spectroscopy as a Versatile Tool for Studying the Properties of Graphene.” *Nature Publishing Group* 8(4): 235–46.

Forn-Díaz, P. et al. 2019. “Ultrastrong Coupling Regimes of Light-Matter Interaction.” *Reviews of Modern Physics* 91(2): 25005.

Frank, I. W., D. M. Tanenbaum, A. M. van der Zande, and P. L. McEuen. 2007. “Mechanical Properties of Suspended Graphene Sheets.” *Journal of Vacuum Science & Technology B: Microelectronics and Nanometer Structures* 25(6): 2558.

Franken, P. A., A. E. Hill, C. W. Peters, and G. Weinreich. 1961. “Generation of Optical Harmonics.” *Physical Review Letters 7(4): 118-119*.

Franken, P. A., and J. F. Ward. 1963. “Optical Harmonics and Nonlinear Phenomena.” *Reviews of Modern Physics 35(1): 23-29*.

Fraser, Michael D. 2017. “Coherent Exciton-Polariton Devices.” *Semiconuctor Science and Technology* 32(9): 093003.

Frenkel, J. 1931. “On the Transformation of Light into Heat in Solids. I.” *Physical Review* 37(1): 17–44.

Fricke, Jens. 1996. “Transport Equations Including Many-Particle Correlations for an Arbitrary Quantum System: A General Formalism.” *Annals of Physics* 252(2): 479–98.

Frindt, R F. 1963. “WSe2 AND MoTe2.” *J. Phys. Chem. Solids* 24: 1107–12.

Frindt, R F, and A D Yoffe. 1962. “Physical Properties of Layer Structures : Optical Properties and Photoconductivity of Thin Crystals of Molybdenum Disulphide.” *Proceedings of the Royal Society of London. Series A. Mathematical and Physical Sciences* 273(1352): 69–83.

Fröhlich, D., K. Reimann, and P. Koidl. 1982. “Investigation of Mixed-mode Polariton Dispersion in AgGas2.” *Physica Status Solidi (B)* 114(2): 553–59.

Fu, Jiyong, Junio M.R. Cruz, and Fanyao Qu. 2019. “Valley Dynamics of Different Trion Species in Monolayer WSe2.” *Applied Physics Letters* 115(8): 082101.

Fujita, Tohru, Yoshihiro Sato, Tetsuya Kuitani, and Teruya Ishihara. 1998. “Tunable Polariton Absorption of Distributed Feedback Microcavities at Room Temperature.” *Physical Review B* 57(19): 12428–34.

Galbraith, I. et al. 2005. “Excitonic Signatures in the Photoluminescence and Terahertz Absorption of a GaAs/AlxGa1-xAs Multiple Quantum Well.” *Physical Review B* 71(7): 073302.

Geim, A. K., and I. V. Grigorieva. 2013. “Van Der Waals Heterostructures.” *Nature* 499(7459): 419–25.

Gerber, Iann C., and Xavier Marie. 2018. “Dependence of Band Structure and Exciton Properties of Encapsulated WSe2 Monolayers on the HBN-Layer Thickness.” *Physical Review B* 98(24): 245126.

Ghatak, Kamalika, Kyung Nam Kang, Eui-Hyeok Yang, and Dibakar Datta. 2019. “Controlled Edge Dependent Stacking of WS2-WS2 Homo- and WS2-WSe2 Hetero-Structures: A Computational Study.” : 1–55. http://arxiv.org/abs/1911.11289.

Gies, S. et al. 2014. “Annealing Effects on the Composition and Disorder of Ga(N,As,P) Quantum Wells on Silicon Substrates for Laser Application.” *Journal of Crystal Growth* 402: 169–74.

Glazov, M. M. et al. 2014. “Exciton Fine Structure and Spin Decoherence in Monolayers of Transition Metal Dichalcogenides.” *Physical Review B* 89(20): 201302.

Gmitra, Martin, and Jaroslav Fabian. 2017. “Proximity Effects in Bilayer Graphene on Monolayer WSe2: Field-Effect Spin Valley Locking, Spin-Orbit Valve, and Spin Transistor.” *Physical Review Letters* 119(14): 146401.

Godde, T. et al. 2016. “Exciton and Trion Dynamics in Atomically Thin MoSe2 and WSe2: Effect of Localization.” *Physical Review B* 94(16): 165301.

Gogna, Rahul, Long Zhang, Zhaorong Wang, and Hui Deng. 2019. “Photonic Crystals for Controlling Strong Coupling in van Der Waals Materials.” *Optics Express* 27(16): 22700.

Grimme, Stefan, Jens Antony, Stephan Ehrlich, and Helge Krieg. 2010. “A Consistent and Accurate Ab Initio Parametrization of Density Functional Dispersion Correction (DFT-D) for the 94 Elements H-Pu.” *The Journal of Chemical Physics* 132(15): 154104.

Guillet, Thierry, and Christelle Brimont. 2016. “Polariton Condensates at Room Temperature.” *Comptes Rendus Physique* 17(8): 946–56.

H.W. Wyld, Jr. 1963. “Quantum Mechanical Kinetic Equations.” *Annals of Physics* 23: 374–89.

Hader, J., J. V. Moloney, and S. W. Koch. 2005. “Supression of Carrier Recombination in Semiconductor Lasers by Phase-Space Filling.” *Applied Physics Letters* 87(20) 201112.

Han, Grace G.D. et al. 2017. “Photoluminescent Arrays of Nanopatterned Monolayer MoS2.” *Advanced Functional Materials* 27(45): 1703688.

Han, Weipeng et al. 2018. “Effect of UV Irradiation and Heat Treatment on the Surface Potential Distribution of Monolayer WS2 on SiO2/Si and Au Substrates.” *Advanced Materials Interfaces* 5(2): 1701083.

Hanamura, Eiichi. 1988. “Rapid Radiative Decay and Enhanced Optical Nonlinearity of Excitons in a Quantum Well.” *Phys. Rev. B* 38(2): 1228–34.

Haug, Hartmut, and Stephan W Koch. 2009. *Quantum Theory of the Optical and Electronic Properties of Semiconductors: Fivth Edition*. World Scientific Publishing Company.

Hauschild, R et al. 2006. “The Exciton Polariton Model and the Diffusion of Excitons in ZnO Analyzed by Time-Dependent Photoluminescence Spectroscopy.” *physica status solidi (c)* 3(4): 980–83.

Hayashi, Masakazu, and Kiichirô Katsuki. 1952. “Hydrogen-like Absorption Spectrum of Cuprous Oxide.” *Journal of the Physical Society of Japan* 7(6): 599–603.

He, Keliang et al. 2014. “Tightly Bound Excitons in Monolayer WSe2.” *Physical Review Letters* 113(2): 026803.

He, Minhao et al. 2020. “Valley Phonons and Exciton Complexes in a Monolayer Semiconductor.” *Nature Communications* 11(1): 618.

He, Zhengyu et al. 2016. “Biexciton Formation in Bilayer Tungsten Disulfide.” *ACS Nano* 10(2): 2176–83.

Heinz, T. F., M. M.T. Loy, and W. A. Thompson. 1985. “Study of Si(111) Surfaces by Optical Second-Harmonic Generation: Reconstruction and Surface Phase Transformation.” *Physical Review Letters* 54(1): 63-66.

Hesse, H. J., W. Fuhs, G. Weiser, and L. Von Szentpaly. 1976. “Directional Dispersion of an Exciton Polariton in a Pentamethinium Cyanine Dye.” *Physica Status Solidi (B)* 76(2): 817–26.

Hill, Heather Marie et al. 2015. “Observation of Excitonic Rydberg States in Monolayer MoS2 and WS2 by Photoluminescence Excitation Spectroscopy.” *Nano Letters* 15(5): 2992–97.

Hopfield, J. J., and D. G. Thomas. 1963. “Theoretical and Experimental Effects of Spatial Dispersion on the Optical Properties of Crystals.” *Physical Review* 132(2): 563–72.

Horng, Jason et al. 2018. “Observation of Interlayer Excitons in MoSe2 Single Crystals.” *Physical Review B* 97(24): 241404.

Hsu, Wei Ting et al. 2014. “Second Harmonic Generation from Artificially Stacked Transition Metal Dichalcogenide Twisted Bilayers.” *ACS Nano* 8(3): 2951–58.

Huang, Bevin et al. 2017. “Layer-Dependent Ferromagnetism in a van Der Waals Crystal down to the Monolayer Limit.” *Nature* 546(7657): 270–73.

Huang, Jiani, Thang B Hoang, and Maiken H Mikkelsen. 2016. “Probing the Origin of Excitonic States in Monolayer WSe2.” *Scientific reports* 6(August 2015): 22414.

HUANG, KUN. 1951. “Lattice Vibrations and Optical Waves in Ionic Crystals.” *Nature* 167(4254): 779–80.

Huang, Shengxi et al. 2016. “Low-Frequency Interlayer Raman Modes to Probe Interface of Twisted Bilayer MoS2.” *Nano Letters* 16(2): 1435–44.

Huber, Andreas J. et al. 2007. “Simultaneous IR Material Recognition and Conductivity Mapping by Nanoscale Near-Field Microscopy.” *Advanced Materials* 19(17): 2209–12.

Itoh, T., P. Lavallard, J. Reydellet, and C. Benoit àla Guillaume. 1981. “Time of Flight of Excitonic Polaritons in CdSe.” *Solid State Communications* 37(12): 925–30.

Ivanov, A. L., and H. Haug. 1993. “Self-Consistent Theory of the Biexciton Optical Nonlinearity.” *Physical Review B* 48(3): 1490–1504.

Jakubczyk, T. et al. 2018. “Impact of Environment on Dynamics of Exciton Complexes in a WS2 Monolayer.” *2D Materials 5(3)*: 031007.

Jariwala, Deep et al. 2014. “Emerging Device Applications for for Semiconducting Two-Dimensional Transition Metal Dichalcogenides.” *ACS nano* 8(2): 1102–20.

———. 2016. “Hybrid, Gate-Tunable, van Der Waals p-n Heterojunctions from Pentacene and MoS2.” *Nano Letters* 16(1): 497–503.

Jariwala, Deep, Tobin J. Marks, and Mark C. Hersam. 2017. “Mixed-Dimensional van Der Waals Heterostructures.” *Nature Materials* 16(2): 170–81.

Jaskólski, W. et al. 2018. “Controlling the Layer Localization of Gapless States in Bilayer Graphene with a Gate Voltage.” *2D Materials* 5(2): 025006.

Jin, Chenhao et al. 2019. “Observation of Moiré Excitons in WSe2/WS2 Heterostructure Superlattices.” *Nature* 567(7746): 76–80.

Jones, Aaron M. et al. 2014. “Spin-Layer Locking Effects in Optical Orientation of Exciton Spin in Bilayer WSe 2.” *Nature Physics* 10(2): 130–34.

Kalikhman, V L, E P Gladchenko, and L L Pravoverova. 1972. “Crystal Structure of Quasibinary Alloys of the System W Se2 - Nb Se2.” *Inorganic Materials* 8: 1020–22.

Kang, Kibum et al. 2015. “High-Mobility Three-Atom-Thick Semiconducting Films with Wafer-Scale Homogeneity.” *Nature* 520(7549): 656–60.

Karanikolas, Vasilios D., Cristian A. Marocico, Paul R. Eastham, and A. Louise Bradley. 2016. “Near-Field Relaxation of a Quantum Emitter to Two-Dimensional Semiconductors: Surface Dissipation and Exciton Polaritons.” *Physical Review B* 94(19): 195418.

Karvonen, Lasse et al. 2017. “Rapid Visualization of Grain Boundaries in Monolayer MoS2 by Multiphoton Microscopy.” *Nature Communications* 8(1): 15714.

Kasprzak, J. et al. 2006. “Bose–Einstein Condensation of Exciton Polaritons.” *Nature* 443(7110): 409–14.

Katsch, Florian, Malte Selig, Alexander Carmele, and Andreas Knorr. 2018. “Theory of Exciton–Exciton Interactions in Monolayer Transition Metal Dichalcogenides.” *Physica Status Solidi (B)* 255(12): 1800185.

Kavokin, Alexey, Jeremy J Baumberg, Guillaume Malpuech, and Fabrice P Laussy. 2017. *Microcavities*. Oxford University Press.

Kavokin, K. V. et al. 2004. “Quantum Theory of Spin Dynamics of Exciton-Polaritons in Microcavities.” *Physical Review Letters* 92(1): 017401.

Keldysh, L. V. 1979. “Coulomb Interaction in Thin Semiconductor and Semimetal Films.” *JETP Letters* 29(11): 658–60.

Khurgin, Jacob B. 2015. “Two-Dimensional Exciton–Polariton—Light Guiding by Transition Metal Dichalcogenide Monolayers.” *Optica* 2(8): 740.

Kim, Dong Hak, Min Ju Shin, and D. Lim. 2015. “Excitonic Valley Polarization and Coherence in Few-Layer MoS2.” *Journal of the Korean Physical Society* 66(5): 806–10.

Kira, M., W. Hoyer, T. Stroucken, and S. W. Koch. 2001. “Exciton Formation in Semiconductors and the Influence of a Photonic Environment.” *Physical Review Letters* 87(17): 176401.

Kira, M., F. Jahnke, and S. W. Koch. 1998. “Microscopic Theory of Excitonic Signatures in Semiconductor Photoluminescence.” *Physical Review Letters* 81(15): 3263–66.

Kira, M., and S. W. Koch. 2006a. “Many-Body Correlations and Excitonic Effects in Semiconductor Spectroscopy.” *Progress in Quantum Electronics* 30(5): 155–296.

Kira, M, and S.W. Koch. 2006b. “Many-Body Correlations and Excitonic Effects in Semiconductor Spectroscopy.” *Progress in Quantum Electronics* 30(5): 155–296.

Kira, M, and S W Koch. 2005. “Microscopic Theory of Optical Excitations, Photoluminescence, and Terahertz Response in Semiconductors.” *The European Physical Journal D* 36(2): 143–57.

Kleinman, D. A., and R. C. Miller. 1985. “Band-Gap Renormalization in Semiconductor Quantum Wells Containing Carriers.” *Physical Review B* 32(4): 2266–72.

Klingshirn, Claus f. 2012. 53 Journal of Chemical Information and Modeling *Semiconductor Optics*. 4th ed. Berlin, Heidelberg: Springer Berlin Heidelberg.

Koch, S. W., M. Kira, G. Khitrova, and H. M. Gibbs. 2006. "Semiconductor Excitons in New Light." *Nature* 5: 523–31.

Konabe, Satoru. 2016. "Screening Effects Due to Carrier Doping on Valley Relaxation in Transition Metal Dichalcogenide Monolayers." *Applied Physics Letters* 109(7): 10–14.

Kormányos, Andor, Viktor Zólyomi, Neil D. Drummond, and Guido Burkard. 2014. "Spin-Orbit Coupling, Quantum Dots, and Qubits in Monolayer Transition Metal Dichalcogenides." *Physical Review X* 4(1): 011034.

Korn, T. et al. 2011. "Low-Temperature Photocarrier Dynamics in Monolayer MoS2." *Applied Physics Letters* 99(10): 102109.

Kresse, G, and J Furthmüller. 1996. "Efficiency of Ab-Initio Total Energy Calculations for Metals and Semiconductors Using a Plane-Wave Basis Set." *Computational Materials Science* 6(1): 15–50.

Kresse, G, and J Hafner. 1994. "Ab Initio Molecular-Dynamics Simulation of the Liquid-Metal--Amorphous-Semiconductor Transition in Germanium." *Phys. Rev. B* 49(20): 14251–69.

Kresse, G, and D Joubert. 1999. "From Ultrasoft Pseudopotentials to the Projector Augmented-Wave Method." *Phys. Rev. B* 59(3): 1758–75.

Kristensen, Philip Trøst, and Stephen Hughes. 2014. "Modes and Mode Volumes of Leaky Optical Cavities and Plasmonic Nanoresonators." *ACS Photonics* 1(1): 2–10.

Kuhnert, Jan. 2018. "Optische Und Magneto-Optische Untersuchungen an Zweidimensionalen Übergangsmetalldichalkogeniden Und Deren Heterostrukturen." Philipps-Universität Marburg.

Kulig, Marvin et al. 2018. "Exciton Diffusion and Halo Effects in Monolayer Semiconductors." *Physical Review Letters* 120(20): 207401.

Kumar, Nardeep et al. 2014. "Exciton-Exciton Annihilation in MoSe2 Monolayers." *Physical Review B* 89(12): 125427.

Kunstmann, Jens et al. 2018. "Momentum-Space Indirect Interlayer Excitons in Transition-Metal Dichalcogenide van Der Waals Heterostructures." *Nature Physics* 14(8): 801–5.

Kutta, Roger Jan, Thomas Langenbacher, Uwe Kensy, and Bernhard Dick. 2013. "Setup and Performance of a Streak Camera Apparatus for Transient Absorption Measurements in the Ns to Ms Range." *Applied Physics B* 111(2): 203–16.

Kuwabara, M., D. R. Clarke, and D. A. Smith. 1990. "Anomalous Superperiodicity in Scanning Tunneling Microscope Images of Graphite." *Applied Physics Letters* 56(24): 2396–98.

Kylänpää, Ilkka, and Hannu-Pekka Komsa. 2015. "Binding Energies of Exciton Complexes in Transition Metal Dichalcogenide Monolayers and Effect of Dielectric Environment." *Physical Review B* 92(20): 205418.

Langer, F. et al. 2018. "Lightwave Valleytronics in a Monolayer of Tungsten Diselenide." *Nature* 557(7703): 76-80

Laturia, Akash, Maarten L. Van de Put, and William G. Vandenberghe. 2018. "Dielectric Properties of Hexagonal Boron Nitride and Transition Metal Dichalcogenides: From Monolayer to Bulk." *npj 2D Materials and Applications* 2(1): 6.

Lee, Changgu et al. 2010. "Anomalous Lattice Vibrations of Single- and Few-Layer MoS2." *ACS Nano* 4(5): 2695–2700.

Lee, Chul Ho et al. 2014. “Epitaxial Growth of Molecular Crystals on van Der Waals Substrates for High-Performance Organic Electronics.” *Advanced Materials* 26(18): 2812–17.

Lekner, J. 1991. “Reflection and Refraction by Uniaxial Crystals.” *Journal of Physics: Condensed Matter* 3(32): 6121–33.

Li, Da et al. 2016. “Nanoimprint-Assisted Shear Exfoliation plus Transfer Printing for Producing Transition Metal Dichalcogenide Heterostructures.” *Journal of Vacuum Science & Technology B, Nanotechnology and Microelectronics: Materials, Processing, Measurement, and Phenomena* 34(6): 06KA01.

Li, H, J M T Wu, Z Y Yin, and H Zhang. 2014. “Preparation and Applications of Mechanically Exfoliated Single-Layer and Multi Layer MoS2 and WSe2 Nanosheets.” *Accounts of Chemical Research* 47(4): 1067–75.

Li, Hong et al. 2012. “From Bulk to Monolayer MoS2: Evolution of Raman Scattering.” *Advanced Functional Materials* 22(7): 1385–90.

Li, Yilei, Alexey Chernikov, et al. 2014. “Measurement of the Optical Dielectric Function of Monolayer Transition-Metal Dichalcogenides: MoS2, MoSe2, WS2 and WSe2.” *Physical Review B* 90(20): 205422.

Li, Yilei, Jonathan Ludwig, et al. 2014. “Valley Splitting and Polarization by the Zeeman Effect in Monolayer MoSe2.” *Physical Review Letters* 113(26): 266804.

Li, Yongzhuo et al. 2017. “Room-Temperature Continuous-Wave Lasing from Monolayer Molybdenum Ditelluride Integrated with a Silicon Nanobeam Cavity.” *Nature Nanotechnology* 12(10): 987–92.

Li, Z. Q. et al. 2008. “Dirac Charge Dynamics in Graphene by Infrared Spectroscopy.” *Nature Physics* 4(7): 532-535.

Li, Zhipeng et al. 2019. “Emerging Photoluminescence from the Dark-Exciton Phonon Replica in Monolayer WSe2.” *Nature Communications* 10(1): 2469.

Liang, W Y A R Beal, and J C Knights. 1971. “Transmission Spectra of Some Transition Metal Dichalcogenides. II. Group VIA: Trigonal Prismatic Coordination.” *Journal of Physics C: Solid State Physics* 5: 3540-3551

Lin, Miao Ling et al. 2018. “Moiré Phonons in Twisted Bilayer MoS 2.” *ACS Nano* 12(8): 8770–80.

Lin, Yuxuan et al. 2014. “Dielectric Screening of Excitons and Trions in Single-Layer MoS2.” *Nano Letters* 14(10): 5569–76.

Lippert, Sina et al. 2017. “Influence of the Substrate Material on the Optical Properties of Tungsten Diselenide Monolayers.” *2D Materials* 4(2): 025045.

———. 2018. “Optische Spektroskopie an Chalkogenen Und Porphyrinen.” Philipps-Universität Marburg.

Liu, Erfu et al. 2019. “Valley-Selective Chiral Phonon Replicas of Dark Excitons and Trions in Monolayer WSe2.” *Physical Review Research* 1(3): 032007.

———. 2020. “Multipath Optical Recombination of Intervalley Dark Excitons and Trions in Monolayer WSe2.” *Physical Review Letters* 124(19): 196802.

Liu, Fang et al. 2020. “Disassembling 2D van Der Waals Crystals into Macroscopic Monolayers and Reassembling into Artificial Lattices.” 367(6480): 903–6.

Liu, Kaihui et al. 2014. “Evolution of Interlayer Coupling in Twisted Molybdenum Disulfide Bilayers.” *Nature Communications* 5(1): 4966.

Liu, Xiaoze et al. 2015. “Strong Light–Matter Coupling in Two-Dimensional Atomic Crystals.” *Nature Photonics* 9(1): 30–34.

Liu, Yuan et al. 2016. “Van Der Waals Heterostructures and Devices.” *Nature Reviews Materials* 1(9): 16042.

Low, Tony et al. 2017. “Polaritons in Layered Two-Dimensional Materials.” *Nature Materials* 16(2): 182–94.

Lucatto, Bruno et al. 2019. “Charge Qubit in van Der Waals Heterostructures.” *Physical Review B* 100(12): 121406.

Ludwig, Arthur. 1973. “The Definition of Cross Polarization.” *IEEE Transactions on Antennas and Propagation* 21(1): 116–19.

Lundt, N., A. Maryński, et al. 2016. “Monolayered MoSe2: A Candidate for Room Temperature Polaritonics.” *2D Materials* 4(1):015006.

Lundt, N., S. Stoll, et al. 2017. “Observation of Macroscopic Valley-Polarized Monolayer Exciton-Polaritons at Room Temperature.” *Physical Review B* 96(24): 241403.

Lundt, Nils et al. 2016. “Room-Temperature Tamm-Plasmon Exciton-Polaritons with a WSe2 Monolayer.” *Nature Communications* 7(1): 13328.

Luo, Xin et al. 2013. .” *Physical Review B* 88(19): 195313.

Luo, Yunqiu Kelly et al. 2017. “Opto-Valleytronic Spin Injection in Monolayer MoS2/Few-Layer Graphene Hybrid Spin Valves.” *Nano Letters* 17(6): 3877–83.

Luo, Zhengqian et al. 2016. “Two-Dimensional Material-Based Saturable Absorbers: Towards Compact Visible-Wavelength All-Fiber Pulsed Lasers.” *Nanoscale* 8(2): 1066–72.

Ma, Eric Yue et al. 2019. “Recording Interfacial Currents on the Subnanometer Length and Femtosecond Time Scale by Terahertz Emission.” *Science Advances* 5(2): eaau0073.

Ma, Renzhi, and Takayoshi Sasaki. 2010. “Nanosheets of Oxides and Hydroxides: Ultimate 2D Charge-Bearing Functional Crystallites.” *Advanced Materials* 22(45): 5082–5104.

Macrea, C.F. et al. 2008. “Mercury CSD 2.0 - New Features for the Visualization and Investigation of Crystal Structures.” *J. Appl. Cryst* 41: 466–70.

Maialle, M. Z., E. A. de Andrada e Silva, and L. J. Sham. 1993. “Exciton Spin Dynamics in Quantum Wells.” *Physical Review B* 47(23): 15776–88.

Mak, Kin Fai et al. 2010. “Atomically Thin MoS2: A New Direct-Gap Semiconductor.” *Physical Review Letters* 105(13): 136805.

Mak, Kin Fai, Keliang He, Jie Shan, and Tony F. Heinz. 2012. “Control of Valley Polarization in Monolayer MoS2 by Optical Helicity.” *Nature Nanotechnology* 7(8): 494–98.

Mak, Kin Fai, and Jie Shan. 2016. “Photonics and Optoelectronics of 2D Semiconductor Transition Metal Dichalcogenides.” *Nature Photonics* 10(4): 216–26.

Mak, Kin Fai, Di Xiao, and Jie Shan. 2018. “Light–Valley Interactions in 2D Semiconductors.” *Nature Photonics* 12(8): 451–60.

Marx, M. et al. 2017. “Large-Area MoS2 Deposition via MOVPE.” *Journal of Crystal Growth* 464(November 2016): 100–104.

———. 2018. “Metalorganic Vapor-Phase Epitaxy Growth Parameters for Two-Dimensional MoS2.” *Journal of Electronic Materials* 47(2): 910–16.

Matsushita, M., J. Wicksted, and H. Z. Cummins. 1984. “Resonant Brillouin Scattering in CdS. II. Theory.” *Physical Review B* 29(6): 3362–81.

Meckbach, L et al. 2018. “Interlayer Excitons in Transition-Metal Dichalcogenide Heterostructures with Type-II Band Alignment.” *Journal of Physics: Condensed Matter* 30(37): 374002.

Meckbach, Lars, Tineke Stroucken, and Stephan W. Koch. 2018a. “Influence of the Effective Layer Thickness on the Ground-State and Excitonic Properties of Transition-Metal Dichalcogenide Systems.” *Physical Review B* 97(3): 035425.

Meckbach, Lars, Tineke Stroucken, and Stephan W Koch. 2018b. “Influence of the Effective Layer Thickness on the Ground-State and Excitonic Properties of Transition-Metal Dichalcogenide Systems.” *Phys. Rev. B* 97: 35425.

Meinhold, H., and G. Weiser. 1976. “Modulation Spectroscopy on MoS2, and MoSe2.” *Physica Status Solidi (B)* 73(1): 105–15.

Mey, Oliver et al. 2019. “Enhancement of the Monolayer Tungsten Disulfide Exciton Photoluminescence with a Two-Dimensional Material/Air/Gallium Phosphide In-Plane Microcavity.” *ACS Nano* 13(5): 5259–67.

Molas, M. R. et al. 2019. “Energy Spectrum of Two-Dimensional Excitons in a Nonuniform Dielectric Medium.” *Physical Review Letters* 123(13): 136801.

Molas, Maciej R., Karol Nogajewski, Marek Potemski, and Adam Babinski. 2017. “Raman Scattering Excitation Spectroscopy in Monolayer WS2.” *Scientific Report* 7(1): 5036.

Molina-Sánchez, A., and L. Wirtz. 2011. “Phonons in Single-Layer and Few-Layer MoS2 and WS2.” *Physical Review B* 84(15): 155413.

Moody, Galan et al. 2015. “Intrinsic Homogeneous Linewidth and Broadening Mechanisms of Excitons in Monolayer Transition Metal Dichalcogenides.” *Nature Communications* 6(1): 8315.

Mott, N. F., and L. Friedman. 1974. “Metal-Insulator Transitions in Vo2, Ti2O3 and Ti2–XVxO3.” *Philosophical Magazine* 30(2): 389–402.

Mouri, Shinichiro et al. 2014. “Nonlinear Photoluminescence in Atomically Thin Layered WSe2 Arising from Diffusion-Assisted Exciton-Exciton Annihilation.” *Physical Review B* 90(15): 155449.

Mrejen, M., L. Yadgarov, A. Levanon, and H. Suchowski. 2019. “ Transient Exciton-Polariton Dynamics in WSe 2 by Ultrafast near-Field Imaging .” *Science Advances* 5(2): eaat9618.

Mu, Congpu, Jianyong Xiang, and Zhongyuan Liu. 2017. “Photodetectors Based on Sensitized Two-Dimensional Transition Metal Dichalcogenides - A Review.” *Journal of Materials Research* 32(22): 4115–31.

Mund, Johannes, Dietmar Fröhlich, Dmitri R Yakovlev, and Manfred Bayer. 2018. “High-Resolution Second Harmonic Generation Spectroscopy with Femtosecond Laser Pulses on Excitons in Cu2O.” *Physical Review B* 98(8): 085203.

Muratore, Christopher, Andrey A. Voevodin, and Nicholas R. Glavin. 2019. “Physical Vapor Deposition of 2D Van Der Waals Materials: A Review.” *Thin Solid Films* 688(June): 137500.

Murray, R. B., and A. D. Yoffe. 1972. “The Band Structures of Some Transition Metal Dichalcogenides: Band Structures of the Titanium Dichalcogenides.” *Journal of Physics C: Solid State Physics* 5(21): 3038–46.

Nagler, Philipp et al. 2017. “Interlayer Exciton Dynamics in a Dichalcogenide Monolayer Heterostructure.” *2D Materials* 4(2): 25112.

———. 2018. “Zeeman Splitting and Inverted Polarization of Biexciton Emission in Monolayer WS2.” *Physical Review Letters* 121(5): 057402.

Naik, Mit H., and Manish Jain. 2018. “Ultraflatbands and Shear Solitons in Moiré Patterns of Twisted Bilayer Transition Metal Dichalcogenides.” *Physical Review Letters* 121(26): 266401.

Nakayama, M., and M. Matsuura. 1986. “Theory of the Quantum Well Excitonic Polariton; Effect of the Valence Subband Splitting.” *Surface Science* 170(1–2): 641–44.

Nakayama, M. 1985. “THEORY OF THE EXCITONIC POLARITON OF THE QUANTUM WELL.” *Solid state Communications* 55(12): 1053–56.

Noori, Yasir J. et al. 2016. “Photonic Crystals for Enhanced Light Extraction from 2D Materials.” *ACS Photonics* 3(12): 2515–20.

Novoselov, K. S. 2004. “Electric Field Effect in Atomically Thin Carbon Films.” *Science* 306(5696): 666–69.

———. 2005. “Two-Dimensional Gas of Massless Dirac Fermions in Graphene.” *Nature* 438(7065): 197–200.

Novoselov, K. S., A. Mishchenko, A. Carvalho, and A. H. Castro Neto. 2016. “2D Materials and van Der Waals Heterostructures.” *Science* 353(6298): aac9439.

O’Donnell, K. P., and X. Chen. 1991. “Temperature Dependence of Semiconductor Band Gaps.” *Applied Physics Letters* 58(25): 2924–26.

Ohkawa, Fusayoshi J., and Yasutada Uemura. 1976. “Valley Splitting in an N-Channel (100) Inversion Layer on p-Type Silicon.” *Surface Science* 58(1): 254–60.

———. 1977. “Theory of Valley Splitting in an N-Channel (100) Inversion Layer of Si, Formulation by Extended Zone Effective Mass Theory.” *J. Phys. Soc. J* 43(3): 907–15.

Olson, Craig et al. 1998. “High-Order Azimuthal Spatial Modes of Concentric-Circle-Grating Surface-Emitting Semiconductor Lasers.” *Applied Physics Letters* 72(11): 1284–86.

Osada, Minoru, and Takayoshi Sasaki. 2009. “Exfoliated Oxide Nanosheets: New Solution to Nanoelectronics.” *Journal of Materials Chemistry* 19(17): 2503–11.

Oskooi, Ardavan F. et al. 2010. “Meep: A Flexible Free-Software Package for Electromagnetic Simulations by the FDTD Method.” *Computer Physics Communications* 181(3): 687–702.

Padhi, Bikash, Chandan Setty, and Philip W. Phillips. 2018. “Doped Twisted Bilayer Graphene near Magic Angles: Proximity to Wigner Crystallization, Not Mott Insulation.” *Nano Letters* 18(10): 6175–80.

Park, Jeongwoo et al. 2019. “ Direct Mapping of the Gate Response of a Multilayer WSe2 /MoS2 Heterostructure with Locally Different Degrees of Charge Depletion .” *The Journal of Physical Chemistry Letters* 10(14): 4010–16.

Park, Soohyung et al. 2018. “Direct Determination of Monolayer MoS2 and WSe2 Exciton Binding Energies on Insulating and Metallic Substrates.” *2D Materials* 5(2): 025003.

Pawłowski, J., D. Zebrowski, and S. Bednarek. 2018. “Valley Qubit in a Gated MoS2 Monolayer Quantum Dot.” *Physical Review B* 97(15): 155412.

Pekar, S I. 1958. “Theory of Electromagnetic Waves in a Crystal with Excitons.” *J. Phys. Chem. Solids* 5(3): 11–22.

Peng, Bo, Priscilla Kailian Ang, and Kian Ping Loh. 2015. “Two-Dimensional Dichalcogenides for Light-Harvesting Applications.” *Nano Today* 10(2): 128–37.

Perdew, John P, Kieron Burke, and Matthias Ernzerhof. 1996. “Generalized Gradient Approximation Made Simple.” *Phys. Rev. Lett.* 77(18): 3865–68.

Persson, Kristin. 2014. “Materials Data on ReS2 (SG:2) by Materials Project.”

———. 2017. “Materials Data on WSe2 (SG:187) by Materials Project.”

Photonics, Hamamatsu. 2018. “Universial Streak Camera C10910, Manual.” www.hamamatsu.com/resources/pdf/sys/SHSS0016E_C10910s.pdf (June 20, 2020).

Plechinger, Gerd et al. 2016. “Trion Fine Structure and Coupled Spin-Valley Dynamics in Monolayer Tungsten Disulfide.” *Nature Communications* 7(1): 12715.

Poellmann, C. et al. 2015. “Resonant Internal Quantum Transitions and Femtosecond Radiative Decay of Excitons in Monolayer WSe2.” *Nature Materials* 14(9): 889–93.

Powell, Richard C. 1975. “REVIEW ARTICLE SINGLET EXCITON ENERGY TRANSFER IN ORGANIC SOLIDS Richard C. POWELL.” *Journal of Luminescence* 11: 1–45.

Puretzky, Alexander A. et al. 2016. “Twisted MoSe2 Bilayers with Variable Local Stacking and Interlayer Coupling Revealed by Low-Frequency Raman Spectroscopy.” *ACS Nano* 10(2): 2736–44.

Qi, Xiao-Liang, and Shou-Cheng Zhang. 2010. “Topological Insulators and Superconductors.” *Physics Letters, Section B: Nuclear, Elementary Particle and High-Energy Physics* 693(2): 175–79.

Qiu, Diana Y., Ting Cao, and Steven G. Louie. 2015. “Nonanalyticity, Valley Quantum Phases, and Lightlike Exciton Dispersion in Monolayer Transition Metal Dichalcogenides: Theory and First-Principles Calculations.” *Physical Review Letters* 115(17): 176801.

Qiu, Diana Y., Felipe H. Da Jornada, and Steven G. Louie. 2013. “Optical Spectrum of MoS2: Many-Body Effects and Diversity of Exciton States.” *Physical Review Letters* 111(21): 216805.

Rahimi-Iman, Arash. 2013. *Nichtlineare Effekte in III/V Quantenfilm-Mikroresonatoren: Von Dynamischer Bose-Einstein-Kondensation Hin Zum Elektrisch Betriebenen Polariton-Laser*. Cuvillier, E.

———. 2020a. “Optically-Excited Polariton Condensates.” In *Polariton Physics: From Dynamic Bose--Einstein Condensates in Strongly-Coupled Light--Matter Systems to Polariton Lasers*, Cham: Springer International Publishing, 195–240.

———. 2020b. “Spectroscopy Techniques for Polariton Research.” In *Polariton Physics: From Dynamic Bose--Einstein Condensates in Strongly-Coupled Light--Matter Systems to Polariton Lasers*, Cham: Springer International Publishing, 167–93.

———. 2020c. “Towards Polariton Condensates and Devices.” In *Polariton Physics From Dynamic Bose--Einstein Condensates in Strongly-Coupled Light--Matter Systems to Polariton Lasers*, Cham: Springer International Publishing, 1–32.

Raja, Archana et al. 2017. “Coulomb Engineering of the Bandgap and Excitons in Two-Dimensional Materials.” *Nature Communications* 8(1): 15251.

Rappel, W. J., L. F. Feiner, and M. F.H. Schuurmans. 1988. “Exciton-Polariton Picture of the Free-Exciton Lifetime in GaAs.” *Physical Review B* 38(11): 7874–76.

Regan, Emma C et al. 2020. “Mott and Generalized Wigner Crystal States in WSe2 / WS2 Moiré Superlattices.” *Nature* 579(7799): 359-363.

Rhodes, Daniel, Sang Hoon Chae, Rebeca Ribeiro-Palau, and James Hone. 2019. “Disorder in van Der Waals Heterostructures of 2D Materials.” *Nature Materials* 18(6): 541–49.

von Ribbeck, H.-G. et al. 2008. “Spectroscopic THz Near-Field Microscope.” *Optics Express* 16(5): 3430.

Ridolfi, Emilia, Caio H. Lewenkopf, and Vitor M. Pereira. 2018. “Excitonic Structure of the Optical Conductivity in MoS2 Monolayers.” *Physical Review B* 97(20): 205409.

Robert, C. et al. 2017. “Fine Structure and Lifetime of Dark Excitons in Transition Metal Dichalcogenide Monolayers.” *Physical Review B* 96(15): 155423.

Robertson, J. 2004. “High Dielectric Constant Oxides.” *The European Physical Journal Applied Physics* 28(3): 265–91.

Roldán, Rafael, Andrés Castellanos-Gomez, Emmanuele Cappelluti, and Francisco Guinea. 2015. “Strain Engineering in Semiconducting Two-Dimensional Crystals.” *Journal of Physics Condensed Matter* 27(31).

Rommel, Patric et al. 2020. “Second Harmonic Generation of Cuprous Oxide in Magnetic Fields.” *Physical Review B* 101(11): 115202.

Rooney, Aidan P. et al. 2017. “Observing Imperfection in Atomic Interfaces for van Der Waals Heterostructures.” *Nano Letters* 17(9): 5222–28.

Rui, Xianhong et al. 2013. “Olivine-Type Nanosheets for Lithium Ion Battery Cathodes.” *ACS Nano* 7(6): 5637–46.

Ruppert, Claudia et al. 2017. “The Role of Electronic and Phononic Excitation in the Optical Response of Monolayer WS2 after Ultrafast Excitation.” *Nano Letters* 17(2): 644–51.

Rytova, Natalia S. 1967. “Screened Potential of a Point Charge in a Thin Film.” *MSU Phys. Astron.* 3(30).

Sahin, H. et al. 2013. “Anomalous Raman Spectra and Thickness-Dependent Electronic Properties of WSe2.” *Physical Review B* 87(16): 165409.

Salehzadeh, Omid et al. 2015. “Optically Pumped Two-Dimensional MoS2 Lasers Operating at Room-Temperature.” *Nano Letters* 15(8): 5302–6.

Sarkar, Deblina et al. 2015. “A Subthermionic Tunnel Field-Effect Transistor with an Atomically Thin Channel.” *Nature* 526(7571): 91–95.

Schäfer, W, and M Wegener. 2002. “BOOK REVIEW: Semiconductor Optics and Transport Phenomena.” *Measurement Science and Technology* 13: 1652.

Schaibley, John R. et al. 2016. “Valleytronics in 2D Materials.” *Nature Reviews Materials* 1(11): 16055.

Scharf, Benedikt, Dinh Van Tuan, Igor Žutić, and Hanan Dery. 2019. “Dynamical Screening in Monolayer Transition-Metal Dichalcogenides and Its Manifestations in the Exciton Spectrum.” *Journal of Physics: Condensed Matter* 31(20): 203001.

Scheuer, Jacob, William M J Green, Guy A. Derose, and Amnon Yariv. 2005. “Lasing from a Circular Bragg Nanocavity with an Ultrasmall Modal Volume.” *Applied Physics Letters* 86(25): 1–3.

Scheuer, Jacob, and Amnon Yariv. 2004. “Circular Photonic Crystal Resonators.” *Physical Review E* 70(3): 036603.

Schmidt, H. et al. 2016. “Quantum Transport and Observation of Dyakonov-Perel Spin-Orbit Scattering in Monolayer MoS2.” *Physical Review Letters* 116(4): 046803.

Schmitt-Rink, S, D S Chemla, and D A B Miller. 1989. “Linear and Nonlinear Optical Properties of Semiconductor Quantum Wells.” *Advances in Physics* 38(2): 89–188.

Schmutzler, Johannes et al. 2015. “All-Optical Flow Control of a Polariton Condensate Using Nonresonant Excitation.” *Physical Review B* 91(19): 195308.

Schneider, Christian et al. 2013. “An Electrically Pumped Polariton Laser.” *Nature* 497(7449): 348–52.

Schneider, Christian, Mikhail M. Glazov, et al. 2018. “Two-Dimensional Semiconductors in the Regime of Strong Light-Matter Coupling.” *Nature Communications* 9(1): 2695.

Schneider, L. M., S. Lippert, et al. 2018. “The Impact of the Substrate Material on the Optical Properties of 2D WSe2 Monolayers.” *Semiconductors* 52(5): 565–71.

Schneider, L.M. et al. 2017. “The Influence of the Substrate Material on the Optical Properties of Tungsten Diselendide Monolayers.” *Optics InfoBase Conference Papers* Part F43-C.

Schneider, Lorenz Maximilian et al. 2017. “The Influence of the Environment on Monolayer Tungsten Diselenide Photoluminescence.” *Nano-Structures & Nano-Objects* 217(2): 169–74. http://linkinghub.elsevier.com/retrieve/pii/S0022510X03002892.

Schneider, Lorenz Maximilian, Jan Kuhnert, et al. 2018. “Density-Dependent Excitonic Properties and Dynamics in 2D Heterostructures Consisting of Boron Nitride and Monolayer or Few-Layer Tungsten Diselenide.” In *Micro-and Nanotechnology Sensors, Systems, and Applications X*, , 106390V.

Schneider, Lorenz Maximilian, Sina Lippert, et al. 2018. “The Influence of the Environment on Monolayer Tungsten Diselenide Photoluminescence.” *Nano-Structures & Nano-Objects* 15: 84–97.

Schneider, Lorenz Maximilian, Shanece S. Esdaille, et al. 2019. “Shedding Light on Exciton’s Nature in Monolayer Quantum Material by Optical Dispersion Measurements.” *Optics Express* 27(26): 37131.

Schneider, Lorenz Maximilian, Jan Kuhnert, et al. 2019. “Spin-Layer and Spin-Valley Locking in CVD-Grown AA’- and AB-Stacked Tungsten-Disulfide Bilayers.” *The Journal of Physical Chemistry C* 123(35): 21813–21.

Schneider, Lorenz Maximilian et al. 2020. “Direct Measurement of the Radiative Pattern of Bright and Dark Excitons and Exciton Complexes in Encapsulated Tungsten Diselenide.” *Scientific Reports* 10: 8091.

Schneider, Lorenz Maximilian et al. 2020b. " Optical dispersion of valley-hybridised coherent excitons withmomentum-dependent valley polarisation in monolayer semiconductor." 2D Materials, in press, abb5eb.

Schuller, Jon A. et al. 2013. “Orientation of Luminescent Excitons in Layered Nanomaterials.” *Nature Nanotechnology* 8(4): 271–76.

Segura, A. et al. 2018. “Natural Optical Anisotropy of H-BN: Highest Giant Birefringence in a Bulk Crystal through the Mid-Infrared to Ultraviolet Range.” *Physical Review Materials* 2(2): 024001.

Selig, Malte et al. 2016. “Excitonic Linewidth and Coherence Lifetime in Monolayer Transition Metal Dichalcogenides.” *Nature Communications* 7(1):13279.

———. 2017. “Dark and Bright Exciton Formation, Thermalization, and Photoluminescence in Monolayer Transition Metal Dichalcogenides.” : *arxiV: 1703.03317*.

———. 2018. “Exciton-Phonon Coupling in Monolayers of Transition Metal Dichalcogenides.” Technische Universität Berlin.

Semiletov, S A. 1961. “The Crystalline Structure of Rhombohedral MoS2.” *Kristallografiya* 6: 536–40.

Seyler, Kyle L. et al. 2018. “Valley Manipulation by Optically Tuning the Magnetic Proximity Effect in WSe2/CrI3 Heterostructures.” *Nano Letters* 18(6): 3823–28.

———. 2019. “Signatures of Moiré-Trapped Valley Excitons in MoSe2 /WS 2 Heterobilayers.” *Nature* 567(7746): 66–70.

Shah, M., L. M. Schneider, and A. Rahimi-Iman. 2019. “Observation of Intralayer and Interlayer Excitons in Monolayered WSe2/WS2 Heterostructure.” *Semiconductors* 53(16): 2140–46.

Sham, L. J., S. J. Allen, A. Kamgar, and D. C. Tsui. 1978. “Valley-Valley Splitting in Inversion Layers on a High-Index Surface of Silicon.” *Physical Review Letters* 40(7): 472–75.

Shang, Jingzhi et al. 2017. “Room-Temperature 2D Semiconductor Activated Vertical-Cavity Surface-Emitting Lasers.” *Nature Communications* 8(1): 543.

Shang, Shun Li et al. 2016. “Lateral Versus Vertical Growth of Two-Dimensional Layered Transition-Metal Dichalcogenides: Thermodynamic Insight into MoS2.” *Nano Letters* 16(9): 5742–50.

Sharpe, Aaron L. et al. 2019. “Emergent Ferromagnetism near Three-Quarters Filling in Twisted Bilayer Graphene.” *Science* 365(6453): 605–8.

Shen, Yuen-Ron. 1984. “The Principles of Nonlinear Optics.” *New York, Wiley-Interscience, 1984,*

Shin, Bong Gyu et al. 2016. “Indirect Bandgap Puddles in Monolayer MoS2 by Substrate-Induced Local Strain.” *Advanced Materials* 28(42): 9378–84.

Shiue, Ren Jye et al. 2019. “Thermal Radiation Control from Hot Graphene Electrons Coupled to a Photonic Crystal Nanocavity.” *Nature Communications* 10(1): 109.

Shkolnikov, Y. P., E. P. De Poortere, E. Tutuc, and M. Shayegan. 2002. “Valley Splitting of AlAs Two-Dimensional Electrons in a Perpendicular Magnetic Field.” *Physical Review Letters* 89(22): 226805.

Shree, S. et al. 2018. “Observation of Exciton-Phonon Coupling in MoSe2 Monolayers.” *Physical Review B* 98(3): 035302.

Siarkos, Anastassios. 1966. “Exciton Center-of-Mass Motion in Quantum Wells and Quantum Wires.” Humboldt Universität Berlin.

Sidler, Meinrad et al. 2017. “Fermi Polaron-Polaritons in Charge-Tunable Atomically Thin Semiconductors.” *Nature Physics* 13(3): 255–61.

Sigl, Lukas et al. 2020. “Condensation Signatures of Photogenerated Interlayer Excitons in a van Der Waals Heterostack.” : http://arxiv.org/abs/2001.07567.

Smolenski, T. et al. 2016. “Tuning Valley Polarization in a WSe2 Monolayer with a Tiny Magnetic Field.” *Physical Review X* 6(2): 021024.

Sommer, Kristian. 2017. “Calculating Excitons , Plasmons , and Quasiparticles in 2D Materials and van Der Waals Heterostructures.” *2D Materials* 4: 022004.

Song, Yang, and Hanan Dery. 2013. “Transport Theory of Monolayer Transition-Metal Dichalcogenides through Symmetry.” *Physical Review Letters* 111(2): 026601.

Stahl, A. 1984. “Electrodynamicxs of the Band-Edge in a Direct Gap Semiconductor.” *Solid State Communications* 49(1): 91–93.

Steiner, Soner, Sergii Khmelevskyi, Martijn Marsmann, and Georg Kresse. 2016. “Calculation of the Magnetic Anisotropy with Projected-Augmented-Wave Methodology and the Case Study of Disordered Fe(1-x) Co(x) Alloys.” *Phys. Rev. B* 93(22): 224425.

Steinhoff, A. et al. 2014. “Influence of Excited Carriers on the Optical and Electronic Properties of MoS 2.” *Nano Letters* 14(7): 3743–48.

Steinhoff, Alexander et al. 2018. “Biexciton Fine Structure in Monolayer Transition Metal Dichalcogenides.” *Nature Physics* 14(12): 1199–1204.

Stier, Andreas V., Kathleen M. McCreary, et al. 2016. “Exciton Diamagnetic Shifts and Valley Zeeman Effects in Monolayer WS2and MoS2to 65 Tesla.” *Nature Communications* 7(1): 10643.

Stier, Andreas V., Nathan P. Wilson, et al. 2016. “Probing the Influence of Dielectric Environment on Excitons in Monolayer WSe2: Insight from High Magnetic Fields.” *Nano Letters* 16(11): 7054–60.

Stroucken, Tineke, Johanna H Grönqvist, and Stephan W Koch. 2011. “Optical Response and Ground State of Graphene.” *Phys. Rev. B* 84: 205445.

———. 2013. “Screening and Gap Generation in Bilayer Graphene.” *Phys. Rev. B* 87: 245428.

Stroucken, Tineke, and Stephan W Koch. 2017. “Microscopic Theory for the Groundstate and Linear Optical Response of Novel Two-Dimensional Materials with Hexagonal Symmetry.” In *Optical Properties of Graphene*, ed. Rolf Binder. Singapur: World Scientific Publishing, 43–84.

Sun, Dezheng et al. 2014. “Observation of Rapid Exciton − Exciton Annihilation in Monolayer Molybdenum Disul Fi De.” *Nono Letters* 14: 5625.

Sun, Liaoxin et al. 2010. “Room Temperature One-Dimensional Polariton Condensate in a ZnO Microwire.” *arxiV: 1007.4686*.

Sun, Zheng et al. 2017. “Optical Control of Roomerature Valley Polaritons.” *Nature Photonics* 11(8): 491–96.

Suna, A. 1970. “Kinematics of Exciton-Exciton Annihilation in Molecular Crystals.” *Physical Review B* 1(4): 1716–39.

Swenberg, C. E., and W. T. Stacy. 1969. “Influence of Resonance Transfer and Exciton Diffusion on Luminescence Decay.” *Physica Status Solidi (B)* 36(2): 717–22.

Ta, Huy Q. et al. 2016. “Stranski-Krastanov and Volmer-Weber CVD Growth Regimes to Control the Stacking Order in Bilayer Graphene.” *Nano Letters* 16(10): 6403–10.

Tahara, Tahei, and Hiro-O Hamaguchi. 1993. “Picosecond Raman Spectroscopy Using a Streak Camera.” *Applied spectroscopy* 47(4): 391–98.

Tang, Yanhao et al. 2020. “Simulation of Hubbard Model Physics in WSe 2 / WS 2 Moiré Superlattices.” *Nature* 579(7799): 353-358.

Tassone, F., F. Bassani, and L. C. Andreani. 1992. “Quantum-Well Reflectivity and Exciton-Polariton Dispersion.” *Physical Review B* 45(11): 6023–30.

Terrones, H. et al. 2014. “New First Order Raman-Active Modes in Few Layered Transition Metal Dichalcogenides.” *Scientific Reports* 4(1): 4215.

Le Thomas, N., R. Houdré, M. V. Kotlyar, and T. F. Krauss. 2008. “Phase-Sensitive Fourier Space Imaging of Optical Bloch Modes.” *Physical Review B* 77(24): 245323.

Le Thomas, Nicolas et al. 2007. “Exploring Light Propagating in Photonic Crystals with Fourier Optics.” *Journal of the Optical Society of America B* 24(12): 2964.

Tiefenbacher, S., C. Pettenkofer, and W. Jaegermann. 2000. “Moire Pattern in LEED Obtained by van Der Waals Epitaxy of Lattice Mismatched WS2/MoTe2(0001) Heterointerfaces.” *Surface Science* 450(3): 181–90.

Tolpygo, K B. 1950. “PHYSICAL PROPERTIES OF A ROCK SALT LATTICE PHYSICAL PROPERTIES OF A ROCK SALT LATTICE MADE UP OF DEFORMABLE IONS.” Zh. Eksp. Teor. Fiz 20(6): 497-509.

Tongay, Sefaattin et al. 2013. “Broad-Range Modulation of Light Emission in Two-Dimensional Semiconductors by Molecular Physisorption Gating.” *Nano Letters* 13(6): 2831–36.

———. 2014. “Tuning Interlayer Coupling in Large-Area Heterostructures with CVD-Grown MoS2 and WS2 Monolayers.” *Nano Letters* 14(6): 3185–90.

Tornatzky, Hans, Anne-Marie Kaulitz, and Janina Maultzsch. 2018. “Resonance Profiles of Valley Polarization in Single-Layer MoS2 and MoSe2.” *Physical Review Letters* 121(16): 167401.

Tran, Kha et al. 2019. “Evidence for Moiré Excitons in van Der Waals Heterostructures.” *Nature* 567(7746): 71–75.

Trolle, Mads L., Thomas G. Pedersen, and Valerie Véniard. 2017. “Model Dielectric Function for 2D Semiconductors Including Substrate Screening.” *Scientific Reports* 7(1): 39844.

Turnbull, G. A. et al. 2005. “Effect of Gain Localization in Circular-Grating Distributed Feedback Lasers.” *Applied Physics Letters* 87(20): 201101.

Varshni, Y. P. 1967. “Temperature Dependence of the Energy Gap in Semiconductors.” *Physica* 34(1): 149–54.

Vasista, Adarsh B., Deepak K. Sharma, and G.V. Pavan Kumar. 2019. “Fourier Plane Optical Microscopy and Spectroscopy.” In *Digital Encyclopedia of Applied Physics*, Weinheim, Germany: Wiley-VCH Verlag GmbH & Co. KGaA, 1–14.

Vitale, Steven A. et al. 2018. “Valleytronics: Opportunities, Challenges, and Paths Forward.” *Small* 14(38): 1801483.

Voiry, Damien, Aditya Mohite, and Manish Chhowalla. 2015. “Phase Engineering of Transition Metal Dichalcogenides.” *Chemical Society Reviews* 44(9): 2702–12.

Walla, Frederik et al. 2018. “Anisotropic Excitation of Surface Plasmon Polaritons on a Metal Film by a Scattering-Type Scanning near-Field Microscope with a Non-Rotationally-Symmetric Probe Tip.” *Nanophotonics* 7(1): 269–76.

Wallauer, R. et al. 2016. “Intervalley Scattering in MoS2imaged by Two-Photon Photoemission with a High-Harmonic Probe.” *Applied Physics Letters* 109(16).

Wang, G. et al. 2014. “Non-Linear Optical Spectroscopy of Excited Exciton States for Efficient Valley Coherence Generation in WSe2 Monolayers.” *Physical Review B* 90(7): 075413.

———. 2017. “In-Plane Propagation of Light in Transition Metal Dichalcogenide Monolayers: Optical Selection Rules.” *Physical Review Letters* 119(4): 047401.

Wang, Gang et al. 2018a. “Colloquium : Excitons in Atomically Thin Transition Metal Dichalcogenides.” *Reviews of Modern Physics* 90(2): 021001.

———. 2018b. “Colloquium: Excitons in Atomically Thin Transition Metal Dichalcogenides.” *Reviews of Modern Physics* 90(2): 21001.

Wang, L. et al. 2013. “One-Dimensional Electrical Contact to a Two-Dimensional Material.” *Science* 342(6158): 614–17.

Wang, Lei et al. 2019. “Magic Continuum in Twisted Bilayer WSe2.” a*rxiV: 1910.12147*.

Wang, Xiaomu, and Fengnian Xia. 2015. “Stacked 2D Materials Shed Light.” *Nature Materials* 14(3): 264–65.

Wannier, Gregory H. 1937. “The Structure of Electronic Excitation Levels in Insulating Crystals.” *Physical Review* 52(3): 191–97.

Watanabe, Kenji, Takashi Taniguchi, and Hisao Kanda. 2004. “Direct-Bandgap Properties and Evidence for Ultraviolet Lasing of Hexagonal Boron Nitride Single Crystal.” *Nature Materials* 3(6): 404–9.

Weber, D., W. Petri, U. Woggon, and C. Klingshirn. 1997. “Quantum Beats of Exciton Polaritons in Hexagonal CdS Crystals.” *Physical Review B* 55(19): 12848–51.

Wei, Guohua et al. 2015. “Interfacing Monolayer MoS2 with Silicon-Nitride Integrated Photonics.” *Integrated Photonics Research, Silicon and Nanophotonics, IPRSN 2015*: 371p.

Weihs, Gregor, Hui Deng, Charles Santori, and Yoshihisa Yamamoto. 2003. “Dynamic Condensation of Microcavity Exciton Polaritons.” *2003 European Quantum Electronics Conference, EQEC 2003* 298(October): 183.

Weisbuch, C., M. Nishioka, A. Ishikawa, and Y. Arakawa. 1992. “Observation of the Coupled Exciton-Photon Mode Splitting in a Semiconductor Quantum Microcavity.” *Physical Review Letters* 69(23): 3314–17.

Weiser, G. 1973. “Modulation Spectroscopy on Anisotropic Systems.” *Surface Science* 37(C): 175–97.

Wierzbowski, Jakob et al. 2017. “Direct Exciton Emission from Atomically Thin Transition Metal Dichalcogenide Heterostructures near the Lifetime Limit.” *Scientific Reports* 7(1): 12383.

Wigner, E. 1934. “On the Interaction of Electrons in Metals.” *Physical Review* 46(11): 1002–11.

Wilson, J. A., and A. D. Yoffe. 1969. “The Transition Metal Dichalcogenides Discussion and Interpretation of the Observed Optical, Electrical and Structural Properties.” *Advances in Physics* 18(73): 193–335.

Withers, F. et al. 2015. “Light-Emitting Diodes by Band-Structure Engineering in van Der Waals Heterostructures.” *Nature Materials* 14(3): 301–6.

Wu, C. et al. 1991. “Optically Pumped Surface-Emitting Dfb GaInAsP/InP Lasers with Circular Grating.” *Electronics Letters* 27(20): 1819–21.

Wu, Congjun, Doron Bergman, Leon Balents, and S. Das Sarma. 2007. “Flat Bands and Wigner Crystallization in the Honeycomb Optical Lattice.” *Physical Review Letters* 99(7): 070401.

Wu, Fengcheng, Timothy Lovorn, and A. H. Macdonald. 2017. “Topological Exciton Bands in Moiré Heterojunctions.” *Physical Review Letters* 118(14): 147401.

Wu, Fengcheng, Fanyao Qu, and A. H. MacDonald. 2015. “Exciton Band Structure of Monolayer MoS2.” *Physical Review B* 91(7): 075310.

Wu, Kan et al. 2015. “WS_2 as a Saturable Absorber for Ultrafast Photonic Applications of Mode-Locked and Q-Switched Lasers.” *Optics Express* 23(9): 11453.

Wu, Sanfeng et al. 2014. “Control of Two-Dimensional Excitonic Light Emission via Photonic Crystal.” *2D Materials* 1(1): 011001.

———. 2015. “Monolayer Semiconductor Nanocavity Lasers with Ultralow Thresholds.” *Nature* 520(7545): 69–72.

Xi, Xiaoxiang et al. 2016. “Ising Pairing in Superconducting NbSe2 Atomic Layers.” *Nature Physics* 12(2): 139–43.

Xia, Fengnian et al. 2014. “Two-Dimensional Material Nanophotonics.” *Nature Photonics* 8(12): 899–907.

Xia, Ming et al. 2015. “Spectroscopic Signature of AA’ and AB Stacking of Chemical Vapor Deposited Bilayer MoS2.” *ACS Nano* 9(12): 12246–54.

Xiao, Di et al. 2012. “Coupled Spin and Valley Physics in Monolayers of MoS2 and Other Group-VI Dichalcogenides.” *Phys. Rev. Lett.* 108: 196802.

Xiao, Jun et al. 2015. “Nonlinear Optical Selection Rule Based on Valley-Exciton Locking in Monolayer WS2.” *Light: Science & Applications* 4(12): e366.

Xu, Xiaodong, Wang Yao, Di Xiao, and Tony F. Heinz. 2014. “Spin and Pseudospins in Layered Transition Metal Dichalcogenides.” *Nature Physics* 10(5): 343–50.

Y., Masumoto, Unuma Y., Tanaka Y., and Shionoya S. 1979. “Picosecond Time of Flight Measurements of Excitonic Polaritons in CuCl.” *Journal of the physical society of japan* 47(6): 1844–49.

Yang, Dan et al. 2014. “Synthesis of Two-Dimensional Transition-Metal Phosphates with Highly Ordered Mesoporous Structures for Lithium-Ion Battery Applications.” *Angewandte Chemie - International Edition* 53(35): 9352–55.

Yang, Eui-Hyeok et al. 2018. “Controlled Growth of 2D Heterostructures and Prevention of TMD Oxidation.” In *Micro- and Nanotechnology Sensors, Systems, and Applications X*, eds. M. Saif Islam, Achyut K. Dutta, and Thomas George. SPIE, 29.

Yang, Tiefeng et al. 2017. “Van Der Waals Epitaxial Growth and Optoelectronics of Large-Scale WSe2/SnS2 Vertical Bilayer p–n Junctions.” *Nature Communications* 8(1): 1906.

Yankowitz, Matthew et al. 2012. “Emergence of Superlattice Dirac Points in Graphene on Hexagonal Boron Nitride.” *Nature Physics* 8(5): 382–86.

———. 2019. “Tuning Superconductivity in Twisted Bilayer Graphene.” *Science* 363(6431): 1059–64.

Ye, Mingxiao, Dongyan Zhang, and Yoke Khin Yap. 2017. “Recent Advances in Electronic and Optoelectronic Devices Based on Two-Dimensional Transition Metal Dichalcogenides.” *Electronics* 6(2): 43.

Ye, Yu et al. 2015. “Monolayer Excitonic Laser.” *Nature Photonics* 9(11): 733-737.

Ye, Ziliang, Dezheng Sun, and Tony F. Heinz. 2017. “Optical Manipulation of Valley Pseudospin.” *Nature Physics* 13(1): 26–29.

Yokota, Ken Ichi, Gouo Kurata, Tomohiro Matsui, and Hiroshi Fukuyama. 2000. “Superconductivity in the Quasi-Two-Dimensional Conductor 2H-TaSe2.” *Physica B: Condensed Matter* 284–288: 551–52.

Yokoya, T. 2001. “Fermi Surface Sheet-Dependent Superconductivity in 2H-NbSe2.” *Science* 294(5551): 2518–20.

You, Yumeng et al. 2015. “Observation of Biexcitons in Monolayer WSe2.” *Nature Physics* 11(6): 477–81.

Yu, Hongyi et al. 2014. “Dirac Cones and Dirac Saddle Points of Bright Excitons in Monolayer Transition Metal Dichalcogenides.” *Nature Communications* 5(1): 3876.

———. 2017. “Moiré Excitons: From Programmable Quantum Emitter Arrays to Spin-Orbit–Coupled Artificial Lattices.” *Science Advances* 3(11): 1–8.

Yu, P., and M. Cardona. 2005. *Fundamentals of Semiconductors: Physics and Materials Properties*. Berlin, Heidelberg: Springer.

Yu, Yifei et al. 2016. “Engineering Substrate Interactions for High Luminescence Efficiency of Transition-Metal Dichalcogenide Monolayers.” *Advanced Functional Materials* 26(26): 4733–39.

Yu, Yijun et al. 2015. “Gate-Tunable Phase Transitions in Thin Flakes of 1T-TaS 2.” *Nature Nanotechnology* 10(3): 270–76.

Yu, Yiling et al. 2016. “Fundamental Limits of Exciton-Exciton Annihilation for Light Emission in Transition Metal Dichalcogenide Monolayers.” *Physical Review B* 93(20): 201111.

Yuan, Long et al. 2017. “Exciton Dynamics, Transport, and Annihilation in Atomically Thin Two-Dimensional Semiconductors.” *Journal of Physical Chemistry Letters* 8(14): 3371–79.

———. 2019. “Twist-angle-dependent interlayer exciton diffusion in WS2/WSe2 Heterobilayers.” *Nature Materials* 19(6): 617-623.

Yuan, Long, and Libai Huang. 2015. “Exciton Dynamics and Annihilation in WS2 2D Semiconductors.” *Nanoscale* 7(16): 7402–8.

Van Der Zande, Arend M. et al. 2014. “Tailoring the Electronic Structure in Bilayer Molybdenum Disulfide via Interlayer Twist.” *Nano Letters* 14(7): 3869–75.

Zeller, Patrick, Xinzhou Ma, and Sebastian Günther. 2017. “Indexing Moiré Patterns of Metal-Supported Graphene and Related Systems: Strategies and Pitfalls.” *New Journal of Physics* 19(1).

Zeng, Hualing et al. 2012. “Low-Frequency Raman Modes and Electronic Excitations In Atomically Thin MoS2 films.” *Physical Review B* 86(24): 241301.

Zhang, Chendong et al. 2017. “Interlayer Couplings, Moiré Patterns, and 2D Electronic Superlattices in MoS2/WSe2 Hetero-Bilayers.” *Science Advances* 3(1): e1601459.

Zhang, Hui et al. 2015. “Interference Effect on Optical Signals of Monolayer MoS2.” *Applied Physics Letters* 107(10): 101904.

Zhang, Jing et al. 2016. “Observation of Strong Interlayer Coupling in MoS2/WS2 Heterostructures.” *Advanced Materials* 28(10): 1950–56.

Zhang, Long et al. 2018. “Photonic-Crystal Exciton-Polaritons in Monolayer Semiconductors.” *Nature Communications* 9(1): 713.

Zhang, Nan et al. 2018. “Moiré Intralayer Excitons in a MoSe2 /MoS Heterostructure.” *Nano Letters* 18(12): 7651–57.

Zhang, Wei Li et al. 2019. “Polaritonic Manipulation Based on the Spin-Selective Optical Stark Effect in the WS 2 and Tamm Plasmon Hybrid Structure.” *Nanoscale* 11(10): 4571–77.

Zhang, Yi et al. 2010. “Crossover of the Three-Dimensional Topological Insulator Bi2Se3 to the Two-Dimensional Limit.” *Nature Physics* 6(8): 584–88.

Zhao, Weijie et al. 2013. “Lattice Dynamics in Mono- and Few-Layer Sheets of WS2 and WSe2.” *Nanoscale* 5(20): 9677.

Zhao, Yanyuan et al. 2013. “Interlayer Breathing and Shear Modes in Few-Trilayer MoS2and WSe2.” *Nano Letters* 13(3): 1007–15.

Zhong, Ding et al. 2017. “Van Der Waals Engineering of Ferromagnetic Semiconductor Heterostructures for Spin and Valleytronics.” *Science Advances* 3(5): e1603113.

Zhu, Dancheng et al. 2017. “Capture the Growth Kinetics of CVD Growth of Two-Dimensional MoS2.” *npj 2D Materials and Applications* 1(1): 8.

Zhu, Haiming et al. 2017. “Interfacial Charge Transfer Circumventing Momentum Mismatch at Two-Dimensional van Der Waals Heterojunctions.” *Nano Letters* 17(6): 3591–98.

Zimmermann, J. E., G. Mette, and U. Höfer. 2016. “Second-Harmonic Imaging Microscopy for Time-Resolved Investigations on Transition Metal Dichalcogenides.” *arxiV: 1608.03434*

Zinka, Srinivasa Rao. 2007. “On the Ludwig ’ s Definitions of Cross-Polarization.” XX(X): 1–5.

Zipfel, Jonas et al. 2019. “Exciton Diffusion in Monolayer Semiconductors with Suppressed Disorder.” *Physical Review B* 101(11): 115430.

Academic Contributions

Publications

K. Kantner, S. Asraf, S. Carregal-Romero, C. Carrillo-Carrion, M. Collot, P. del Pino, W. Heimbrodt, D. De Aberasturi, U. Kaiser, L. Kazakova, M. Lelle, N. de Baroja, J. Montenegro, M. Nazarenus, B. Pelaz, K. Peneva, P. Gil, N. Sabir, **L. M. Schneider**, L. Shabarchina, G. Sukhorukov, M. Vazquez, F. Yang, W. Parak, Particle-Based Optical Sensing of Intracellular Ions at the Example of Calcium - What Are the Experimental Pitfalls?, *Small* 8, 896-904 (2015)

W. Lai, N. Born, **L. M. Schneider**, A. Rahimi-Iman, J.C. Balzer, M. Koch, Broadband antireflection coating for optimized terahertz beam splitter, Opt. Mat. Ex. 5, 2812-2819 (2015)

R. Li[*], **L. M. Schneider**[*], W. Heimbordt, H. Wu, M. Koch, A. Rahimi-Iman, Gate Tuning of Förster Resonance Energy Transfer in a Graphene - Quantum Dot FET Photo-Detector, *Sci. Rep.* 6, 28224 (2016)

R. Gente, S. Busch, E. Stübling, **L. M. Schneider**, C. Hirschmann, J. Balzer, M. Koch, Quality Control of Sugar Beet Seeds With THz Time-Domain Spectroscopy, *IEEE Transactions on Terahertz Science and Technology* 6, 754-756 (2016)

S. Lippert[*], **L. M. Schneider**[*], D. Renaud, K.N. Kang, O. Ajayi, J. Kuhnert, M. Halbich, O.M Abdulmunem, K. Hassoon, S. Edalati-Boostan, Y.D. Kim, W. Heimbrodt, E-H. Yang, J.C. Hone, A. Rahimi-Iman, Influence of the substrate material on the optical properties of tungsten diselenide monolayers, *2D Mater*. 4, 025045 (2017).

L. M. Schneider[*], S. Lippert[*], J. Kuhnert[*], O. Ajayi, D. Renaud, S. Firoozabadi, Q. Ngo, R. Guo, Y.D. Kim, W. Heimbrodt, J.C. Hone, A. Rahimi-Iman, The influence of the environment on monolayer tungsten diselenide photoluminescence, *NANOSO* 15, 84-97 (2017).

D. Jahn, R. Eckstein, **L. M. Schneider**, N. Born, G. Hernandez-Sosa, J. C. Balzer, I. Al-Naib, U. Lemmer, M. Koch, Digital Aerosol Jet Printing for the Fabrication of Terahertz Metamaterials, Adv. Mater. Technol., 3, 1700236 (2017)

L. M. Schneider[*], S. Lippert[*], J. Kuhnert[*], D. Renaud, K.N. Kang, O. Ajayi, M.-U. Halbich, O. Abdulmunem, X. Lin, K. Hassoon, S. Edalati-Boostan, Y.D. Kim, W. Heimbrodt, E.H. Yang, J.C. Hone, A. Rahimi-Iman, The Impact of the Substrate Material on the Optical Properties of 2D WSe_2 Monolayers, *Semiconductors* 52, 565-571 (2018).

L. M. Schneider[*], J. Kuhnert[*], S. Lippert, D. Renaud, W. Heimbrodt, O. Ajayi, Y.D. Kim, J.C. Hone, K.N. Kang, E.H. Yang und A. Rahimi-Iman, Density-dependent Excitonic Properties and Dynamics in 2D Heterostructures consisting of Boron Nitride and Monolayer or fewlayer Tungsten Diselenide, *Proc. SPIE 10639, Micro- and Nanotechnology Sensors, Systems, and Applications X*, 106390V (2018).

O. Mey, F. Wall, **L. M. Schneider**, D. Günder, F. Walla, A. Soltani, H. Roskos, N. Yao, P. Qing, W. Fang, A. Rahimi-Iman, Enhancement of the Monolayer Tungsten Disulfide Exciton Photoluminescence with a Two-Dimensional Material/Air/Gallium Phosphide In-Plane Microcavity, *ACS Nano*, 13, 5259-5267 (2019).

D. Abdrabou, **L. M. Schneider**, A. Rahimi-Iman, M. A. Khedr, A. M. Hussien, T. El-Sherbini, Study of laser-induced-plasma parameters for molybdenum targets, Study of laser-induced-plasma parameters for molybdenum targets, Plasma Research Express, 1, 035004 (2019)

L. M. Schneider, J. Kuhnert, S. Schmitt, W. Heimbrodt, U. Huttner, L. Meckbach, T. Stroucken, S. W. Koch, S. Fu, X. Wang, K. Kang, E.-H. Yang, A. Rahimi-Iman, Spin-Layer- and Spin-Valley-Locking in CVD-Grown AA'- and AB-Stacked Tungsten-Disulfide Bilayers, *J. Chem. Phys. C,* 123, 21813-21821 (2019).

M. Shah*, **L. M. Schneider***, and A. Rahimi-Iman, Observation of Intralayer and Interlayer Excitons in Monolayered WSe2/WS2 heterostructure, *Semiconductors, 53, 2140-2146 (2019)*

L. M. Schneider, S. S. Esdaille, D. A. Rhodes, K. Barmak, J. C. Hone, A. Rahimi-Iman, Shedding Light on Exciton's Nature in Monolayer Quantum Material by Optical Dispersion Measurements, *Optics Express, 27, 37131 (2019)*

F. Wall, O. Mey, **L. M. Schneider**, Arash Rahimi-Iman, Continuously-tunable light–matter coupling in optical microcavities with 2D semiconductors, Sci. Rep., 10, 8303 (2020)

L. M. Schneider, S. S. Esdaille, D. A. Rhodes, K. Barmak, J. C. Hone, A. Rahimi-Iman, Direct Measurement of the Radiative Pattern of Bright and Dark Excitons and Exciton Complexes in Encapsulated Tungsten Diselenide, *Sci. Rep., 10, 8091 (2020)*

L. M. Schneider, S. S. Esdaille, D. A. Rhodes, K. Barmak, J. C. Hone, A. Rahimi-Iman, Optical Measurement of Pseudo-Spin Texture of the Exciton Fine-Structure in Monolayer WSe_2 within the Light Cone, submitted (2020), online on ArxiV: 2005.13900

K. Krüger, J. Onrik, **M. Schneider**, A. Jäckel, C. L. Koch-Dandolo, E. Castro-Camus, M. Koch, W. Viöl, Terahertz inspection of buildings and architectural art, submitted (2020)

* These authors contributed equally.

Conference Contributions

L. M. Schneider* et al., calcium sensing with nanoparticles, 1st Sino-German Symposium on Functional (Nano-)Biomaterials Sciences, Marburg, Germany 2014

N. Born*, **L. M. Schneider**, J. Balzer, I. Al-Naib, R. Singh, A. Velauthapillai, M. Scheller, J. V. Moloney, Martin Koch, Multi-band Metamaterials with a Distinguished Angular Sensitivity, 40th International Conference on Infrared, Millimeter, and Terahertz Waves (IRMMW-THz) 2015.

N. Born, **L. M. Schneider***, J. Balzer, I. Al-Naib, R. Singh, A. Velauthapillai, M. Scheller, J. V. Moloney, Martin Koch, Multi-band metamaterials with a distinguished angular sensitivity.", 8th THz Days 2015

U. Kaiser*, M. Wilhelm, J. Röder, N. Sabir, **L. M. Schneider**, P. del Pino, C. Carrillo-Carrion, W. Parak, and W. Heimbrodt, Energy transfer characteristics of Mn doped CdS/ZnS quantum dots, DPG Frühjahrstagung 2015

L. M. Schneider*, R. Li, W. Heimbrodt, H. Wu, M. Koch, A. Rahimi-Iman, Gate-Voltage Dependency of Förster Transfer in Graphene - Quantum Dot Photo Detection, CLEO 2016

L. M. Schneider, R. Li, W. Heimbrodt, H. Wu, M. Koch, A. Rahimi-Iman*, Gate-Voltage Dependency of Förster Transfer in Graphene-Quantum-Dot Photodetection, 24th International Symposium Nanostructures: Physics and Nanotechnology (NANO2016), St. Petersburg, Russia 2016

R. Li, **L. M. Schneider**, W. Heimbrodt, H. Wu, M. Koch, A. Rahimi-Iman*, Gate-Voltage Dependency of Förster Resonance Energy Transfer in Graphene, International Conference on Internal Interfaces (ICII-2016), Marburg, Germany 2016

L. M. Schneider, P. Lu*, R. Li, A. Rahimi-Iman, H. Wu, Systematic Study on the Band Alignement of cQD-Graphene Heterostructures, Annual Meeting NSRL Hefei, China 2016

L. M. Schneider*, D. Jahn, R. Eckstein, U. Lemmer, N. Born, J. C. Balzer, M. Koch, Aerosol printed THz metamaterial with angle dependent resonance, Annual meeting Deutsches Terahertz Zentrum 2016

R. Gente, S. F. Busch, E.-M. Stübling, **L. M. Schneider**, C. B. Hirschmann, O. Peters, R. Holzwarth, T. Müller-Wirts, J. C. Balzer*, M. Koch, Detection good and faulty sugar beet seeds using THz time domain spectroscopy, OTST 2017

S. Lippert, **L. M. Schneider**, D. Renaud, K. N. Kang, O. Ajayi, M. Halbich, O. Abdulmunem, X. Lin, J. Kuhnert, K. Hassoon, S. Edalati-Boostan, Y. Duck Kim, W. Heimbrodt, E.-H. Yang, J. Hone, A. Rahimi-Iman*, The Influence of the Substrate Material on the Optical Properties of Tungsten-Diselenide Monolayer, 25th International Symposium Nanostructures: Physics and Technology (NANO2017), St. Petersburg, Russia 2017

S. Lippert, **L. M. Schneider***, D. Renaud, K. N. Kang, O. Ajayi, M. Halbich, O. Abdulmunem, X. Lin, J. Kuhnert, K. Hassoon, S. Edalati-Boostan, Y. Duck Kim, W. Heimbrodt, E.-H. Yang, J. Hone, A. Rahimi-Iman, The Influence of the Substrate Material on the Optical Properties of Tungsten-Diselenide Monolayer, DPG Frühjahrstagung 2017

L. M. Schneider*, S. Lippert, D. Renauld, J. Kuhnert, K. N. Kang, O. Ajayi, M.-U. Halbich, O. M. Abdulmunem, X. Lin, K. Hassoon, S. Edalati-Boostan, Y. Duck Kim, W. Heimbrodt, E.-H. Yang, J. C. Hone, A. Rahimi-Iman, The Influence of the Substrate Material on the optical properties of Tungsten Diselendide Monolayers, CLEO 2017

L. M. Schneider*, S. Lippert, J. Kuhnert, O. Ajayi, D. Renaud, Y. D. Kim, W. Heimbrodt, J. C. Hone, A.Rahimi-Iman, The Influence of the environment on monolayer tungsten diselenide photoluminescence, DPG Frühjahrstagung 2018

L. M. Schneider, J. Kuhnert, W. Heimbrodt, K. Kang, Y. D. Kim, E.-H. Yang, J. C. Hone, A. Rahimi-Iman*, The Influence of the environment on optical properties of 2D semiconductors, 1st Sino-German Symposium on Functional Nano-Materials Sciences (FNMS2018), Hangzhou, China

L. M. Schneider*, J. Kuhnert, S. Lippert, D. Renauld, W. Heimbrodt, O. Ajayi, Y.D. Kim, J. C. Hone, K. N. Kang, E. H. Yang, A. Rahimi-Iman, Density-dependent excitonic properties and dynamics in 2D heterostructures consisting of boron nitride and monolayer or few-layer tungsten diselenide, SPIE Defense and Commercial Sensing 2018, Micro- and Nanotechnology Sensots, Systems, and Applications X (invited talk, substituting A. Rahimi-Iman)

J. Kuhnert*, **L. M. Schneider**, S. Lippert, D. Renaud, O. Ajayi, Y. D. Kim, W. Heimbrodt, J. Hone, Arash Rahimi-Iman, The Influence of hBN on the Pump-dependent Time-evolution of Monolayer Photoluminescence in WSe2, CLEO 2018

L. M. Schneider*, J. Kuhnert, D. Renaud, S. Firoozabadi, O. Ajayi, Y. D. Kim, W. Heimbrodt, J. Hone, A. Rahimi-Iman, Exciton Dynamics in WSe2 Monolayers for Different Stacking Schemes Involving h-BN, CLEO 2018

H. Alaboz*, **M. Schneider**, J. Ornik, E. Stünling, D. Jahn, M. Koch, A laser cut THz metal mesh bandpass filter with high transmission, EOS Topical Meeting on Terahertz Science & Technology (TST 2018)

L. M. Schneider*, J. Kuhnert, S. Schmitt, U. Huttner, L. Meckbach, T. Strouken, S. W. Koch, W. Heimbrodt, S. Fu, X. Wang, K. N. Kang, A. Rahimi-Iman, Optical Valleytronic Properties of CVD-grown Tungsten Disulfide AA' and AB Bilayers, DPG Frühjahrstagung 2019

O. Mey, F. Wall, **L. M. Schneider***, F. Walla, A. Soltani, H. G. Roskos, N.Yao, P. Quing, W.Fang, A. Rahimi-Iman, Enhanced Photoluminescence from Monolayer WS2 Excitons with a 2D-material-air-GaP in-plane Microcavity, DPG Frühjahrstagung 2019

J. Ornik*, Y. Zhang, **M. Schneider**, M. Taherkhani, H. Alaboz, M. Koch, THz Gratings Produced By Laser Cutting, 44th International Conference on Infrared, Millimeter, and Terahertz Waves (IRMMW-THz) 2019.

K. Krüger, J. Ornik*, **M. Schneider**, A. Jaeckel, E. Castro-Camus, M. Koch, W. Vioel, On-site Inspection of Conservation Works Using THz TDS, 44th International Conference on Infrared, Millimeter, and Terahertz Waves (IRMMW-THz) 2019.

O. Mey, F. Wall, **L. M. Schneider**, D. Günder, F. Walla*, A. Soltani, H. G. Roskos, N. Yao, P. Qing, W. Fang, A. Rahimi-Iman, Near-field nano-imaging of buried microcavity for enhancement of WS2 monolayer exciton photoluminescence, 10th International Conference on Metamaterials, Photonics Crystals and Plasmonics (META2019), Lisbon, Portugal 2019

L. M. Schneider*, J. Kuhnert, S. Schmitt, U. Huttner, L. Meckbach, T. Stroucken, S. W. Koch, W. Heimbrodt, S. Fu, X. Wang, K. Kang, E.-H. Yang, A. Rahimi-Iman, Spin-Layer- and Spin-Valley-Locking due to Symmetry in Differently-Stacked Tungsten Disulfide Bilayers, CLEO Europe/EQEC 2019

L. M. Schneider, S. S. Esdaille, D. A. Rhodes, K. Barmak, J. C. Hone, A. Rahimi-Iman*, Direct Optical Evidence of Free Excitons in a Monolayer Quantum Material and Effective-Mass Measurements, CLEO Europe/EQEC 2019

Danksagung

Ich danke Prof. Koch, für die Möglichkeit der Promotion und die vielfältigen Forschungstätigkeiten von THz-Metamaterialien über archäologische, biologische Untersuchungen, neuronalen Netzwerken für Proof-of-Principal Demonstrationen für die Anwendung bis zur Halbleitergrundlagenforschung. Des Weiteren danke ich für die lockere Atmosphäre und das gute Arbeitsklima in seiner Gruppe.
Dr. Arash Rahimi-Iman danke ich für die Aufnahme in sein Team, viele hilfreiche Diskussion und die langjährige Betreuung meiner Forschungsarbeiten. Darüber hinaus danke ich für die Ermöglichung wertvoller internationaler Kooperationen und Auslandaufenthalte, worüber die essenziellen hochwertigen Proben bezogen und neue Untersuchungen in die Wege geleitet werden konnten. Des Weiter danke ich Dr. Chernikov, Prof. Dehnen und Prof. Gebhard dass Sie sich bereit erklärt als Prüfer für diese Dissertation zu Verfügung zu stehen.

Prof. Heimbrodt gilt mein Dank für hilfreiche Diskussionen und die unkomplizierte Nutzung seiner Labore und das ebenso unkomplizierte Ausleihen allerlei optischer Komponenten. Des Weiteren Prof. Weiser für hilfreiche Stichworte über Exzitonen-Polaritonen.

Meinen ehemaligen Dr. Sina Lippert, Dr. Jan Kuhnert, und Marc Halbich danke ich für die gute Zusammenarbeit, die guten Daten und die nette Atmosphäre auch an langen Messtagen. Außerdem meinen Studenten Saleh Firoozabadi, Manan Shah, Oliver Mey, Franziska Wall, Quyet Ngo, Leonie Gomell, Chirag Palekar und Shachi Machchhar für gute Daten, gute Zusammenarbeit und eine gute Büroatmosphäre. Darüber hinaus danke ich Dylan Renaud für das Herstellen benötigter Probe über Nacht und die Unterweisung in der Herstellung exfolierter und gestapelter Monolagen ohne die weite Teile dieser Arbeit nicht möglich gewesen wären.

Dr. David Jahn, Dr. Ralf Gente und Jan Ornik für die gute Zusammenarbeit an allerlei THz Projekten sowie für die netten Dienstreisen. Dr. Marina Gerhard für die Einführung in die Messung zeitaufgelöster Photolumineszenzmessungen und der Ti:Sa Justage ohne die viele Messungen ebenfalls nicht möglich gewesen wären. Darüber hinaus für die schönen Bananenpflanzen im Büro, welche die Arbeit im Büro angenehmer gestaltet haben. Marcel Weidenbach für Hilfe und Einführung in den 3D-Druck sowie Ralf Gente für die Einführung in das Machine Learning. Lars Meckbach und Dr. Tineke Stroucken für gute Diskussionen und hilfreiche Rechnungen. Christian Kriso, Mohammed Aly und Markus Stein danke ich für die guten Gespräche und Diskussionen und so manch guten Ratschlag sowie allen derzeitigen und ehemaligen Mitgliedern der Koch und Heimbrodt Gruppe mit denen ich zusammen forschen durfte danke ich für die gute Zusammenarbeit und die lockere Atmosphäre.

Prof. Eui-Hyeok Yang und Dr. Kyungnam Kang für das mehrfacht Wachstum und die zuvorkommende Bereitstellung guter CVD Proben. Sowie Prof. James. Hone, Prof. Daniel Rhodes, Prof. Katayun Barmak and Shanece S. Esdaille für hochqualitative exfolierte und eingekapselte Proben und den schnellen Nachschub für publikationsrelevante Nachmessungen. Ebenso Prof. Huizen Wu und Prof. Wei Fang für die diverse Unterstützungen im Rahmen der Zusammenarbeit mit dem Team sowie die freundliche Aufnahme in die Forschungsgruppe während des Auslandsaufenthaltes. Ebenfalls Prof. Roskos, Dr. Amin Sultani und Frederik Wall für die gute Zusammenarbeit bei SNOM und AFM Messungen. Darüber hinaus danke ich allen verbliebenen Koautoren für die gute Resultate und die gute Zusammenarbeit.

Dem MiNa-Gießen insbesondere Dr. Henning für die unkomplizierte Nutzung des Reinraums und die fachmännische Unterstützung sowie den feinmechanischen und elektronische Werkstätten für hilfreiche Diskussionen, Reparaturen und Fertigung benötigter Teile.

Dem DAAD, MARA sowie Prof. Koch für die Finanzierung etlicher Dienstreisen in die USA. Sowie der DFG und dem BMBF für die Finanzierung der Projekte und meiner Stelle.

Zu guter Letzt meiner Lebensgefährtin Malina Schöne und meiner Familie fürs Rücken freihalten, Verständnis und Geduld an langen Messtagen und der Korrektur der Dissertation.